

**Finite element evaluation and
experimental validation by selective laser
melting of metallic auxetic structures for
enhanced performance attributes**

Kusum Meena

A thesis submitted to
Auckland University of Technology in fulfilment of the
requirement for the degree of Doctor of Philosophy

July 2019

School of Engineering, Computer and Mathematical Sciences

Abstract

Auxetic metamaterials exhibit certain extraordinary properties such as negative Poisson's ratios, which means lateral compression and expansion under compressive and tensile loads respectively. This abnormal deformation of these materials eventually leads to the enhancement of some mechanical properties in the form of enhanced shear resistance, indentation resistance, fracture resistances etc., and qualify them to be used in numerous applications areas, be it medical, such as stents with controlled deformation or industrial, for example, as crash-worthy helmets. Over the years, numerous structural auxetic forms evolved, falling into a general classification of three specific groups, re-entrant, chiral, and rotating units. While analytical models dominated these endeavours and went far ahead in claiming extremely auxetic nature with specific structural models, the main bottleneck had always been the physical implementation of the structures and the experimental verification of the analytical claims.

The volumetric compression methods in single and multi-stage heating and compression, the thermoforming route, melt-spinning techniques, chemical and mechanical compression method and the CO₂ gas assisted compression techniques evolved in the past, but for most part these were restricted to developing simple polymeric or metallic auxetic foams. With the recent developments in additive manufacturing, the freedom to produce more complex auxetic shapes is enhanced significantly. However, the overall development considering metallic materials and selective laser melting technique was still limited. Also the focus was mainly limited to geometrically optimising the structures for better auxeticity of the re-entrant structures. The other structural forms such as

square grid and chiral forms did not get much attention. The critical aspects of structural analyses such as stress concentration effects were also neglected largely. The research reported in this thesis is designed to address these issues and fill the gaps.

The square-grid auxetic structure is used initially as the basis for developing the experimental and numerical schemes and their integration to find answers to the research questions raised. Numerical simulations based on the finite element methods and the compression tests conducted on laser melted structures are used to correlate the data generated and fine-tune and bring the numerical schemes close to the reality. The final numerical simulation schemes are then used to optimise the square-grid structures into non-square-grid structures, targeting much higher auxetic responses, which led to the invention of a non-square grid form with Poisson's ratio as high as -7. Further, the numerical schemes established are also used to evaluate the stress concentration aspects which eventually led to the design of a new chiral type S-shaped structural form. The new S-shaped structure is auxetic to a reasonable extent, while also allowing to avoid the stress concentration issues but at the cost of reduced mechanical properties against the re-entrant structural model. Further, a few hybrid structures were also proposed and evaluated which outperformed the parent S-shaped models, by means of acquiring the best qualities of both the unit cells used to form the structures. Overall, the fabrication of metallic auxetic structures by selective laser melting together with the optimisation by the finite element schemes proved to be effective in developing truly auxetic structures with controlled responses and performance attributes and ready for real world applications.

List of Publications

Journal Articles:

Meena, K., Calius, E. P., & Singamneni, S. (2019). An enhanced square-grid structure for additive manufacturing and improved auxetic responses. *International Journal of Mechanics and Materials in Design*, 15(2), 413-426.

Meena, K., & Singamneni, S. (2019). A new auxetic structure with significantly reduced stress concentration effects. *Materials & Design*, 173, 107779.

Meena, K., & Singamneni, S. (2019). The role of filleting on the stressed state of a square grid auxetic structure. *Procedia Manufacturing*, 30, 650-657.

Meena, K. and Singamneni, S. B., Hybrid S-shaped auxetic structures for enhanced auxeticity and in-plane mechanical properties. To be communicated shortly.

Table of Contents

Abstract.....	II
List of Publication.....	IV
List of Figures.....	X
List of Tables	XVIII
List of terms and Abbreviations	XIX
Attestation of Authorship	XXI
Acknowledgments	XXII

Chapter 1 Introduction

1.1. Auxetic mechanical metamaterials.....	1
1.2. Conventional manufacturing.....	5
1.3. Evolution of the different auxetic structures.....	7
1.4. Additive manufacturing.....	8
1.5. Research gaps and objectives.....	11
1.6. Thesis structure.....	13

Chapter 2 Literature review, research gaps, questions, and objectives

2.1. Structure-based material attributes	15
2.2. Applications in different areas.....	16

2.2.1 Medical applications.....	16
2.2.2 Industrial applications.....	20
2.3. Conventional Processing methods.....	24
2.4. Auxetic models.....	27
2.4.1 The Re-entrant model.....	27
2.4.2 Chiral.....	34
2.4.3 Rotating units.....	36
2.5. Additive manufacturing.....	40
2.6. Research gaps, questions and hypotheses.....	59
2.7. General methodology.....	66

Chapter 3 Methodology

3.1. The overall scheme of the research.....	68
3.2. CAD modelling.....	69
3.3. Finite element simulations.....	72
3.4. Selective laser melting.....	75
3.5. Post processing.....	79
3.6. Characterisation.....	83
3.6.1. Mechanical testing.....	83
3.6.2. Data extraction and analysis.....	86

3.6.3. Structural deflection.....	88
-----------------------------------	----

Chapter 4 Enhancing the auxetic responses of a square grid structure

4.1. The square grid structure.....	95
4.2. CAD modelling.....	98
4.3. Simulation.....	100
4.3.1. Effects of varying the flap angle and the thickness.....	102
4.3.2. Role of the H/L ratio and the stress concentration in the structure.....	103
4.4. Additional experimental details.....	104
4.5. Results and discussion.....	105
4.5.1. Experimental and numerical verification of the initial square grid structure.....	105
4.5.2. Roles of the flap inclination angle and the strut thickness.....	107
4.5.3. Optimisation of the H/L ratio.....	112
4.5.4. Experimental verification of the optimized structure.....	117
4.5.5. Stress concentration effects of the auxetic geometry.....	121
4.6. Summary of the evaluation of the square grid structure.....	129

Chapter 5 Stress concentration effects and an enhanced auxetic structure

5.1.	Auxetic structures and stress concentrations.....	131
5.2.	CAD modelling	132
5.3.	Analytical and experimental methods.....	134
5.3.1	<i>Analytical modelling</i>	134
5.3.2	<i>Experimental methods</i>	139
5.3.3	<i>Finite element simulation</i>	140
5.4.	Results and discussion.....	144
5.4.1	<i>Deformation modes</i>	144
5.4.2	<i>Analytical results</i>	146
5.4.3	<i>Mechanical Characterisation</i>	149
5.4.4	<i>Numerical Simulation</i>	153
5.5.	Summary of auxetic S-structure and stress concentration.....	158

Chapter 6 Hybrid auxetic structures to enhance the in plane mechanical properties

6.1.	Enhancement of the in plane mechanical properties.....	160
6.2.	Design, simulation and mechanical testing.....	162

<i>6.2.1 CAD modelling</i>	162
<i>6.2.2 Mechanical testing, measurements and numerical simulation</i>	166
6.3. Results and discussion	169
<i>6.3.1 Deformation modes</i>	169
<i>6.3.2 Mechanical characterisation</i>	173
<i>6.3.3 Numerical simulations</i>	184
6.4. Summary	190

Chapter 7 Conclusions

7.1. Objectives and Achievements	192
7.2. General Conclusions	194
7.3. Quantitative Conclusions	197
7.4. Future Scope	201
References	203
Appendices	221
Critical values of θ , k and γ and their interdependence in the S-shaped structure.....	221

List of Figures

Fig. 2.1 Normal and auxetic behaviour of materials under tension and compression (Novak et al. 2016).....	14
Fig. 2.2 Differential deformation under indentation of non-auxetic and auxetic materials (Evans and Alderson 2000).....	16
Fig. 2.3 Dilator employing an auxetic end sheath (Evans and Alderson 2000)....	17
Fig. 2.4 Deformation behaviour of the artificial artery made up of (a) Non-auxetic material (b) Auxetic material (Evans and Alderson 2000).....	18
Fig. 2.5 Behaviour of (a) Non-auxetic and (b) Auxetic material under bending (Lakes 1987).....	21
Fig. 2.6 Piezoelectric composite sensor (a) Non-auxetic ceramic cores within auxetic polymer matrix (b) lateral contraction of auxetic polymer matrix allowing lateral expansion to ceramic cores for enhanced device sensitivity (Evans and Alderson 2000).....	22
Fig. 2.7 2D Re-entrant honeycomb deformation mechanism under uniaxial tensile loading (Robert 1985).....	28
Fig. 2.8 Cell geometries used by Masters et al. (Masters et al. 1996) (a) hexagonal and (b) re-entrant cells.....	29
Fig. 2.9 Two forms proposed by Smith et al. (Smith et al. 2000) (a) intact and (b) Missing rib model.....	31
Fig. 2.10 Square grid structure (a) Unit cell (b) deformed unit cell (Gasper et al. 2005).....	32

Fig. 2.11 The re-entrant design of (a) double arrowhead, (Larsen et al. 1997) (b) star re-entrant honeycomb (Grima et al. 2005), and (c) sinusoidal re-entrant models (Warmuth et al. 2016)	34
Fig. 2.12 Chiral structure (a) Unit cell and (b) deformation kinematics of ligaments (Prall and Lakes 1997).....	35
Fig. 2.13 The chiral unit cells of n=3, 4 and 6 rotational symmetry and the meta chiral model developed by Grima et al. (Grima et al. 2008).....	36
Fig. 2.14 The rotating rigid auxetic model of (a) rectangles (Grima et al. 2005) (b) Triangles (Grima et al. 2006)	37
Fig. 2.15 Rotating semi rigid square model (Grima et al. 2007).....	38
Fig. 2.16 The3D tetrapod re-entrant auxetic structure (a) 3D unit cell (b) top view and (c) side view (Schwerdtfeger et al. 2010).....	42
Fig. 2.17 (a) the four structural forms and (b) Design parameters of the 2-D re-entrant lattice structures (Yang et al. 2012a).....	43
Fig. 2.18 Re-entrant unit cell with stiff (light) and elastic (dark region) material (Wang et al. 2015).....	45
Fig. 2.19 (a) Conventional and (b) Modified re-entrant auxetic unit cell (Li et al. 2016).....	46
Fig. 2.20 Auxetic re-entrant 3D unit cell (Fu et al. 2016).....	47
Fig. 2.21 (a) Conventional and (b) Modified re-entrant auxetic unit cell (Xiong et al. 2017).....	48
Fig. 2.22 The re-entrant (a) 2D honeycomb, (b) 3D unit cell (c) fully fledged 3D auxetic structure (Xue et al. 2018).....	49

Fig. 2.23 a) Decagonal honeycomb b) cubic floral honeycomb, and conventional c) Cubic sinus wave and d) cubic chiral honeycomb (Rehme and Emmelmann et al. 2009).....	50
Fig. 2.24 Cubic chiral (a) front view (b) bottom view and (c) 3D view of the structure (Warmuth et al. 2016).....	51
Fig. 2.25 3D Auxetic metamaterial (a) designed metamaterial with and without support (b) 3D printed auxetic structure with and without support (Shen et al. 2014).....	52
Fig. 2.26 3D bcc 6H Auxetic bucklicrystal (a) front view (b) 3D view (c) 3D printed structure (Yuan et al. 2016).....	53
Fig. 2.27 Different forms of re-entrant auxetic structures (a) conventional re-entrant (b) modified re-entrant (c) re- entrant hybrid AH- V1 (d) re-entrant hybrid AH- V2 (Ingrole et al. 2017).....	54
Fig. 2.28 Auxetic hybrid structure (a) Unit cells (b) fully developed hybrid structure (Jiang and Li 2018).....	55
Fig. 2.29 Interlocking assembly fabrication of 3D re-entrant auxetic structures (Wang et al. 2016).....	56
Fig. 3.1 (a) 2D Sketching and (b) 3D extrusion form of a unit cell in SolidWorks 2015.....	71
Fig. 3.2 Schematic diagram of selective laser melting technique (Jiao et al. 2018).....	75
Fig. 3.3 Renishaw AM400 SLM machine (from AUT 3D Printing Lab).....	77
Fig. 3.4 (a) 3D CAD models of different structures (b) Selective laser melted structures built on a single build-plate stacking one over the other.	78
Fig. 3.5 Nabertherm heat treatment furnace (AUT 3D Printing Lab).....	79

Fig. 3.6 Schematic diagram of wire electric discharge machining (American Wire EDM).....	81
Fig. 3.7 Wire electron discharge machining equipment (AUT Mechanical Lab)	81
Fig. 3.8 Tinius Olsen tensile testing machine used for the compression tests (at AUT Mechanical Lab).....	84
Fig. 3.9 Graphic user interface of the WebPlotDigitizer.....	86
Fig. 3.10 Schematic of the principle of laser triangular measurement technique (www3.panasonic.biz).....	90
Fig. 3.11 The laser displacement setup (Materials testing lab, AUT).....	90
Fig. 3.12 Image capturing setup during compression testing (at AUT Mechanical Lab).....	92
Fig. 4.1 2D sketch of (a) a network of cells and (b) missing rib model after removing the selected cells (Smith et al. 2000).....	96
Fig. 4.2 (a) The unit cell (b) 2D sketch and (c) 3D CAD model of the initial square grid auxetic structure.....	97
Fig. 4.3 Lateral displacement with varied mesh size.....	99
Fig. 4.4 Compression tests on the initial square grid structure printed by laser melting CoCr (a) Prior to compression (b) at the maximum compression.....	102
Fig. 4.5 Finite element simulation of the initial square-grid structure of CoCr alloy (a) prior to compression (b) under compression.....	104
Fig. 4.6 (a) Lateral displacement vs. force (b) lateral displacements vs. longitudinal displacements in both experimental and numerical cases.....	105
Fig. 4.7 Finite element simulations of obtained lateral displacements for (a) 0° (b) 10° (c) 15° (d) 20° (e) 25° (f) 30° flap angles.....	106

Fig. 4.8 Finite element simulation of Poisson's ratio vs. flap angle.....	107
Fig. 4.9 FEM simulation of square grid structure with the varying thickness of (a) 1.5 mm (b) 2 mm (c) 2.5 mm (d) 3mm.....	108
Fig. 4.10 Strut thickness versus Poisson's ratio based on FE simulation.....	109
Fig. 4.11 FEM simulation of decreasing H/L ratios (a) 1 and (b) 0.6.	110
Fig. 4.12 Finite element simulation images for H/L ratio 1 (a) Von Mises stress (b) lateral displacement.....	112
Fig. 4.13 Finite element simulation images for H/L ratio 2 (a) Von Mises stress (b) lateral displacement.....	112
Fig. 4.14 Finite element simulation images for H/L ratio 3 (a) Von Mises stress (b) lateral displacement.....	113
Fig. 4.15 Effect of H/L ratio over Poisson's ratio.....	115
Fig. 4.16 3D printed square grid structure (a) Prior to compression (b) after compression (c) Image processed deformed structure.....	116
Fig. 4.17 Poisson's ratio vs compressive loads in the non-square grid structure.....	117
Fig. 4.18 Auxetic nature of the 3D non-square-grid structure (a) CAD model, (b) finite element simulated the deformed structure.....	118
Fig. 4.19 Finite element mesh of (a) Non-fillet and (b) Filleted ($r=0.5$ mm) square grid structures.....	120
Fig. 4.20 Effect of Fillet radius on stress distribution patterns with fillet radius (a) 0 mm, (b) 1 mm and (c) 1.5 mm for linear elastic analysis.....	121
Fig. 4.21 Effect of Fillet radius on (a) Poisson's ratio and (b) maximum Von-Mises stress with the linear materials option.....	123

Fig. 4.22 Effect of Fillet radius on stress distribution patterns with fillet radius (a) 0 mm, (b) 1 mm and (c) 1.5 mm for non- linear materials.....	124
Fig. 4.23 Effect of Fillet radius on (a) Poisson's ratio; (b) Von-Mises stress for non-linear material analysis.....	126
Fig. 5.1 The unit cell (a) & (d), 2D (b) & (e) and 3D (c) & (f) CAD model of the S-shaped and Re-entrant structures.....	132
Fig. 5.2 (a) The S-shaped unit cell (b) Simplified undeformed and deformed model of the S-shaped unit cell.....	133
Fig. 5.3 Geometrical parameters of 2D model of S-shaped unit cell.....	138
Fig. 5.4 Finite element mesh of (a) Re-entrant and (b) S- shaped structures.....	141
Fig. 5.5 Sequence of pictures for applied displacement of re-entrant (a to e) and s structures (f to j); recorded frames corresponding to displacement boundary conditions: (a) & (f) 0mm, (b) & (g) 5mm, (c) &(h) 10mm, (d) & (i) 15mm, and (e) & (j) 20mm,.....	143
Fig. 5.6 Poisson's ratio variation w.r.t to θ_1 and θ_2 for (a) &(b) Unit cell 1 (c) & (d) Unit cell 2 (e) & (f) Unit cell 3 (g) & (h) Unit cell 4.....	146
Fig. 5.7 The nominal stress-strain curve for (a) S-shaped (S1, S2, and S3) and (b) re-entrant (R1, R2, and R3) structures.....	149
Fig. 5.8 Variation of Poisson's ratios with the applied strain in S and re-entrant structures.....	150
Fig. 5.9 Numerical simulation of re-entrant and S-shaped structures based on the linear ((a) and (c)), and non-linear ((b) and (d)) material conditions.....	152
Fig. 5.10 Numerical simulation of obtained lateral deformation of the (a) Re-entrant and the (b) S-shaped structures for the same longitudinal load.	153

Fig. 5.11 Experimentally and numerically obtained deformation patterns of the S Structure at different levels of applied strains.....	155
Fig. 5.12 Comparative sequence deformation modes of experimental and numerical analysis for the given applied strain.....	156
Fig. 6.1 The unit cell CAD models of (a) the re-entrant (b) the S-shaped and (c) the star shaped re-entrant designs.....	161
Fig. 6.2 The front elevation and the isometric rendering of the re-entrant (a & b), S-shaped (c & d), H1 (e & f), H1NC (g & h), H2 (l & j) and H2NC (k & l) structures.....	163
Fig. 6.3 Finite element mesh and boundary conditions applied on (a) Re-entrant and (b) S- shaped (c) Hybrid H1 (d) Hybrid H1 NC (e) Hybrid H2 (f) Hybrid H 2 NC structures.....	166
Fig. 6.4 Deformation modes of the re-entrant, S-shaped and hybrid auxetic structures.....	169
Fig. 6.5 The nominal stress-strain curves for (a) re-entrant (b) S-shaped (c) H1 (d) H1NC (e) H2 (f) H2NC structures.....	173
Fig. 6.6 Comparative levels of Young's modulus responses of the R, S and hybrid structural models (H1, H1NC, H2 and H2NC).....	177
Fig. 6.7 Comparative compressive strength representation of R, S and hybrid structural models (H1, H1NC, H2 and H2NC)	178
Fig. 6.8 Poisson's ratio vs nominal strain plots for (a) re-entrant (b) S-shaped (c) H1 (d) H1NC (e) H2 and (f) H2NC structures.....	181
Fig. 6.9 Von Mises stress distribution patterns in the (a) R, (b) S, (c) H1 (d) H1NC (e) H2 (f) H2NC structures based on the non- linear material conditions.....	184

Fig. 6.10 Numerical and experimental deformation corresponding to -5 mm of displacement load for S and all hybrid structural models.....	186
Fig. 6.11 Comparative chart of numerically and experimentally evaluated Poisson's ratio of all the structural models for the same loading condition.....	188

List of Tables

Table 2.1 Elastic constants of the honeycomb model as developed by Masters et al. (Masters et al. 1996) based on different deformation mechanisms.....	30
Table 2.2 Analytical models for lozenge and square grid models.....	33
Table 2.3 Analytically developed equations of rotating rigid and semi-rigid models.....	39
Table 5.1 Significant geometrical parameters of the unit cells.....	131
Table 5.2 Varied geometrical parameters of the S-shaped structure.....	139
Table 5.3 The values of θ_1 and θ_2 for the given displacement load.....	144
Table 6.1 Significant geometrical parameters of the unit cells.....	161

List of terms and Abbreviations

AM: Additive Manufacturing

ABS: Acrylonitrile butadiene-styrene polymer

PTFE: Polytetrafluoroethylene

HA: Hydroxyapatite

PLGA: Poly-lactide-co-glycolide

ESCs: Embryonic stem cells

hiPSCs: Human induced pluripotent stem cells

UHMWPE: Ultra-high-molecular-weight polyethylene

SAN: Styrene acrylonitrile copolymer

PU: Polyurethane

SLM: Selective laser melting

FE: Finite element

FEA: Finite elemental analysis

CAD: Cad design modelling

MRI: Magnetic resonance imaging

TPU: Thermoplastic polyurethane

CoCr: Cobalt-chromium

SS: Stainless steel

EDM: Electric discharge machining

AUT: Auckland University of Technology

H/L ratio: Height to length ratio

S: S-shaped model

R: Re-entrant model

Attestation of Authorship

I hereby declare that this submission is my own work and that, to the best of my knowledge and belief, it contains no material previously published or written by another person (except where explicitly defined in the acknowledgments), nor material which to a substantial extent has been submitted for the award of any other degree or diploma of a university or other institution of higher learning.

Kusum Meena

Signature:

Acknowledgments

Foremost, I would like to express my utmost gratitude to my primary supervisor Assoc. Professor Sarat Singamneni for the continuous support of my Ph.D. study and research, for his patience, motivation, enthusiasm and immense knowledge. His guidance helped me in all time of research and writing this thesis. I could not have imagined having a better advisor and mentor for my Ph.D. study. I wish to further acknowledge my secondary supervisor Assoc. Professor Loulin Huang for his supplementary assistance.

I am also grateful to AUT Additive Manufacturing Research Centre and the school of engineering and mathematical sciences for providing me with all the computational and mechanical facilities. In particular, I would like to thank mechanical engineering technical staff; Mark Masterton and Ross Jamieson for providing me with equipment and knowledge to conduct the experiments presented.

I wish to express my special thanks to my friend Malaya Prasad Behera and my partner Abhikalp Kaushik for their endless support and motivation. Further, I am grateful to my parents Ramdayal Meena and Latur Meena who supported my academic decisions throughout. I am also thankful to my sister Kavita Meena and my brother Anand Meena to be a part of my thick and thin during this journey. Last but not the least my utmost gratitude to my mother in law Urmila Kaushik and my father in law Vidya Nand Kaushik who immensely supported me emotionally, without them I don't know where I would have been.

Kusum Meena

Chapter 1

Introduction

1.1. Auxetic mechanical metamaterials

Meta-materials are often the results of deliberately designed structural forms, undertaken to achieve improvements in specific mechanical property responses in materials. Initially the term meta-materials was used in the context of optics and electromagnetism (Shalaev et al. 2005, Valentine et al. 2008, Chen et al. 2010, Soukoulis et al. 2010, Zhao et al. 2012). As a result, the term meta-material sometimes is understood to refer to the optical and electromagnetic meta-materials. The concept of mechanical metamaterials was developed relatively recently, and the broad class of mechanical metamaterials includes extremal materials with negative elastic moduli (Dong et al. 2017), negative compressibility and negative Poisson's ratios (Lakes et al. 2008, Zadpoor 2016).

Materials with negative Poisson's ratios are known as auxetic materials (Evans 1991), and their deformation responses are anomalous. Auxetic or negative Poisson's ratio materials are specific mechanical metamaterials that exhibit unusual properties due to the macro, micro, and nano topologies or architectures of the building block units, rather than the bulk composition of the material (Grima and Caruana 2012). By changing the micro or nano architecture of the material, it

is possible to engineer different application-specific properties (Konken and Zadoopr, 2017). Unlike the traditional options, these materials laterally expand and contract under longitudinal tension and compression respectively, as depicted in Fig. 1.1 (Novak et al. 2016). These are scale independent responses and can be achieved at different levels of structures, from molecular to macroscopic scales. The term auxetic was first introduced by Evans et al., in 1991 and was derived from the Greek word “auxetikos,” meaning that it tends to increase (Evans et al. 1991).

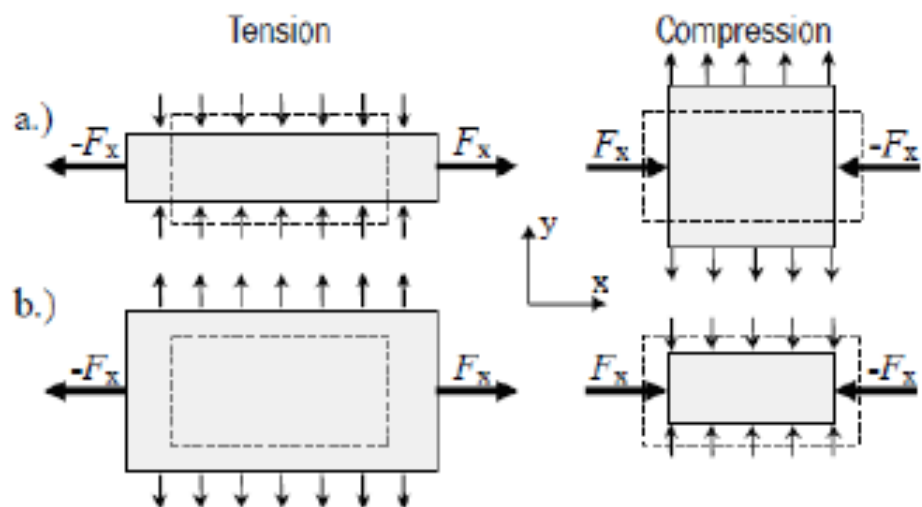


Fig. 1.1 Normal and auxetic behaviour of materials under tension and compression (Novak et al. 2016)

Poisson's ratio is the ratio of transverse strain (ϵ_2) to longitudinal strain (ϵ_1) in simple tension and compression situations as given by Eq. 1 (Lakes 1993) and the effect of Poisson's ratio on the mechanical behaviour of an isotropic material can be expressed using Eq. 2 (Lakes 1993).

$$\nu = \frac{\varepsilon_2}{\varepsilon_1} \dots \dots \dots \quad (1)$$

$$G = \frac{3K(1-2\nu)}{2(1+\nu)} \dots \dots \dots \quad (2)$$

Where G is the shear modulus, K the bulk modulus, and ν is the Poisson's ratio.

According to the theory of elasticity, it may be shown that the Poisson's ratio ranges from -1 to 1/2 for isotropic materials while it ranges from $-\infty$ to $+\infty$ in the case of anisotropic materials (Lakes 1993). For most conventional materials, the Poisson's ratio is around 1/3, while with rubbery materials; it is at around 1/2, which is the upper limit for the isotropic materials. From Eq.2, it is implied that conventional materials with positive Poisson's ratio resist bulk deformation while the shear deformation is easier, i.e. $G \ll K$. When Poisson's ratio approaches the negative limit (-1) of the isotropic materials, the shear modulus approaches infinity and the material preserves its shape during loading due to high shear resistance. It may be pertinent to note that these relationships are only valid with isotropic materials (Lakes 1993). However, it is evident that auxeticity of a material leads to enhancement of some mechanical properties such as shear resistance (Evans and Alderson 2000, Jin et al. 2019), indentation resistance (Lakes and Elms 1993, Hu et al. 2019, Wang et al. 2019), fracture toughness (Lakes 1993, Choi and Lakes 1996, Yang et al. 2017), energy absorption capabilities (Mohsenizadeh et al. 2015, Imbalzano et al. 2016, Lan et al. 2019), vibration damping, and sound absorption (Scarpa et al. 2003). Evans and Alderson (Evans and Alderson 2000) explained

the differences between non-auxetic and auxetic materials as depicted in Fig. 1.2. When an object impacts on a non-auxetic material, the substrate material immediately below the impact flows away in the lateral direction, leading to a reduction in the density. Whereas, material actually flows into the vicinity of the impact in the case of the auxetic substrates, due to the lateral contraction accompanying the longitudinal compression. Consequently, the indentation resistance increases under impact in the case of the auxetic materials (Evans and Alderson 2000).

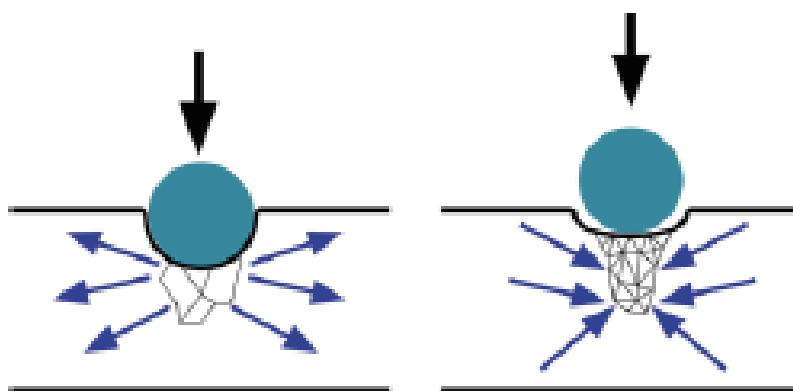


Fig. 1.2 Differential deformation under indentation of non-auxetic and auxetic materials (Evans and Alderson 2000)

These unique attributes make auxetic materials attractive to numerous uses in both industrial and biomedical application areas. For example, the unusual lateral compression and expansion under compression and tensile loadings respectively, and the controlled expansion and compression under specific loading conditions were utilised to develop the auxetic scaffolds (Soman et al. 2012, Choi et al. 2016,

Warner et al. 2017, Yan et al. 2017), nanofiber membranes (Bhullar et al. 2017), stents (Bhullar et al. 2013, Douglas et al. 2014, Ali and Rehman 2015, Wu et al. 2018), drug delivery systems (Evans and Alderson 2000, Jiang and Li 2018), bio prosthetics (Scarpa 2008), artery dilators (Evans and Alderson 2000), smart bandages (White 2009), and artificial blood vessels (Evans and Alderson 2000). The industrial applications possible through auxetic materials are smart fasteners (Choi et al. 1991), auxetic nails (Ren et al. 2018) sound absorption systems (Howell et al. 1991, Howell et al. 1994), energy absorption devices (Chang et al. 2017), filter membranes (Alderson et al. 2000), and crashworthy helmets and body armours (Sanami 2014, Imbalzano et al. 2017).

1.2. Conventional manufacturing

Auxetic materials in their natural forms were identified in iron pyrites (Love 1944), cat skin (Veronda and Westmann 1970), cancellous bones (Williams and Lewis 1982), cow teat skin (Lees et al. 1991) and alpha cristobalite polymorphs (Yeganeh- Haeri et al. 1992) etc. However, the attention towards physically building auxetic material structures began in 1987, when Lakes (Lakes 1987) investigated and developed a volumetric compression method to convert an open cell polymeric foam into an auxetic foam by heating and compressing in three orthogonal directions into a mould. Further to this, a few other methods have also evolved in similar lines, for the fabrication of polymeric and metallic auxetic materials. Chan and Evans (Chan and Evans 1997) managed to upgrade the single stage volumetric compression method into a multistage volumetric compression

technique to fabricate large sized foams. Alderson and Evans (Alderson and Evans 1992) developed the thermoforming route involving compaction, sintering and extrusion of ultra-high molecular weight polyethylene (UHMWPE) to fabricate auxetic micro-porous materials. The melt spinning method was also developed by Alderson and Evans to produce auxetic fibres (Alderson et al. 2002, Ravirala et al. 2006). A chemical mechanical compression method was developed by Grima et al., (Grima et al. 2009) to bypass the high process temperatures as in the case of the volumetric compression method, for better quality of the fabricated materials. The CO₂ gas assisted compression (Li and Zeng 2016) technique eliminated the need for the volatile organic solvents, though limited to the electron donating group of polymers that strongly react with the CO₂ gas.

Despite the progress and the emergence of all these methods, fabrication of auxetic structures has always been a major challenge. Most of these methods were only limited to producing some metallic or polymeric foams and fibres. Apart from this, the quality assurance levels and the repeatability of the production processes remain uncertain. In almost all these cases, the freedom to control the shape complexities is generally limited and it is practically impossible to produce very complex 2D and 3D auxetic designs with a diverse range of base materials. There has been a lot of theoretical interest though, and a prolific growth in the proposed ideas and structural concepts based on auxetic material solutions.

1.3. Evolution of the different auxetic structures

Many different forms of auxetic structures were developed over the years, and based on the deformation mechanisms, they can be classified into mainly three different categories; re-entrant, chiral, and rotating units. The re-entrant structures deform auxetically due to either the individual or combined action of mechanisms such as hinging, flexing, and stretching. This is the most common type of auxetic structures and encompasses a variety of auxetic designs. The re-entrant honeycomb (Gibson and Ashby, 1982, Robert 1985, Masters *et al.* 1996,), the missing rib (Smith *et al.* 2000), the square grid (Gasper *et al.* 2005), the arrowhead (Larsen *et al.* 1997, Spagnoli *et al.* 2015), and the star (Grima *et al.* 2005) structural models are common examples.

The chiral design employs auxetic deformation mechanisms arising from the wrapping and unwrapping of the straight ligaments around the central nodes. Based on the direction of the ligaments and the nodes the chiral model was further divided into the chiral and antichiral categories (Prall and Lakes 1997). Also, depending on the number of ligaments attached to the central node, several models like trichiral, tetrachiral (Grima *et al.* 2008) and hexachiral (Wojciechowski 1989) came into existence.

The concept of the rotating units was relatively a recent development and introduced by Grima and Evans (Grima and Evans 2000a), while attempting to explain the auxeticity in foams (Grima *et al.* 2005a), nanostructured polymers

(Grima and Evans 2000b), zeolites (Grima et al. 2000) and silicates (Grima et al. 2005b). The deformation mechanism was controlled by the relative rotation of specific units, while these units can be rectangular (Grima et al. 2004), triangular (Grima et al. 2006) or square in form (Grima and Evans 2000a, Grima et al. 2007).

It may be pertinent to elucidate here that most of these developments were based on analytical models (Masters et al. 1996, Larsen et al. 1997, Grima et al. 2000). The precursor to these developments was the urge to explain the auxeticity in foams, fibres, and the molecular deformations. Considering that the conventional methods available to physically produce these structures were seriously limited (Lakes 1987, Alderson and Evans 1992, Alderson et al. 2002, Grima et al. 2009), experimental verification was seriously restricted in all the cases, until the recent developments and the wider availability of additive manufacturing technologies.

1.4. Additive manufacturing

In recent years, additive manufacturing technologies, and in specific, the electron beam melting and selective laser melting methods emerged as viable means to fabricate the complex auxetic structural designs with a variety of materials. Unlike the subtractive methods, the additive manufacturing (AM) processes are essentially based on point-by-point material consolidation mechanisms, allowing to construct complex 3D models based on the digital computer aided design model data (Gibson et al. 2014). In particular, the methods are especially suited for

fabricating the relatively complex auxetic structural forms. A gradual trend indicating the move from traditional methods to additive manufacturing was noticed based on a review of the recent research reported on experimental evaluation of auxetic structural forms.

Rehme and Emmelmann (Rehme and Emmelmann 2009) fabricated four structural designs, cubic sinus wave, chiral honeycomb, decagonal honeycomb, and cubic floral forms by selective laser melting stainless-steel powders for experimental evaluation of the auxetic nature of these structural forms. Schwerdtfeger et al. (Schwerdtfeger et al. 2010) fabricated a 3D re-entrant auxetic anisotropic structure based on the electron beam melting of a Titanium alloy. Further examples include fabrication of, a 3D cubic chiral auxetic structure by the electron beam melting of Ti-6Al-4V (Warmuth et al. 2016), a 2D re-entrant modified design by selective laser melting of a TiNi alloy (Li et al. 2016), a 3D re-entrant model by the selective laser melting of AlSi10Mg (Xiong et al. 2017). Using the polymer based additive manufacturing processes, Wang et al. (Wang et al. 2015) fabricated a 3D re-entrant model using dual materials (two different materials) based on the multi-material polyjet 3D printing technique. A modified 3D re-entrant model was fabricated by Fu et al. (Fu et al. 2016) based on the 3D printing of the acrylonitrile butadiene-styrene (ABS) polymer.

Evidently, additive processing methods have progressed into fabricating both 2D and 3D auxetic structures of relatively complex forms. Re-entrant designs in the 2D form (Yang et al. 2012, Li et al. 2016), their extension into the 3D form

(Schwerdtfeger et al. 2010, Wang et al. 2015, Fu et al. 2016) and in various other modified versions (Li et al. 2016, Xiong et al. 2017, Ingrole et al. 2017) were produced and analysed based on the metal and polymer additive manufacturing methods. The combined action of hinging, flexing, and bending leading to enhanced auxetic nature in terms of large negative Poisson's ratios in re-entrant sections was only possible to be demonstrated by means of additive manufacturing (Elipe and Lantada 2011). However, other structural designs, e.g. missing rib (Koudelka et al. 2016), double arrowhead (Yang et al. 2016) and sinusoidal forms (Warmuth et al. 2017) drew almost negligible attention. Along these lines, the square-grid auxetic structure (Gasper et al. 2005) received almost no attention so far. As was reported earlier, the auxetic range of re-entrant structures was limited (Wan et al. 2004, Jiang and Li 216), while the chiral geometries were depicted to be auxetic for a wide range of loading conditions (Wang 2014). It may also be pointed out that auxetic responses from other structural forms, missing rib (Smith et al. 2000), square grid (Gasper et al. 2005), different forms of chiral designs (Prall and lakes 1997, Grima 2000, Grima et al. 2005) etc. should also be given enough attention by experimental evaluation based on physically produced structures using the additive manufacturing methods.

Further, the main focus in applying additive methods to re-entrant structures was mostly on enhancing the auxetic nature (Schwerdtfeger et al. 2010, Yang et al. 2012, Li et al. 2016). In some cases, attempts were also made to improve the in-plane mechanical properties through hybridisation of structures (Ingrole et al. 2017 and Jiang and Li 2018). Auxetic structures are often complex in geometrical forms and the desire to enhance auxeticity leads to further escalation of these

complications. Stress concentration problems might arise due to these geometrical requirements (Wang et al. 2015, Xiong et al. 2017), which have been neglected largely in the past. Apart from the geometry, the fabrication processes also are likely to add stress concentration effects to varying degrees, more significantly with fabrication methods based on melting of metals (Yang 2011, Schwerdtfeger et al. 2012, Yadroitsev & Yadroitseva 2015, Abdeen and Palmer 2016). Evidently, both the structural geometries and the fabrication methods need be evaluated to reduce or eliminate the stress concentration issues. Attempts have been made to modify the existing geometry by incorporating some stress relieving features (Xiong et al. 2017) and to indirectly fabricate the auxetic structures (Xue et al. 2018, Wang et al. 2016).

1.5. Research gaps and objectives

Evidently, auxetic structures have definite roles to play in numerous medical and industrial applications. The structural shapes are complex and the traditional manufacturing methods suffer to deliver the required levels of freedom to physically produce them. This has been the main bottle neck in the widespread evaluation, development and application of the auxetic structures. With the advent of additive manufacturing, the freedom to produce such complex forms in a variety, of materials has significantly increased. Consequently, research has progressed experimentally evaluating different auxetic forms physically produced by means of different additive manufacturing technologies.

The main gap lies in that the more flexible selective laser melting has not been significantly exploited to expand the experimental evaluation and the eventual performance enhancement of auxetic structures. The most predominant approach employed to ascertain auxeticity was analytical modelling, while numerical methods had also been used often. The experimental verification was quite rare, due to manufacturing limitations. Overall, there was very little evidence of all these three methods integrated into a unified scheme that can be used to design and optimise auxetic structural forms. In a more particular context, the other re-entrant structures (square, missing rib, arrowhead etc.) were not significantly analysed, while the roles of the stress concentration effects were neglected for most part. The current research is designed to fill these gaps and the following are the main objectives:

- Establishing the use of selective laser melting to produce auxetic structures of specific designs with at least a couple of metallic material options
- Within the context of the above objective, experimentally verify the auxetic performance of a re-entrant square grid structure
- Develop a numerical evaluation scheme to simulate the experimental conditions on the auxetic structures analysed.
- Correlate the experimental and numerical results and develop an integrated assessment scheme for establishing the performance of auxetic structures.
- Use the above context to optimise the geometry of a selected auxetic structure.
- Use the numerical simulation scheme and analyse the stress concentration aspects in the specific auxetic structure.

- Based on the integrated manufacturing, experimental, and numerical scheme, design a new auxetic structure, effectively handling the stress concentration concerns.
- Extend the above objective to develop and evaluate hybrid structures, targeted at combining the beneficial roles of different forms of unit cells.

1.6. Thesis structure

The research methods to be used are predominantly experimental and numerical in nature, while analytical modelling will also be used for designing new auxetic unit cells. The Renishaw selective laser melting system is used to fabricate the auxetic structures based on two material systems, cobalt chromium and stainless steel 316L. The square grid re-entrant structure is employed for all the initial assessment of the fabrication, experimental testing, and numerical simulation tasks. Initial impressions on the stress concentration aspects are also established based on this structure. An S-shaped unit cell is designed and evaluated by the experimental and numerical procedure developed as part of this research. Hybrid structures are designed, integrating star shaped re-entrant unit cells into the S-structures in different configurations.

Chapter 3 is devoted to a detailed discussion of the methodologies employed for the experimental and numerical schemes developed. Details of all the equipment used, measurement and characterisation techniques, tools and other

instrumentation are all presented in this chapter. Chapter 4 is all about the preliminary work done based on the re-entrant square-grid structure which has also been the context used to establish the experimental and numerical frame work to be used for the rest of the thesis. The role of stress concentration in the auxetic structural responses is also established in this chapter. The experimental and numerical scheme developed is also used to further optimise the geometrical features of the structure.

Chapter 5 introduces the design and development of a new auxetic structure based on the S-unit cells specifically focussed on reducing the stress concentration effects. The analytical models leading up to the design of the basic form of the auxetic unit cells are elucidated. Geometrical optimisation based on numerical simulations and further experimental verification are also presented in detail. Chapter 6 is focussed on the hybridisation of the structures used, by incorporating star unit cells in the S-structural formats. Experimental and numerical evaluations leading to the understanding of the combined roles of two different unit cells in the auxetic structure are detailed. Chapter 7 presents a comprehensive consolidation of the conclusions drawn based on the work done achieving the aims of the proposed research.

Chapter 2

Literature review, research gaps, questions, and objectives

2.1. Structure-based material attributes

Auxetic cellular structures consist of a number of unit cells arranged in such a way that the overall structure expands when stretched and contracts when compressed. This unusual deformation gives rise to negative Poisson's ratios and enhanced mechanical properties. Increased shear modulus and indentation resistance (Evans et al. 2000, Alderson et al. 1994), higher energy absorption capabilities (Scarpa et al. 2003), and better fracture toughness (Lakes et al. 1993) have been reported. All auxetic cellular materials are design-centred and their properties can be altered by varying the unit cell architecture. Over the years, several new 2D and 3D auxetic cellular structures based on the re-entrant, chiral, lozenge and square grid, rotating rectangle and triangle forms etc. have evolved. Applications in diverse fields have opened, including aerospace (Lira et al. 2011) and medical which will be reviewed briefly, before dwelling into the research leading to the identification for the research gaps and formulation of research questions.

2.2. Applications in different areas

The auxetic nature and the special attributes possessed by these materials compared to conventional materials qualify them for specific applications in different areas. In particular, applications in the medical and industrial fields have progressed substantially as elaborated next:

2.2.1 Medical applications

Bio prosthetic implants are specific applications that can gain significant advantages by employing the auxetic material characteristics. The main reported bio prosthetics were artificial intervertebral disks (Sabatino 2016), annuloplasty prostheses (Burriesci and Bergamasco 2011), cushion pads (Scarpa 2008), and knee prosthetics (Scarpa 2008). It was reported that, the sandwich core of an artificial intervertebral disk made of re-entrant honeycomb cells exhibited auxetic effects through the thickness of the plates. Lateral compression was noticed under the axial compression loading (Sabatino 2016). Burriesci proposed an auxetic annuloplasty prosthesis for plastic repair of the cardiac valve (Burriesci and Bergamasco 2011). The lack of crimping in the truss-like tubular structure valve has been the motivation for the development of the highly flexible stem for cardiac applications. The uniform stress distribution and the reduction in the local peak stress characteristics against the conventional foams make auxetic polymer foams suitable to be used as cushion pads for people with a disability or with a medical

condition and as knee prosthetics (Scarpa 2008). An auxetic dilator is a device that can be used to open an artery. The lateral expansion of a flexible auxetic polytetrafluoroethylene (PTFE) hollow rod or sheath under tension was employed to open the artery (Moyers 1992) as depicted in Fig. 2.3

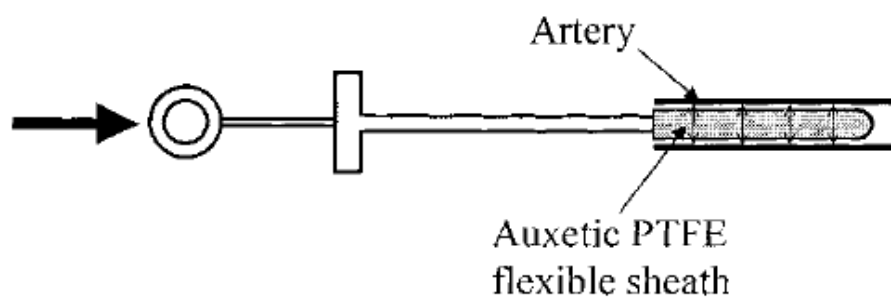


Fig. 2.3 Dilator employing an auxetic end sheath (Evans and Alderson 2000)

Smart bandages made of auxetic foams can be impregnated with medication to work as effective drug delivery devices in swollen wound cases. The effect of the wound pushing against such a dressing would be to release the medication based on the auxetic form changes in the bandage (White 2009). An artificial blood vessel made of non-auxetic materials will decrease the wall thickness of the vein in response to a pulse of blood flowing through it, as shown in Fig. 2.4 (a). An auxetic alternative was proposed to increase the wall thickness of the blood vessel under the same condition as depicted in Fig. 2.4 (b) thus reducing the risk of rupture (Evans and Alderson 2000).

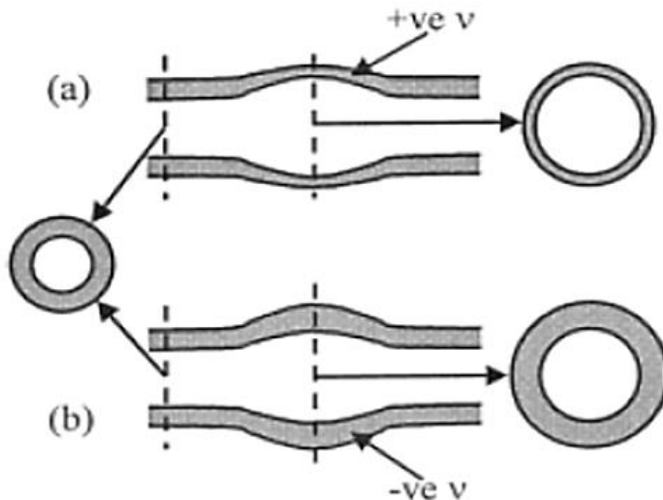


Fig. 2.4 Deformation behaviour of the artificial artery made up of (a) Non-auxetic material (b) Auxetic material (Evans and Alderson 2000)

Auxetic scaffolds are relatively recent developments in the medical applications. Scaffolds made of hydroxyapatite (HA) and poly(lactide-co-glycolide) (PLGA) exhibiting negative Poisson's ratios were found to help in the regeneration of bones through better osteo-compatibility and effective isotropic compression, stimulating the proliferation of bone cells in comparison with the simple PLGA scaffolds (Choi et al. 2016). Likewise, Yan et al. (Yan et al. 2017) evaluated the role of negative Poisson's ratio (auxetic) scaffold in expansion and neural differentiation of mouse embryonic stem cells (ESCs) and human induced pluripotent stem cells (hiPSCs) as compared to conventional (positive Poisson's ratio) scaffold. The induced neural differentiation in both type of scaffolds resulted in higher neuronal marker expression for auxetic scaffold compared to the conventional scaffold.

In recent years, auxetic stents also came up as viable alternatives, to overcome the clinical limitations of the conventional stents such as getting crushed and removed, and leading to restenosis. Bhullar et al. (Bhullar et al. 2013) designed and manufactured the oesophageal stent models, based on a rotating solid square and a rotating square with circular holes, by laser cutting of a polyurethane sheet to evaluate the influence of negative Poisson's ratio on stents. The fabricated models were characterised by tensile and compression tests and the deformation modes and stress strain curves generated. The rotating square stent model with circular holes, due to its lightweight configuration, depicted enhanced mechanical properties with the Poisson's ratio at -0.76. The lateral expansion under tension along with enhanced mechanical properties led to reduced stresses and enhanced food and liquid passage, making swallowing less painful. Wu et al. (Wu et al. 2018) proposed the anti-tetra chiral and hierarchical anti- tetra chiral stent models. The in-plane mechanical properties of the proposed models were investigated by theoretical and experimental analyses (Uniaxial tensile tests). The numerical simulations of the effects of geometrical topology on the tensile mechanical behaviour predicted that, the mechanical behaviour of both types of the stent models could be tailored by changing the unit cell geometrical parameters and by adjusting the level of the hierarchical structure. The Finite element analysis of coupled mechanical behaviour of the stent-plaque-artery was also investigated. The results of the numerical analysis depicted the remarkable radial expansion of the proposed stent models while maintaining the axial stability and possible clinical applications.

Evans and Alderson (Evans and Alderson 2000) predicted the use of molecular auxetic materials in ion exchange, molecular sieve and drug delivery system applications. In reality, Jiang and Li (Jiang and Li 2018) proposed a hybrid structure with chiral cells and re-entrant cores, and numerically proved it to be suitable for sequential particle release. The sub-sequential opening mechanism of the proposed hybrid structure under a very large range of strains allowed selective removal of particles of various sizes. The ability of the proposed hybrid structure to sequentially release the particles based on the applied strains proved it a viable option in drug delivery systems.

2.2.2 Industrial applications

Theoretical prediction of the advantages and possible applications with auxetic structures began as early as in 1987 (Lakes et al. 1987). Choi et al. (Choi et al. 1991) predicted that, a whole new kind of smart fasteners could be made which transversally contract when pushed into a socket (compression load) and expand when removed (tension load) (Choi et al. 1991). Howell et al. (Howell et al. 1991) undertook a study to measure the effects of the negative Poisson's ratio materials on the acoustic properties. For experimental evaluation, an open cell polyurethane reticulated foam was volumetrically compressed (Lakes 1987) to convert it into an auxetic foam. Acoustic tests were conducted on the auxetic and non-auxetic polyurethane foams comparing the reflection properties. The results depicted lesser sound reflection for the auxetic foam against the non-auxetic foam at all frequencies and proved the auxetic nature to be crucial for sound absorption

applications. The auxetic foams undergo doubly curved (synclastic) deformation when bent (Lakes 1987) as against the saddle (anticlastic) deformation of conventional foams as shown in Fig. 2.5. This doubly curved phenomenon can possibly be exploited for auxetic composite sandwich panels which find applications in the aerospace and automotive industries.

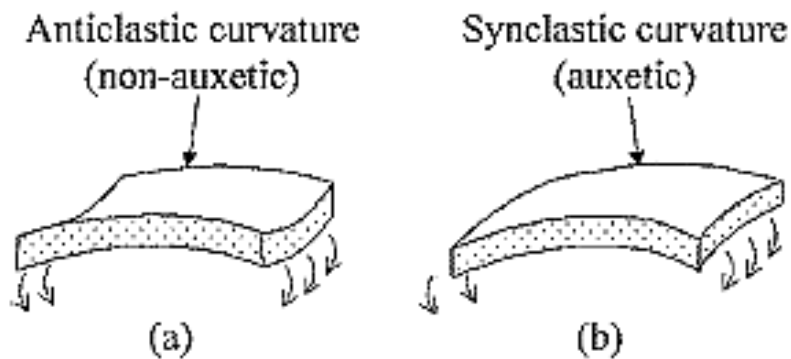


Fig. 2.5 Behaviour of (a) Non-auxetic and (b) Auxetic material under bending
(Lakes 1987)

Bettini et al. (Bettini et al. 2009) conducted a study, employing chiral geometries into the design of an airfoil wing for a race car, with morphing characteristics. The experimental and numerical tests showed the effectiveness of the chiral geometry to enhance the performances of the wings and rotor blades by improving the flow conditions and minimising the drag. The incorporated chiral geometry provided compliance and allowed continuous deformation of the airfoil due to its negative Poisson's ratio, in order to modify itself to adapt to the wind force. A piezoelectric sensor made up of ceramic cores within a passive polymer matrix was used in

medical ultrasonic imagers (Smith 1994). The passive polymer matrix when replaced by the auxetic polymer material allowed free lateral expansion of ceramic rods under surface compression loading as shown in Fig. 2.6. The enhanced lateral expansion of the ceramic rods was shown to provide better electromechanical coupling of the device, enhancing the overall performance of the sensor.

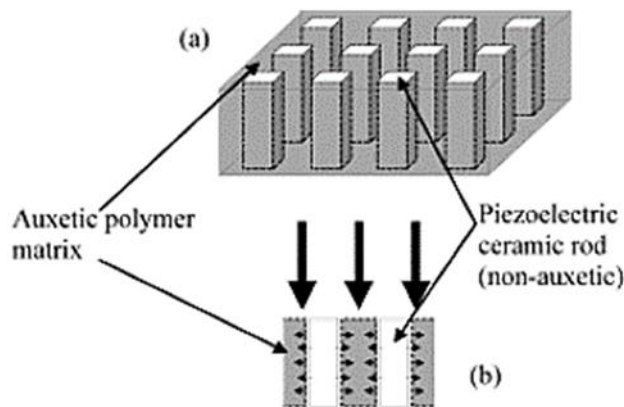


Fig. 2.6 Piezoelectric composite sensor (a) Non-auxetic ceramic cores within auxetic polymer matrix (b) lateral contraction of auxetic polymer matrix allowing lateral expansion to ceramic cores for enhanced device sensitivity (Evans and Alderson 2000).

The auxetic re-entrant filter membrane produced by the laser ablation technique was found to enhance both the cleaning efficiency and the ability to select different sizes of particles based on the variation of the pore sizes based on the variation in properties under tensile loading (Alderson et al. 2000). These responses, emanating from the auxetic nature were reported to be crucial in decreasing the number of filters to be replaced over time, plant down times, and the minimisation

of waste, while also increasing the process efficiencies. Jayanti et al. (Jayanti et al. 2011) proposed an auxetic fiber composite structure that is capable of a greater pull-out resistance resulting from the increasing cross-sectional area under the action of the applied tensile forces. It was shown to be suitable for making crash-worthy helmets and body armours (Sanami 2014).

Scarpa et al. (Scarpa et al. 2005) evaluated the mechanical performance of an auxetic polyurethane foam for the anti-vibration glove application. The conventional and auxetic foams were characterised by the compression and transmissibility test analyses. Significant increase in stiffness was obtained under compression testing of the auxetic foam. The increased stiffness under compression loading, transmissibility greater than one within 10-31.5 Hz frequency range, and the better distribution of pressure between human hand and the glove interface of the auxetic foams proved their suitability to be used as anti-vibration gloves as against the conventional foams (Scarpa 2005). Apart from these applications, the auxetic materials are also under investigation to be used in defence, for producing light weight and thinner body armour (Burke 1997) and ballistic protective equipment requiring high impact resistance compared to the conventional materials (Imbalzano et al. 2018).

2.3. Conventional Processing methods

Auxetic materials were known among the scientists since 1944 as natural auxetic materials were reported in the form of iron pyrites (Love 1944), cat skin (Veronda and Westmann 1970), cancellous bone (Williams and Lewis 1982), cow teat skin (Lees et al. 1991) and alpha cristobalite polymorph (Yeganeh- Haeri et al. 1992) etc. However, they did not get much attention until 1987, when Lakes introduced a method to fabricate an auxetic structure in reality. A conventional open cell polyester foam was converted into a novel re-entrant structural foam by heating it in a mold and compressing in three orthogonal directions (volumetric compression), followed by cooling. The converted auxetic foam has a -0.7 Poisson's ratio (Lakes 1987). This method was suitable for the fabrication of small-sized foams. The same volumetric compression technique was also applied to produce ductile copper and aluminum foams (Friis 1988). The fabricated copper foam was uniaxially compressed and the results clearly established the auxetic nature of the converted copper foam. The comparative small strain region of the stress- strain graph for the auxetic copper foam depicted the auxetic foam to be lesser in stiffness compared to the conventional foam.

A novel thermoforming route was developed by Alderson and Evans (Alderson and Evans 1992) to produce Ultra-high-molecular-weight polyethylene (UHMWPE) microporous material with a negative Poisson's ratio. This process consisted of three distinctive stages; compaction, sintering, and extrusion, in a specially designed extrusion rig. The first stage ensured the formation of the fully compacted

rods. The sintering and extrusion stages were varied based on the die diameter, temperature, and the extrusion rate. Repeated trials led to optimum levels process parameters for sintering temperature and speed of extrusion at 160°C for 20 minutes and 500mm/min respectively for forcing the compacted rod through a 5 mm diameter of the die. The microstructure achieved was reported to result in a Poisson's ratio up to -1.24 in UHMWPE. Chan and Evans proposed a multi-stage heating and cooling and compression method to fabricate large sized foams and produced an auxetic polyether foam from the conventional open cell foam (Chan and Evans 1997). The one stage processing method developed by Lakes (Lakes 1987) was converted into a multistage processing, system, to minimise the risk of surface creasing. It was a better-controlled technique than the one-stage processing method and was reported to produce more homogeneous specimens.

While all these initial methods were based on the conversion of different polymer foams into auxetic foams, Alderson et al. (Alderson et al. 2002) developed a novel melt spinning process route to produce auxetic polypropylene fibers. They employed an extruder and an archimedian screw mechanism and identified the critical process parameters required to produce the auxetic fibers. The melt extruder temperature was set to 159 °C together with a screw speed of 1.05 radian per second and take off speed of 0.03 meters per second. The produced polypropylene fiber was auxetic with Poisson's ratio at around -0.60. An auxetic polyester fiber was also produced using the same thermal melt spinning route (Ravirala et al. 2006). The Poisson's ratio of the fabricated fibre was found to vary from -0.65 to -0.75.

Alderson (Alderson and Alderson 2005) extended the knowledge of the powder metallurgy technique involving compaction, sintering and extrusion to develop a continuous partial-melt extrusion process to produce auxetic polymeric monofilaments. The filament produced had a microstructure of interconnected and surface-melted powder particles. The microlevel deformation mechanisms as against the molecular level ones as in the case with the conventional filaments produced by extruding fully molten polymer, were found to be responsible in inducing the auxetic nature in the filament. Grima et al. (Grima et al. 2009) introduced a novel chemical-mechanical method to avoid the high process temperatures and improve the quality of the structure. The conventional open polymeric foam was compressed and placed in acetone for an hour and then air dried in a compressed state. The resulting foam was auxetic with Poisson's ratios ranging from -0.32 to -0.36.

Li and Zeng (Li and Zeng 2016) introduced the use of CO₂ as a processing agent, eliminating the need for a volatile organic solvent. CO₂ strongly reacts with polymers possessing electron-donating groups, like the styrene acrylonitrile copolymer (SAN) found in polyurethane (PU) foams, and enhances the polymer chain mobility, which significantly reduces the glass transition temperature. The process, involving the compression of a foam specimen into a CO₂ fed pressure reactor, can, therefore, be executed at ambient temperatures. After equilibrium, the pressure can be released, and the styrene-acrylonitrile particles resume their glassy state, fixing the inwardly buckled structure. This process is efficient for large-scale manufacturing of auxetic foams.

The conventional processing methods (Lakes 1987, Alderson and Evans 1991, Chan and Evans 1997, Alderson and Evans 2002, Ravirala et al. 2006, Grima et al. 2009, Li and Zeng 2016) reviewed have allowed production of auxetic microporous materials, foams, fibers, composites, etc., with different degrees of auxeticity. Along with the evolution of these fabrication techniques, parallel progress was also noted in the understanding of the micro and macro level deformation mechanisms in foams, fibres, and the other structures at the macro level. In accordance with the reviews by Evans and Alderson 2000, Alderson and Alderson in 2007, and Liu and Hu in 2010, the deformation mechanisms identified could be grouped into five categories. However, most of the developed auxetic models fall in the three broad categories as discussed next. In most cases, the auxetic designs were evaluated and explained by analytical, numerical and experimental means, while various other models have also evolved based on modifications done to the standard auxetic structures.

2.4 Auxetic models

2.4.1 *The Re-entrant model*

The re-entrant model is the most common type, encompassing a number of auxetic forms. The 2D and 3D re-entrant models are the most widely studied structural forms for auxeticity, due to their simplicity and the ability to exhibit the best Poisson's ratios (Elipe and Lantada 2012). The first 2D re-entrant auxetic model

was proposed by Gibson and Ashby (Gibson and Ashby 1982). The simplest deformation mechanism of the 2D re-entrant models giving rise to the auxetic nature as demonstrated by Robert (Robert 1985) is presented in Fig. 2.7. The horizontal alignment of the diagonal ribs under uniaxial tensile loading is responsible for the auxetic nature. The 2D re-entrant model was employed to describe the microstructural deformation mechanisms that are responsible for the auxetic nature in the converted foams (Lakes 1987, Choi and Lakes 1996).

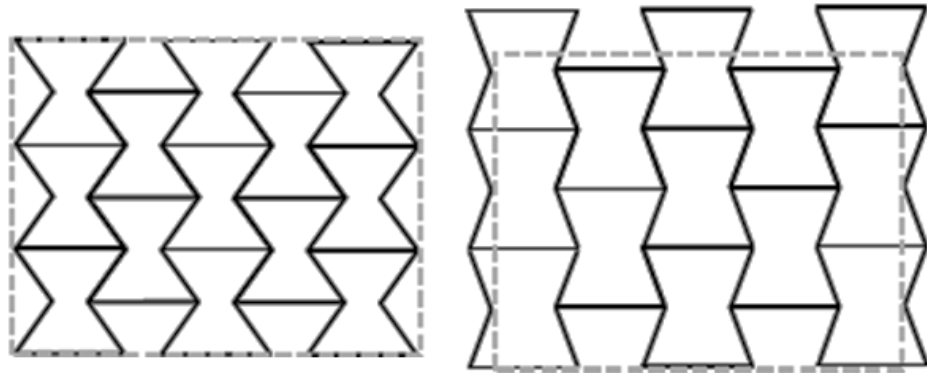


Fig. 2.7 2D Re-entrant honeycomb deformation mechanism under uniaxial tensile loading (Robert 1985)

Masters et al. (Masters et al. 1996) developed analytical models to obtain elastic constants of honeycomb structures as shown in Fig. 2.8, for different types of deformation (flexural, stretching, and hinging) mechanisms under uniaxial loading. Each failure mechanism was expressed mathematically based on the properties of the cell wall material and using simple mechanics principles. These mechanisms could be combined to produce a general model, by summing up the deflections in directions 1 and 2 to obtain expressions for the elastic constants. Expressions for

the elastic constants established based on different deflection mechanisms are listed in Table 2.1.

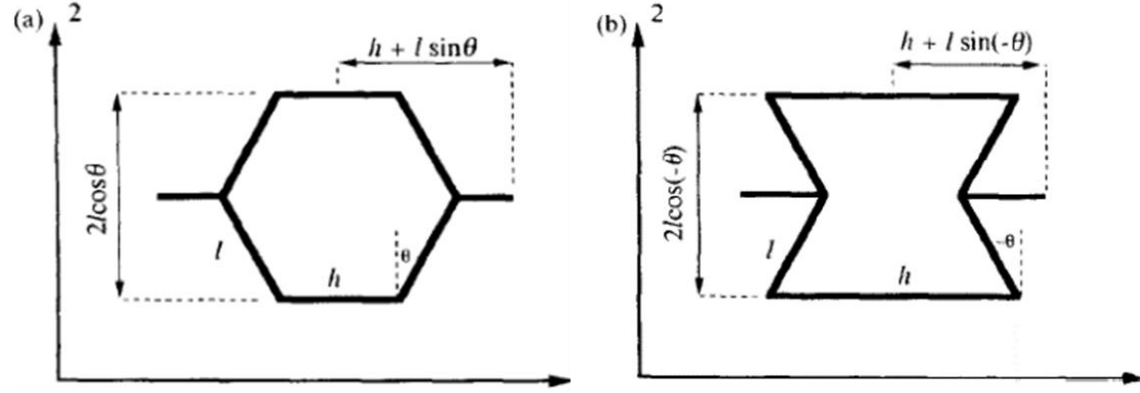


Fig. 2.8 Cell geometries used by Masters et al. (Masters et al. 1996) (a) hexagonal and (b) re-entrant cells.

Table 2.1: Elastic constants of the honeycomb model as developed by Masters et al. (Masters et al. 1996) based on different deformation mechanisms

	Flexure	Stretching	Hinging
E_1	$\frac{K_f(h/l + \sin\theta)}{b \cos^3\theta}$	$\frac{K_s(h/l + \sin\theta)}{b \cos\theta (2h/l + \sin^2\theta)}$	$\frac{K_h(h/l + \sin\theta)}{b \cos^3\theta}$
E_2	$\frac{K_f \cos\theta}{b(h/l + \sin\theta) \sin^2\theta}$	$\frac{K_s}{b \cos\theta (h/l + \sin\theta)}$	$\frac{K_h \cos\theta}{b \sin^2\theta (h/l + \sin\theta)}$
ϑ_{12}	$\frac{\sin\theta (h/l + \sin\theta)}{\cos^2\theta}$	$\frac{-\sin\theta (h/l + \sin\theta)}{2h/l + \sin^2\theta}$	$\frac{\sin\theta (h/l + \sin\theta)}{\cos^2\theta}$
ϑ_{21}	$\frac{\cos^2\theta}{(h/l + \sin\theta) \sin\theta}$	$-\left(\frac{\sin\theta}{\sin\theta + h/l}\right)$	$\frac{1}{v_{21}}$
G_{12}	$\frac{K_f(h/l + \sin\theta)}{b(h/l)^2(1 + 2h/l) \cos\theta}$	$\frac{K_s}{b} \left[\frac{l \cos\theta (h + l \sin\theta)}{(l \cos^2\theta + (h + l \sin\theta) \sin\theta)^2} \right]$	$\frac{K_h}{b \cos\theta} \left[\frac{Cl(h + l \sin\theta)}{Ch(h + l \sin\theta) + l(2l - Ch \sin\theta)} \right]$

E_1 , E_2 , ν_{12} , ν_{21} and G_{12} , are the elastic constants and K_f , K_s and K_h are force constants for the honeycomb structure. If θ is made negative, then the Poisson's ratio of the cells becomes negative, resulting an auxetic structures. The lowest value of force constant determines the deformation mechanism of the structure. It was shown how the properties can be tailored by varying the relative magnitudes of the force constants for different deformation mechanisms. Different mechanical properties including Poisson's ratio, elastic modulus, and yield strength of the 3D re-entrant auxetic structure could be determined by the geometrical design parameters and solid material properties.

The other 2D re-entrant design models are lozenge (Smith et al. 2000) and square grid (Gasper et al. 2005) structures. The lozenge missing rib design model was developed to explain the deformation mechanisms in reticulated foams (Smith et al. 2000) as shown in Fig. 2.9. A 2D missing rib model was developed by Smith et al. (Smith et al. 2000) based on the observations with broken ribs while converting an open cell foam into an auxetic foam, by means of the volumetric compression technique. The proposed model was found to predict the better strain-dependent Poisson's ratio and stress-strain behaviour compared to experimental results as well as the performance of an already existing model proposed by Gibson and Ashby (Gibson and Ashby 1999).

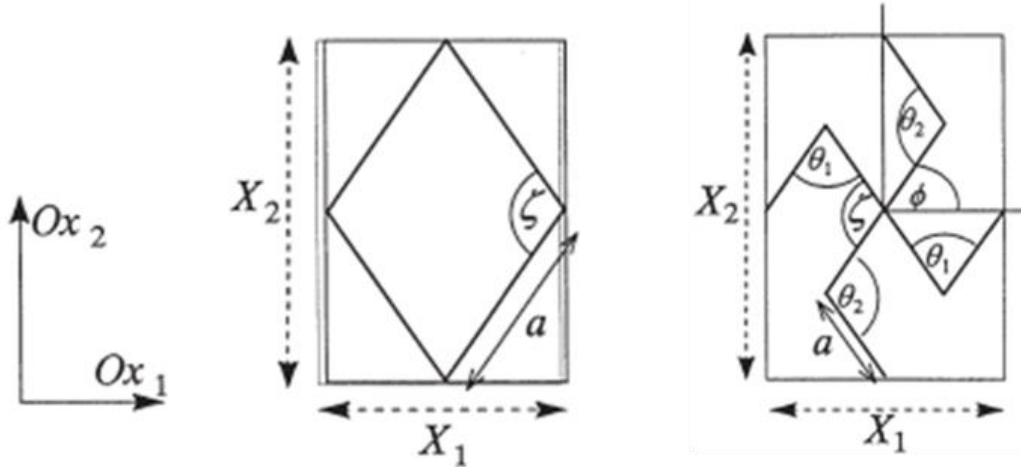


Fig. 2.9 Two forms proposed by Smith et al. (Smith et al. 2000) (a) intact and
(b) Missing rib model

Gasper et al. (Gasper et al. 2005) modified the existing missing rib model (Smith et al. 2000) as shown in Fig. 2.9 by fixing θ_1 , θ_2 and ϕ at 90° leading to the emergence of the square grid structure depicted in Fig. 2.10. The model was verified by analytical and experimental investigations. A -1 Poisson's ratio was achieved for the square grid structure. The higher negative Poisson's ratio was obtained for square grid auxetic structure than the missing rib lozenge model (Smith et al. 2000). The auxetic effects in both missing rib and square grid models were obtained due to rotation and extension of each side of unit cells. The analytical models developed to calculate the elastic constants are listed in Table 2.2.

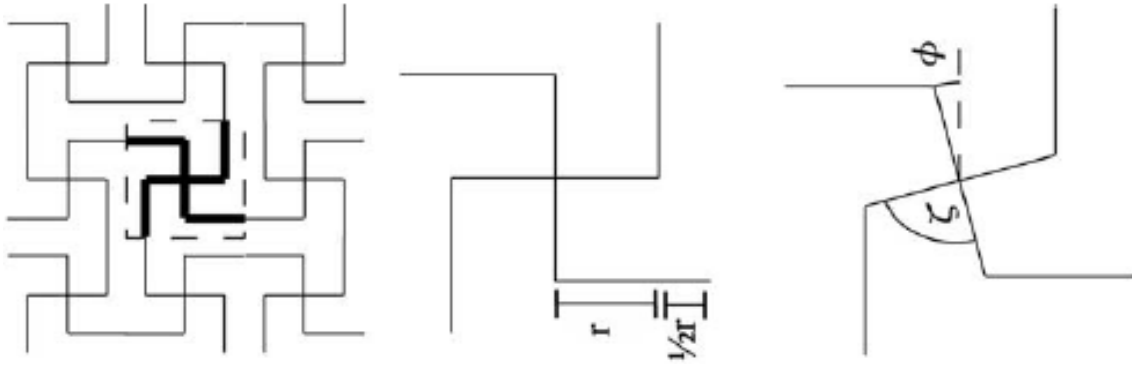


Fig. 2.10 Square grid structure (a) Unit cell (b) deformed unit cell (Gasper et al. 2005)

Table 2.2 Analytical models for lozenge and square grid models

Missing rib Lozenge model (Smith et al. 2000)			
E_1	E_2	ϑ_{12}	ϑ_{21}
$\kappa_\theta \frac{1}{4a^2} \frac{\cot(\zeta - \phi)}{\sin(\phi) \sin(\zeta - \phi)}$	$\kappa_\theta \frac{1}{4a^2} \frac{\tan(\phi)}{\cos(\phi) \cos(\zeta - \phi)}$	$-\tan(\phi) \tan(\zeta - \phi)$	$\frac{1}{-\tan(\phi) \tan(\zeta - \phi)}$
Square grid model (Gasper et al. 2005)			
$v_{yx}^{ratio} = \frac{(\cos(\zeta_0 - \phi_0 + \Delta\phi(\kappa - 1)) - (\cos(\zeta_0 - \phi_0)) \left(\frac{3}{2} + \sin \phi_0 \right)}{(\sin(\phi_0 + \Delta\phi) - \sin \phi_0) \left(\frac{3}{2} + \cos(\zeta_0 - \phi_0) \right)}$			

Where E_1 , E_2 , v_{12} and v_{21} are the elastic constants. The ξ is the intact angle between two ribs, the θ is rib angle with the horizontal and vertical directions, and

K_θ is the spring hinge constant (Smith et al. 2000). The ξ_0 and ϕ_0 represent the initial angle values; k denotes the relative deformation of ξ and ϕ . The other reported re-entrant models include double arrowhead (Larsen et al. 1997) and star structures (Grima et al. 2005) as shown in Fig. 2.11 (a) & (b). Both models were found auxetic by the opening and closing of arrowheads and stars respectively by hinging or flexure mechanisms. The re-entrant sinusoidal ligament design model as shown in Fig. 2.11 (c) derives the auxetic deflection by opening the sine waves almost in straight lines under tensile loading. The rotational expansion mechanism was utilised for drug diffusion (Dolla et al. 2007).

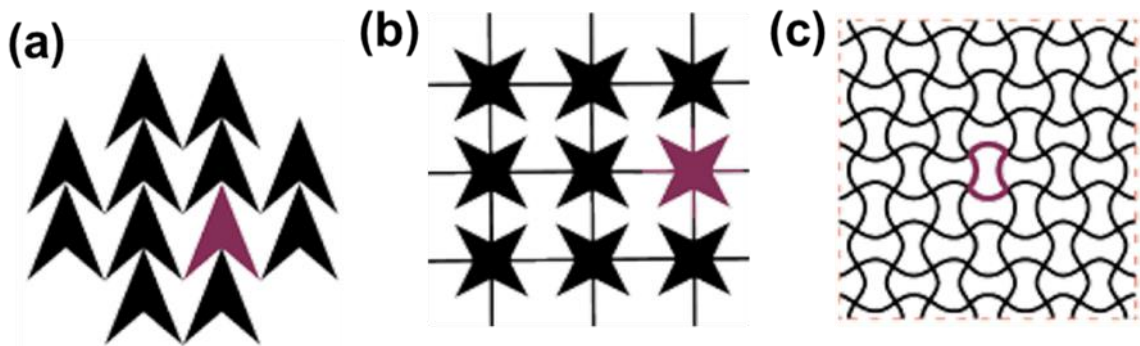


Fig. 2.11 The re-entrant design of (a) double arrowhead, (Larsen et al. 1997) (b) star re-entrant honeycomb (Grima et al. 2005), and (c) sinusoidal re-entrant models (Warmuth et al. 2016).

2.4.2 Chiral

The concept of the hexagonal chiral system was proposed by Wojciechowski (Wojciechowski 1989) and later developed by Lakes (Lakes 1991). The constructed hexachiral model was built from unit cells in which a cylindrical node was attached to six ligaments tangentially and providing the symmetry of the order of six as shown in Fig. 2.12. The same model was analysed theoretically and experimentally (Prall and lakes 1997) and led to establish a -1 Poisson's ratio through wrapping or unwrapping of the straight ligaments around the central nodes under loading. The model is to be said chiral if all the nodes rotate in one direction and antichiral, if nodes rotate in opposite directions. The analytical models developed to calculate mechanical properties for the chiral structures are presented in Equations 3 to 7.

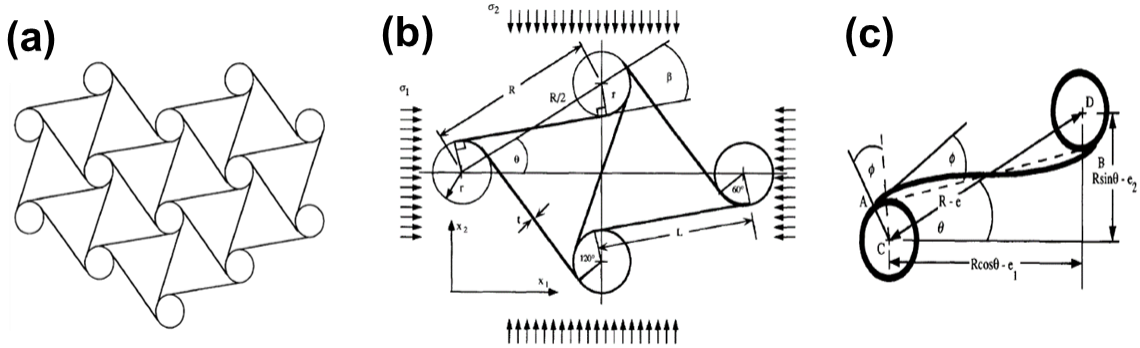


Fig. 2.12 Chiral structure (a) Unit cell and (b) deformation kinematics of ligaments
(Prall and Lakes 1997)

$$\varepsilon_1 = \frac{e_1}{(0.866)R} = \frac{0.866r\emptyset}{0.866R} = \emptyset \frac{r}{R} \quad (3)$$

$$\varepsilon_2 = \frac{e_1}{(0.5)R} = \frac{0.5r\emptyset}{0.5R} = \emptyset \frac{r}{R} \quad (4)$$

$$v_{12} = -\frac{\varepsilon_2}{\varepsilon_1} = -1 \quad (5)$$

$$v_{21} = -\frac{\varepsilon_1}{\varepsilon_2} = -1 \quad (6)$$

$$E = E_s \sqrt{3} \frac{t^3}{L^3} \frac{L^2}{r^2} \quad (7)$$

Where $\varepsilon_1, \varepsilon_2$ are the strains in the X_1 and X_2 direction. V_{12}, V_{21} , and E , are the elastic constants for the chiral honeycomb.

The other forms of chiral basic unit cells can be obtained from building blocks exhibiting rotational symmetry of order 'n'. Although there may be infinite number of building blocks having rotational symmetry of order n, only n= 3, 4, and 6 can be used to construct space filling periodic structures (Grima 2000). The chiral structures of orders 3 (tri-chiral), 4 (tetra chiral) and 6 (hexa-chiral) (Grima et al. 2008) were developed as shown in Fig. 2.13 (a) (b) and (c). Based on the same nodes and ligament rotational mechanisms, Grima et al. (Grima et al. 2008) developed a new "meta- chiral" auxetic model by replacing the cylindrical nodes to rectangles as shown in Fig. 2.13 (d).

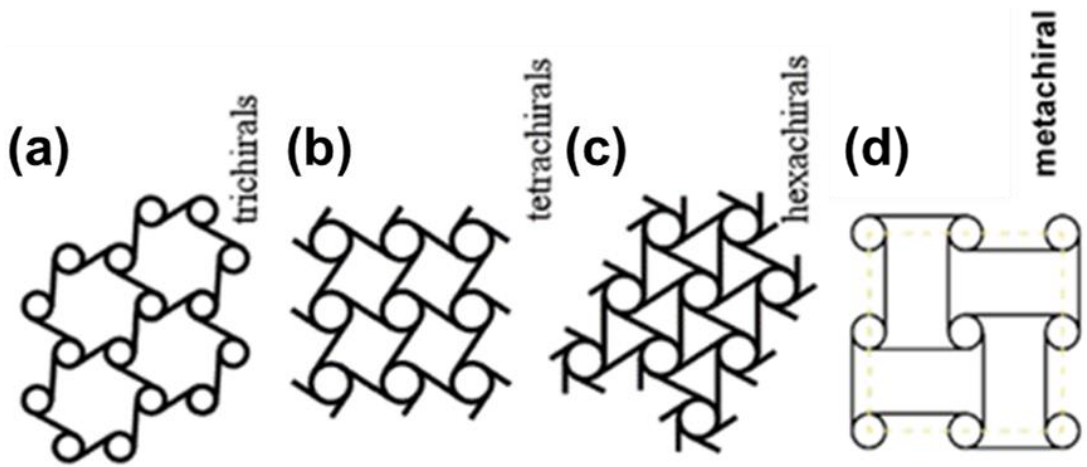


Fig. 2.13 The chiral unit cells of $n=3, 4$ and 6 rotational symmetry and the meta chiral model developed by Grima et al. (Grima et al. 2008)

2.4.3 Rotating units

Grima et al. (Grima et al. 2005) introduced alternative deformation mechanism based on “rotating rigid units” to explain the auxeticity in foams (Grima et al. 2005), nanostructured polymers (Grima and Evans 2000), zeolites (Grima et al. 2000) and silicates (Grima et al. 2005). This new model required the rotating units to be rigid, while only relative rotation of unit cells were allowed. The auxetic nature was obtained due to relative rotation of rigid units connected through vertices as shown in Fig. 2.14 (a) and (b). Analytical modelling was undertaken for the in-plane mechanical properties of rotating rigid rectangles (Grima et al. 2005) and rigid triangles (Grima et al. 2006) and the final equations are presented in Table 2.3. If rotating rigid rectangles to be replaced by rotating squares the Poisson’s ratio would reduce to $\nu_{12} = \nu_{21} = -1$.

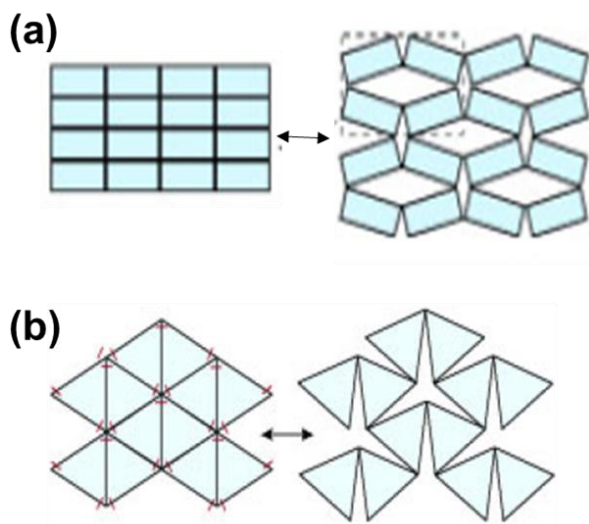


Fig. 2.14 The rotating rigid auxetic model of (a) rectangles (Grima et al. 2005)

(b) Triangles (Grima et al. 2006)

In 2007, Grima et al. (Grima et al. 2007) extended their original “rotation of rigid squares” model to a modified “semi-rigid square” model including the possibility of concurrently changing shapes of the squares with respect to each other. In doing so, they introduced an extra degree of freedom by providing an angle between the diagonals of the squares like a scissor as shown in Fig. 2.15 and obtained equations for mechanical properties as given in the Table 2.3. These equations for Poisson’s ratio predicted the dependency of auxeticity on the extent of the rigidity of the squares and the direction of loading, instead of just the relative rotations of the squares, as was the case with the previous model.

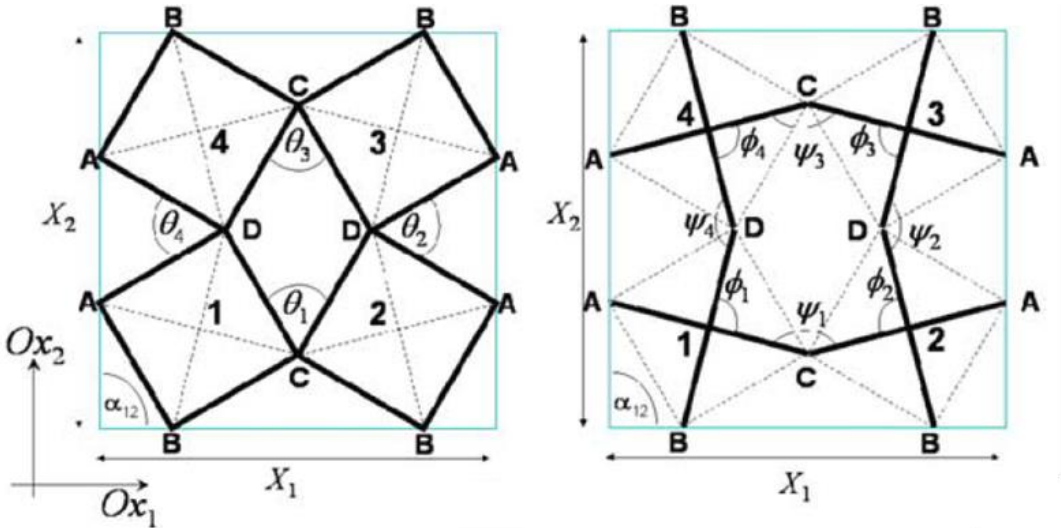


Fig. 2.15 Rotating semi rigid square model (Grima et al. 2007)

Table 2.3 Analytically developed equations of rotating rigid and semi-rigid models

	Rotating rigid rectangles	Rotating rigid triangles	Semi rigid squares
E ₁	$8K_h \left(\frac{[a \cos(\frac{\theta}{2}) + b \sin(\frac{\theta}{2})]}{[a \sin(\frac{\theta}{2}) + b \cos(\frac{\theta}{2})][-a \sin(\frac{\theta}{2}) + b \cos(\frac{\theta}{2})^2]} \right)$	$K_h \frac{4\sqrt{3}}{l^2 [1 + \cos(\frac{\pi}{3} + \theta)]}$	$\frac{[8k_\psi(k_\phi + 2k_\psi)]}{(k_\phi + 4k_\psi)} \times \frac{\sin(\frac{\psi_2}{2})}{\sin(\frac{\psi_1}{2}) \cos^2(\frac{\psi_2}{2}) l^2 dz}$
E ₂	$8K_h \left(\frac{[a \cos(\frac{\theta}{2}) + b \sin(\frac{\theta}{2})]}{[a \sin(\frac{\theta}{2}) + b \cos(\frac{\theta}{2})][a \sin(\frac{\theta}{2}) - b \cos(\frac{\theta}{2})^2]} \right)$	$E_{1-} E_2$	$E_{1-} E_2$
ϑ_{12}	$\frac{a^2 \sin^2(\frac{\theta}{2}) - b^2 \cos^2(\frac{\theta}{2})}{a^2 \cos^2(\frac{\theta}{2}) - b^2 \sin^2(\frac{\theta}{2})}$	$-\frac{d\varepsilon_1}{d\varepsilon_2} = -1$	$-\cot(\frac{\psi_1}{2}) \tan(\frac{\psi_2}{2}) \times \left[1 + 4 \left(\frac{k_\psi}{k_\phi} \right)^{-1} \right]$
ϑ_{21}	$\frac{1}{a^2 \sin^2(\frac{\theta}{2}) - b^2 \cos^2(\frac{\theta}{2})}$	$v_{21} = (v_{12})^{-1}$	$v_{21} = (v_{12})^{-1}$

Where ψ was the angle between the diagonals of the same square with K_ψ as the rotational stiffness and ϕ was the angle between the diagonals of the adjacent

squares with K_ϕ as the rotational stiffness. The symmetric geometry makes angles $\psi_1 = \psi_3$, $\psi_2 = \psi_4$, $\phi_1 = \phi_3$ and $\phi_2 = \phi_4$ and thus the shape of this structure particularly became dependent on the four angles $\psi_1, \psi_2, \phi_1, \phi_2$.

Most of the auxetic designs developed so far mainly fall into the three broad categories as discussed above, while there are also some other auxetic designs. The angle ply laminated composite was designed and fabricated to show auxeticity (Milton et al. 1992) by incorporating stiff and compliant matrix inclusions. The auxetic nature being scale independent, can be achieved from macro to molecular level. The attachment of the molecules of cyclic hexamer model attached through the vertices in a perfect hexagonal shape was found auxetic (Wojciechowski, 1989). It was also stated that the 69% of cubic elemental metals and face centred cubic rare gas solids exhibit auxeticity for a specific dimensional loading (Baughman et al. 1998).

Evidently, the auxetic material aspects were mostly evaluated and emphasised by means of theoretical predictions and simplified analytical models for most part (Prall and Lakes 1997, Masters et al. 1996, Smith et al. 2000, Gasper et al. 2005, Grima et al. 2006, Grima et al. 2007). The design models developed from the deformation mechanics of foams were mainly useful in understanding the basic means of deriving auxetic responses from specific material structures (Larsen et al. 1997, Grima et al. 2005, Grima et al. 2008). However, the conventional manufacturing methods were not able to produce these structures in reality. These manufacturing limitations have rendered the fabrication of auxetic forms to be

limited to a few simple structural forms. The thermo-mechanical volumetric compression methods could not be used for all kinds of materials and were also limited in terms of achieving complex geometries (Lakes 1987). The chemical-mechanical methods require the chemistry of the materials to be matched (Li and Zeng 2016). Consequently, fabrication of auxetic structures was limited to polymers mainly, developing structural forms such as foams and microporous fibres until 2010 (Lakes 1987, Alderson and Evans 1991, Chan and Evans, 1997, Alderson and Evans 2002, Alderson and Alderson 2005, Grima et al. 2009, Li and Zeng 2016). Though some metallic structures were experimented, it was mainly limited to forms such as foams (Friis 1988). The processing limitations led to the lack of consistency in the reproduction of auxetic structures, while also seriously limiting the base material options. The growth in the additive manufacturing technologies, and in particular the progress made in metal additive processing opened up new opportunities and a renewed interest in the fabrication, testing, and practical implementation of auxetic structures of more complex configurations. It is apt to turn the attention to some of the developments in the application of additive manufacturing methods in the auxetic material realm at this stage.

2.5 Additive manufacturing

Additive manufacturing constitutes a group of advanced manufacturing processes that allow construction of 3D forms mostly by the point-by-point consolidation of materials in different forms. Depending on the form of the raw material and the energy sources used, there are different processing techniques; selective laser

sintering/melting, 3D printing, fused deposition modeling, and electron beam melting being the most common and successful methods. The common attribute of all additive processing techniques is the ability to attain the intended geometrical characteristics deterministically (Koudelka et al. 2016). The layer-by-layer consolidation of the desirable materials to manufacture parts of complex geometries provides broad freedom in design and manufacturing. Customized objects can be produced directly from computer data such as computer-aided design (CAD), computed tomography (CT) and magnetic resonance imaging (MRI) data. Apart from opening up opportunities to produce a wide range of structural forms, these methods also allow a high degree of control over the resulting mechanical properties.

Considering the advantages of additive manufacturing of auxetic structures over conventional methods Schwerdtfeger et al. (Schwerdtfeger et al. 2010) fabricated a 3D re-entrant auxetic anisotropic structure of Ti alloy based on a tetrapod basic unit element as depicted in Fig. 2.16. The relative density of the structure was varied by changing the energy deposited by the electron beam per unit length, and characterized by compression tests. More energy translates to a larger amount of metal being molten and the struts becoming thicker and possessing higher relative densities. An increase in relative density was shown to increase the modulus of elasticity, almost in a linear fashion. The Poisson's ratio responses were found to be directional. The direction in which the elemental faces appear to be hexagonal resulted in positive Poisson's ratios in the range 0.45–0.5 with no auxetic behaviour. The direction along the other faces led to negative Poisson's ratios in the range –0.2 to –0.4, depending on the orientation (Schwerdtfeger et al. 2010).

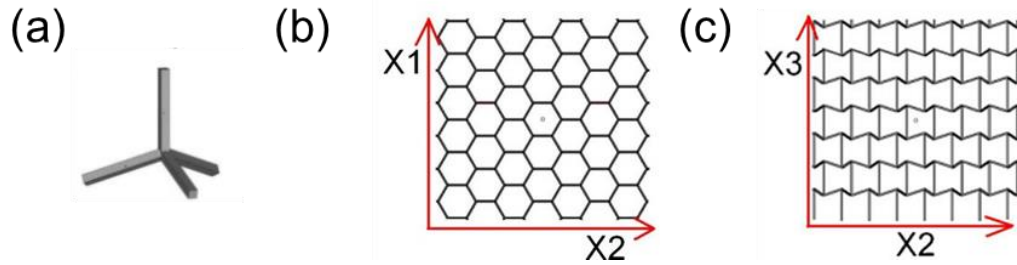


Fig. 2.16 The 3D tetrapod re-entrant auxetic structure (a) 3D unit cell (b) top view and (c) side view (Schwerdtfeger et al. 2010)

Yang et al. (Yang et al. 2012a) fabricated four different designs of 3D re-entrant lattice structures as shown in Fig. 2.17 by electron beam melting of the Ti–6Al–4V alloy. The changes in the structural strength and the elastic modulus due to variations in the Poisson's ratio and relative density were evaluated by means of compressive testing. With increase in relative density of the design models (design model 1 & 2), enhanced values of compressive strength and elastic modulus were obtained while keeping the Poisson's ratio constant. Similarly, an increasing trend in compressive strength and elastic modulus was also achieved with increase in negative Poisson's ratio while keeping the relative density constant (design model 2 and 3). However, the Poisson's ratio was found to have a more pronounced effect on the compressive strength and the elastic modulus values than the relative density of the lattice design. As a result, higher structural strength and stiffness responses could be obtained at lower mass, due to higher negative Poisson's ratios resulting from the structure. The Poisson's ratio could be made more

negative by either decreasing the re-entrant strut angle or increasing the ratio of the vertical to the re-entrant strut lengths.

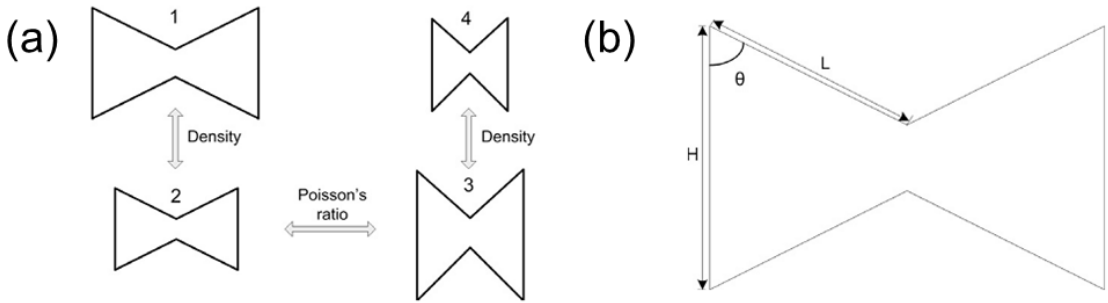


Fig. 2.17 (a) the four structural forms and (b) Design parameters of the 2-D re-entrant lattice structures (Yang et al. 2012a)

In 2012, Yang et al. (Yang et al. 2012b) fabricated two design variations of a non-stochastic auxetic foam of Ti-6Al-4V by electron beam melting technique. The design variations were targeted at achieving different negative Poisson's ratios. The compressive and bending analysis were performed to evaluate the effects of the design variations on the mechanical properties. The structures with higher negative Poisson's ratios achieved enhanced compressive strength and bending properties compared to the conventional structures and the ones with lesser negative Poisson's ratios. Further, in 2013, Yang et al. introduced sandwich panels with different cellular cores, including auxetic and other 3D reticulated designs. The samples were printed with electron beam melting of Ti-6Al-4V and bending tests were carried out on all the printed samples. Under bending loads, sandwich panels with auxetic designs showed homogeneous stress distribution and deformation,

while the other sandwich structures showed significant stress concentration effects. A significantly higher resilience was also obtained with the auxetic sandwich structure under bending loads, compared to the non-auxetic structure panels (Yang et al. 2013).

Wang et al. (Wang et al. 2015) designed and printed a 3D re-entrant structure using dual material conditions as shown in Fig. 2.18, with the joints elastic, while the beam members are made of stiff materials options, based on the connexTM series 3D printer using polyjet technique. Samples were characterized by experimental and FE analyses. The dual material auxetic structures demonstrated a unique and constant negative Poisson's ratio, for different strain levels, from 5% to 20%. It was due to the controlled deformation at elastic regions that prevented stiff regions from buckling, keeping the auxeticity at the same level as the strain increases. Effects of altering the materials selected and the fraction of the stiff regions, were investigated both computationally and experimentally. Material selection for the elastic region also affected the other elastic properties, with the stiffer materials yielding higher equivalent Young's moduli values. The ability to change the material selection and the stiffness regions allowed the flexibility to tune the auxeticity and the mechanical properties of the dual material auxetic structures, paving ways to alter the properties, without changing the overall geometry of the base auxetic unit cell.

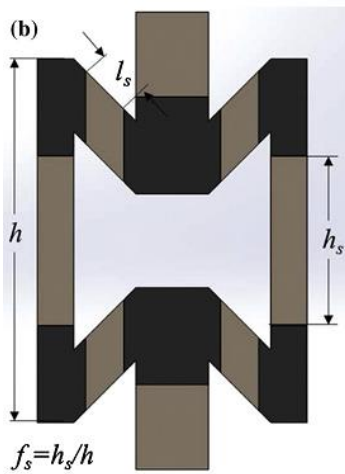


Fig. 2.18 Re-entrant unit cell with stiff (light) and elastic (dark region) material
(Wang et al. 2015)

The TiNi-based shape memory alloy structures were developed by Li et al. (Li et al. 2016) using selective laser melting (SLM) as depicted in Fig. 2.19. Two types of re-entrant structures were employed in this study; a conventional and a modified design. Characterization was done by compression tests and finite element analyses to predict the mechanical behaviour of the developed structures. Decreasing Poisson's ratios were observed for both the structures as the angle of the re-entrant structure decreased. The highest negative Poisson's ratios observed were -1.88 and -1.74 for conventional and modified re-entrant auxetic structures respectively. Influences of process parameters (laser power, scan speed, and track spacing) were studied to achieve the microstructural and structural integrity in Ti-rich TiNi alloys. It was observed that a post-process homogenisation treatment allows to achieve a higher negative Poisson's ratio close to -2 (Li et al. 2016).

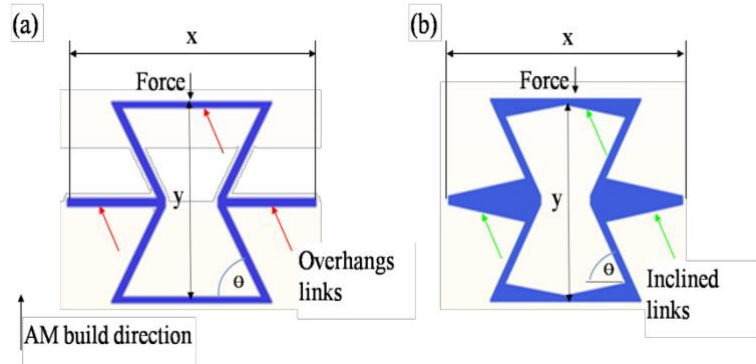


Fig. 2.19 (a) Conventional and (b) Modified re-entrant auxetic unit cell (Li et al. 2016)

In another attempt, Fu et al. (Fu et al. 2016) developed a 3D re-entrant auxetic structure made of 3D printed acrylonitrile butadiene-styrene (ABS) as shown in Fig. 2.20 and characterised the same by compression tests. Bending deformation mechanism was observed under uniaxial compression loading which allowed the structure to undergo large deformations without buckling. A systematic numerical simulation was also performed through the experimentally validated finite element models to analyse the effects of structural parameters. The deformation and auxetic behaviour were established for different re-entrant angles as viewed from different directions. The FE models were validated by comparing the stress–strain curves obtained from experiments. The effective modulus (ratio of effective stress and strain) values of the sample under compression in the elastic regime along the three principal axis were obtained. From these results, it was concluded that the proposed structure has a very obvious auxetic nature, when it was uniaxially compressed. Substantial correlation between numerical and experimental results was also noted.

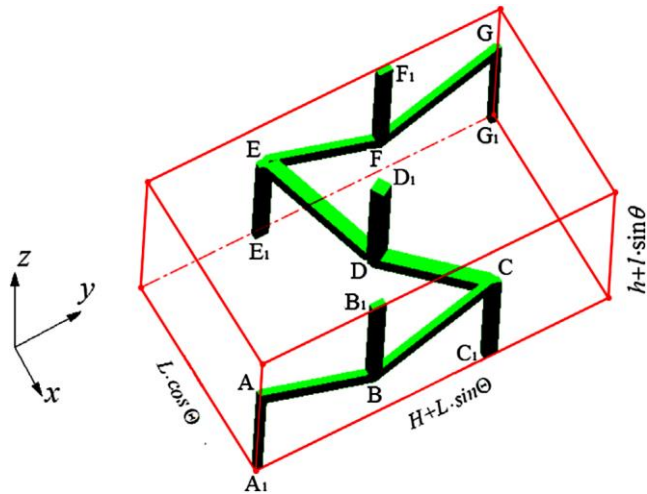


Fig. 2.20 Auxetic re-entrant 3D unit cell (Fu et al. 2016)

Xiong et al. (Xiong et al. 2017) introduced a modified 3D re-entrant structure, replacing the overhang links of the conventional structure with inclined links as shown in Fig. 2.21. The stress concentration and distribution effects were also evaluated by introducing the fillets at the corners of the inclined links and the re-entrant angles. The structure was fabricated by selective laser melting of AlSi10Mg and was optimized quantitatively in terms of the strut inclination and re-entrant angles. The optimum inclination and re-entrant angles 9° and 79° respectively were obtained from numerical and experimental analyses. The additional fillet radius feature was observed to suppress the stress concentration effects up to some extent.

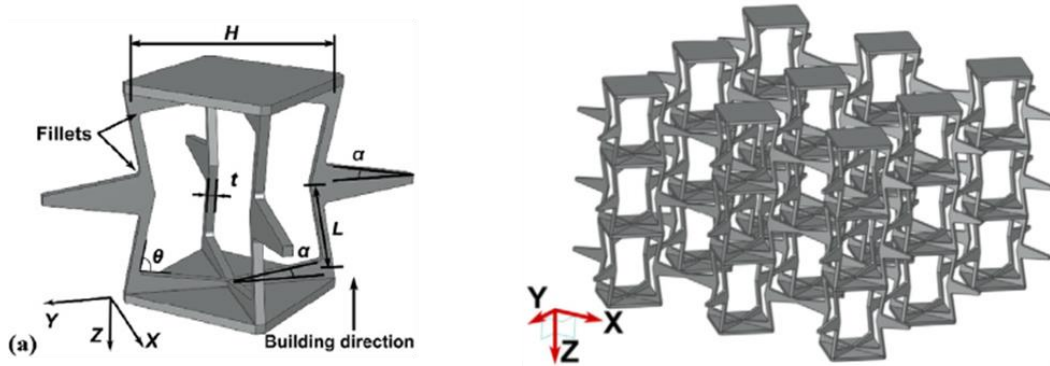


Fig. 2.21 (a) Conventional and (b) Modified re-entrant auxetic unit cell (Xiong et al. 2017)

Xue et al. (Xue et al. 2018) on realisation of the issues such as oxidation, inclusion, shrinkage-void and porosity in the direct printing of metal structures,, resorted to an indirect 3D printing method to fabricate the aluminium based 3D re-entrant structure as shown in Fig. 2.22. In this technique, a photosensitive resin structure was first fabricated by 3D printing, to be used as a sacrifice pattern for the investment casting of the final structure with aluminium. The compressive properties and the auxetic nature were established by compressive testing. With the indirect 3D printing method, the quality of the internal surface achieved was reported to be better. Variations in the geometric parameters were found to be responsible for the changes in the compressive strength and the auxetic behaviour of the structure. Increase in negative Poisson's ratio while keeping the relative density constant was found to enhance the compressive strength.

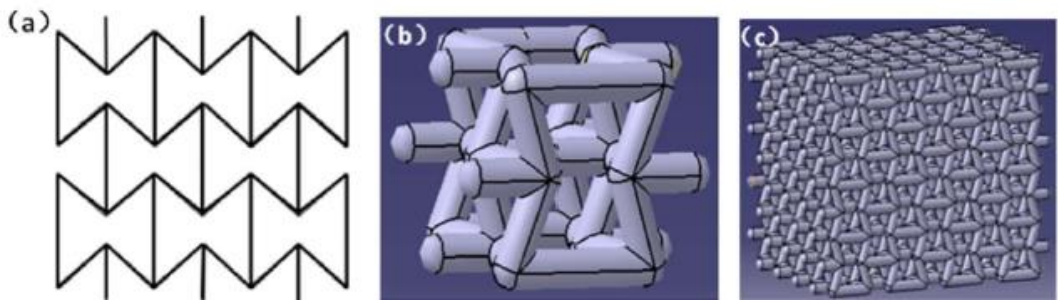


Fig. 2.22 The re-entrant (a) 2D honeycomb, (b) 3D unit cell (c) fully fledged 3D auxetic structure (Xue et al. 2018)

Rehme and Emmelmann (Rehme and Emmelmann 2009) developed and produced four different auxetic structures based on selective laser melting. Two of them were new and novel structures, decagonal honeycomb and cubic floral, while the other two were conventional forms, cubic sinus wave and cubic chiral honeycombs as shown in Fig. 2.23. All four structures were fabricated based on selective laser melting of stainless-steel powders and characterized by a universal testing machine under elastic compressive deformation. Two of these structures, named cubic sinus waves and cubic chiral honeycombs clearly showed negative Poisson's ratios at -0.12 and -0.28 respectively. The other two structures cubic floral and decagonal showed slightly positive values close to zero probably because the honeycomb unit cells were adjacent to each other leaving no space for preferred direction of lateral compaction.

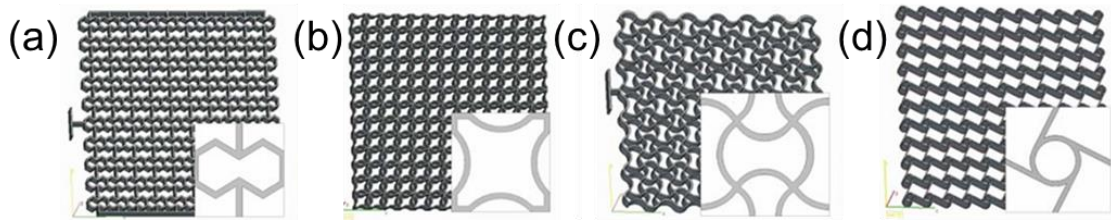


Fig. 2.23 a) Decagonal honeycomb b) cubic floral honeycomb, and conventional
c) Cubic sinus wave and d) cubic chiral honeycomb (Rehme and Emmelmann et
al. 2009)

Warmuth et al. (Warmuth et al. 2016) presented a three-dimensional chiral cellular structure as shown in Fig. 2.24 with different amplitudes and fabricated the same using electron beam melting of Ti- 6Al- 4V. The samples were characterised with the help of compression tests. The deformation mechanism was noted to change from stretching to bending based on the choice of the amplitude of the strut. Both elastic modulus and Poisson's ratio were strongly influenced by the amplitude of the chiral structure, while density variation left the Poisson's ratio unchanged (Warmuth et al. 2016).

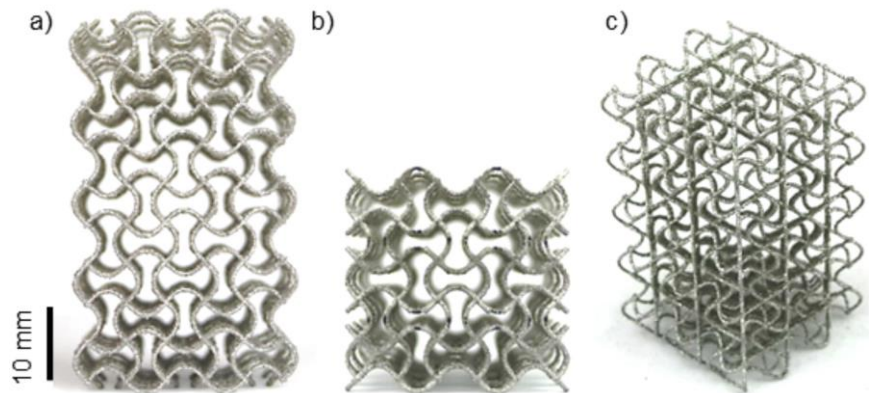


Fig. 2.24 Cubic chiral (a) front view (b) bottom view and (c) 3D view of the structure (Warmuth et al. 2016)

Shen et al. (Shen et al. 2014) introduced a new concept, desirable buckling mode analysis, to produce the 3D auxetic metamaterials by identifying the suitable buckling modes. The identified buckling mode can be introduced in the structure as an imperfection to achieve the auxetic behaviour. Using this technique, a novel 3D auxetic metamaterial was designed from a simple cubic building unit cell by creating a cavity, using a hollow sphere as shown in Fig. 2.25. The structure was inspired by the elastic instability of elastomers that can be tuned in auxetic metamaterials using different buckling modes under large deformations or strains. The building unit cell was replicated in 3D to develop the full structure. The developed structure was analysed numerically and mechanically and was found to be auxetic for large stress-strain range and this range could also be altered by providing different buckling modes or imperfections in the structure. This large stress strain range feature could be used as light-weight cellular materials options with enhanced energy absorption for motor vehicles.

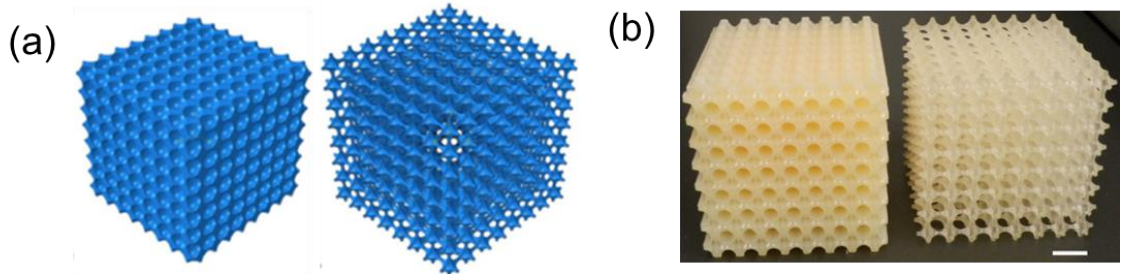


Fig. 2.25 3D Auxetic metamaterial (a) designed metamaterial with and without support (b) 3D printed auxetic structure with and without support (Shen et al. 2014)

Inspirations from the buckling modes also led to other structures as introduced by Yuan et al. (Yuan et al. 2017), fabricating 3D soft auxetic lattice bucklicrystals structures of thermoplastic polyurethane (TPU) powder by means of selective laser sintering techniques as shown in Fig. 2.26. The thermal and physical properties of TPU powder were evaluated and laser-sintering parameters were optimised accordingly. The fabricated bcc 6-hole bucklicrystal structure was found auxetic and could sustain repeated compression cycles for the applied wide range of strains under compression making it suitable for applications such as damping, energy absorption, and mechanical actuation.

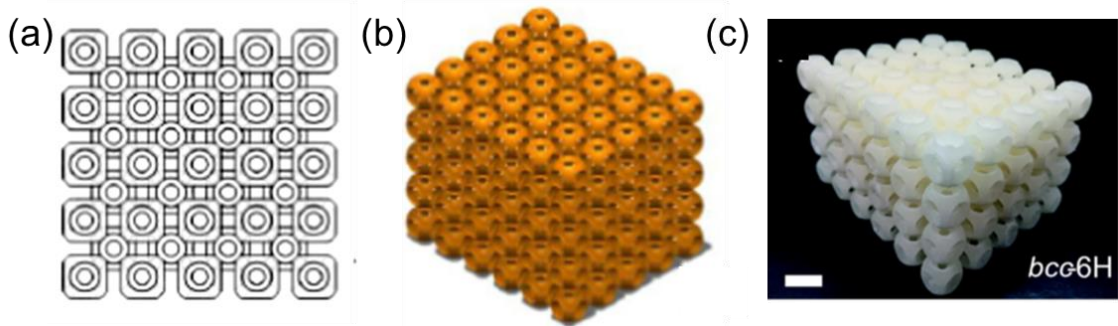


Fig. 2.26 3D bcc 6H Auxetic bucklicrystal (a) front view (b) 3D view (c) 3D printed structure (Yuan et al. 2016)

Ingole et al. (Ingole et al. 2017) attempted to improve the mechanical properties of the re-entrant auxetic structure by modifying the original 2D re-entrant structure (Fig. 2.27 (a)) by introducing the split vertical struts (Fig. 2.27 (b)). This was to reduce the local stress concentration effects during large deformations and distribute the applied load evenly throughout the structure. With the modification of the conventional re-entrant structure, two hybrid structures were also proposed by adding the conventional honeycomb unit cell in between two re-entrant unit cells as shown in Fig. 2.27 (c) and (d) to analyse the load carrying and deformation capabilities of the hybrid structure. The proposed structures were fabricated by fused deposition modelling of acrylonitrile butadiene styrene polymer (ABS) and analysed numerically and experimentally. The modified re-entrant structure was found to exhibit 65% more compressive strength and 30% more energy absorption than the conventional one. The differential deformation modes of the hybrid structures under loading paved ways to tailor the properties of the structures for specific applications.

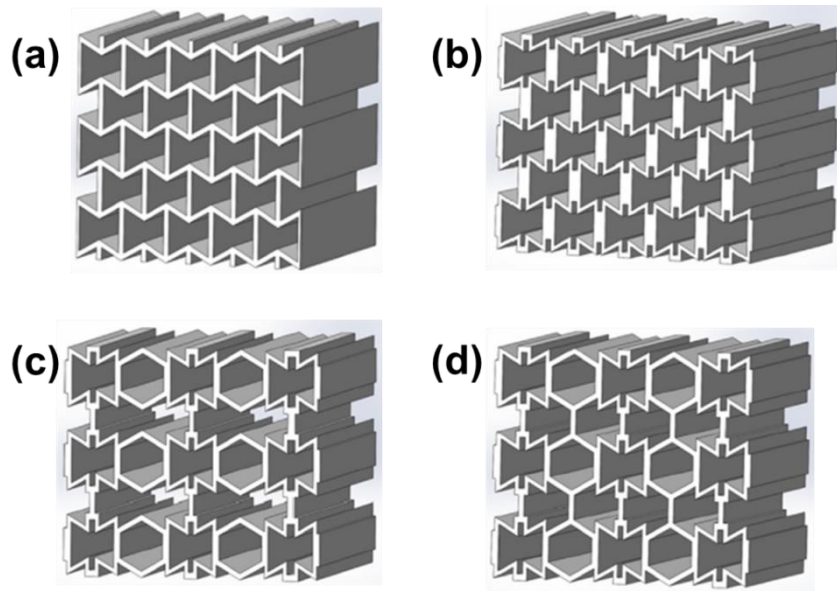


Fig. 2.27 Different forms of re-entrant auxetic structures (a) conventional re-entrant (b) modified re-entrant (c) re-entrant hybrid AH- V1 (d) re-entrant hybrid AH- V2 (Ingrole et al. 2017)

A new hybrid structure by combining the two-deformation mechanism of re-entrant and chirality was proposed by Jiang and Li (Jiang and Li 2018). The proposed structure was fabricated by multi material 3D printer as shown in Fig. 2.28 and analysed numerically and experimentally. The proposed hybrid structure was found to have substantial cell opening mechanism under a very large strain ranging from 2.91% to 52.6%. The two geometric parameters namely cell size ratio c_0/b_0 and re-entrant angle were found to effectively govern the stiffness, the Poisson's ratio and the cell opening mechanism of the newly designed hybrid structure. The particle release experiment was performed to evaluate the capability of the new hybrid

design deformation mechanism that could possibly be used in drug delivery system and colour change for camouflage.

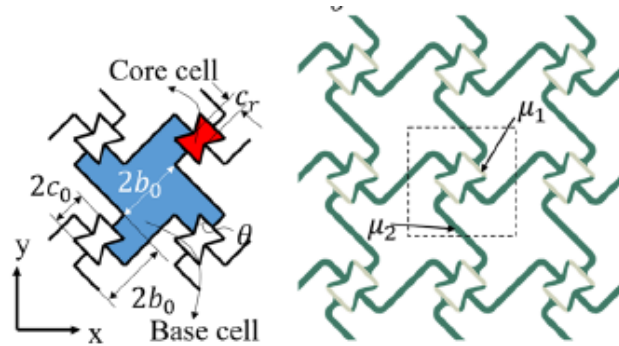


Fig. 2.28 Auxetic hybrid structure (a) Unit cells (b) fully developed hybrid structure
(Jiang and Li 2018)

Wang et al. (Wang et al. 2016) introduced a new interlocking assembly method of fabricating 3D re-entrant metamaterials to avoid the defects of additive manufacturing such as surface roughness, irregular cross sections and stair-stepping effects. The effects of geometrical parameters of built structure as shown in Fig. 2.29 were analysed on mechanical properties, Young's modulus and Poisson's ratio, numerically and experimentally. Increase in the re-entrant angle and the strut thickness led to increased compressive elastic modulus while decreasing the negative Poisson's ratio. The 45-degree re-entrant angle was found to give the maximum auxeticity which contradicts with the former theories (Li et al. 2016, Xiong et al. 2017).

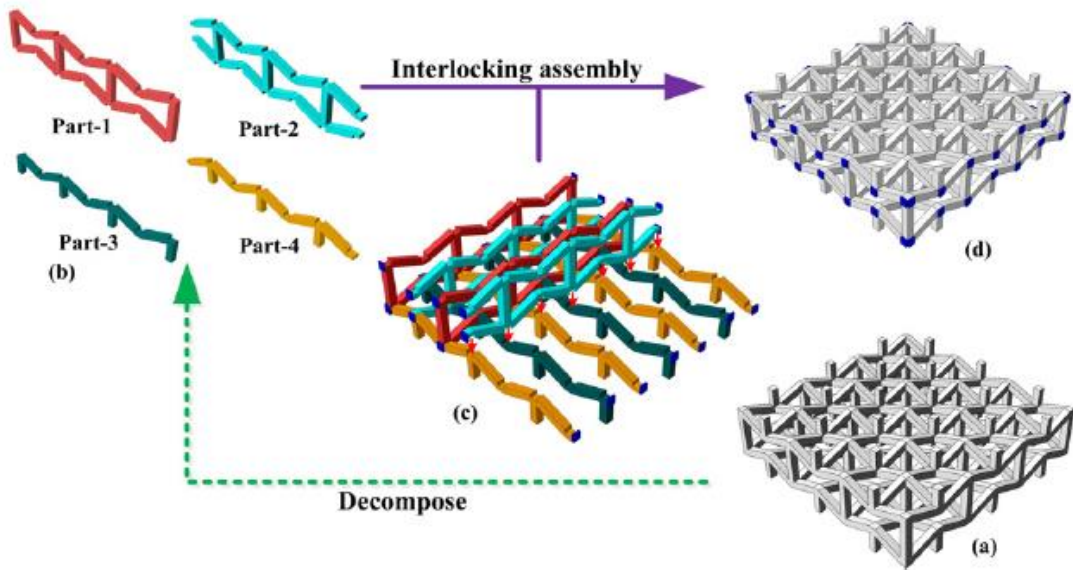


Fig. 2.29 Interlocking assembly fabrication of 3D re-entrant auxetic structures
(Wang et al. 2016).

Evidently, the additive processing methods prove to be more promising solutions to develop complex auxetic structures in a variety of materials, while conventional solutions are too limited in terms of both the freedom and the flexibility. However, the above reviewed reports clearly show the re-entrant auxetic structures enjoying a significantly higher importance in terms of being fabricated by the additive manufacturing against the other auxetic structures. Also, most of the reports were centred around the fabrication of conventional re-entrant structures (Yang et al. 2012a, Li et al. 2016), the extension of 2D re-entrant structures to 3D (Schwerdtfeger et al. 2010, Wang et al. 2015, Fu et al. 2016) and modified re-entrant structures (Li et al. 2016, Xiong et al. 2017, Ingole et al. 2017). Other structures of re-entrant design, missing rib, square grid, double arrowhead and sinusoidal did not get much attention.

It may be pertinent to point out that each deformation mechanism has its own advantages in realising the auxetic responses. The unfolding of re-entrant honeycombs through combined hinging, flexing and bending deformation mechanisms in the re-entrant design model allow re-entrant structures to obtain dramatically improved auxetic effects. This will allow isotropic structures with re-entrant angles to easily reach the limiting Poisson's ratio values of around -1 (Lakes1987) while this can go even higher with the anisotropic structures, in specific directions (Jiang and Li 2016). However, it was observed that under high compressive loading, the re-entrant auxetic structures are unstable and tend to lose the auxeticity due to the breakage of the re-entrant symmetry after instability (Jiang and Li 2016). While the other auxetic design model like chiral geometry as compared to the re-entrant one has capability to show more robust Poisson's ratio performance with both small and large deformation conditions (Wang et al. 2014). Further, other reported auxetic structures like missing rib, square grid and rotating polygons may offer further advantages as needed for specific applications. Apart from the lack of diversity in the analysis of auxetic structural forms, the main focus has always been to achieve the Poisson's ratio on the negative side, while a certain degree of attention was also on improving the other in-plane mechanical properties by altering the geometrical parameters. The hybrid structures reported relatively recently are examples where auxeticity and mechanical property enhancements were paid specific attention (Ingole et al. 2017, Jiang and Li 2018, Wang et al. 2019).

However, most of the current auxetic structures, including all geometries of the re-entrant structures, lozenge grid square and oblong and square grid structures

suffer from design limitations arising out of the numerous sharp corners and joints. Consequently, the more the number of joints, the higher the possible points of high-stress concentration and the higher the chances of failure of the structures due to critical stresses generated at the joints (Wang et al. 2015). Further, additive manufacturing, though of great help in building both 2D and 3D complex structures, may result in surface defects, often leading to stress concentration issues. This is in particular true with metal powders consolidated by processes such as electron beam melting (Abdeen and Palmer 2016). The electron beam melting technique suffers from irregular cross section (Yang 2011) and stairs stepping effects (Schwerdtfegeret al. 2012). Residual stresses and crack formation are also common with structures built by selective laser melting of metals (Yadroitsev & Yadroitsava 2015). Thermal histories and the ensuing melting and solidification of metals could also lead to metallurgical defects (Yang et al. 2012a).

Evidently, both the structural forms and the process attributes could lead to stress concentration issues in auxetic structures, and the problems are more pronounced, if the structure has more number of joints with sharp corners. Realising the problems such as oxidation, inclusions, shrinkage voids, and porosity, Xue et al. (Xue et al. 2018) actually resorted to building auxetic structural forms by indirectly using additive technologies to process aluminium through investment casting. Xiong et al. (Xiong et al. 2017) introduced a modified 3D re-entrant structure with inclined links and fillets and optimized in terms of the strut inclination and re-entrant angles. Evaluating the effects of the fillet radius, it was noted that increasing the fillet radius would suppress the stress concentration effects up to some extent.

While Wang et al. (Wang et al. 2016) chose an interlocking method over additive manufacturing processes.

2.6 Research gaps, questions and hypotheses

The literature review so far clearly elucidates the importance of auxetic materials in the medical (Evans and Alderson 2000, Bhullar et al. 2013, Yan et al. 2018, Wu et al. 2018, Jiang and Li 2018) and industrial applications (Howell et al. 1991, Smith 1991, Alderson et al. 2000, Bettini et al. 2009, Imbalzano et al. 2018). The wide acceptance of the auxetic materials, in view of their abilities to enhance specific mechanical properties and the wider applications in different fields demand advances in the manufacturing methods that can be employed to produce the macro structural forms. The conventional processing methods volumetric compression (Lakes 1987), thermoforming (Alderson and Evans 1991), multistage heating and cooling (Chans and Evans 1997), melt spinning (Alderson and Alderson 2005) and chemical mechanical route (Li et al. 2016) can be used to fabricate different forms of physical models of auxetic structures, but have seriously limited capabilities. The thermo-mechanical volumetric compression methods cannot be used for all kinds of materials and are also limited in terms of achieving complex geometries. The chemical-mechanical methods require the chemistry of the materials to be tuned appropriately. Until 2010, the fabrication methods were mainly based on polymers and that too limited to producing foams and even if metals were considered, the structural shapes targeted were limited to producing foam like forms. Consequently, the conventional methods lack the freedom not only

to operate on different materials but also in obtaining complex free-form structures. Considering the wider benefits and the need to be able to produce complex structural forms in real engineering materials, and in particular, the metallic options, the attention gradually turned towards additive manufacturing methods.

A series of attempts followed using different additive manufacturing methods to produce varying auxetic structural forms (Schwerdtfeger et al. 2010, Wang et al. 2015, Li et al. 2016, Fu et al. 2016, Xue et al. 2018). With additive manufacturing, it has become possible to physically produce relatively more complex shapes, beyond what was realistic, with the traditional methods. This has given a further impetus to the research on auxetic structures, exploring different geometrical aspects of auxetic cellular structures with a variety of base materials. However, for most part, the printed auxetic structures were polymer prototypes that could only serve as models to validate certain theoretical predictions. Additive manufacturing of metals was only employed to a limited extent and in particular the ability of selective laser melting to produce complex shapes in a wide variety of metals has not been exploited fully. While the re-entrant 2D and 3D auxetic forms attained some attention, the freedom to operate on different metal systems and the abilities to build real complex forms has not been utilised fully to stretch the limits and invent new auxetic forms.

Overall, the research related to auxetic cellular structures has been for most part theoretical, and focussed on enhancing the negative Poisson's ratios. Significant practical implementation has begun to take the front seat only with the advent of

the additive processing technologies. Nevertheless, numerous auxetic structural forms such as the missing rib, square grid, star-shaped, and chiral designs attained no significant attention. Another intriguing aspect is the general negligence of the role of the stress concentration effects which are highly likely, given the complex structural forms used to build the base unit cells. Very few trials were noticed attempting to fabricate the cubic chiral (Warmuth et al. 2016), missing rib (Koudelka et al. 2016), and star shaped (Yang et al. 2016) models using the additive manufacturing technologies. However, the square grid structure did not get any attention.

A couple of attempts also touched on the stress concentration aspects (Wang et al. 2015, Xiong et al. 2017) evaluating the effects of locally modifying the sharp corners either by introducing materials with lesser stiffness properties in the critical zones or by filleting the joints. The use of materials with different properties relies on the multi-material polymer jetting technologies such as the erstwhile Connex systems, with serious restrictions on the material properties. Such fabricated structures are only useful as prototypes to test the theoretical concepts but are not good for any real world application. Filleting, though a viable means of eliminating stress concentration zones, the additional benefits of employing additive manufacturing of metals based on processes such as the selective laser melting has not been evaluated sufficiently in this context. The following research gaps are clearly evident from the foregoing discussion:

Research gaps

The research gaps in the overall scheme of designing, evaluating, and testing auxetic structures include:

- Firstly, the more flexible selective laser melting method that can be used to process a variety of metallic systems has not been fully utilised to evaluate different auxetic forms.
- Secondly, most previous research on auxetic models was based on theoretical modelling, with experimental verification attempted only scarcely.
- Also, numerical modelling was used earlier in order to evaluate the auxetic nature of specific structural forms, but the experimental verification of the simulation results and integrating both to obtain the most optimum structural forms were not done to the necessary extent.
- The role of the geometrical complications in inducing stress concentration zones was neglected by far.

Research gaps specific to the application of the additive manufacturing methods to produce auxetic structures include:

- The re-entrant square grid structure though promising in terms of the auxetic responses, did not attain any attention so for the application of the additive manufacturing methods

- Also, the possibility to optimise the geometries of such structures has not been paid any attention due to the limitations of the current manufacturing methods.
- The materials choice has been mostly limited to Ti64 alloys while the processing route in most cases was electron beam melting. Other materials and the more flexible selective laser melting attained no significant attention.
- The possibility to utilise these new manufacturing methods to develop new metallic auxetic structures targeting specific attributes such as lesser stress concentration zones was not undertaken significantly so far.

The overarching hypothesis for the proposed research is that selective laser melting is the pathway to producing better and more refined auxetic structural forms using specific metal systems. The research proposed around this more specific hypotheses such as:

- A combination of the numerical and experimental verification schemes is necessary to be developed in order to thoroughly evaluate and completely understand and control the auxetic nature of different structural forms
- The auxeticity of re-entrant square-grid auxetic structures can be optimised by carefully analysing and suitably adjusting the geometrical features of the unit cell configurations.
- Better auxetic structural unit cells can be designed to avoid the stress concentration zones of the structures
- A judicious combination of different auxetic cellular forms integrated into an overall structural format can be effective in combining the good characteristics of both cells in the final auxetic structure.

The overarching research question is: What is the most appropriate scheme of ascertaining the true auxetic response of a given macro structure? The research to be undertaken to answer this question will lead to sub questions as follows:

- Is selective laser melting the most flexible manufacturing method to produce metallic auxetic structures of different forms rapidly and effectively?
- Is a combination of the experimental verification by means of loading structures produced by selective laser melting and numerical simulation of the same tests and the correlation of the results the best way to establish the true auxetic nature of structures?
- Can geometrical optimisation of unit cells help enhance the auxetic performance of re-entrant square-grid structures?
- What is the role of the unit cell geometry in inducing stress concentration zones in auxetic structures?
- What new geometrical forms of unit cells could help reduce or eliminate the stress concentration zones in auxetic structures?
- How can unit cells of different geometrical forms be integrated into a hybrid structure targeting specific auxetic outputs together with mechanical attributes at specific levels?

Research objectives:

The primary objective is to evaluate the selective laser melting approach as a possible manufacturing method to develop different auxetic structures based on at least a couple of metal systems. This will be achieved by considering one of the promising structural forms such as the re-entrant square-grid structure developing both numerical evaluation schemes and experimental verification methods based on structures produced using selective laser melting. The overarching objective in this preliminary work is also to establish a numerical and experimental evaluation scheme that can be used for both the development of new structural forms as well as optimise the geometrical forms of these models.

The next target is to focus on the stress concentration effects in auxetic structures based on the numerical evaluation methods established. Based on the results of preliminary tests done on the square grid forms, better structural forms with unit cell geometries altered to reduce stress concentration effects have to be designed. Also, the new models have to be analysed by the numerical and experimental evaluation schemes developed in order to establish the relationships between external applied loads and the auxetic performance of the new structures designed.

Finally, the flexibility to physically produce more complex auxetic structural forms by selective laser melting will be employed to develop and analyse hybrid structural forms targeting specific output qualities. Again, the experimental and numerical evaluation schemes will be utilised to design, evaluate and test these auxetic

structures, with an aim to combine the beneficial roles of different forms of unit cells in a given single structural form.

2.7 General methodology

The research aims at developing metallic auxetic structures by selective laser melting for experimental evaluation of the auxetic nature. The experimental conditions will also be simulated by means of numerical evaluation and the results have to be correlated in order to establish a reliable scheme of evaluating the auxetic structural forms. The overarching methodology is essentially numerical simulation of auxetic structures and the experimental verification of the same, searching for answers to the critical research questions raised. The numerical simulations will be undertaken by means of the finite element methods. Physical production of the structures will be done by employing selective laser melting. Also, analytical modelling will be done where necessary, and in particular when new auxetic structural unit cells are conceptualised, designed and developed.

Appropriate build patterns and support structure designs will have to be developed while implementing the selective laser melting method to produce complex auxetic structural forms with metals. Experimental verification of the auxetic responses involves use of appropriate systems for measuring the deflections of the different units and points of the structure. Both imaging and physical measuring techniques will be considered for this. Numerical simulations will necessitate the establishment of appropriate boundary conditions for each structure. Trial and error

methods will be developed using an experimental value as the benchmark to establish the appropriate conditions that can be used in all the subsequent numerical trials.

Chapter 3

Methodology

3.1. The overall scheme of the research

Several auxetic structures will be analysed, designed, fabricated, and tested in the current research, in order to develop a comprehensive understanding of the auxetic behaviour and associated responses. With newly designed structures, the first step usually is to develop an analytical model to predict the auxetic responses, which is, mostly at the level of the basic unit cell. Numerical methods will have to be employed to further evaluate the nature and variation of these responses with varying loading conditions. The numerical simulations will also be extended to the full structures stitched by integrating several unit cells in specific orders. The numerical simulations once established, will pave ways to identifying the best possible geometrical features of each of the structures. The optimised form of the structures have to be fabricated then and experimentally loaded to capture the real auxetic responses. Correlation of the experimental and numerical results will finally allow to ascertain the auxetic performance of the structures evaluated. Once the reliability of the numerical schemes is established, the scope of the analysis can be extended to capture further finer aspects of the structure such as the variations in the stress fields under varying loads.

The initial auxetic responses were evaluated based on analytical models describing the geometrical relationships between members of unit cells under specific loading conditions. Numerical simulations were undertaken by means of finite element methods implemented in the commercial ANSYS software. Experimental measurements were based on the auxetic deformation of the structures under uniaxial compression implemented on a universal tensile testing system. Both contact and non-contact type measurements were used to capture the displacements of critical points of the auxetic structures deforming under loading. Overall, the research task is a mixture of analytical, numerical, and experimental methods, and the results are integrated to develop the understanding and the scientific knowledge on the auxetic behaviour of specific structural forms. Further details on the actual methods used for different tasks of the research are presented in the following sections.

3.2. CAD modelling

Designing a complex structural form such as the auxetic structures evaluated in the current research often requires a sophisticated computer aided design (CAD) tool. Commonly used CAD tools in engineering are CATIA, ProEngineer, and SolidWorks allowing the design process, from the concept to the production of end-use parts. The ease of conceptualizing and digitalizing complex forms together with the high precision and quality and the ability to incorporate design changes without the need to go back to start particularly aid tasks such as the design of the auxetic structures. Availing the advances in CAD modelling, Elipe and Lantada (Elipe and

Lantada 2012) reported a comparative study of auxetic geometries by means of computer-aided design and engineering. All the designs were built in Solid Edge (Siemens PLM Solutions) and simulated numerically in NX-8.0 (Siemens PLM Solutions). For the current research purpose, all the auxetic design models are modelled using the SolidWorks 2015 software. Though, the software is also capable of performing the numerical simulation of the auxetic responses, only the design feature of the software is used for structural designs while the numerical simulations are performed on another software platform as discussed later in this chapter. The standard design procedure followed to model the various shapes is as follows:

- The basic 2D sketch of the critical form of the unit cell is created in SolidWorks 2016, as shown in the example in Fig 3.1, using the sketching tools on the graphics user interface of the SolidWorks suite using one of the drafting views, front, top or side planes.
- Once unit cell is built, the 2D form is constructed by replicating the cells in the X- and Y- directions by copying and mirroring, as many times as needed. The arrangement of the unit cells in the X and Y-direction is structure-specific and may differ from one structure to the other.
- The 3D form of the full structure is then generated by extruding the whole sketch in the Z-direction, as depicted in Fig. 3.1 (b).

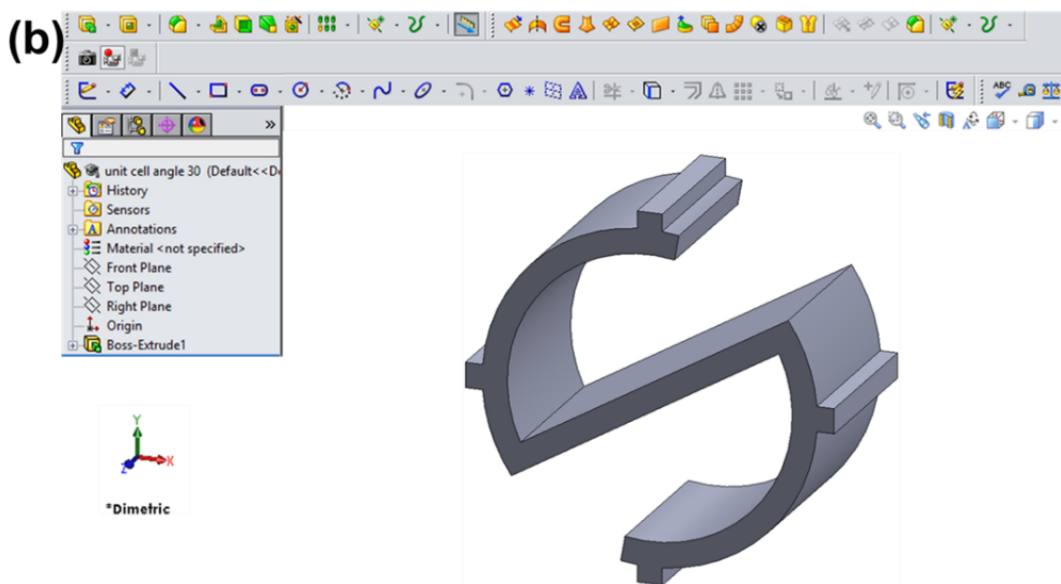
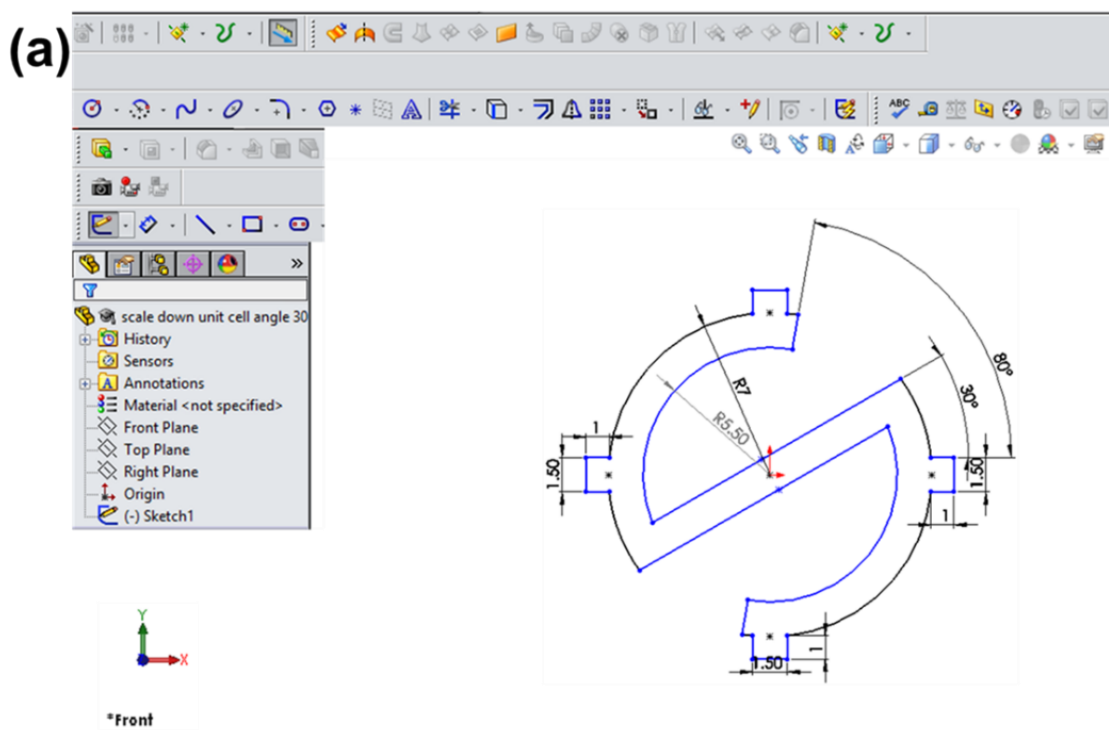


Fig. 3.1 (a) 2D Sketching and (b) 3D extrusion form of a unit cell in SolidWorks

2015

3.3. Finite element simulations

The finite element method is a powerful tool to simulate complex engineering situations and continuum mechanics problems. As has been the case with numerous examples in widely varying fields such as structural and fluid mechanics and potential type problem domains, the method also found its way to the simulation and analysis of the auxetic structural forms.

Abdelaal et al. (Abdelaal et al. 2012), presented a 3D finite element analysis of periodic regular hexagonal, auxetic re-entrant hexagonal, and functional graded auxetic (FGA) honeycombs based on the ANSYS software. The effects of the unit cell geometry and the relative density on the structural mechanical properties were established under compression, tension and cantilever bending test loading. In similar lines, Aslam et al. (Aslam et al. 2015), reported the effects of varying density of an auxetic structure on Poisson's ratio and other mechanical properties under compression and tension based on finite element simulations. Carniero et al. (Carniero et al. 2016) also numerically analysed the geometrical (changing rib length, rib width, and rib angle) and base material dependence on the auxetic behaviour of a 2D re-entrant structure using COMSOL Multiphysics software.

Rad et al. (Rad et al. 2014) proposed a novel 3D re-entrant structure establishing the effects of geometrical modifications on the stiffness properties including the Poisson's ratio and fracture toughness and the overall performance attributes of

the structure, based on both numerical and analytical modelling. The numerical simulations performed in Abaqus software were validated with the analytical results. In similar lines, Zhang et al. (Zhang et al. 2018) investigated a 2D re-entrant structure under large tensile deformation, simulating the post-yield behaviour. An analytical model choosing the idealized perfect rigid plastic material and the numerical simulations considering two material conditions, a rigid-perfectly plastic and strain hardening material model were formulated. The numerical results were reported to be in general, agreement with the finite element results.

The critical role of numerical simulation in establishing the auxetic behavior of new structures, or to evaluate the mechanical properties of the existing structures, or optimizing the geometrical parameters to enhance various mechanical and geometrical aspects is clearly evident from these examples. Considering the potential advantages, the auxetic structures experimented in the current research are initiated, optimized and finally established based on finite element simulations using the ANSYS FE simulation software package version 16.2. The square grid, S- shaped and hybrid structures to be presented in Chapters 4, 5, and 6 were numerically simulated and geometrically optimized using finite element modelling based on ANSYS Workbench by following these steps:

- First, the designed CAD models of the respective structures as discussed in Section 3.2 were directly imported into the ANSYS FE package version 16.2 for structural analysis. For importing the CAD files directly into the ANSYS platform, the SolidWorks files need to be converted into one of the

file formats supported by ANSYS. In the current research, all the SolidWorks files were converted into the ACIS file format which is compatible with the ANSYS software.

- Depending on the requirements of the analysis, structural linear, bilinear isotropic hardening and other specific material conditions of ANSYS were selected for analyses with linear and non-linear materials conditions. The structural properties of different base materials were chosen from the ANSYS material library.
- Establishing the optimum mesh size is an important step as the accuracy of any numerical model is highly dependent on the choice of the shape and size of the mesh. A mesh convergence scheme was used with all the structures modeled and the actual details are included in different chapters.
- The boundary conditions were chosen to be able to simulate the compression testing, therefore fixing the displacement zero in the load direction, while leaving the other two perpendicular dimensions free. Displacement boundary conditions were used, to simulate the compressive loading of the structures and capture the mechanical and auxetic responses. The actual magnitudes of the displacement boundary conditions applied to simulate the corresponding compressive loading conditions varied with the structures analysed and are reported in the respective chapters.

3.4. Selective laser melting

The additive manufacturing method employed in the current work is based on selective laser melting of metal powders. The critical steps followed to print the various parts are:

- First, the CAD model of specific design is converted in to the .stl file format to load the design into the selective laser melting software.
- The optimum fabrication process parameters for stainless steel 316L and CoCr alloys are fed to the system using the appropriate materials files as provided by the manufacturer.
- Once the file is submitted to the system, the powder spreading and the laser melting process takes place alternatively in an automated routine as controlled by the machine central control system.
- A schematic diagram of the SLM process is depicted in Fig. 3.2. An argon protective atmosphere is employed on the Renishaw commercial system used for the purpose of producing the auxetic structural forms used in the current research.

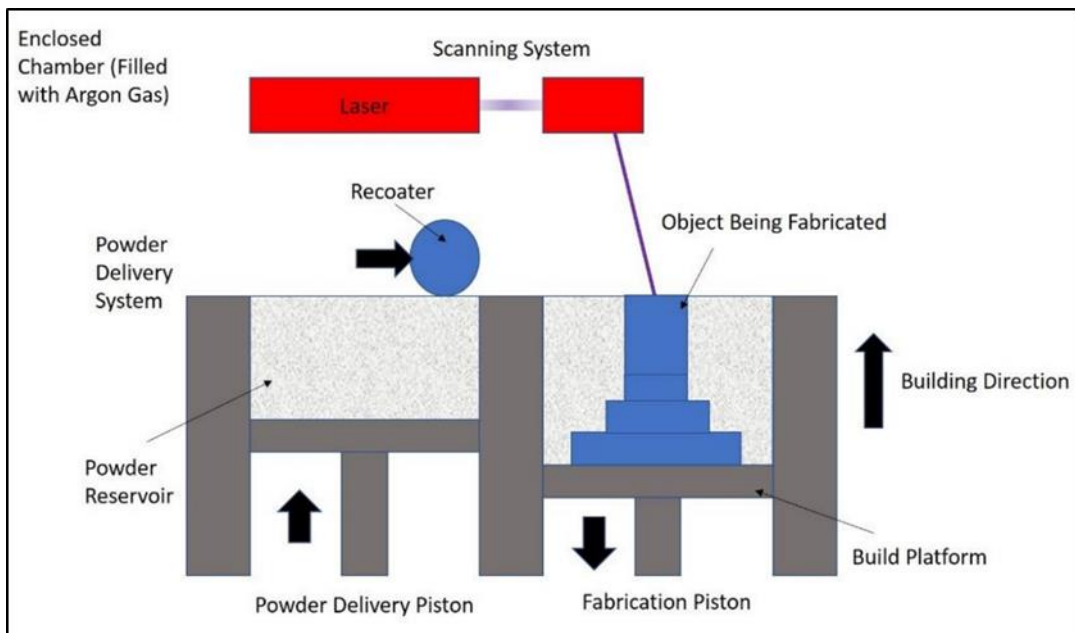


Fig. 3.2 Schematic diagram of selective laser melting technique (Jiao et al. 2018)

The Selective laser melting technique was used to produce the structural forms of all auxetic structures evaluated in the current research. The Renishaw AM 400 laser melting system (Fig. 3.3) available at the 3D printing laboratory of Auckland University of Technology was employed for all the printing tasks. The AM 400 system is equipped with a solid state Nd: YAG laser (wavelength = 1070 nm) of 75 μm spot size. The laser melting process is thermally complex and is influenced by numerous experimental factors. The most significant of them being the base metal powder, the laser power, scan speed and spacing and the thickness of powder layer. The energy density is often used as a representative factor.

Two different base materials, cobalt-chromium (CoCr) alloy and stainless steel (SS) 316L were employed in the fabrication of the square grid auxetic structures by selective laser melting for the experimental work reported in Chapter 4. Practical difficulties were faced with the availability of the expensive selective laser melting system together with the choice of the experimental materials at different times. As a result, these two different materials were used to produce the auxetic structures at different times. The process parameters for each materials were fixed as per the material data file specifications provided by Renishaw. In the case of CoCr alloy, the parameters were laser power 275 W, laser scan speed 850 mm/s, and the layer thickness 30 µm. With stainless steel 316 L, these were laser power 250 W, scan speed 800 mm/s and layer thickness 30 µm.

The initial square grid structures built by using CoCr and stainless steel 316L reported in Chapter 4 were built horizontally, raised by the support structures through a height of 5mm above the build plate. The newly designed S-structures and all the other hybrid structural forms were built using 316L stainless steel powder. Three replicas of each structure were built one over the other, for each of the process and geometrical parameter combination. This was done to reduce the total number of builds, as each build was very expensive in terms of the preparation and post-processing times. In between the stacked structures, suitable support structures were included, as shown in Fig. 3.4. The mechanical properties of the Co–Cr alloy consolidated by selective laser melting are; yield strength 714 MPa and modulus of elasticity 220 GPa, while in the case of stainless steel 316L, the yield strength is 547 MPa and the modulus of elasticity 197 GPa, as per the specifications by Renishaw (2016, 2018).



Fig. 3.3 Renishaw AM400 SLM machine (from AUT 3D Printing Lab)

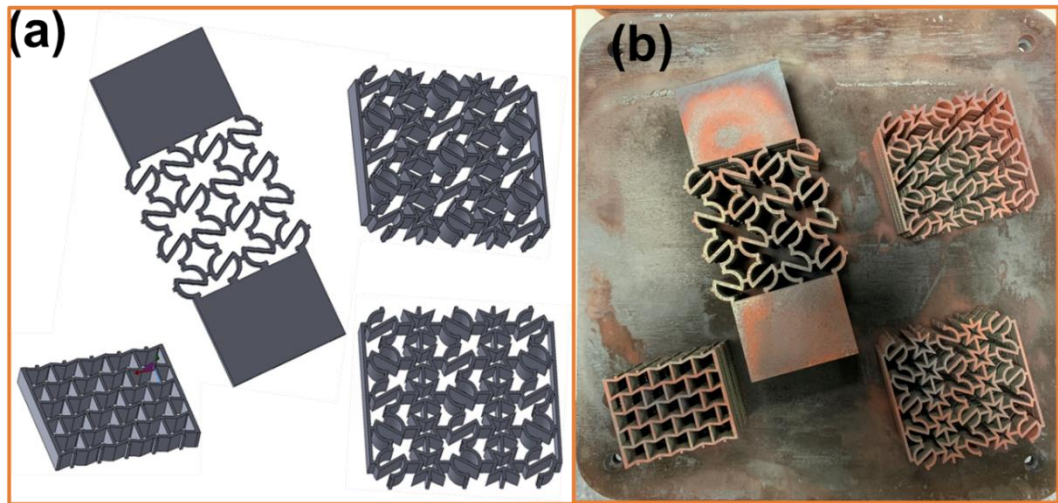


Fig. 3.4 (a) 3D CAD models of different structures (b) Selective laser melted structures built on a single build-plate stacking one over the other.

3.5 Post processing

The first post processing task is to heat treat the selectively laser melted parts for the stress relieving annealing and to ensure the higher strength as specified by Renishaw. Both CoCr and stainless steel 316L structures built by laser melting were kept in the Nabertherm furnace depicted in Fig. 3.5, together with the build plate, before removing the support structures. The heat treatment process essentially is heating the parts slightly above 900 °C, holding for a couple of hours and then furnace cooling to room temperature. This procedure was chosen based on the recommendation by Renishaw.



Fig. 3.5 Nabertherm heat treatment furnace (AUT 3D Printing Lab)

The next step is the removal of the support structures. As already stated, support structures were included between the bottom structural part and the base plate and between the parts in the upper levels. This was done to facilitate the easy separation of the printed structures from each other and from the base plate. Also, the thermal conditions are more uniform, and confined to each structural part due to the relatively sparse connection by the supporting legs between each structural section. Otherwise, three structures continuously built as one integral part would make the mass a huge heat sink as the build process progresses from the bottom

upwards and makes the thermal conditions variant from the bottom part to the upper one. The support structures were removed by using the wire cut electrical discharge machine available in the mechanical engineering workshops of Auckland University of Technology as depicted in Fig. 3.7. The wire-cut (electric discharge machining) EDM is a non-traditional electro-thermal machining process, in which material removal occurs due to a plasma generated between electrodes. The schematic diagram of the wire EDM is provided in Fig. 3.6 as a dielectric medium is employed, there is no direct mechanical force induced nor any thermal distortion occurs in the specimens.

The structural parts closer to the base plate are first separated by removing the structures using the wire cut EDM process. The process is then repeated to remove the support structures in between the structural specimens. However, there will be residual legs still remaining on the sides where wire EDM is applied, which requires further processing. The specimens are mounted on a milling machine and gently clamped, A light skim cut was applied on each surface with the residual support structure legs to complete clear the surface and also bring it to a smooth finished plane, with no possible stress concentration points.

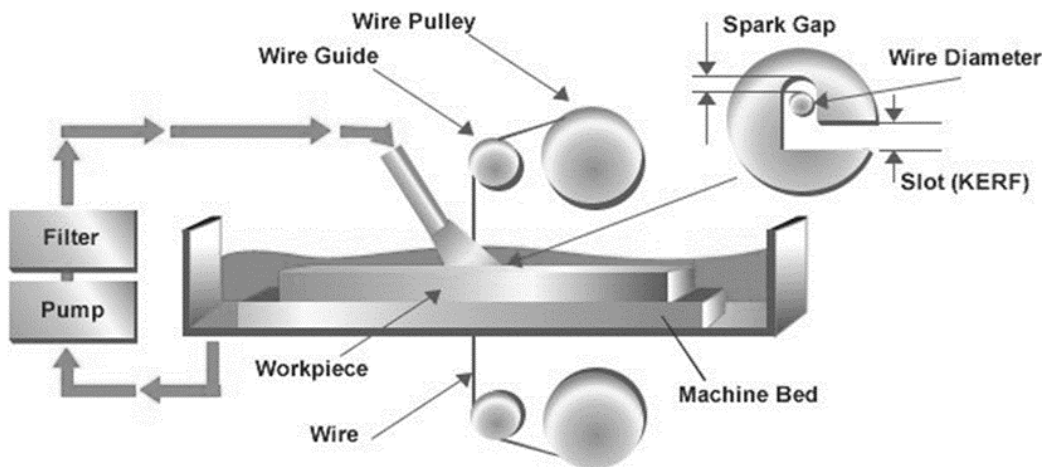


Fig. 3.6 Schematic diagram of wire electric discharge machining (American Wire EDM)



Fig. 3.7 Wire electron discharge machining equipment (AUT Mechanical Lab)

3.6. Characterisation

3.6.1 Mechanical testing

Mechanical properties of materials are often established through tensile testing based on standard dog bone shaped specimens. The additive manufactured materials are also evaluated by the same procedures, in order to establish the process property relationships. Karnati et al. (Karnati et al. 2016) tested the selectively laser melted and rolled-annealed stainless dog bones of varied size to map material property anisotropy on an Intron universal tensile testing machine. Flodberg et al. (Flodberg et al. 2018) reported the tensile test analyses of two different geometries, standard test samples dumb-bells (dog bones) and tubes (\varnothing 30mm and 150mm long) of two different materials, PA12 (polyamide) with and without the addition of carbon fibres (CFs). The tests were performed on a Static Test Machine number K1 Tinius Olsen 25ST from Tinius Olsen TMC, USA, to analyse the occurrence of pores in selectively laser sintered samples and their effect on the tensile strength.

The same universal tensile testing machines were also used for analysing the auxetic structures. Tanaka et al. (Tanaka et al. 2017) analysed the behaviour of an orthotropic laminated open cell auxetic framework under large uniaxial loading on a simple universal testing machine (AG-50KNX, Shimadzu Corp.) with a crosshead speed of 1 mm/min. The experimentally calculated Poisson's ratios were found

close to the numerically obtained results. Jiang and Li (Jiang and Li 2017) did the Quasi-static compression mechanical experiments on the 3D printed cellular chiral structures specimens on a Zwick/Roell material testing machine (zwickiLine) at the rate of 10^{-3} per second. An oesophageal stent fabricated by laser cutting of polyurethane tubes was tested on a Lloyds Instruments TA500 tensile tester with 500 N with the speed of 5mm/min. The mechanical results were compared with a finite element model of the oesophageal stent with a good agreement. Evidently, all these reports (Karnati et al. 2016, Tanaka et al. 2017, Flodberg et al. 2018) establish the tensile test procedures to be used to evaluate auxetic structures, paving ways to the adoption of the same technique in the current research also.

In the current research, compression testing of all the 3D printed specimens, the square grid, S-shaped, and hybrid structures was conducted on the H50K-S model of the Tinius Olsen universal tensile testing machine of the materials testing lab of Auckland University of Technology, New Zealand. The H50K-S model is equipped with the external peripherals (computer, gauge devices or other optional serial devices) with a serial port connection and it operates at the 50 KN full capacity of the load frame. A control display unit as shown in Fig. 3.8 allows to set the test parameters as per the requirements. The same control panel can also be used for printer setup such as changing the headings and setting identifiers for the printouts. All the selectively laser melted structures were kept in between the platen and the base plate for the compressive test. A plate of the same width as the structure was incorporated in between the structure and the gripping platen to ensure the equal distribution of the applied load. The quasi- static and continuous compressive loads

were applied at different rates on the structures based on the nature of the deformations required to be simulated during the experiments.

The displacements of the structures in the lateral directions were established both by digital Vernier calliper and digital image processing technique. The externally applied longitudinal displacements of the end plate were recorded automatically by the tensile testing system. These two displacement measurements were used to calculate the macro level Poisson's ratio of the overall auxetic structure. The critical points, which are crucial for measuring the displacements, were highlighted with specific markers. A Nikon DSLR camera was setup at the same level in front of the tensile testing machine, and used to capture images of the deforming structure at different load or time intervals as shown in Fig. 3.12. The load-displacements curves obtained from the tests were used to calculate the other mechanical properties of the structures that will be discussed later in the thesis.

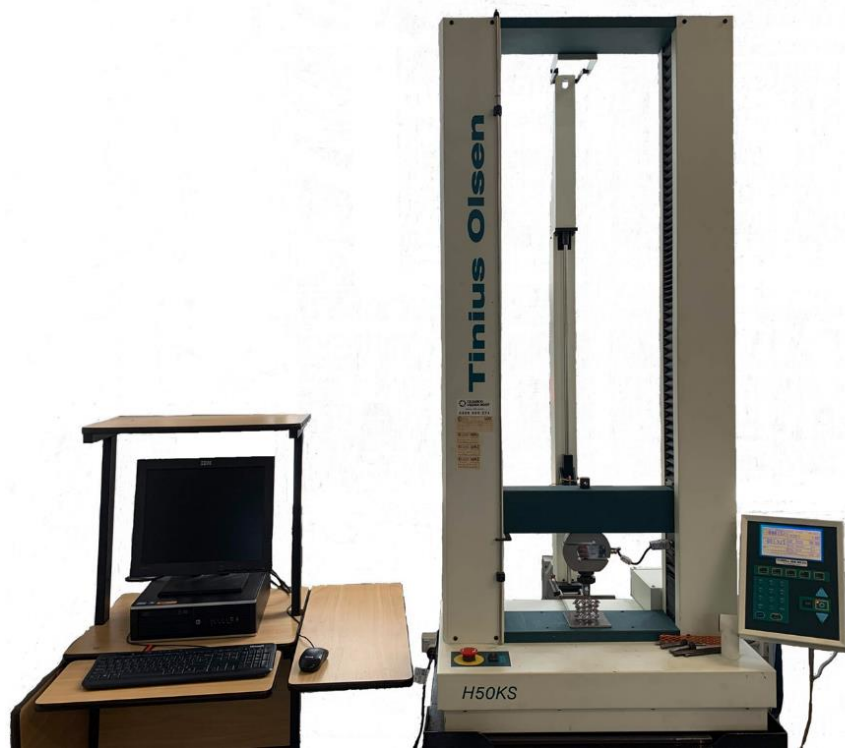


Fig. 3.8 Tinius Olsen tensile testing machine used for the compression tests (at AUT Mechanical Lab)

3.6.2 Data extraction and analysis

The load- displacement data from various compression tests were obtained in the form of curves. The manual extraction of the numerical data pertaining to each load-displacement curve is difficult in terms of accuracy and efficiency. The software solution called WebPlotDigitizer version 4.1 was used for data extraction from the load-displacement curves. It can extract data from images and maps also. The WebPlotDigitizer is a semi-automated tool, which makes it extremely easy to operate. A simple JPG or JPEG file of a plot can be imported into the

WebPlotDigitizer's workspace using the simple "Load image button". Once imported, it allows the user to manually select the four known points, two on the X-axis and two on the Y- axis. The maximum and minimum values of the plot along X and Y- axis can be entered at this stage.

The software also provides both manual and automatic data extraction options. Automatic extraction though simpler than the manual method, leads to huge numerical data extracted from numerous points, spaced as close as a micron on the graph. As points spaced at millimetre distances suffice this research, the manual extraction method is used. This allowed to add points on the curve from the start to the end, adjusting the distance between successive points. A series of densely packed data points could be added at locations where the curve was changing the shape, thus capturing data more closely in critical regions. After selection of data points on the curve, "view data," allows finding the positions of the selected points on the X and Y-axis sequentially. The obtained numerical data can be copied from the source, and a data repository can be generated in the form of an excel file, and the associated mechanical properties can be calculated further. The graphic user interface (GUI) of the WebPlotDigitizer is shown in Fig. 3.9, depicting the different options available in the manual and automatic data extraction processes. The curve as shown in Fig. 3.9 is marked by a series of red dots, which are the critical points, for which numerical data is to be extracted for the subsequent analysis. The same data extraction method was also employed to extract the deformation data of the S-shaped and hybrid structures reported in chapters 5 and 6.

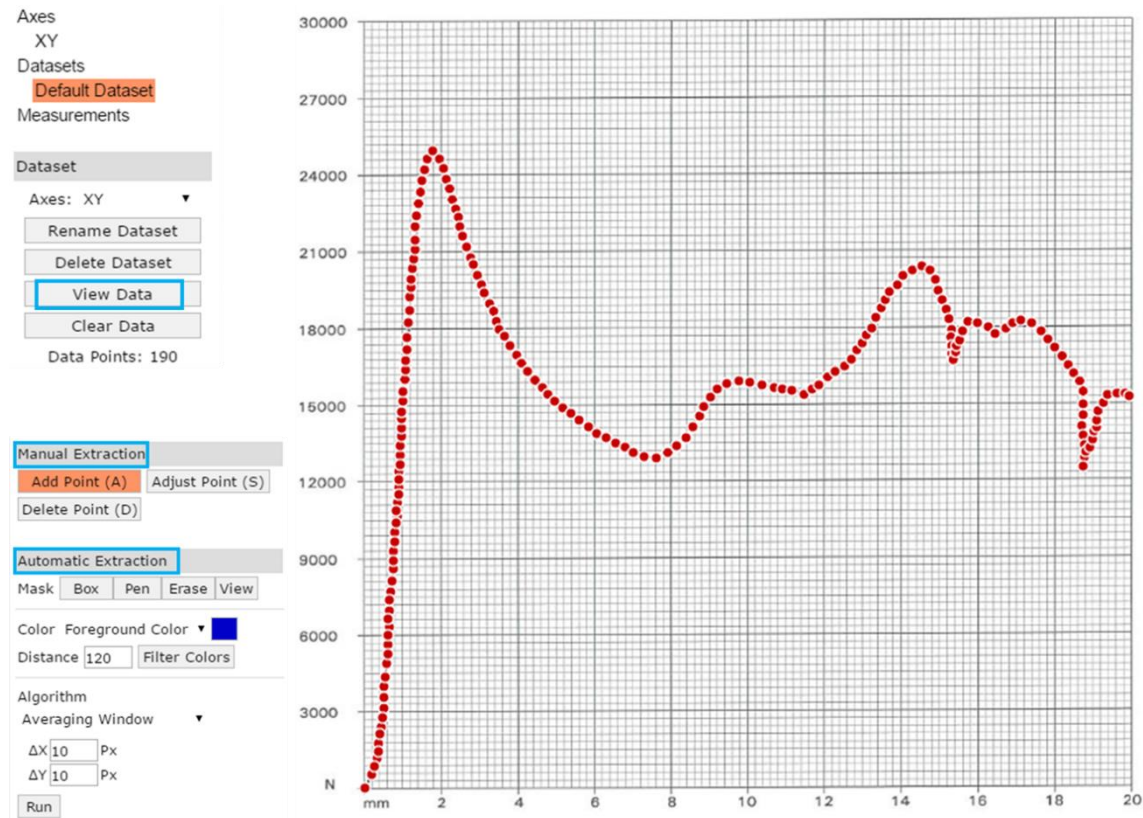


Fig. 3.9 Graphic user interface of the WebPlotDigitizer

3.6.3 Structural deflection

The auxetic responses of structures are all about the deflections of different points and sub-sections of the overall macro structure. The effectiveness of the method used to measure the deflections plays a key role in establishing the true auxetic response. A number of different methods were used and reported earlier to measure the internal deflections of the auxetic structures. Broadly, these may be classified into contact and non-contact methods.

Contact methods allow physical contact of the measuring equipment with the structures. Fu et al. (Fu et al. 2016) established the auxeticity of a 3D printed ABS re-entrant structure by the contact measuring method. The experiment on the structure was carried out on a universal testing machine with a speed of 0.5 mm/min. The deformation in the lateral direction was measured with a digital Vernier calliper, while the longitudinal displacement was recorded on the machine. In another report by Schwerdtfeger et al. (Schwerdtfeger et al. 2010), the Poisson's ratio of an inverted tetrapod based on 3D re-entrant structure was experimentally evaluated. The selective laser melted Ti- alloy structure was compressed on the Instron testing machine (Inspekt Retrofit 100) with a crosshead speed of 1 mm/min. An extensometer setup was attached to measure the distance between the compression stamps and so the strains and consequently the Poisson's ratio. Yang et al. (Yang et al. 2012a) also reported the compression testing of a 3D re-entrant auxetic structure using an extensometer, attached with the platens of the tensile testing equipment.

The contact methods such as the Vernier calliper measurements though simple and easy to use, are limited by both accuracy and the access to different points of deflection. Gross variations on the outer edges are relatively simple to measure, but internal points that are deflecting in different directions and also probably twisting are likely to pose problems. Further, difficulties arise when the contact surfaces are not properly aligned with the measuring surfaces. The non-contact methods such as the use of digital imaging systems allow to resolve some of these difficulties.

Ghaedizadeh et al. (Ghaedizadeh et al. 2016) attempted to tune the performance of metallic auxetic metamaterials by using buckling and plasticity. The Quasi-static uniaxial compression tests were conducted based on a Shimadzu tensile testing machine (Shimadzu Company, Kyoto, Japan) at a fixed strain rate of $5 \times 10^{-3} \text{ s}^{-1}$. The structural deformation was captured using two cameras; the first camera was used to capture photos in the lateral direction for every 30 s while the second camera was employed to record a performance video of the test. The data gathered from the cameras was analysed by digital image processing technique and the negative Poisson's ratio was established for the structure. Two different structures: re-entrant and chiral, fabricated by the 3D printing of the digital material DM9760, were quasi statically compressed on Zwick/Roell material testing machine with the rate of 10^{-3} per second, to determine the limiting strain for auxeticity under large compressive deformation. A high-resolution camera was used to capture the images of specific marked points of the structures under loading. Thus deformation was tracked, and mechanical properties were calculated (Jiang and Li 2018). An aluminium based auxetic structure fabricated by 3D printing and investment casting was loaded under compression. During the compression tests, a camera recorded the deformation responses of the marked struts. The deformation data from the camera was fed into the Image J software, and the horizontal and vertical strains were measured effectively (Xue et al. 2018).

Both contact and non-contact measuring methods were employed in the current research based on the accessibility of the deflected points. First, a Keyence laser displacement sensor LK –H050 of LK - G5000 was employed to measure the lateral

displacements of the external flaps of the square grid structure reported in Chapter 4. The setup of the equipment used is shown Fig. 3.11. The sensor used is dedicated for fine target measurements (focused spot type) of 50 ± 10 mm reference distance and measurement range with a repeatability of 0.025 micrometres. The sensor works on the triangulation method as schematically depicted in Fig. 3.10, in which a laser light emitting from the laser head focuses on the targeted object. A light beam reflecting from the object makes a spot on the position receiving device and when the object moves the position of the reflecting beam also changes which reflects digitally on the controller unit of the sensor. This laser displacement sensor technique is very sensitive to environment, in which the equipment is installed. At the time of conducting these experiments, a building demolition and construction activity was ongoing very close to the materials testing laboratory. The ground vibrations and other problems caused hindrances to the proper use of this sensitive equipment and resulted in large experimental errors and variations in measurements from time to time. As a result, the use of the laser displacement sensor technique was discarded from the current experimental measurements.

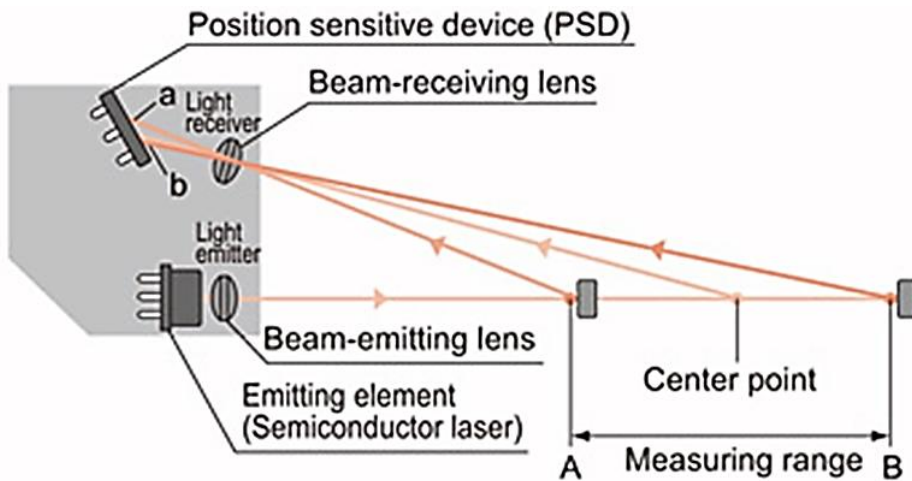


Fig. 3.10 Schematic of the principle of laser triangular measurement technique
 (www3.panasonic.biz)

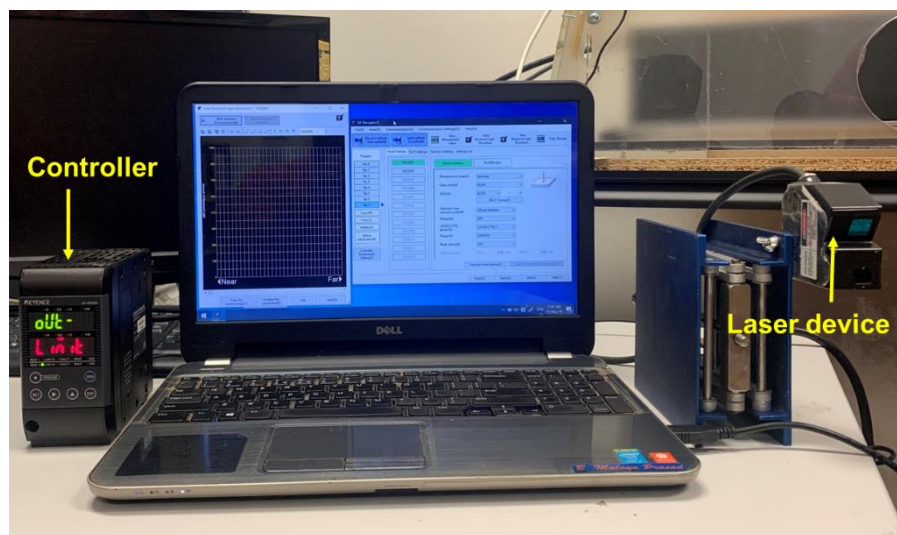


Fig. 3.11 The laser displacement setup (Materials testing lab, AUT)

In chapter 4, the auxeticity of the square grid structure was established by measuring the lateral displacements of the external flaps. A Nikon digital camera

was installed facing the samples at the same level and at some distance as depicted in Fig. 3.12. The camera was focussed at the centre of the samples and photographs were taken in the undeformed state of the samples prior to mechanical testing. Once the test started, a number of photographs were taken at specific intervals of the applied compressive displacement of each sample. The easy accessibility of the square grid structure's external flaps during mechanical testing also allowed to measure the lateral displacements using a Vernier calliper. Further, lateral displacements of the S-shaped and Hybrid structures reported in Chapters 5 and 6, were established by measuring the lateral displacements of specific internal marked points, instead of the external points used in Chapter 4. Considering the difficulties in using a Vernier calliper to measure the displacement of internal points, a digital imaging technique was used for these measurements. The compressive displacements applied and the number of photographs taken at different intervals of the deformed states of the samples were different from one another and the specific information is mentioned later in the relevant chapters.

The photographs taken at different intervals of compressive displacements were fed into the digital image processing "Image J" software. It can read data from various image formats such as "TIFF, JPEG, PNG, GIF, DICOM, FITS, and BMP". The software supports all the standard image processing operations including contrast manipulation, convolution, Fourier analysis, sharpening, smoothing, edge detection, median filtering and logical and arithmetical operations between images. The distance and angle measurement features of the software were used in the current scenario. The un-deformed known length, width or height of the structure can be entered as the reference dimension for the undeformed sample picture. The

software converts this known dimension into a number of pixels. The software uses that number of pixels as the benchmark and corresponding to this the Image J assess and establishes the locations of different points on the structure during deformation under the compressive loads and thus allows to measure the lateral and longitudinal deflections.



Fig. 3.12 Image capturing setup during compression testing (at AUT Mechanical Lab)

Chapter 4

Enhancing the auxetic responses of a square grid structure

4.1. The square grid structure

Gasper et al. (Gasper et al. 2005) derived the square grid structure from the missing rib model of the reticulated foams, developed by Smith et al. (Smith et al. 2000). The modifications required to obtain the square grid structure (Gasper et al. 2005) from the missing rib model (Smith et al. 2000), were discussed in section 2.4.1 of Chapter 2 and further depicted in Fig. 4.1. The assumptions made for the deformation mechanisms for the analytical modelling were; (a) elastic deformation of strut angles, (b) no change in the lengths of individual struts, (c) constant translational symmetry of the unit cells throughout the deformation. The final analytical model derived to calculate the Poisson's ratio, was stated in the Table 2.2, of Chapter 2 which was verified by means of experimental data generated through image processing. The results obtained from the analytical and experimental analysis clearly elucidated auxetic nature of the square grid structure, with Poisson's ratio values at around -1. The Poisson's ratio values were observed to remain constant irrespective of the load, due to the concurrent infolding and rotation of the unit cells (Smith et al. 2000, Gaspar et al. 2005).

In the past, the fabrication of these auxetic foams highly relied on conventional techniques (Lakes 1987, Chan and Evans 1997, Ravirala et al. 2005, Grima et al. 2009, Li and Zeng 2016) as elaborated in section 2.3 of Chapter 2. However, all these methods suffer from practical limitations and are only suitable to process specific polymers and metals. Alternatively, additive manufacturing emerged as a viable means to produce relatively more complex shapes with a variety of materials, including metals and polymers (Gibson et al. 2010, Bourell et al. 2017, Attaran 2017). A few attempts were also made to additively manufacture different auxetic forms for experimental validation of the otherwise theoretical predictions.

Yang et al. (Yang et al. 2016) developed auxetic polymer re-entrant and arrowhead structures to be used as protective pads based on fused deposition modelling and verified the auxetic nature numerically and experimentally. Three different auxetic structures, produced by using the acrylic materials on a multi-jet 3D printing system allowed Koudelka et al. to use FEA to fine-tune and optimize the auxetic nature and experimentally validate the same (Koudelka et al. 2016). Other studies reporting about the different additive manufacturing processes using different varieties of materials have been discussed in detail in Chapter 2 (Schwerdtfeger et al. 2010, Yang et al. 2012a, Yang et al. 2012b, Wang et al. 2015, Li et al. 2016, Fu et al. 2016, Xiong et al. 2017, Xue et al. 2018).

However, the applications of the different additive manufacturing processes are by far limited to a few structural variants as mentioned in section 2.5 of Chapter 2

based on both polymeric and metallic material options. Apart from this, the stress concentration problem arises within the auxetic structures under loading, due to the complex geometric shapes of the auxetic structures. Additionally, the metal additive manufacturing processes add to the problem of stress concentration due to the specific limitations of the fabrication processes as elaborately discussed in Chapter 2.

Considering the potential benefits of achieving more complex structural shapes relatively easily, it is essential that metal additive manufacturing methods were used more extensively, together with numerical and analytical modelling, to push the boundaries of the current structures as well as extend the understanding to envision new auxetic structural forms. The stress concentration problem should also be given due consideration, and measures should also be taken to eliminate or reduce it, in order to enhance the overall performance of the auxetic structures. This Chapter is devoted to the implementation of this experimental and numerical evaluation scheme and correlation of the results in the context of the square grid structure reported to result Poisson's ratio at around -1 (Gasper et al. 2005). This structural form was not yet produced using the metal additive manufacturing techniques for experimental evaluation. Further, the geometrical optimisation of the square grid structure may increase the auxeticity as in the case of the re-entrant structures (Yang et al. 2012a, Li et al. 2016, Xiong et al. 2017), which has not been done earlier. Overall, the square grid structure which has not been analysed so far using the additive manufacturing is selected for the experimental verification. This Chapter presents the experimental and numerical modelling work done based on a square grid auxetic structure and the results leading up to a better understanding

of the auxeticity, stress concentration effects, and the geometrical optimisation for enhancing the auxetic nature.

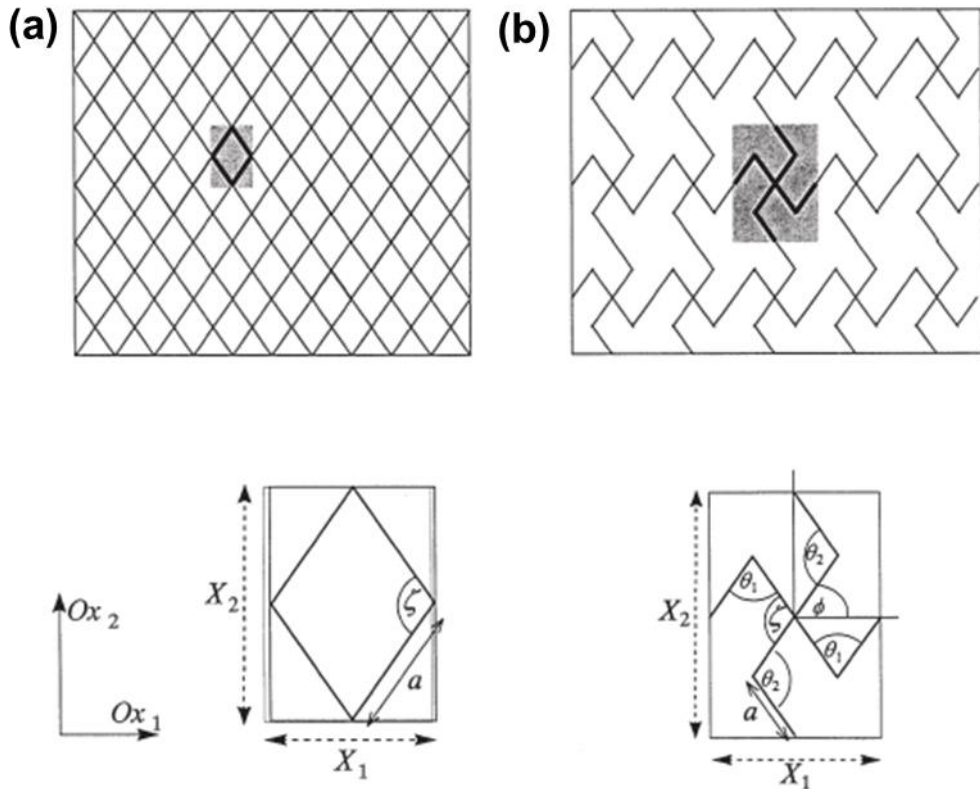


Fig. 4.1 2D sketch of (a) a network of cells and (b) missing rib model after removing the selected cells (Smith et al. 2000)

4.2. CAD modelling

The 2D and 3D models of the square grid unit cell and then subsequent fully-fledged structure are designed in the SolidWorks 2016. The unit cell is essentially

made up of four L shaped struts that meet orthogonally at the common central point, forming the square grid unit cell as shown in Figure 4.2 (a). L and H are the horizontal and vertical strut lengths respectively, θ is the flap angle with the vertical and horizontal struts, t is the thickness and r is the adjoining length to be used while joining adjacent unit cells.

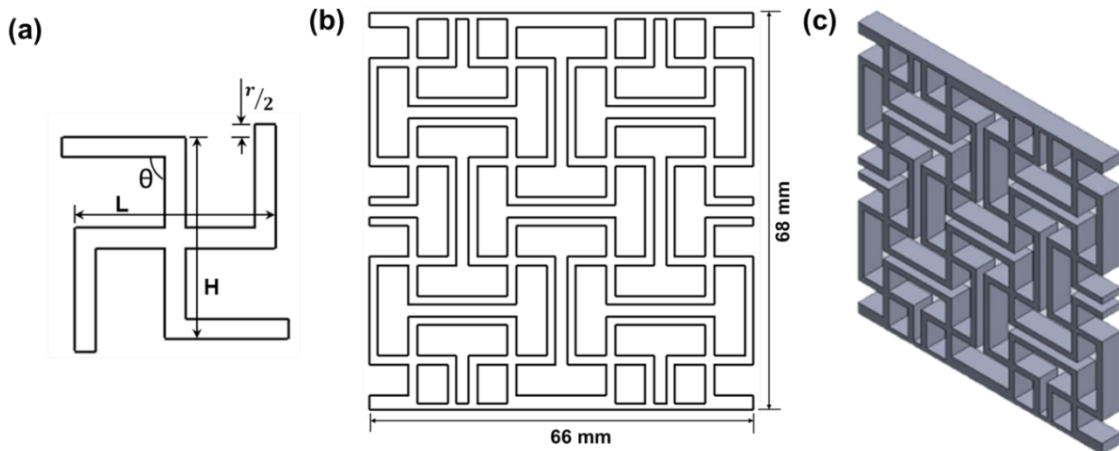


Fig. 4.2 (a) The unit cell (b) 2D sketch and (c) 3D CAD model of the initial square grid auxetic structure

The initial square grid structure model was developed by integrating four unit cells, each along the x- and y- directions. The unit cells are 15 mm \times 15 mm in size and cross linked appropriately to develop the square grid model in SolidWorks, with an adjoining distance of 2 mm. A uniform depth of 8 mm is given in the Z-direction all over. The 2D sketch of the frontal geometry of the structure is shown in Fig. 4.2 (b). A 1 mm thick plate is attached both at the top and the bottom for better holding within the grips of the universal tensile testing equipment. The overall size of the structure came out to be 68 mm \times 66 mm and an image of the solid model

developed is presented in Fig. 4.2 (c). The basic steps followed in designing the models were already mentioned in Chapter 3. This built structure is used for initial numerical and experimental verification. Structural variations induced by varying the geometrical parameters were also implemented in SolidWorks as already explained, by altering the unit cell dimensions as required.

4.3. Simulation

The CAD models of square grid structures designed using SolidWorks were imported into the ANSYS finite element package version 16.2, as discussed in section 3.3 of Chapter 3. Numerous of simulation tests were undertaken on the initial square grid structure by varying the critical geometric parameters, to optimise the Poisson's ratio responses, without compromising on the other mechanical properties. The geometric parameters are mentioned later in the chapter. Considering the nature of the analysis required, an elastic linear structural model was considered to perform the simulation. Generally, beam elements are considered when one of the structural dimensions is significantly greater than the others. However, as this is not true in the current case, the struts were not treated as the beam elements and instead, considered as solid elements for the numerical analysis. The mesh convergence solution was carried out by varying the mesh sizes and the results are presented in Fig. 4.3. A less amount of variation was seen in the lateral displacement values when mesh size decreased from 0.75 mm to 0.25 mm. Therefore, 0.75 mm mesh size of tetrahedron element (patch confirming algorithm) was chosen for the meshing of all solid models.

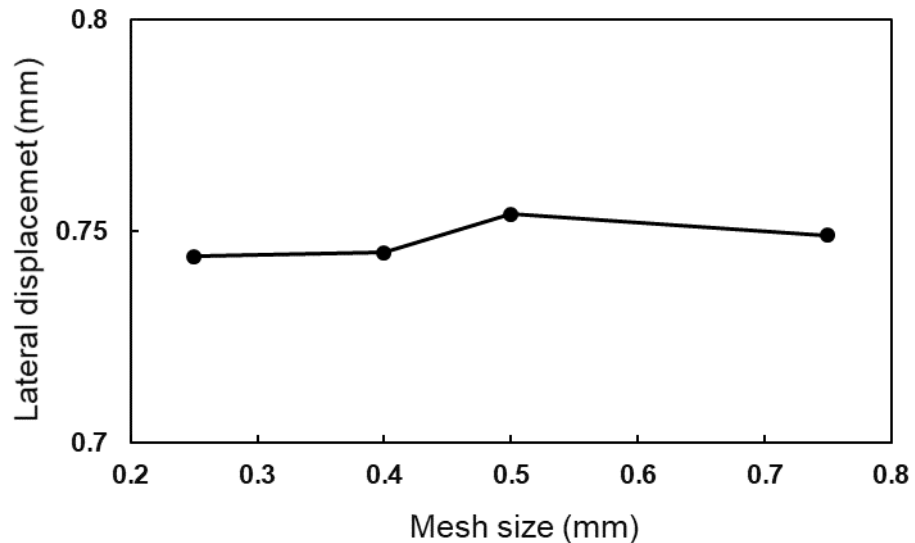


Fig. 4.3 Lateral displacement with varied mesh size

The finite element simulation results, as will be discussed in more detail later, indicated that the auxetic nature is typically a structural response, and is independent of the base materials used for fabricating the structure, as long as the experimental domain is within the limits of the yield stress of the material with the lower elastic limits. In the current study, the initial square grid structure was produced by laser melting of CoCr alloy with modulus of elasticity 220 GPa and Poisson's ratio 0.3, while the final optimized rectangular grid structure was made of stainless steel 316L alloy with modulus of elasticity 197 GPa and Poisson's ratio 0.26, as will be discussed later.

The applied boundary conditions were chosen as to simulate the compression testing. The Y- directional displacement (U_Y) of the bottom face was kept zero while leaving the other two dimensions (U_X, U_Z) displacement free. The displacement based load was applied on the top face of the structure in $-Y$ direction.

Deformations in X and Y directions obtained from the nodal solution were converted into lateral and longitudinal strains using equations (1) and (2). Further, The Poisson's ratio was estimated based on the longitudinal and lateral strains, using the expression in Equation. (3).

$$\varepsilon_{lateral} = \Delta l / l \quad (1)$$

$$\varepsilon_{longitudinal} = \Delta h / h \quad (2)$$

$$\vartheta = -\frac{\varepsilon_{lateral}}{\varepsilon_{longitudinal}} \quad (3)$$

4.3.1. Effects of varying the flap angle and the thickness

The Critical geometrical parameters of the square grid structure were varied to evaluate their influences on the auxetic responses of the structure. In this section, the two geometrical parameters namely flap angle and thickness are considered. Only one geometrical parameter is varied at a time keeping the other geometrical parameters constant. For example, the thickness (t) and the H/L ratio of the unit cell were kept constant while varying the angles (θ) of the flaps from 0° to 30° . Variation in the strut thickness was implemented keeping the other geometrical parameters and the gaps between adjacent struts the same. A series of structures

were built in SolidWorks and imported into the ANSYS workbench platform for simulating the auxetic responses with the boundary conditions as discussed in section 4.3. The linear elastic properties of Stainless steel 316L were assigned to the model as the base material with the same modulus of elasticity and Poisson's ratio as discussed in Section 4.3.

4.3.2. Role of the H/L ratio and the stress concentration in the structure

The other dimensions that can be changed are the lengths of the struts in both horizontal and vertical directions. In order to unify these two changes, the H/L ratio of the overall dimensions of the unit cell was considered as the factor for evaluating the possible roles of the strut lengths to alter Poisson's ratio and stress concentration in the structure. When the length of horizontal or vertical struts was changed, the structural shape of the unit cell changes from square to Non-square or rectangle. Therefore, the structure with H/L ratio greater or less than 1, will be referred to as Non-square grid type, from now on. The non-square grid structures with H/L ratios varying both below and above 1 were generated and subjected to finite element evaluations with boundary conditions remaining the same as discussed in Sect. 4.3 with stainless steel 316L as the base material.

4.4. Additional experimental details

The fabrication, post processing and mechanical testing tasks were performed as per the details provided in section 3.4, 3.5 and 3.6 of Chapter 3 respectively. The quasi-static compressive load was applied based on axial displacements at the rate of 1mm/min in the Y- direction. The lateral displacements of the endpoints of the central horizontal struts were measured using digital Vernier calipers while longitudinal displacements of the end plates were recorded automatically by the tensile testing system. Three readings at every load condition were taken, and their average was taken to calculate the strains and then Poisson's ratio. Points corresponding to the minimum width (due to the auxetic nature) across the structure under compression were used for measuring the lateral displacement readings as shown in Fig. 4.4 (b).

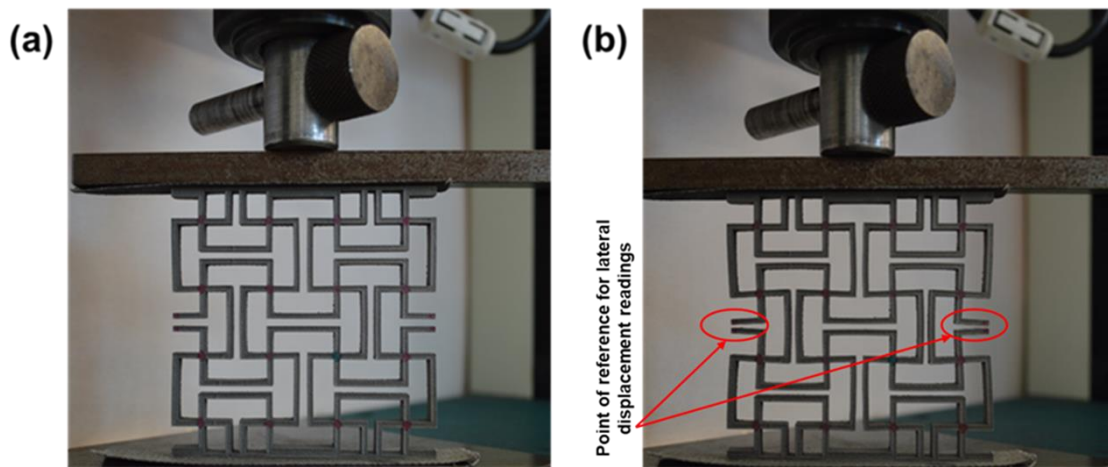


Fig.4.4 Compression tests on the initial square grid structure printed by laser melting CoCr (a) Prior to compression (b) at the maximum compression

The auxetic responses of the final optimized non-square grid structure were quantified by measurements based on both Vernier Callipers readings and digital image processing technique. The compression test was repeated three times to establish the repeatability of the data and error bars based on standard deviations were plotted against the results.

4.5. Results and discussion

4.5.1. *Experimental and numerical verification of the initial square grid structure*

Fig. 4.4 (a) & (b) present the photographs of the printed structure mounted on the tensile testing machine, before and under maximum loading conditions respectively. Fig. 4.5 (a) is the finite element mesh used for the simulation studies and Fig. 4.5 (b) is the final deformed structure showing the displacement predictions. The lateral displacements obtained from the numerical and experimental analysis are considered as negative and plotted against the force and longitudinal displacement as shown in Fig. 4.6 (a), (b) respectively. Evidently, as the applied load increases, the lateral strain also increases on the negative side, due to the inward movement of the struts, which is clearly visible in Figs. 4.4 and 4.5 and graphically from Fig. 4.6 (a). This is the result of the elastic deformation of the horizontal and vertical struts at the joints. The actual structure as depicted in Fig. 4.4 is symmetrical about the central vertical line. The part on the right is a mirror image of the part on the left of the central line. After the compressive load was applied, a unit cell in the left part tries to rotate in the clockwise direction,

forcing its mirror image on the right side to rotate in the opposite direction, due to the arrangement of the unit cells in the overall structure. This is also true with each pair of the unit cells on either side of the central line of geometrical symmetry. Eventually, the geometry and the arrangement of the unit cells in the structure lead to an overall reduction in the width under the compressive loading, giving rise to negative Poisson's ratios and the auxetic behaviour. The structural movements also lead to gradually increasing the density of packing within the structure, as the compressive load increases. The auxetic nature leads the structure to assume a double curved shape under the load and shows the synclastic property, which is highly desirable in applications such as the aircraft nose cones (Evans and Alderson 2000). The variation of the lateral displacement with longitudinal displacement is depicted in Fig. 4.6 (b), elucidating an almost linear relationship between the two, and both decreasing under compression, leading to the auxetic nature.

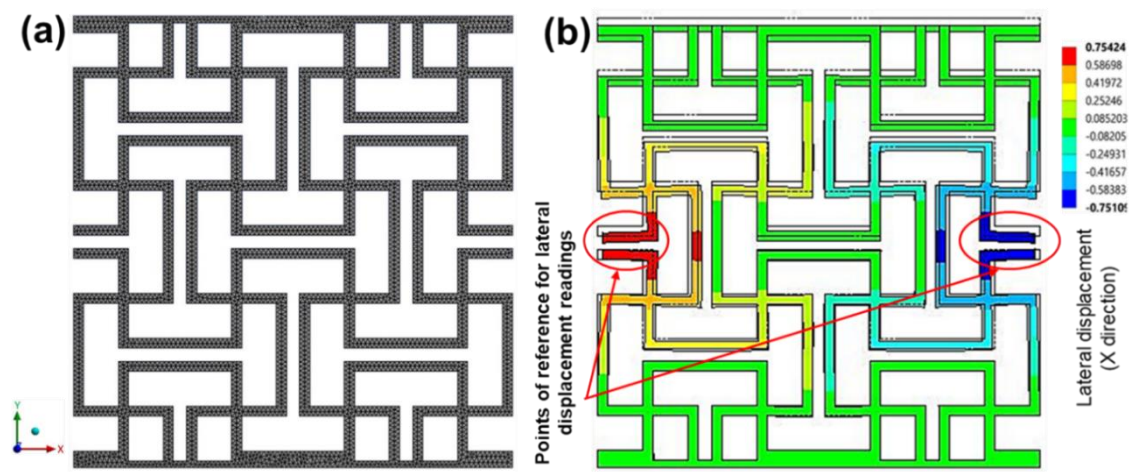


Fig.4.5 Finite element simulation of the initial square-grid structure of CoCr alloy
 (a) prior to compression (b) under compression

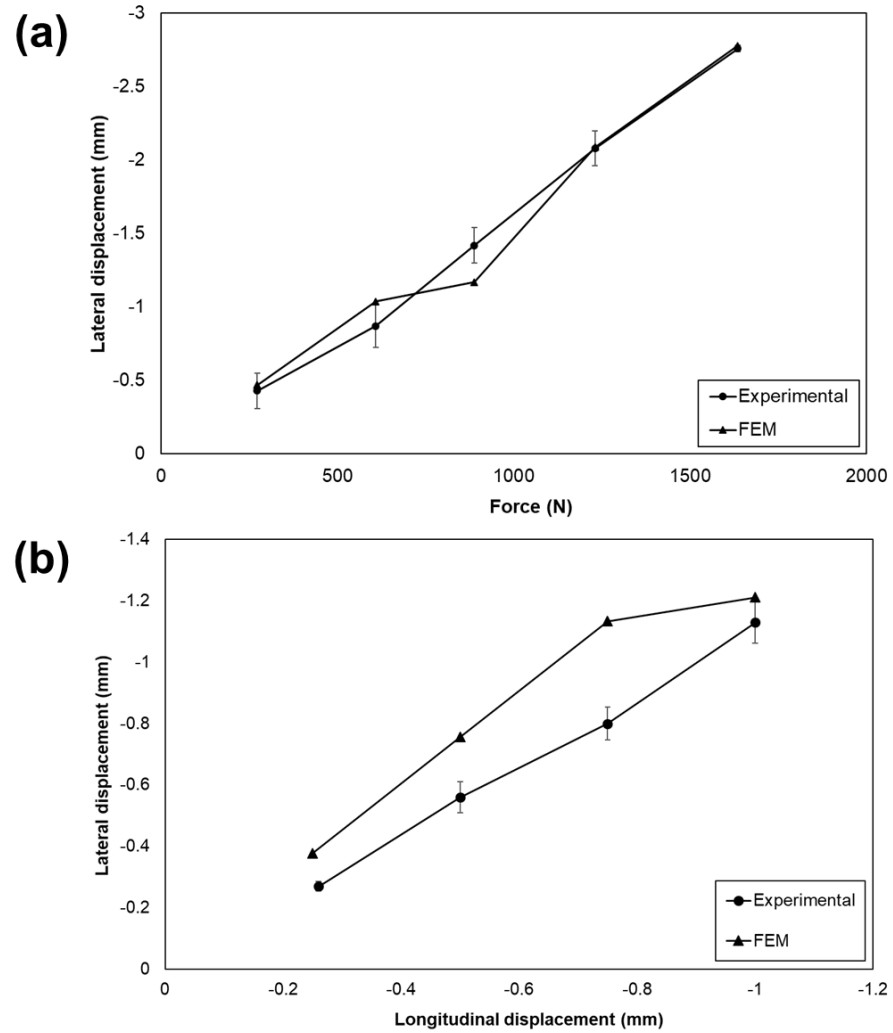


Fig.4.6 (a) Lateral displacement vs. force (b) lateral displacements vs. longitudinal displacements in both experimental and numerical cases

4.5.2. Roles of the flap inclination angle and the strut thickness

The lateral displacement patterns generated in the square grid structure while changing the flap angles (θ) from 0° to 30° are presented in Fig. 4.7. (a) to (f). The lateral displacement may be noted to change from -1.512 mm to -1.794 mm as the flap angles are varied from 0° to 30° . The Poisson's ratios calculated based on the

lateral displacements obtained using Equation 3 are consolidated in a graphical form and presented in Fig. 4.8. It is evident from Fig. 4.8 that the flap angle has a negligible influence on the Poisson's ratio.

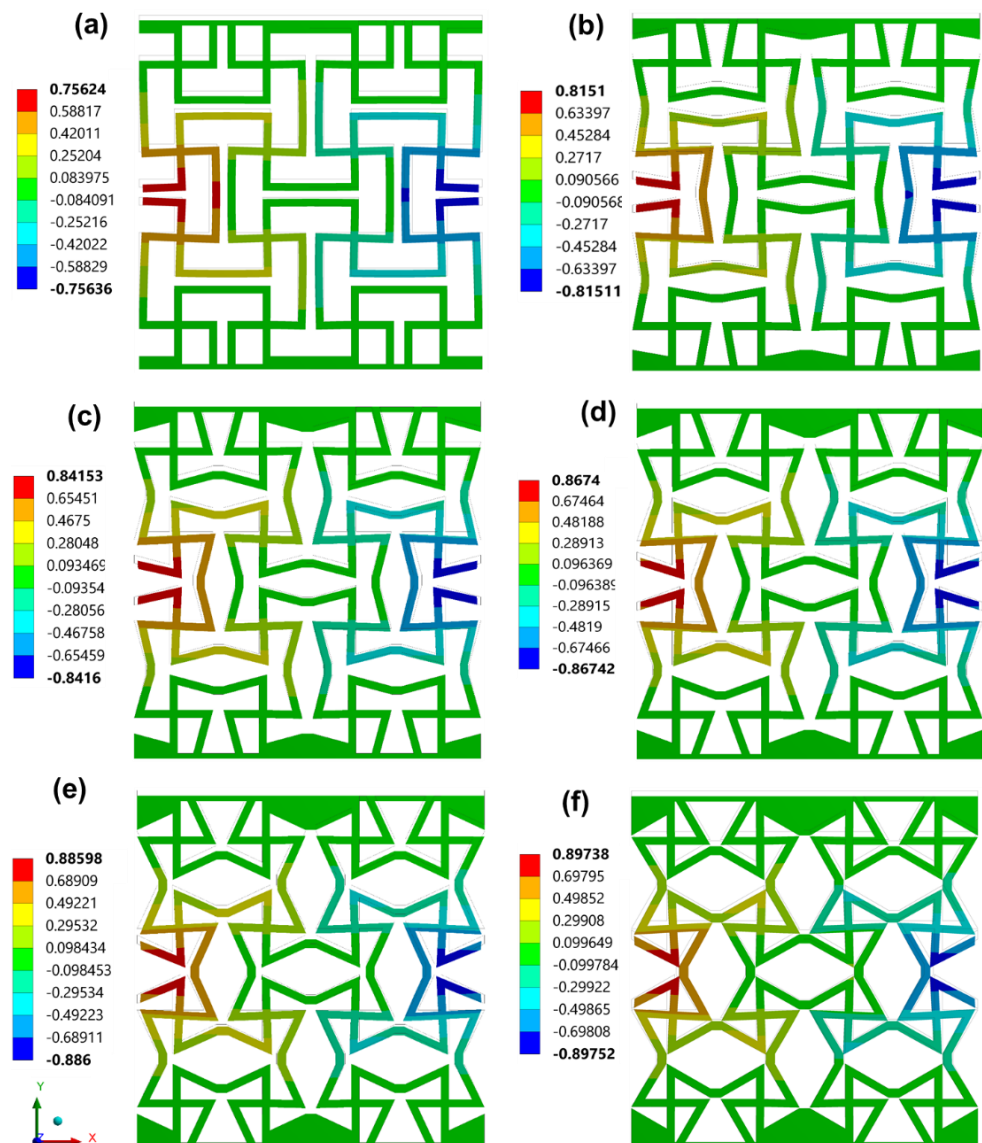


Fig.4.7 Finite element simulations of obtained lateral displacements for (a) 0° (b) 10° (c) 15° (d) 20° (e) 25° (f) 30° flap angles

Based on the results presented in Fig. 4.7 and 4.8, the change in the lateral displacement and the Poisson's ratio though varied to a minor extent, do not appear to be significantly affected by the flap angle. Further, as the flap angle reaches 30° , the inclining struts tend to touch the horizontal struts and create geometrical constraints. Based on these results, it is understood that the strut angle is not a critical parameter for achieving any drastic differences in the auxetic responses of the structure and so was kept constant at 0° , in the subsequent geometrical modifications.

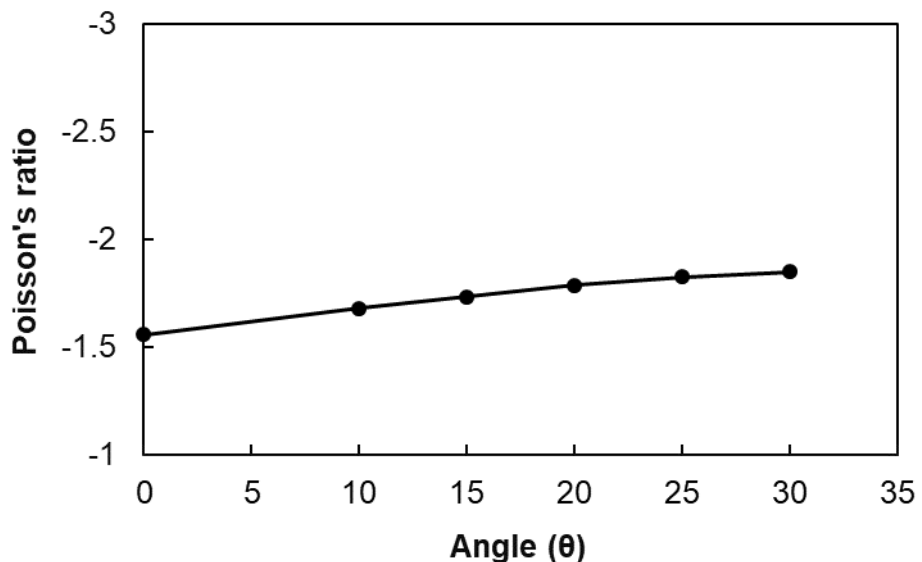


Fig.4.8 Finite element simulation of Poisson's ratio vs. flap angle

The numerical simulation of the responses of the square grid structure with varying thickness is presented in Fig. 4.9. With the thickness varied from 0 to 3 mm, the density of the square grid structure increases. However, no significant changes in the lateral displacement values were recorded. In the current case, the strut thickness was varied, keeping the gaps between adjacent struts the same. The

Poisson's ratio values calculated based on the lateral displacements obtained as shown are consolidated and drawn against the varying thickness in Fig. 4.10. It may be noted that the Poisson's ratio values remained almost the same, at all the flap thickness values used,

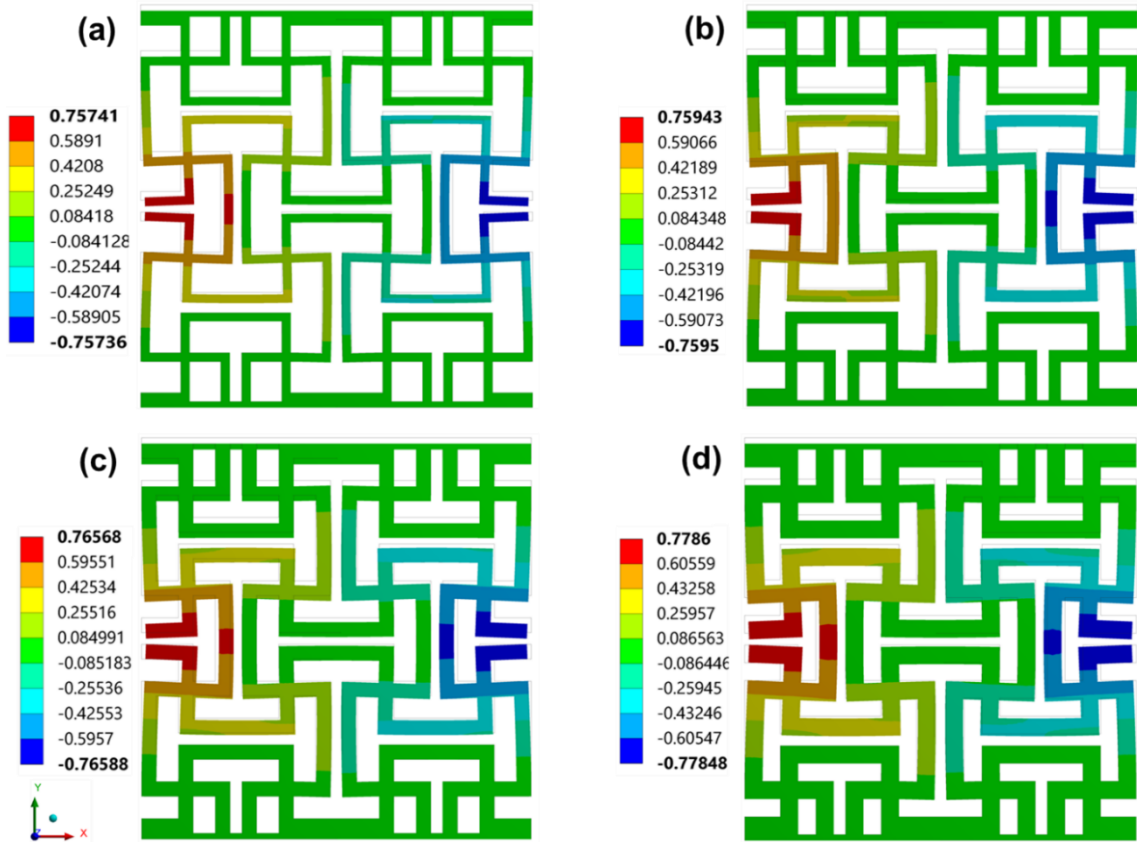


Fig. 4.9 FEM simulation of square grid structure with the varying thickness of (a) 1.5 mm (b) 2 mm (c) 2.5 mm (d) 3mm

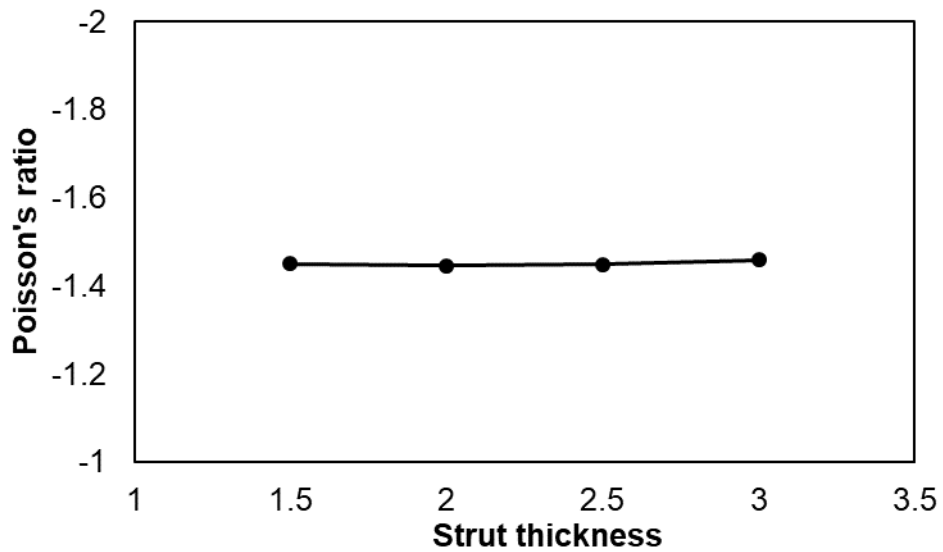


Fig. 4.10 Strut thickness versus Poisson's ratio based on FE simulation

Evidently, the thickness has also no discernible effect on the auxetic response of the structure. Earlier reports indicated a loss of the auxetic nature, as the increasing thickness of structural elements leads to interference between the deflecting elements of the structure (Schwerdtfeger et al. 2012, Ren et al. 2015). In the current structure, the gap between adjacent unit cells is critical to achieving auxeticity. As a result, the gap was maintained constant at 2 mm, irrespective of the thickness of the structural elements. In spite of this, the thickness did not show any significant influence on the Poisson's ratios of the structure and so will be discarded as an experimental parameter.

4.5.3. Optimisation of the H/L ratio

The numerical simulations were performed for varying H/L ratios. Two conditions of varied H/L ratios were taken, First, the simulation was performed for H/L less than 1 ($H < L$) and, then for H/L ratio greater than 1 ($H > L$). Simulation results for the H/L ratio less than 1 as compared to the H/L ratio 1 are depicted in Fig. 4.11. It was noted that the non-square grid structures with H/L ratios less than 1 resulted in a loss of the lateral displacement for the same applied longitudinal loading as compared to H/L ratio 1 and consequently a loss of the auxetic nature. Quantitatively, as the H/L ratio changes from 1 to 0.6, the Poisson's ratio was noted to change from – 1.45 to – 0.6. Observing the loss of auxeticity, this modification was discarded at the end.

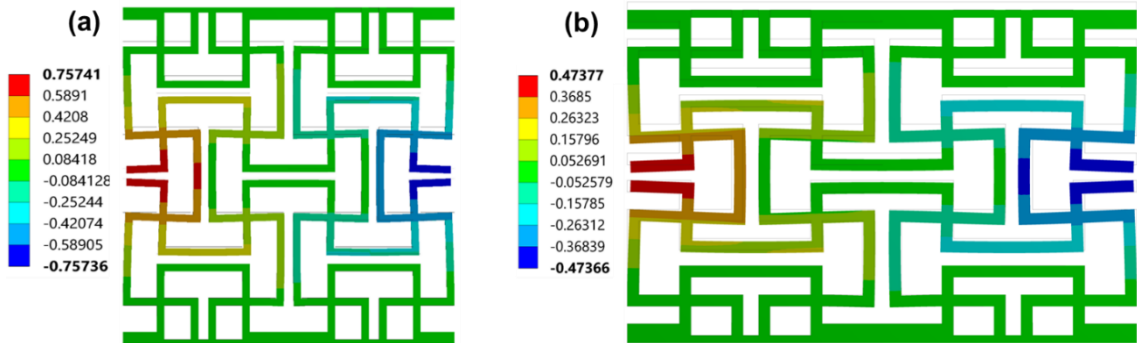


Fig. 4.11 FEM simulation of decreasing H/L ratios (a) 1 and (b) 0.6.

On the other hand, increasing H/L ratios above 1 (Horizontal struts are shorter than the vertical struts) resulted in increasing negative Poisson's ratios. The finite element depiction of the deformed shapes of both square-grid ($H=L$) and non-square grid structures with H/L ratios 1, 2, and 3 are presented in Figs. 4.12(b), 4.13(b) and 4.14(b) respectively. The square-grid structure in Fig. 4.12(b) shows the horizontal flaps at the centre to fold inwards due to the combined action of the buckling and rotational motions of the struts. It must be noted here that Figs. 4.5(b) and 4.12(b) are FE simulation results based on CoCr and stainless steel 316L as the base materials, respectively, but are still showing the same lateral displacements for the given longitudinal displacement, which shows that auxeticity is structure-based property rather than the chemical or mechanical constitution of the material (Grima and Caruana 2012). However, with increasing vertical strut length, the non-square grid structure experienced enhanced buckling and rotational motions of the longer vertical struts, leading to increased inward pushing of the horizontal struts as shown by the red circle markings in Figs. 4.13(b) and 4.14(b). This has resulted in the higher inward deflection of the central flaps, leading to increased negative Poisson's ratios. These effects are clearly depicted in the deformed structures of Figs. 4.13(b) and 4.14(b).

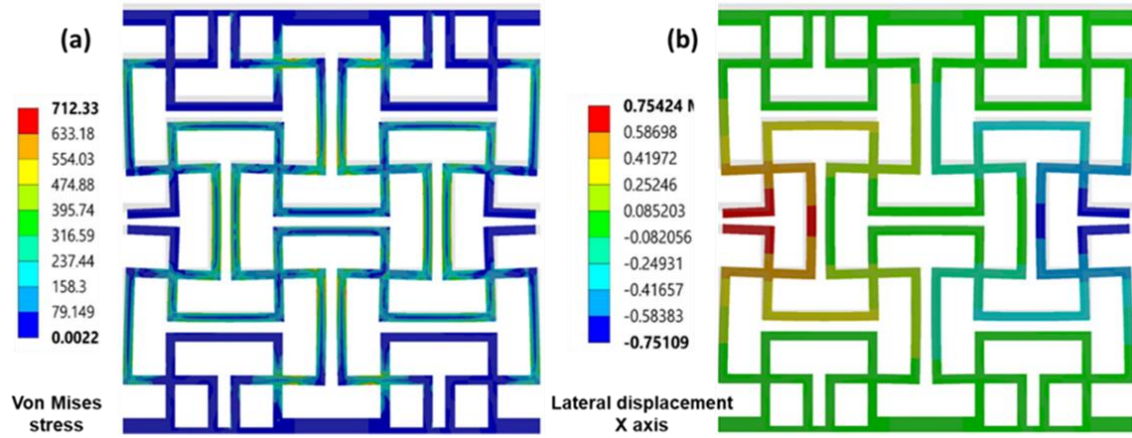


Fig. 4.12 Finite element simulation images for H/L ratio 1 (a) Von Mises stress (b)
lateral displacement

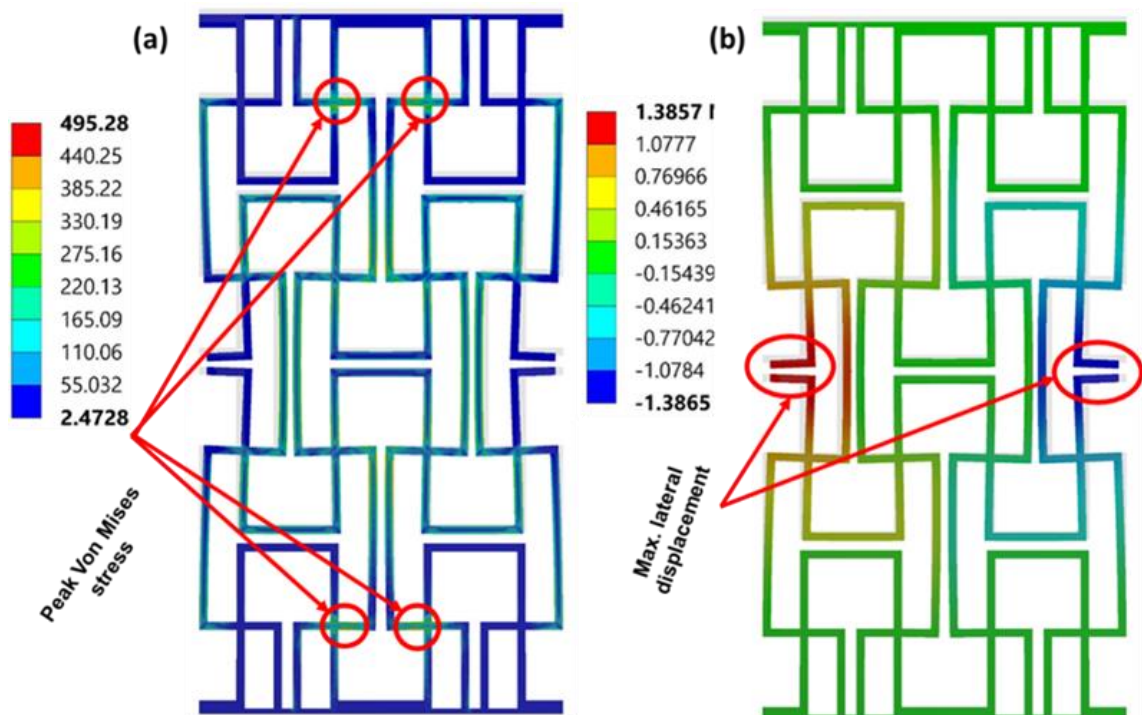


Fig. 4.13 Finite element simulation images for H/L ratio 2 (a) Von Mises stress (b)
lateral displacement

Increased auxeticity was clearly established with increasing H/L ratio as the non-square grid structure was compressively loaded. A certain degree of out-of-plane bending was noticed in the structure with the H/L ratio above 3. It is now important to establish the possible stress concentration effects arising out of the structure. The Von Mises stress distribution obtained from the FE analysis of the square grid and the non-square grid structures of H/L ratios 2 and 3 are presented in Figs. 4.12(a), 4.13(a) and 4.14(a) respectively.

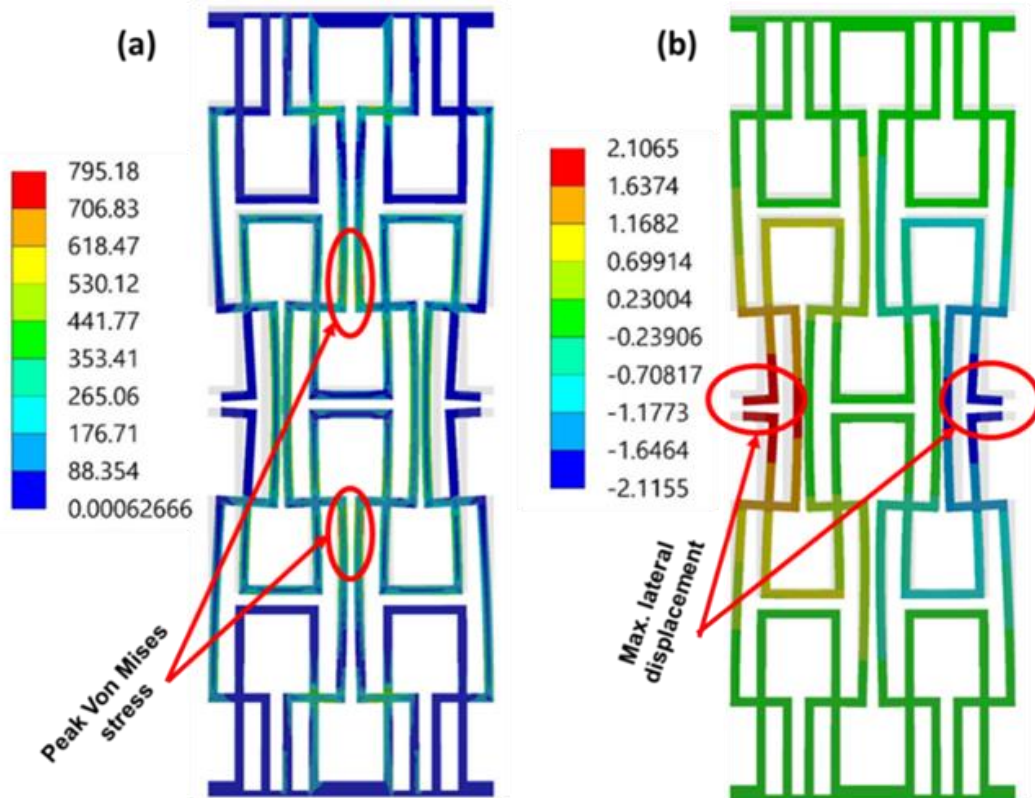


Fig. 4.14 Finite element simulation images for H/L ratio 3 (a) Von Mises stress (b)
lateral displacement

It may be observed from Figs. 4.12(a) and 4.13(a) that the peak Von Mises stress is reduced from 715 to 495 MPa, as the H/L ratio increases from 1 to 2. The increased lengths of the vertical struts appear to have a favourable effect in terms of the horizontal flaps easily folding inwards, without being subjected to excessive stressing, for similar loading conditions as compared to the square grid structure. The mechanism of deformation in the case of the non-square grid structure is predominantly buckling, as against the mostly compressive loading experienced by the vertical struts in the square grid structure.

However, a further increase in the H/L ratio to 3 led to a sharp rise in the peak Von Mises stress again to around 795 MPa. Evidently, the vertical struts are severely buckled and stressed excessively. Consequently, the stress concentration locations are also shifted to specific points on the long vertical columnar members in Fig. 4.14(a) as against the horizontal flaps as observed in Fig. 4.13(a). It is also noted that the structure becomes unstable as the H/L ratio reaches 3, as a result of the buckling of the vertical columns. In an essentially 2D form, the maximum limit of the H/L ratio appears to be somewhere between 2 and 3. However, this situation may change, if a 3D replication of this structure is evaluated, as the geometry is likely to provide more rigidity. On further increase in the H/L ratio, increasing stress concentration trend was seen while the Poisson's ratio was also increasing. It may be noted that the finite element results predict Poisson's ratios as low as - 20 when the H/L ratio of the non-square grid structure reaches 4 as shown in Fig. 4.15. While these results are quite interesting, owing to practical limitation of the instability of the structure and the fabrication of the part on the available selective laser melting system, the maximum value of H/L ratio 3 has been taken for the experimental verification.

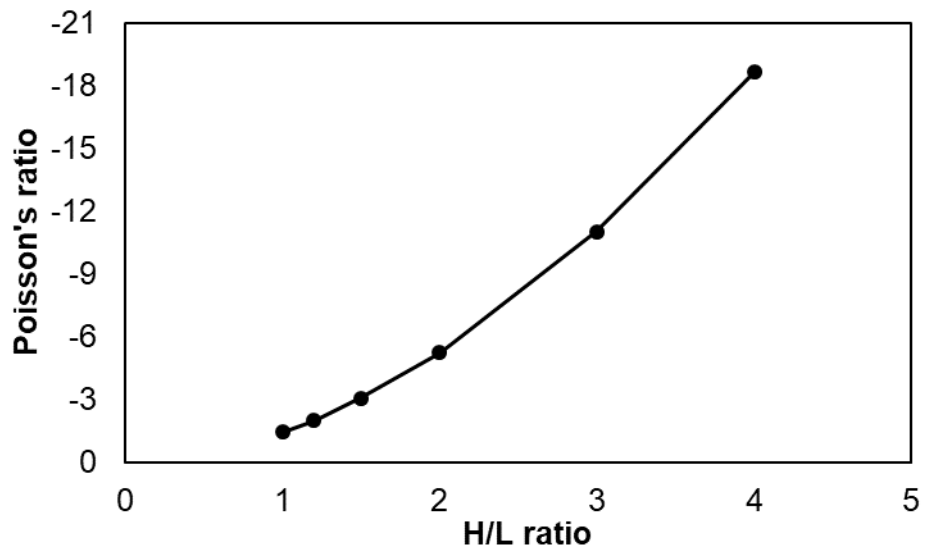


Fig. 4.15 Effect of H/L ratio over Poisson's ratio

4.5.4. Experimental verification of the optimized structure

For experimental verification, the non-square grid structure of H/L ratio 3 was printed based on the selective laser melting of 316L stainless steel, as discussed earlier. Figure 4.16(a) shows the printed non-square grid structure of H/L ratio 3 mounted on the Tinius Olsen Tensile testing system for compression testing as discussed in section 3.5 of Chapter 3. An image of the structure deflected upon loading is presented in Fig. 4.16(b) along with the digitally processed image shown in Fig. 4.16(c). Evidently, the deformation mechanism is predominantly governed by the buckling of the vertical struts, considering the relative length to width ratio of the overall structure. Further, the horizontal constraints led to the outward buckling of each of the vertical columnar members on either side of the box-like configurations. On the other hand, the long columnar vertical struts joining the

horizontal struts of the unit cell are buckled inwards. The buckling effects, in turn, are coupled with the rotational deflections of the non-square unit cell structures. The buckling of the vertical members and the rotational deflections of the unit cells ultimately led to a horizontal deflection of the flaps inwards. The mechanism is similar to the square grid counterpart, but, the elongated non-square grid configuration led to a magnification of these effects as depicted in FE results also, eventually, leading to an enhanced auxetic response from the structure. In the square grid structure, the horizontal and vertical displacements are equal, while the vertically elongated structure results in unequal displacements, leading to enhanced negative Poisson's ratios.

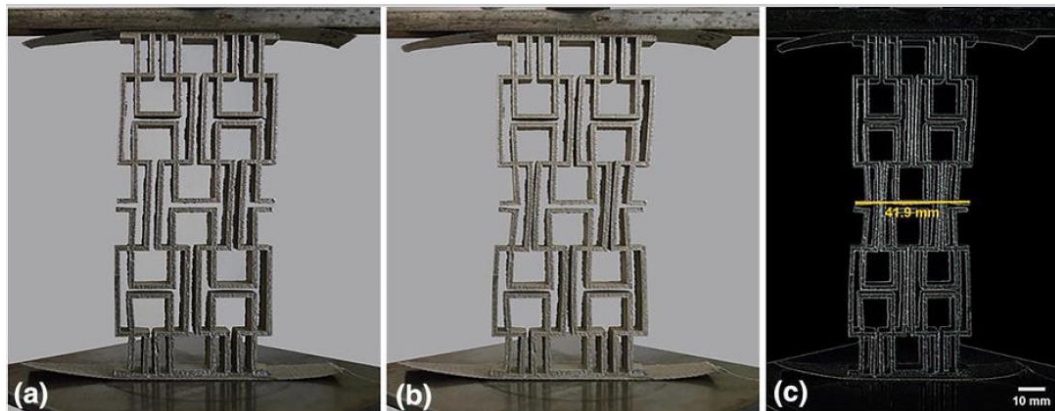


Fig. 4.16 3D printed square grid structure (a) Prior to compression (b) after compression (c) Image processed deformed structure

The Poisson's ratio values calculated based on the dimensions measured by both Vernier Callipers and the Image J software are plotted along with the values

generated from the FE simulation against the compressive load as depicted in Fig. 4.17. It is evident again that the finite element simulation estimated higher values than the experimental methods. There is a slight variation in the values of the Poisson's ratios with varying compressive loads. Also, there are differences between the values calculated based on Vernier Callipers and Image j software measurements. However, these differences are not too high, and considering the practical difficulties in the measurements by Vernier Callipers, it may be stated that the Poisson's ratios from the image processing are more reliable. The average value of the Poisson's ratio based on the results from the image processing is at around – 7.0, which is around 36% lower than the average value predicted from the finite element results. While the differential displacement constraints and inherent structural issues emanating from the selective laser melting process could be the reasons, the most important observation is that the structure was practically proved to exhibit a Poisson's ratio of – 7.0, which is a substantial improvement compared to the – 1 reported earlier with the same base unit, but square-grid form of the structure.

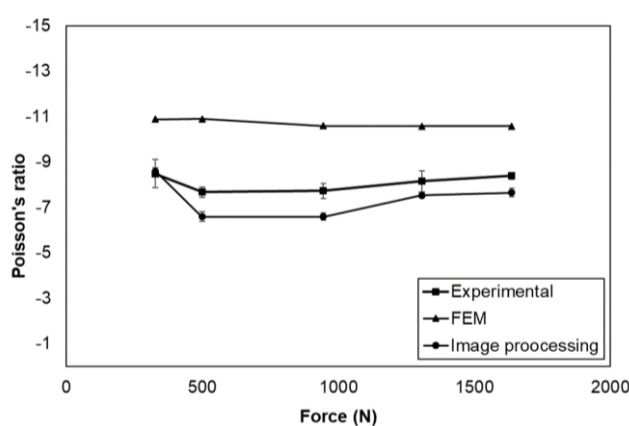


Fig. 4.17 Poisson's ratio vs compressive loads in the non-square grid structure

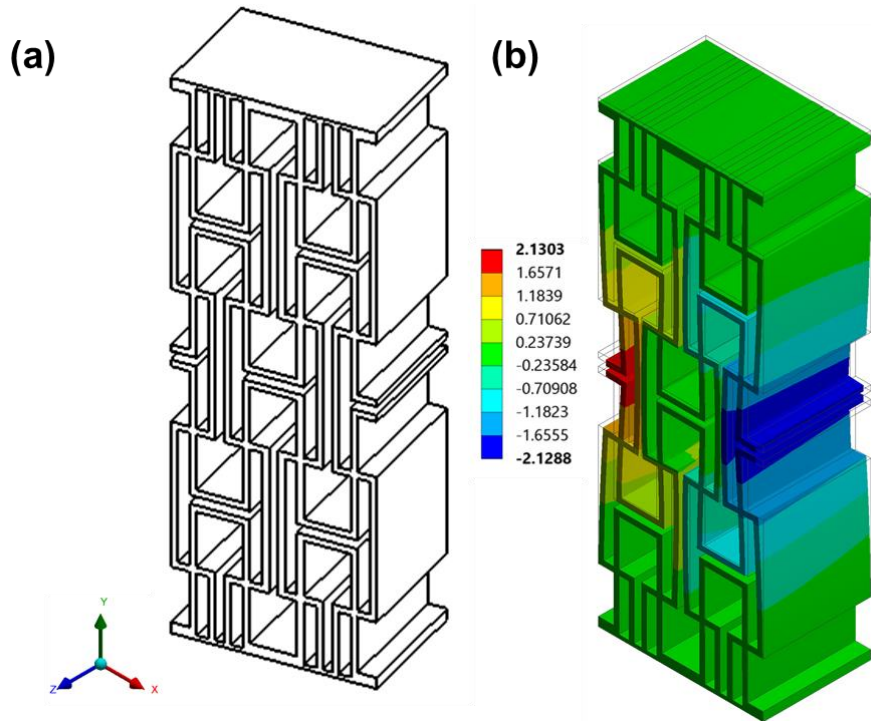


Fig. 4.18 Auxetic nature of the 3D non-square-grid structure (a) CAD model, (b) finite element simulated the deformed structure

The results obtained are encouraging in terms of the high auxetic nature reflected by the negative Poisson's ratios achieved with the non-square grid structures of H/L ratios 3 and above. However, as may be noted from Fig. 4.16(b), the 2D form with the higher slenderness ratio tends to buckle. This could adversely affect the stability of the structure, but the expansion of the structural form in the third dimension is likely to avoid this constraint. Finite element simulation of the 3D structural form is undertaken to verify this. The CAD model of the 3D form developed is depicted in Fig. 4.18(a) and the deformed shape of the structure as predicted by the finite element simulation is presented in Fig. 4.18(b). It may be

noticed that the results indicate the buckling problem to be eliminated, while the Poisson's ratio is still the same as in the case of the 2D auxetic structure.

4.5.5. Stress concentration effects of the auxetic geometry

The overall performance of an auxetic structure depends on the flow of stresses under deformation along with the auxetic responses. In general, simplification of any structure by avoiding sharp corners or providing fillets in the corners helps to a certain extent to reduce the stress concentration problems. In the case of the square grid structure, the geometry can influence not only the auxetic behaviour but the stress concentration responses also. The stress distribution patterns are numerically evaluated to ascertain the possible influences of filleting the critical points of the geometry of the auxetic structures. The numerical simulation was performed considering the SS 316L as the base material and for the same boundary conditions as stated in section 4.3. A -0.5 mm displacement load in the Y direction was applied for the linear analysis. For non-linear analysis, a bi-linear curve was selected, with a -5 mm displacement in the vertical (Y direction) direction. The mesh models of the filleted (fillet radius, 0.5 mm) and non-filletted structural forms are shown in Fig. 4.19.

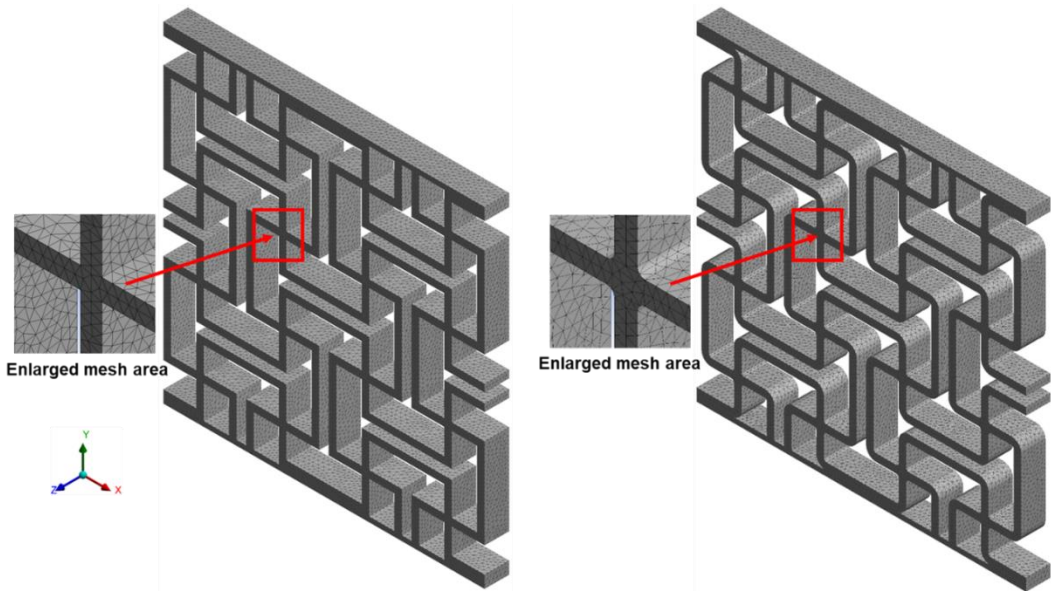


Fig. 4.19 Finite element mesh of (a) Non-fillet and (b) Filleted ($r=0.5$ mm) square grid structures

Fig. 4.20 shows the stress patterns, obtained in the auxetic structures analysed with the elastic loading conditions, which is corresponding to a -0.5 mm deflection of the top face of the structure in the vertical direction. Fig. 4.20 (a) represents the stress distribution pattern in the non-fillet square grid structure. The circled portions are the parts subjected to the maximum stresses for the loading conditions used. The dark red areas are indicating the stress concentration zones. As the fillet radius was introduced into the structure as shown in Fig. 4.20(b) the intensity of the stress concentration effects are reduced to some extent. Depending on the location, the stress concentration points moved towards the center of the arc of the fillet, rather than being on the edges as is the case with the non-fillet structure. The movement of the stress concentration points and the reduction in the intensity of stress are more pronounced in the case of the 1.5 mm fillet radius as shown in Fig. 4.20 (c).

Evidently, filleting not only reduced the stress intensity, but also allowed to improve the stress distribution.

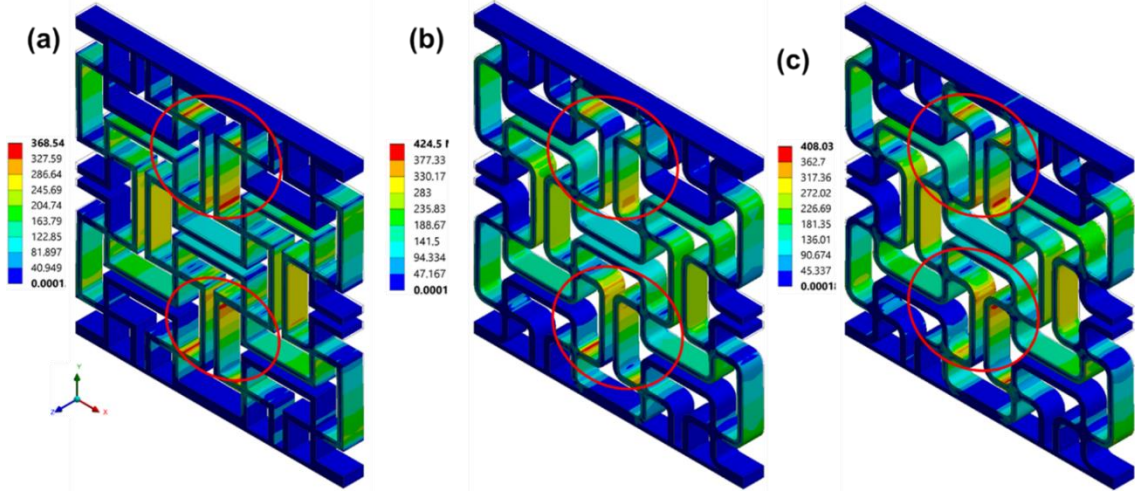


Fig. 4.20 Effect of Fillet radius on stress distribution patterns with fillet radius (a) 0 mm, (b) 1 mm and (c) 1.5 mm for linear elastic analysis.

The effects of varying the fillet radius values from 0 to 2mm are captured by plotting both the Poisson's ratios and the maximum Von-Mises stress values against the fillet radius as depicted in Fig. 4.21 (a) and (b) respectively for the case of the linear materials option. It may be noted from Fig. 4.21(a) that the negative values of the Poisson's ratio initially decreased slightly and then increased continuously, as the fillet radius is increased. The overall variation is from -1.55 to -1.65, which is not that significant in terms of the total range. Overall, the negative trend of the Poisson's ratio increased slightly with the increase in the fillet radius. Xiong et al. (Xiong et al. 2017) reported a decreasing trend in the negative Poisson's ratio with increasing fillet radius, based on a re-entrant structure. Here, it must be noted that the auxetic nature is dependent on the negative values of the Poisson's ratio, and

the more negative the Poisson's ratios, the better auxetic the structure is. Evidently, the fillet radius will influence the auxetic nature differently in different structural forms. Apparently, filleting a square grid structure is leading to a more streamlined structural form, allowing for a better lateral movement and eventually improved the auxetic behavior, as compared to the re-entrant structure.

Fig. 4.21(b) represents the variations of the Von-Mises stresses with respect to the fillet radius. The stress value increased from around 370 MPa for non-fillet to around 570 MPa for 0.5 mm fillet radius. However, as fillet radius changed from 0.5 mm to 1 mm and further to 1.5 mm, the stress values tend to decline and reached around 400 MPa for 1.5 mm fillet radius. On further increase in the fillet radius up to 2 mm, increased stress value was obtained but not as much as was in 0.5 mm fillet radius. Xiong et al. (Xiong et al. 2017) reported the same decreasing effect of stress values. While there is a variation in the maximum stress values obtained with different fillet radii, this result is to be viewed together with the distribution patterns, as the filleting has drastically reduced the areas of the higher stress values. Further, it may be noted that the most optimum stress values can be obtained by maintaining the fillet radius at around 1 to 1.5 mm.

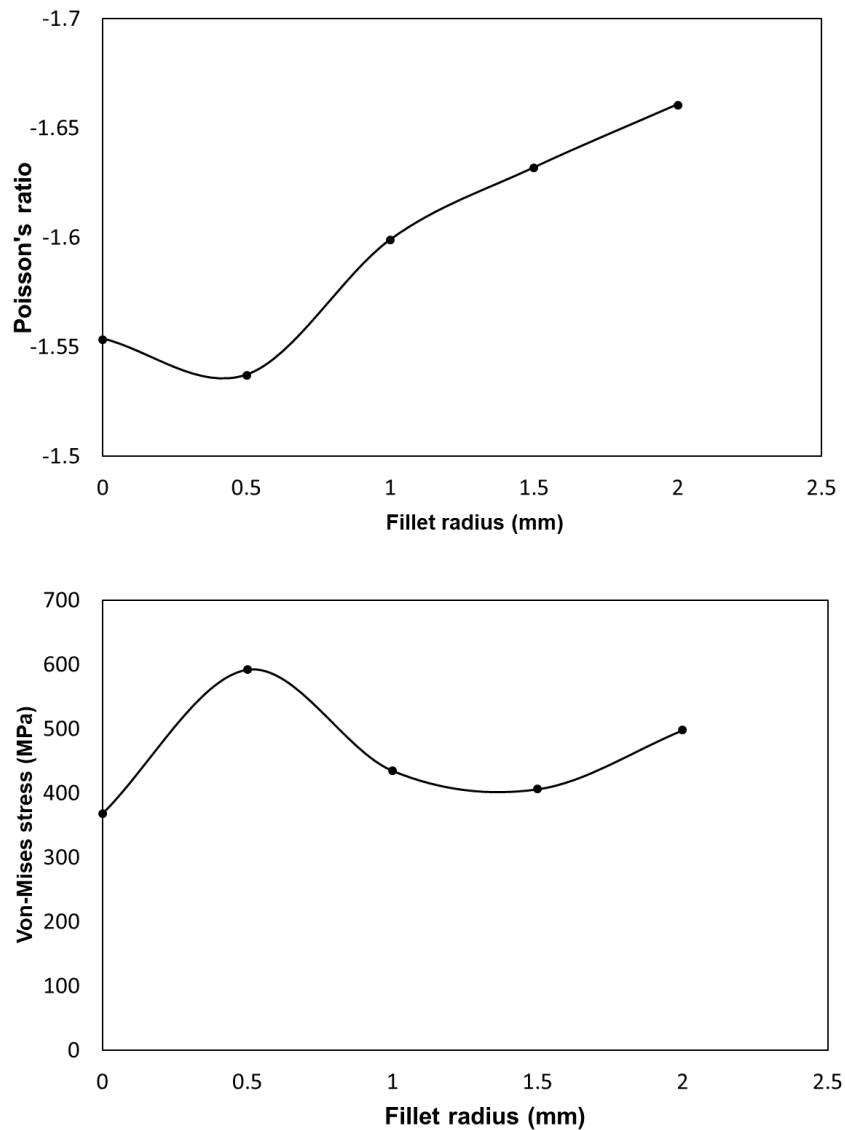


Fig.4.21 Effect of Fillet radius on (a) Poisson's ratio and (b) maximum Von-Mises stress with the linear materials option

Fig. 4.22 shows the Stress distribution patterns in the square grid structures for the non-linear analysis. As shown in Fig. 4.22 (a) in the circled parts, stresses are concentrated at the center portion and at the edges of laterally outward struts unlike stress distribution patterns resulting from the linear analysis as shown in Fig. 4.20. The movement of stresses from upper and bottom part of the structures to the

middle portion as shown in Fig. 4.20 and 4.22 respectively show the difference in the failure pattern of the same structure for two different structural analysis.

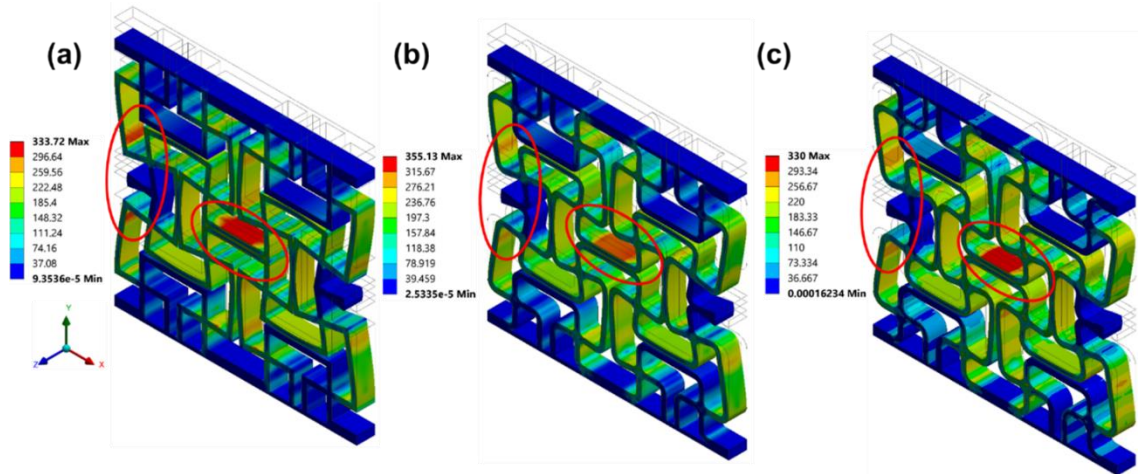


Fig.4.22 Effect of Fillet radius on stress distribution patterns with fillet radius (a) 0 mm, (b) 1 mm and (c) 1.5 mm for non- linear materials.

In non-linear analysis, due to large applied loading, the out of plane deformation could be seen in Fig. 4.22. However, this problem can easily be addressed by increasing the Z dimension as also discussed earlier in section 4.5.4.

Fig. 4.23 (a) and (b) shows the effect of fillet radius on the Poisson's ratio and the Von-Mises stress. These results are based on the non-linear structural analysis as the structure is subjected to large compressive displacements. Fig. 4.23(a) shows the variation of the Poisson's ratio along with the increase in the fillet radius. The same increasing trend of negative Poisson's ratio was also achieved for the linear

material analysis as discussed earlier, though the increasing trend in both cases is different. Here also these results of increasing negative Poisson's ratio can be attributed to the modification of the unit cells on filleting in such a way that leads to more lateral rotation of the individual unit cells for the same longitudinal compressive displacement and improving the auxeticity of the structure.

The Von-Mises curve in Fig. 4.23(b) is similar to the curve obtained for the linear analysis in Fig. 4.21(b) except peak value for stress is achieved for 1 mm radius instead of 0.5 mm. One thing needs to point out here that the stress values in the non-linear analysis are not varying too much as were in the linear analysis. However, a slight increase and then decrease in the Von-Mises stress has been shown in Fig. 4.23(b) with the increased fillet radius. An optimum fillet radius can be chosen from Fig. 4.23 (a) and (b) for non-linear analysis, which is 1.5 mm in the present case, which is showing maximum negative Poisson's ratio and minimum Von-Mises stress.

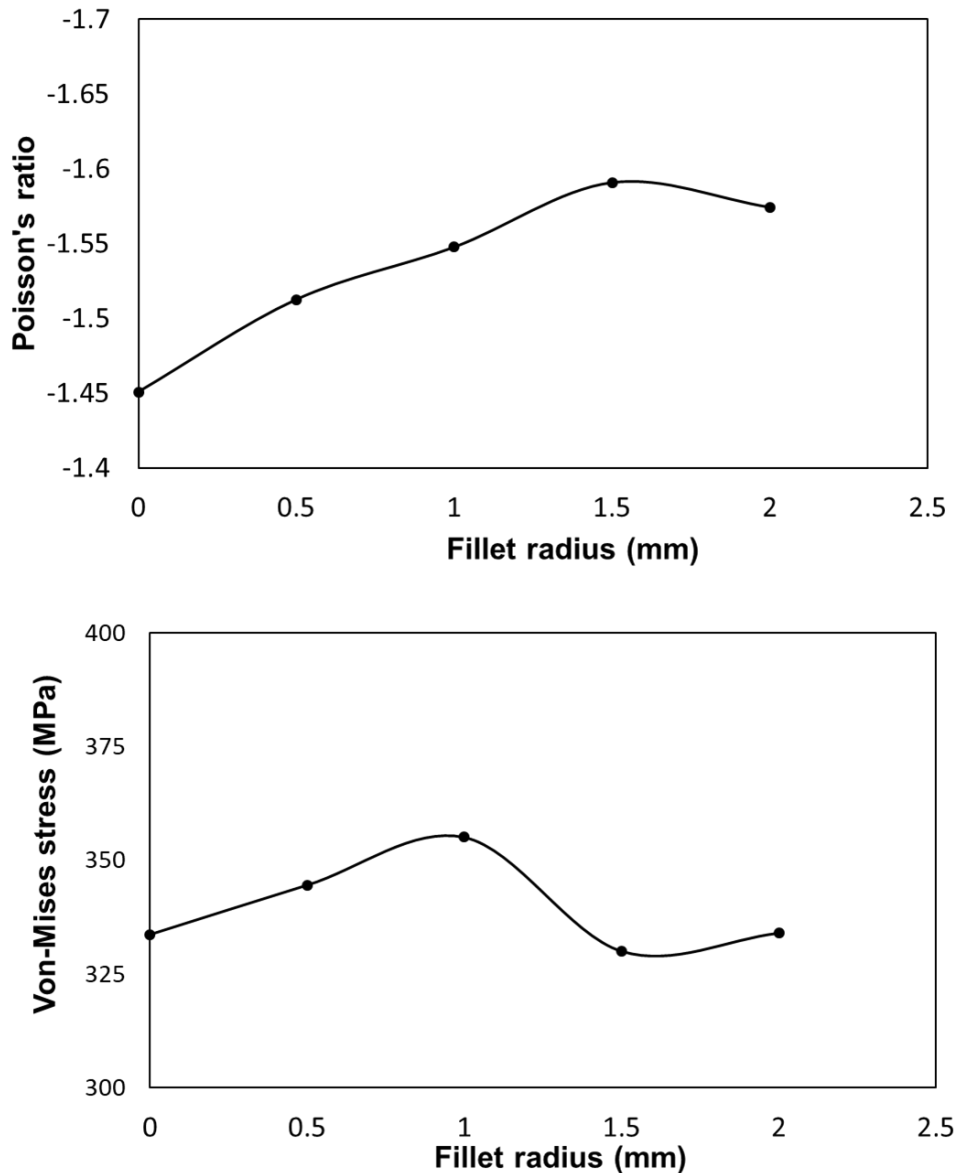


Fig. 4.23 Effect of Fillet radius on (a) Poisson's ratio; (b) Von-Mises stress for non-linear material analysis.

4.6. Summary of the evaluation of the square grid structure

A 2D square grid auxetic structure was evaluated with varying geometric features, based on both finite element analysis and experimental validation using structures produced by selective laser melting. The auxetic nature of the initial square grid structure was found to be similar to what was reported in the literature for the square form of the base unit cell, as the Poisson's ratio was close to -1 from both finite element predictions and experimental measurements. Geometrical modifications based on the varying angle of the flaps and the thickness of the struts was found to have negligible influences on the final auxetic responses. The height to length ratio greater than 1 was found to give rise to improved auxeticity. The finite element prediction based on the non-square grid structure with the H/L ratio equal to 3 indicated a possible Poisson's ratio of around -10.0 . However, experimental validation based on non-square grid structures fabricated by selective laser melting of 316L resulted in a Poisson's ratio of -7.0 . The instability and buckling problems of the non-square grid structures arising due to increased H/L ratio can be overcome if the 2D structures are expanded into the 3D forms.

The stress concentration effects in the square grid auxetic structure were also studied numerically. The corners of the structure were filleted in an attempt to reduce the stress concentration effects. The results based on varying fillet radii have shown negligible improvements in the Von-Mises stresses generated and a slight improvement in the auxetic nature were noticed. The incorporation of the fillets in the corners streamlined the overall structure, which enhanced the lateral

movement and as a result, the auxetic Poisson's ratio. However, the role of the fillets in reducing the concentrated stress in any structure is geometry-specific. Fillets reducing the concentrated stress in a given geometry may not necessarily do so in other geometrical forms. A robust solution to this problem lies in developing a structural form with relatively lesser geometrical complications and the consequent reduction in the build of stresses within the domain of the structure. A new and novel S-shaped structural architecture developed along these lines is the focus of the next chapter.

Chapter 5

Stress concentration effects and an enhanced auxetic structure

5.1 Auxetic structures and stress concentrations

The detailed investigation of the square grid structure by means of numerical and mechanical methods in the previous chapter established the high auxetic nature for the structure with the optimised geometrical parameters. The analysis of stress concentration issues in the auxetic geometries arising due to complex structural geometries and metal fabrication process attributes are as important as the establishment of the auxetic nature. However, the stress concentration issues have largely been overlooked in the previous research, except for a few of attempts made to reduce the internal stresses. Realising the problems such as oxidation, inclusions, shrinkage voids, and porosity which were leading to stress concentration issues, Xue et al. (Xue et al. 2018) built auxetic structural forms by indirectly using additive technologies to process aluminium through investment casting. Xiong et al. (Xiong et al. 2017) introduced a modified 3D re-entrant structure with inclined links and fillets and optimized in terms of the strut inclination and re-entrant angles. Evaluating the effects of the fillet radius, it was noted that increasing the fillet radius would suppress the stress concentration effects up to some extent. The filleting phenomenon to reduce the stress concentration has also

been evaluated in the previous chapter (Chapter 4) with the square grid structural form. However, the fillets were not fully effective in reducing the stress concentration problems. Evidently, the effectiveness of the fillet is geometry sensitive. Fillets may help to reduce the stress concentration in one geometry but may not be necessarily be effective with other structural geometries. Alternatively, a robust solution lies in the alteration of the design of the structure itself, targeting less design complexity and geometrically lesser susceptive forms.

A novel and new S-shaped structure is proposed in this chapter, targeting structural forms with auxetic responses, comparable to the standard re-entrant form, but with greatly reduced degree of stress concentration. The S-shaped unit cell is analytically modelled first and then the structural form is ascertained for the auxetic responses based on experimental measurements and semi-empirical equations. Finite element simulations conducted next clearly demonstrated the reduced stress concentration levels, compared to the re-entrant structures of comparable sizes and other geometrical features.

5.2 CAD modelling

The unit cell, 2D and 3D models of the S-shaped and the re-entrant structures designed in SolidWorks 2016 are depicted in Fig. 5.1 (a), & (c) and (d), (e) & (f) respectively. The S-shaped unit cell is made out of a full circle. The circle is divided in four parts, out of which two parts were specifically removed and the remaining

two parts were joined by an inclined strut as shown in Fig. 5.1(a). The re-entrant unit cell model is essentially made of a typical honeycomb unit cell, in which the inclined links of the honeycomb are protruded inward instead of the outward as depicted in Fig. 5.1 (d). The resultant unit cells of both the structures were then arrayed in X- and Y- directions and formed a 2D models, which were then extruded in Z- direction to build 3D full models. A thick plate of same thickness (t) and same width (W) was attached at the top and bottom of all the all printed samples for better holding during mechanical testing.

The parametric values of the critical geometrical parameters of the S-shaped and the re-entrant unit cells as shown in Fig. 5.1 (a) and (d) are mentioned in Table 5.1. It must be noted here that the geometrical size of the initial unit cell in both the cases was made in the 14×14 mm size square box. However, the final sizes of both the structure came out different, the S-shaped unit cells were connected by providing an extra link between two unit cells which is not the case in the re-entrant structure.

Table 5.1: Significant geometrical parameters of the unit cells

S Structure					
L (mm)	R (mm)	C (mm)	$\theta_1 & \theta_2$ ($^{\circ}$)	t (mm)	W (mm)
14	7	10.6	30	1.5	10
Re-entrant Structure					
H (mm)	L (mm)	α ($^{\circ}$)	t (mm)	W (mm)	d& r (mm)
14	7.25	75	1.5	10	0

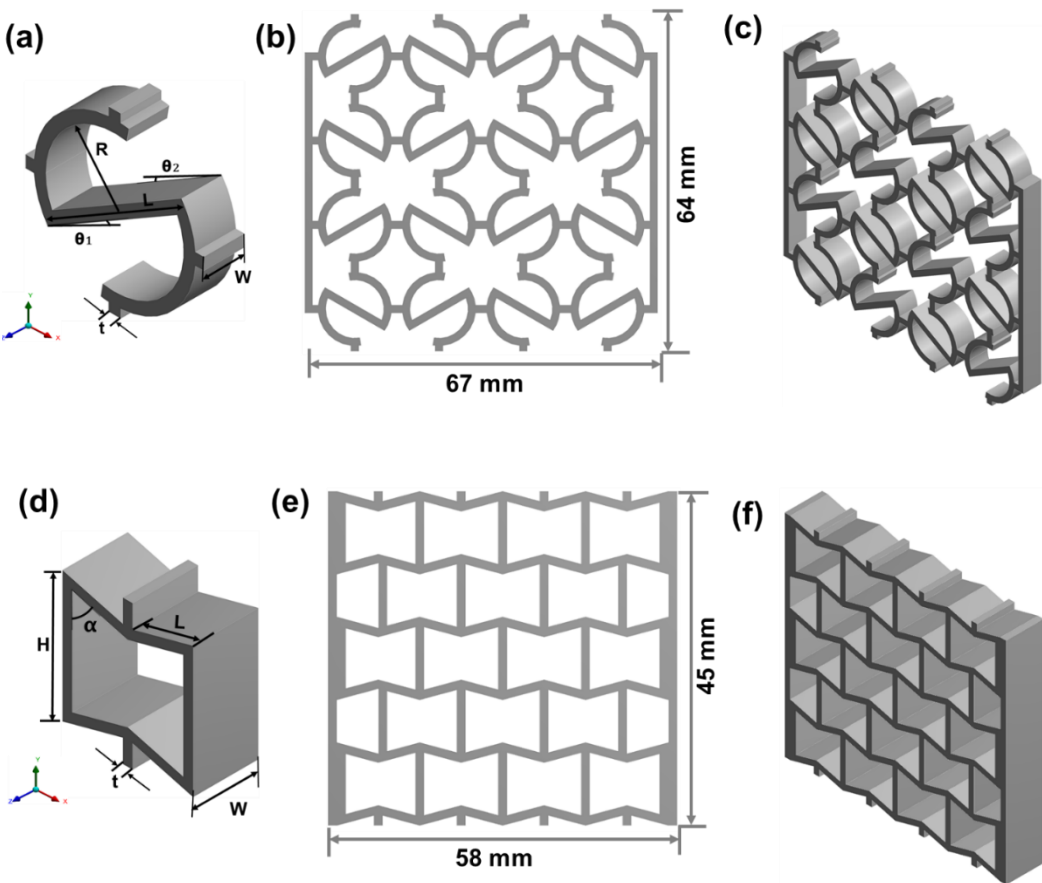


Fig. 5.1 The unit cell (a) & (d), 2D (b) & (e) and 3D (c) & (f) CAD model of the S-shaped and Re-entrant structures

5.3 Analytical and experimental methods

5.3.1 Analytical modelling

The line diagram of the unit cell form of the proposed S-shaped structure is shown in Fig. 5.2 (a). The unit cell configuration is simplified in the form as shown in Fig. 5.2 (b) for the analytical modelling. Arcs AB and CD in Fig. 5.2 (a) are reduced to

straight line segments MN and PQ in Fig. 5.2 (b), each having a constant length of C. The deformed model M'N'P'Q' is shown in Fig. 5.2 (b) by the dotted lines which is the result of loading the unit cell along XX' axis. Liu and Hu (Liu and Hu 2010) grouped auxetic geometries into different types, mainly categorising them into re-entrant, chiral and rotating models. The current S structure follows the deformation patterns of a node-ligament based chiral structure, attaining the auxetic nature through rotation and so can be classified as a chiral model.

In the unit cell, γ is the angle between struts MN & MP and PQ & MP, it acts as the spring hinge with spring constant K_γ , and thus it is assumed that when the unit cell is loaded along the XX' axis, it will deform solely due to the change in the angle γ . The angles made by MN and PQ are represented by ϕ , while θ is the angle made by MP with respect to the x-axis. Change in the angle ϕ ($\Delta\phi$) is represented by $\Delta\phi = k\Delta\theta$, where k is the ratio of change in the angle ϕ ($\Delta\phi$) and change in the angle θ ($\Delta\theta$).

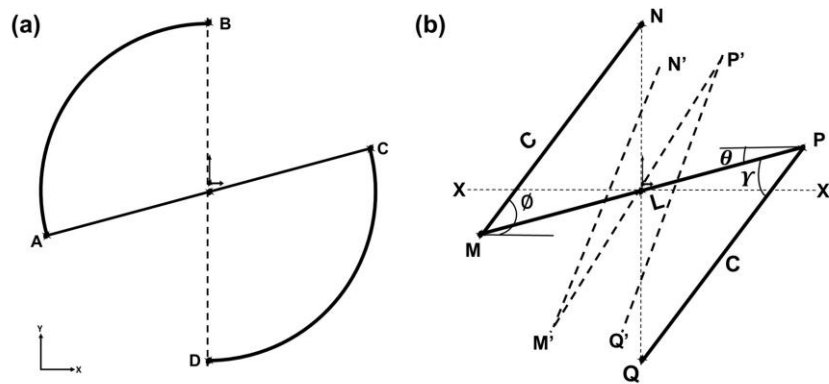


Fig. 5.2 (a) The S-shaped unit cell (b) Simplified undeformed and deformed model of the S-shaped unit cell

Hence

$$\Delta\phi = k\Delta\theta \quad (1)$$

$$d\phi = kd\theta, \quad (2)$$

The assumptions made are; (a) There is no change in the length of the individual struts MN, MP, PQ. (b) Under deformation, the central strut MP always follows the circular path due to the translation symmetry as shown in Fig. 5.2 (b).

Unit cell dimensions in the x and y-directions, in terms of angle θ and ϕ are:

$$x = L\cos\theta, \quad (3)$$

and,

$$y = 2C\sin\phi - L\sin\theta, \quad (4)$$

and the Poisson's function is given by:

$$\vartheta_{xy} = (\vartheta_{yx})^{-1} = -\frac{d\varepsilon_y}{d\varepsilon_x}, \quad (5)$$

Where $d\varepsilon_x$ and $d\varepsilon_y$ are the small incremental strains in the longitudinal and lateral directions respectively, which may be expressed as:

$$d\varepsilon_x = \frac{dx}{x} = \frac{1}{x} \frac{dx}{d\theta} d\theta, \quad (6)$$

$$d\varepsilon_y = \frac{dy}{y} = \frac{1}{y} \frac{dy}{d\theta} d\theta, \quad (7)$$

Putting the values of equation (6) and (7) in equation (5) gives:

$$\vartheta_{xy} = -\frac{d\varepsilon_y}{d\varepsilon_x} = -\frac{x}{y} \left\{ \frac{dy/d\theta}{dx/d\theta} \right\}, \quad (8)$$

Where,

$$\frac{dx}{d\theta} = -L\sin\theta, \quad (9)$$

and,

$$\frac{dy}{d\theta} = 2C\cos\theta \frac{d\phi}{d\theta} - L\cos\theta, \quad (10)$$

Combining equation (2), (9) and (10), and putting in equation (8) gives

$$\vartheta_{xy} = (\vartheta_{yx})^{-1} = \cot\theta \left\{ \frac{2Ck\cos\theta - L\cos\theta}{2C\sin\theta - L\sin\theta} \right\}, \quad (11)$$

The Young's modulus for the given structure can be obtained from the conservation of the energy. The strain energy per unit volume due to strain $d\varepsilon_x$ and $d\varepsilon_y$ is given by:

$$U = \frac{1}{2}E_x(d\varepsilon_x)^2, \quad (12)$$

$$U = \frac{1}{2} E_y (d\varepsilon_y)^2, \quad (13)$$

While the work done per unit cell by the hinges is given by:

$$W = N \left[\frac{1}{2} k_\gamma (d\gamma)^2 \right], \quad (14)$$

Where N is the no. of hinges in the unit cell, that are participating in the work done by the unit cell. Thus from the conservation of energy, equations (12), (13) and (14) are related through:

$$U = \frac{1}{V} W, \quad (15)$$

Where V is the volume of the unit cell which assuming to have a unit thickness in the z-direction

$$V = xy \quad (16)$$

Thus combining equation (6), (12), (13) and putting all into equation (15) gives:

$$E_x = \frac{2k_\gamma x}{y(dx/d\theta)^2} = \frac{2k_\gamma \cot\theta \cosec\theta}{L(2Cs\in\theta - L\sin\theta)} \quad (17)$$

Moreover, combining equation (7), (13), (14) and putting all into equation (15) gives:

$$E_y = \frac{2k_\gamma y}{x(dy/d\theta)^2} = \frac{2k_\gamma (2Csin\theta - Lsin\theta)}{Lcos\theta (2Ckcos\theta - Lcos\theta)} \quad (18)$$

Where E_x and E_y are the Young's modulus in the X and Y- directions respectively.

It may be pertinent to point out at this stage that the expressions derived in this section are semi-analytical in nature and will depend on quantities developed from the experimental results. A direct verification of these equations though interesting, is not currently undertaken due to practical limitations.

5.3.2 Experimental methods

All the information relevant to the fabrication, post processing and compression testing is provided in Chapter 3. To perform the mechanical test, Compressive loads were applied on the printed structures of the S-shaped and the re-entrant structures, achieving a maximum displacement of 20 mm at a rate of 2mm/min for 10 minutes. The critical junction points of the structures were highlighted by means of the green marks seen in Fig. 5.5, in order to closely capture the deformation responses through image capturing and subsequent analysis. The entire compression process was video recorded from the start to the end, for further analysis of the displacement patterns of different sections of the structure. The data from the obtained load-displacement curves under compression, of all the samples were extracted and image processed as per the details provided in the section

3.6.2 and 3.6.3 of Chapter 3. The deformed angles of the structures were also measured using the ImageJ software to measure the Poisson's ratio analytically (By putting the values of the theta (θ) and phi (ϕ) in the analytically derived Poisson's ratio equation.

5.3.3 Finite element simulation

The 3D CAD models of the re-entrant and the S shaped structures were designed in the SolidWorks 2015 software as discussed above, and presented in Fig. 5.1. The geometrical parameters of the S-shaped structure, namely θ , fillet radius (r) as depicted in Fig. 5.1 (a) and (d) and load distance from centre (d) in Fig. 5.3 were varied and number of numerical simulation were performed in the ANSYS 16.2 Software. The resultant Von- Mises stresses, lateral and longitudinal displacements for the varied S-shaped geometrical parameters are tabulated in Table 5.2.

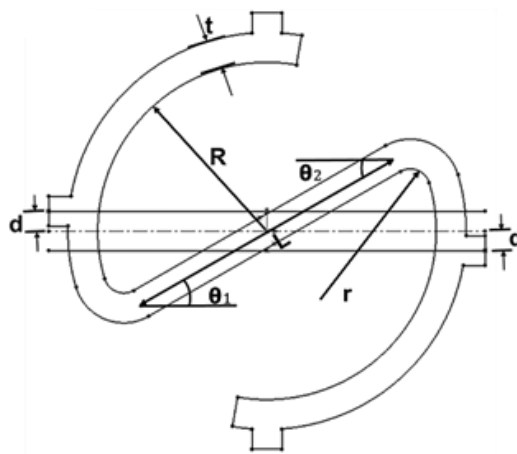


Fig. 5.3 Geometrical parameters of 2D model of S-shaped unit cell

Table 5.2: Varied geometrical parameters of the S-shaped structure

No.	θ	Fillet radius (r) (mm)	Load distance from centre (d) (mm)	Lateral displacement (mm)	Von Mises stress (MPa)	Lateral strain	Longitudinal strain	Poisson's ratio (v)
1	20	0	0	-0.313	605.15	-0.0142	-0.0045	-3.13
2	20	0	1	-0.288	528.87	-0.0130	-0.0045	-2.88
3	20	0	2	-0.241	484.7	-0.0109	-0.0045	-2.41
4	20	0.5	0	-0.316	978.29	-0.0143	-0.0045	-3.16
5	20	0.5	1	-0.301	681.22	-0.0136	-0.0045	-3.01
6	20	0.5	2	-0.257	760.49	-0.0116	-0.0045	-2.57
7	20	1	0	-0.312	762.56	-0.0141	-0.0045	-3.12
8	20	1	1	-0.293	631.4	-0.0133	-0.0045	-2.93
9	20	1	2	-0.237	650.56	-0.0107	-0.0045	-2.37
10	30	0	0	-0.212	338.75	-0.0096	-0.0045	-2.12
11	30	0	1	-0.204	356.98	-0.0092	-0.0045	-2.04
12	30	0	2	-0.171	317.3	-0.0077	-0.0045	-1.71
13	30	0.5	0	-0.214	634.84	-0.0097	-0.0045	-2.14
14	30	0.5	1	-0.205	354.08	-0.0093	-0.0045	-2.05
15	30	0.5	2	-0.1884	468.77	-0.0085	-0.0045	-1.884
16	30	1	0	-0.216	529.16	-0.0098	-0.0045	-2.16
17	30	1	1	-0.209	414.23	-0.0095	-0.0045	-2.09
18	30	1	2	-0.188	354.96	-0.0085	-0.0045	-1.88
19	40	0	0	-0.14	227.48	-0.0063	-0.0045	-1.4
20	40	0	1	-0.154	284.9	-0.007	-0.0045	-1.54
21	40	0	2	-0.14	234.85	-0.0063	-0.0045	-1.4
22	40	0.5	0	-0.158	339.41	-0.0071	-0.0045	-1.58
23	40	0.5	1	-0.155	322.32	-0.0070	-0.0045	-1.55
24	40	0.5	2	-0.146	327.48	-0.0066	-0.0045	-1.46
25	40	1	0	-0.163	282.78	-0.0074	-0.0045	-1.63
26	40	1	1	-0.1589	268.96	-0.0072	-0.0045	-1.589
27	40	1	2	-0.149	259.74	-0.0067	-0.0045	-1.49

The final values of the optimum structural geometrical parameters for the S-shaped structure were chosen by considering the balance between the negative Poisson's ratio and the generated Von Mises stresses under loading. The optimum geometric parameters for the S-shaped and re-entrant structure (Li et al. 2016) are listed in Table 5.1. According to Li et al., (Li et al., 2016), the angle α plays a significant role in influencing the auxetic responses in the re-entrant structure, and the optimum value 75^0 as identified by them is adopted here. Again, in the case of the S structure, the angles θ_1 & θ_2 play more significant roles in controlling the auxeticity, and based on initial evaluation they are fixed at 30^0 each.

The designed full structural models based on the optimum unit cells were imported into Ansys Workbench 16.2 package for numerical simulation. The FEA mesh generated for the re-entrant and the S-shaped structures and the displacement boundary conditions employed for numerical simulation are depicted in Fig. 5.4 (a) and (b) respectively. The images in the inset show the tetrahedral discretisation more closely. A uniform tetrahedral element of size 0.50 mm was employed all through. This was obtained based on a mesh convergence analysis result indicating the lateral displacement to converge on a fixed value when the element size was iteratively reduced to around 0.50 mm. The element uses a liner interpolation scheme for the displacement based on the nodal values.

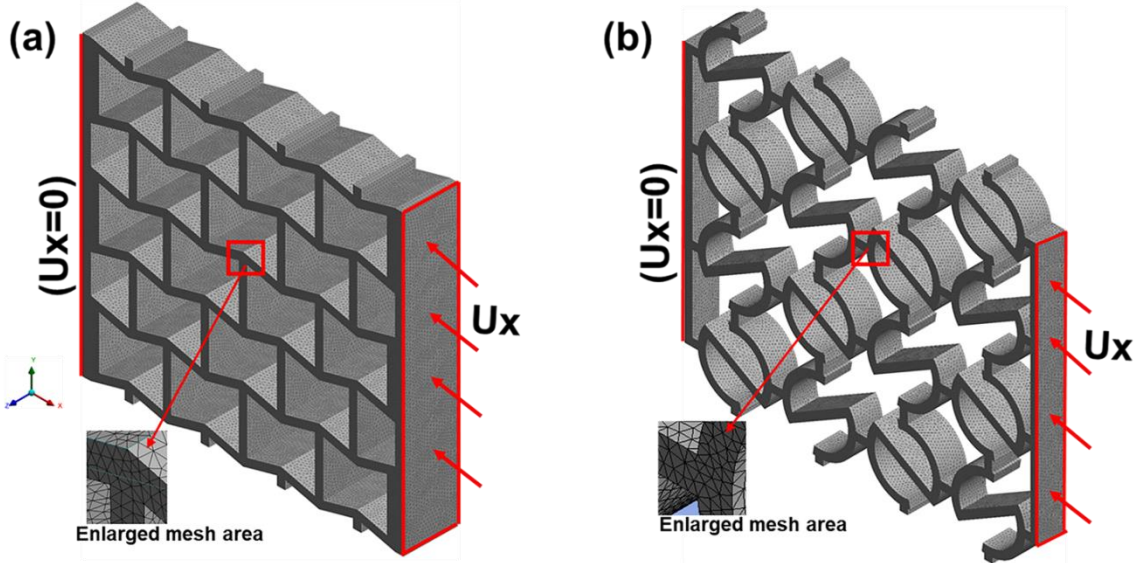


Fig. 5.4 Finite element mesh of (a) Re-entrant and (b) S- shaped structures

The boundary conditions were applied on the structures to simulate the compression behaviour, and so, both structures were fixed from one end (+X direction), and displacement based compressive load was applied at the another end (-X direction) leaving Y- and Z- directions free. The structures were simulated for linear and non- linear material conditions, assigning the properties of the stainless steel 316 L as the base material. The linear and bi-linear curves were chosen for the linear and non- linear materials respectively. For the non-linear material analysis, the bilinear isotropic hardening option of ANSYS was used to characterise the material property. This provides different material properties (two different values for the Young's modulus in the linear and non-linear regions of the curve) for the linear and non-linear material conditions. The contact conditions used in the simulation was the Augmented Lagrange method, to ensure the compatibility between the contact elements (interface of the specimen and the top

plate) with a coefficient of friction of 0.2. In the linear range a displacement condition of -0.1 mm was applied, while for the non-linear material it was a -4 mm in the X direction, in order to simulate the application of the corresponding mechanical loads, keeping all other boundary conditions same.

5.4 Results and discussion

5.4.1 Deformation modes

The displacement controlled deformation of both the structures were recorded and images corresponding to applied displacements at 5 mm intervals are shown as the photographs presented in Fig. 5.5. The deformation behavior of the marked unit cells of both the structures were obtained with the increasing strain values. Under loading, the vertically inclined struts of the re-entrant structure behave like an empirically loaded column under loading and deform initially and then tend to collapse row by row with subsequent increase in displacement. The horizontal struts remain perpendicular to the applied load direction until buckling. The combined effects of buckling and bending of these struts deform the structure and result in the movement of each row laterally towards a side (Ingrole et al. 2017).

The deformation behaviour of the S-structure was recorded by tracing the movements of the 4 central unit cells marked as shown in Fig. 5.5 (f). The S structure deforms by the rotation of its inclined struts around the periphery of a

virtual circular path. The curved parts and columns of the middle rows of unit cells tend to move towards their respective inclined struts to fill the provided gap between them. Secondly, While trying to fill the gaps, the struts widen up the space between the curved and the inclined parts of the corner unit cells due to pulling from the adjacent cells. Once the gap between the curved part and the inclined strut of the unit cells close up, the whole structure tends to collapse within itself, instead of going sideways as in the case of the re-entrant structure. The inward deformation movements of the unit cells as against the sideways movements can be utilised for applications involving impact loading (Alderson 1999).

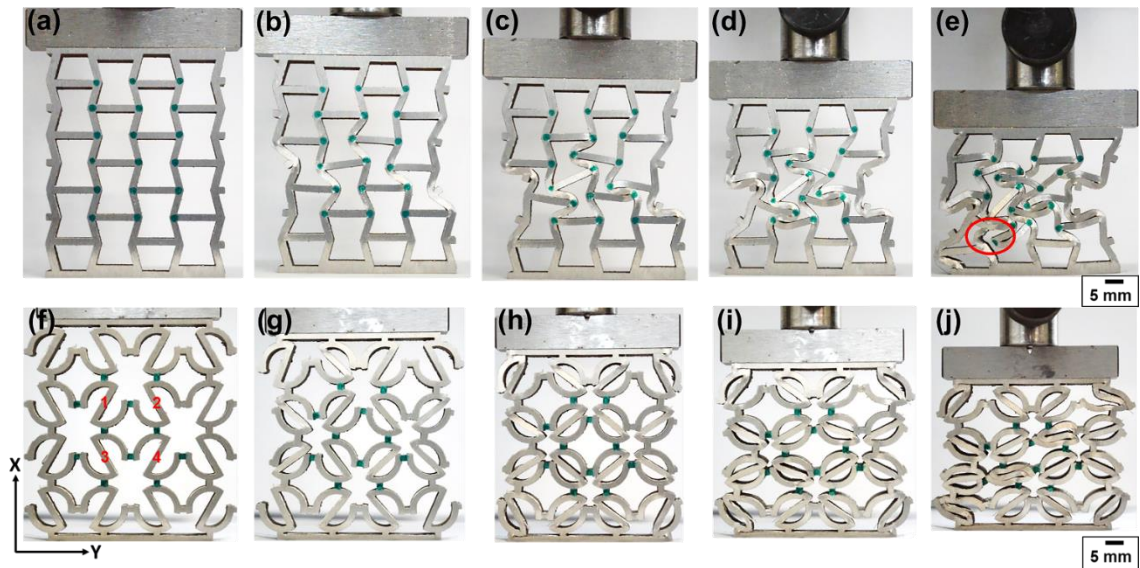


Fig. 5.5 Sequence of pictures for applied displacement of re-entrant (a to e) and s structures (f to j); recorded frames corresponding to displacement boundary conditions: (a) & (f) 0mm, (b) & (g) 5mm, (c) & (h) 10mm, (d) & (i) 15mm, and (e) & (j) 20mm,

5.4.2 Analytical results

The analytical model as discussed in section 5.3.1, was developed to calculate the Poisson's ratio, and according to equation 11, the deformation of each unit cell is dependent on the values of the angles θ . However, while capturing the structural transformations during experiments involving the compressive behaviour of the S-structures as shown in Fig. 5.5 (f-j), it was observed that the two curves AB and CD of the unit cell deform unequally for a given displacement load, as also mentioned in section 5.3.1 referring to Fig. 5.2 (a). This leads to the possible use of two different angles represented as θ_1 and θ_2 for each unit cell to calculate the Poisson's ratios as shown in Fig. 5.3. However, the initial values of θ_1 and θ_2 will be same under no loading conditions. The experimentally measured values of the angles θ_1 and θ_2 for different displacement loads applied for each selected unit cell are tabulated in Table 5.3.

Table 5.3: The values of θ_1 and θ_2 for the given displacement load

Displacement load (mm)		1	2	3	4	5	6	7	8	9	10	11	12	13	14	15
Unit cell	θ_1	30.90	33.60	37.67	43.31	41.23	41.69	40.69	43.77	48.42	51.40	53.16	54.25	56.51	58.38	60.04
	θ_2	31.26	33.42	37.20	43.63	41.17	41.99	41.01	43.31	47.97	51.12	53.09	54.24	56.44	58.23	59.77
Unit cell	θ_1	31.24	33.76	34.04	34.62	40.82	46.47	50.32	51.22	51.42	51.51	53.35	55.28	59.21	64.68	69.20
	θ_2	30.65	33.75	34.07	34.33	39.76	45.23	50.75	51.0	52.11	51.03	53.46	55.49	59.36	64.97	68.98
Unit cell	θ_1	31.79	32.62	32.08	32.13	37.60	41.99	40.10	43.15	47.72	51.55	53.47	55.54	59.75	65.68	70.05
	θ_2	31.85	32.67	32.45	32.35	37.96	42.29	41.02	44.29	47.50	51.77	53.31	55.62	59.58	65.80	70.31
Unit cell	θ_1	30.70	34.49	40.81	45.25	46.49	48.07	51.50	52.22	51.91	51.21	53.38	54.73	56.72	58.59	59.84
	θ_2	30.75	34.36	40.19	45.09	46.10	48.15	51.01	51.96	51.29	50.96	52.79	54.47	56.66	58.50	59.65

Fig. 5.6 shows the variation of the Poisson's ratio with changes in angles θ_1 , θ_2 based on the experimentally deformed four central unit cells (1 to 4) of the S structure as identified in Fig. 5.5 (f-j). It may be noted that the differential deformation attributes of the unit cells in different locations are captured by the differences in the measured values of the angles θ_1 and θ_2 . The k-factor is the ratio of, change in the angle ϕ with respect to change in the angle θ , and it will reflect the relative weightings of the individual angles based on the deformation responses of a given S-structure unit cell. The values of θ , k and γ and their interdependence is clearly demonstrated in the given appendix.

At lower values of deformation loads, the structural changes were too small and prone to errors in measurements of the critical angles and so, the responses corresponding to too low displacements are discarded. The θ , K, and ϕ values measured based on the analysis of the structural images captured at regular time intervals indicate variations from one unit cell to the other within the four unit cells selected for the evaluation. This is reflected in the variations of the Poisson's ratios evaluated by the analytical model applied to the different unit cells as depicted in the results of Fig. 5.6. A diagonal deformation symmetry may be observed between the unit cells 1 and 4, and then 2 and 3 in Fig. 5.5 (f-j). Comparing unit cells 1 and 4 of the S structure, the predominantly loaded elements are the ones inclined at angles θ_1 and θ_2 in unit cells 1 and 4 respectively and the same is applicable for the other pair of diagonal unit cells (2 and 3). Therefore, the comparison must be between Poisson's ratios calculated using θ_1 in unit cell 1 and θ_2 in unit cell 4. This is reflected clearly by the trend lines indicating the variation of the Poisson's ratio which are similar, comparing Figs 5.6 (a) and (h), and 5.6 (b) and (g) for unit cells

1 and 4. Same way, similar trend lines are observed in Figs. 5.6 (c) and (f), and 5.6 (d) and (e) for diagonal unit cells 2 and 3.

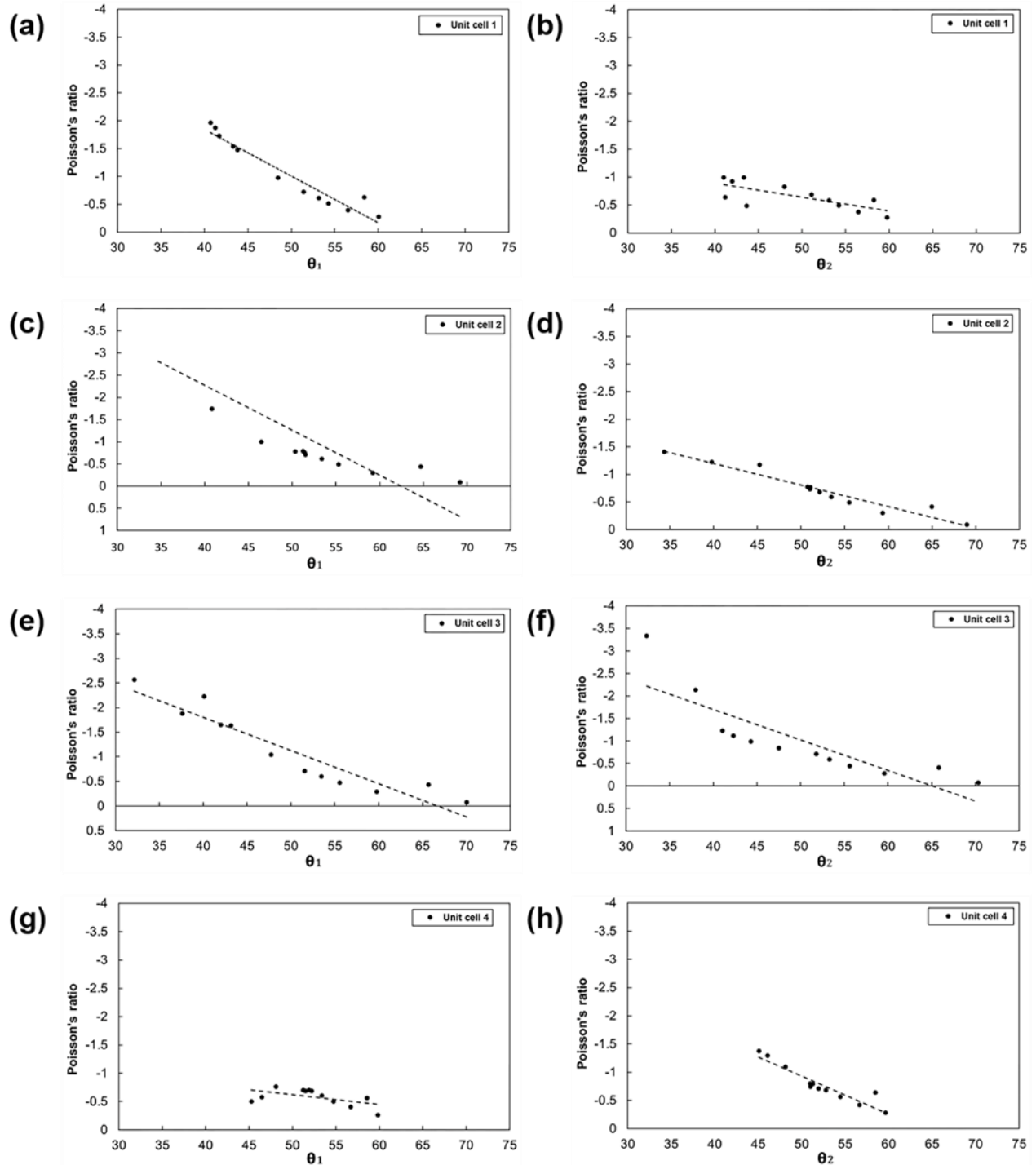


Fig. 5.6 Poisson's ratio variation w.r.t to θ_1 and θ_2 for (a) &(b) Unit cell 1 (c) & (d) Unit cell 2 (e) & (f) Unit cell 3 (g) & (h) Unit cell 4

Overall, as the given load was gradually increased, the values of θ_1 and θ_2 also increased. Further, as the values of θ_1 and θ_2 increased, as per the equation 11 and as depicted in Fig. 5.6, the Poisson's ratios also increased. Angles θ_1 and θ_2 reached a maximum value of around 60^0 , within the 1st and the 4th unit cells, while the peak values are at around 70^0 , in the 2nd and the 3rd unit cells. Differences in the values of these angles led to the variations in the Poisson's ratios in the unit cells under the action of the applied displacement loads. In all the cases, the structure always responded with high auxeticity at lower loads. The negative Poisson's ratios gradually moved towards the positive side and reached up to 0, at the higher loads applied. Further increase in the load will only result in the physical contact between struts and dense packing.

5.4.3 Mechanical Characterisation

Fig. 5.7 shows the stress-strain patterns of the S-shaped and the re-entrant structures depicting the elastic-plastic deformation responses. The initial linear stress-strain regions of both structures represent the uniform deformation of the unit cells. In the case of the S-shaped structure (Curves S₁, S₂, and S₃), the stress value almost linearly increased with the strain in the elastic region. Once the plastic deformation begins there is a certain amount of waviness, but there is a steady increase in the stress values with increasing strain values. At around 20% strain, the structure was almost compressed to its limits and there was no further increase in the stress, as the struts were almost being crumpled against each other, leading

to a densely packed distorted form, which is beyond the form depicted in Fig. 5.5 (j).

The re-entrant structure responded in a completely different manner in the stress-strain graphs generated. The stress values steeply increased in linear relationship with the strain in the elastic region. Beyond the yield point, there is a substantial reduction in the stress with increasing strain and subsequent stabilisation to a great extent, beyond 15% strain. The peak stress generated in the re-entrant structure went up to around 55 MPa, which is much more than the stress generated in the S-structure for the same applied loads. This is possibly due to the relatively lesser design complications in the form of the S-structure. There are only two corner points in the S-structure, as against the eight corners in the re-entrant structure, making it more prone to stress build up (Wang et al. 2015) and probable instability under loading conditions. Young's modulus values of 635 MPa and 2500 MPa and compressive strengths at 37 MPa and 55 MPa were noted for the S-shaped and re-entrant structures. The mechanical properties of the re-entrant structures are better, but the main problem is the stress concentration effects, that are more detrimental in the case of the re-entrant structure. Cracks were generated due to the high-stress concentration effects in the re-entrant structure which led to the fracturing of the struts at around 16 mm of displacement loads applied, as evident from Fig. 5.5 (e). In contrast, the S-shaped structure was completely free from cracking all through the loading and beyond.

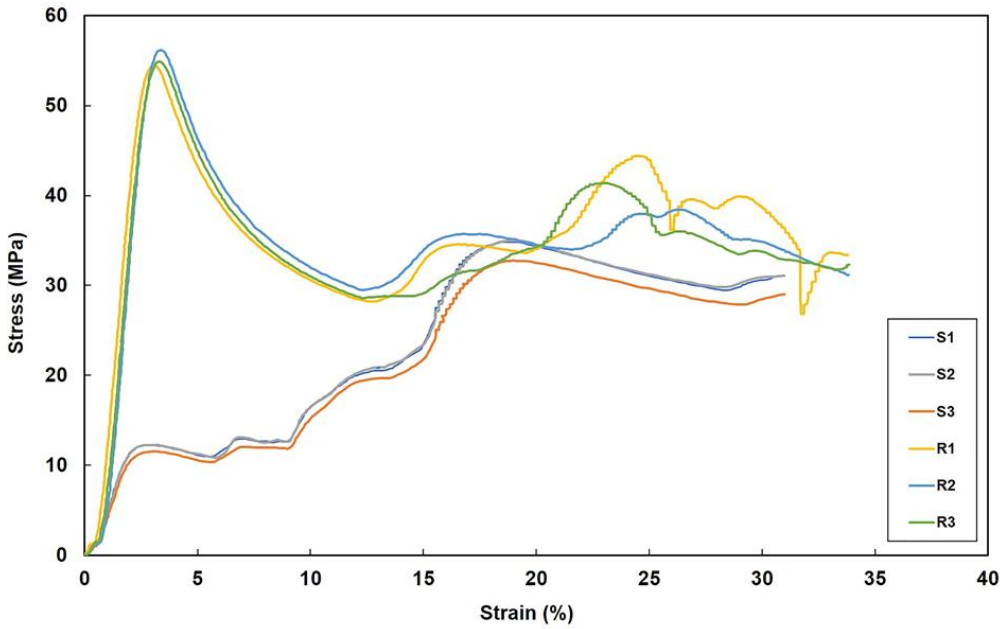


Fig. 5.7 The nominal stress-strain curve for (a) S-shaped (S1, S2, and S3) and (b) re-entrant (R1, R2, and R3) structures

The overall variation of the Poisson's ratio with increasing strain values is depicted in Fig. 5.8 for both the S-shaped and the re-entrant structures. Again, a marked difference may be observed clearly between the two cases. The S-shaped structure begins with relatively double the negative Poisson's ratios, at around -2.5, compared to the re-entrant cases, at lower levels of applied strains. Further, the auxetic nature of the S-shaped structure is intact and stable at about -1.5 Poisson's ratio, for almost up to 15% of straining the structure. Whereas, the re-entrant structure quickly lost the negative Poisson's ratio as the strain values increased, this due to the geometrical weakness and the easy collapsing of the different struts around the multiple sharp corners of the structure. The differences in the deformation modes, caused this abrupt changes in the auxetic responses of the two structural forms. The S-shaped structure is characterised by the unit cells

working together to resist the loads, as against the row-wise collapsing of the re-entrant structure, as evident from the photographs of Fig. 5.5. The eventual loss of auxeticity in both the structures is due to the packing of the collapsing struts and densification of the structures over time. The total applied strain was up to 39%, where the Poisson's ratios became almost equal to zero and a complete loss of the auxeticity.

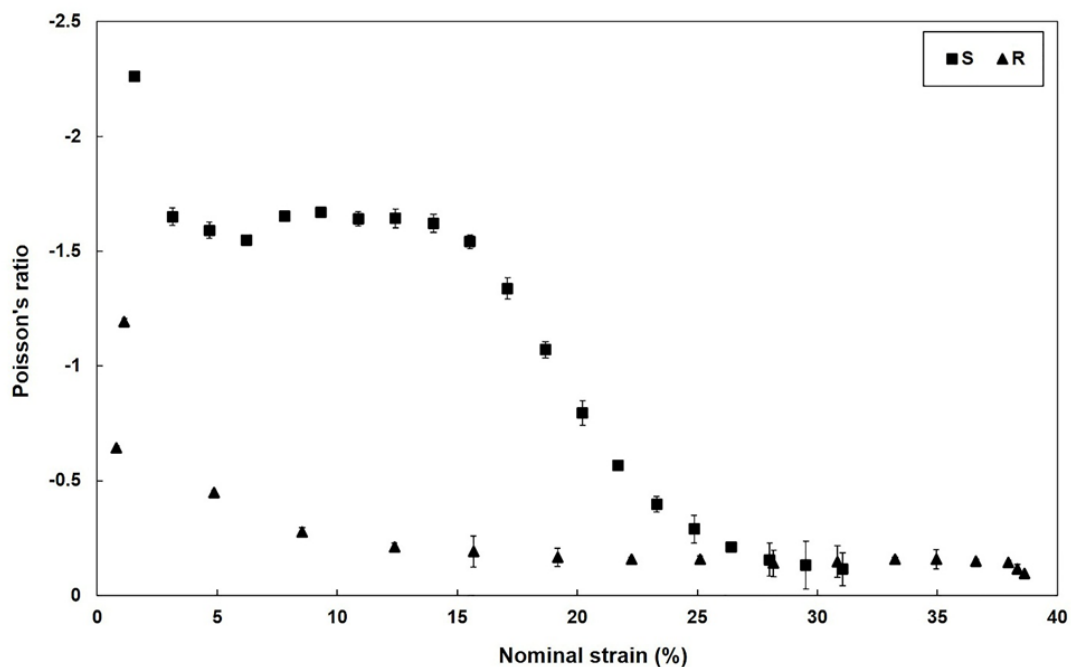


Fig. 5.8 Variation of Poisson's ratios with the applied strain in S and re-entrant structures

5.4.4 Numerical Simulation

The finite element simulations of the re-entrant and the S structures were undertaken with the same boundary conditions as discussed in section 5.3.3. The stress distribution patterns and the lateral displacements for the given displacement loads are presented in Fig. 5.9 and Fig. 5.10 for both the structures. Images in Column 1 correspond to the re-entrant structures, while those in column 2 represent the responses from the S-structure. The light shaded areas in Figs 5.9 (a), (b), (c), and (d) represent zones of stress concentration in the two structures which may be more clearly seen in the 2D close-up views of the unit cells, extracted from the overall structure and presented as in Fig. 5.9 (a) and (c).

First, more number of stress concentration points may be observed in the case of the re-entrant structure as compared to the S-shaped counterpart. Secondly, the peak stress values are higher in the case of the re-entrant structures, the ranges of the differences being dependent on the nature of material considerations. A comparison of the Von Mise's stresses with two different loading cases applied to the re-entrant and the S structures can be undertaken by comparing Figs. 5.9 (a) and (c), and 5.9 (b) and (d) respectively. Under similar loading conditions, subtle changes in the locations and also the distribution patterns of peak stresses may be noted between the two structures, by comparing Fig. 5.9 (a) with 5.9 (c) and then Fig. 5.9 (b) with 5.9 (d). Quantitatively, the peak Von Mise's stresses observed are at around 834 MPa with the re-entrant structure as against the 336 MPa with the S Structure, under linear material conditions. With non-linear material conditions, the difference is not as dramatically different but still considerable, with the re-

entrant section showing a peak stress at 649 MPa, as against the 339 MPa obtained with the S-structure. In any case, the most important aspect to be noted is that the re-entrant structures are stressed more severely compared to the proposed S-structure and are likely to collapse under loads as also evident from the other results presented above.

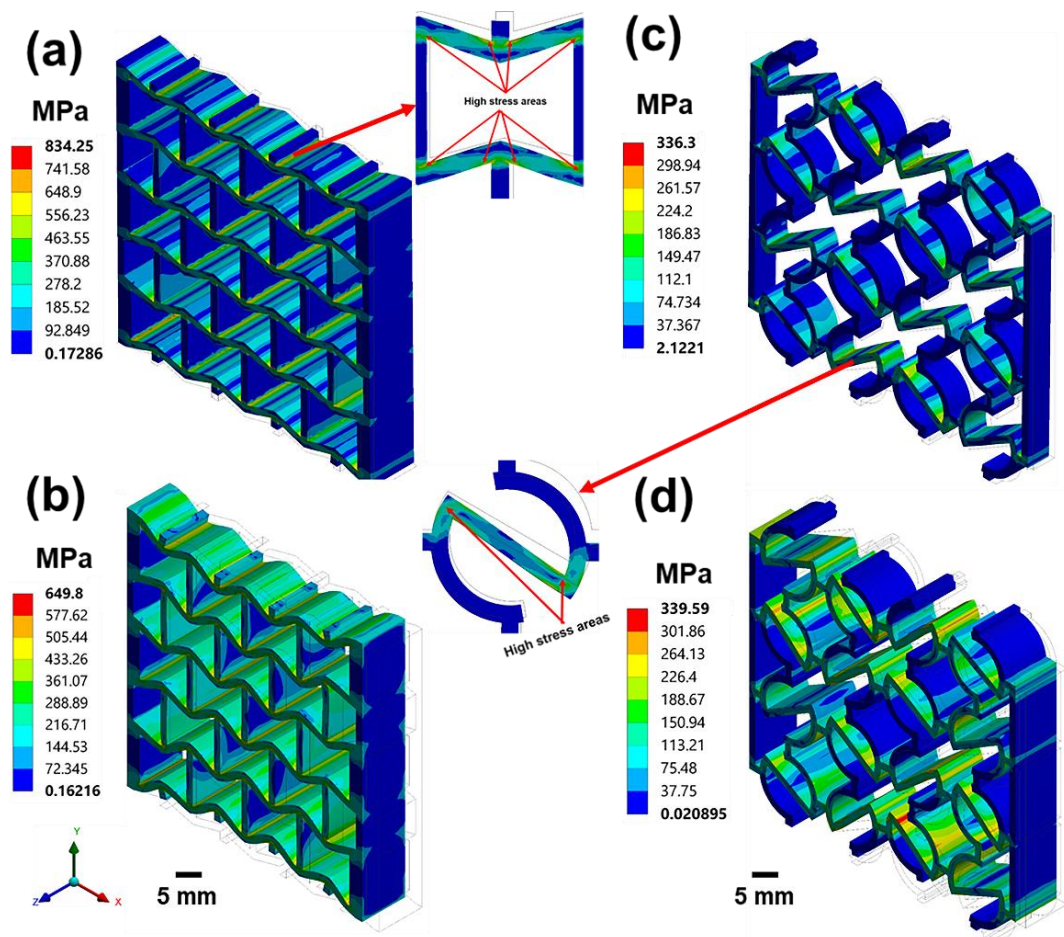


Fig. 5.9 Numerical simulation of re-entrant and S-shaped structures based on the linear ((a) and (c)), and non-linear ((b) and (d)) material conditions.

In the case of the re-entrant structure, the peak stresses are focussed at the sharp corners, leading to possible plastic deformation and subsequent row-wise collapsing as discussed above. On the other hand, the peak stress locations are shifted upward into the curved arm regions in the case of the S-shaped structures, leading to a possible reduction in the chances of failure. Also, this will lead to a more favourable deformation of the arch-type strut members, allowing for a combined deformation of the whole structure as one unit, as against each unit cell getting severely loaded and collapsing consequentially, as in the case of the re-entrant structure. The peak values of the lateral deflection are quite similar between the two structures, as may be observed by comparing Fig. 5.10 (a) and 5.10 (b), though the distribution patterns are drastically different, showing the more flexible S structures undergoing substantial deformation along the strut length of the unit cell.

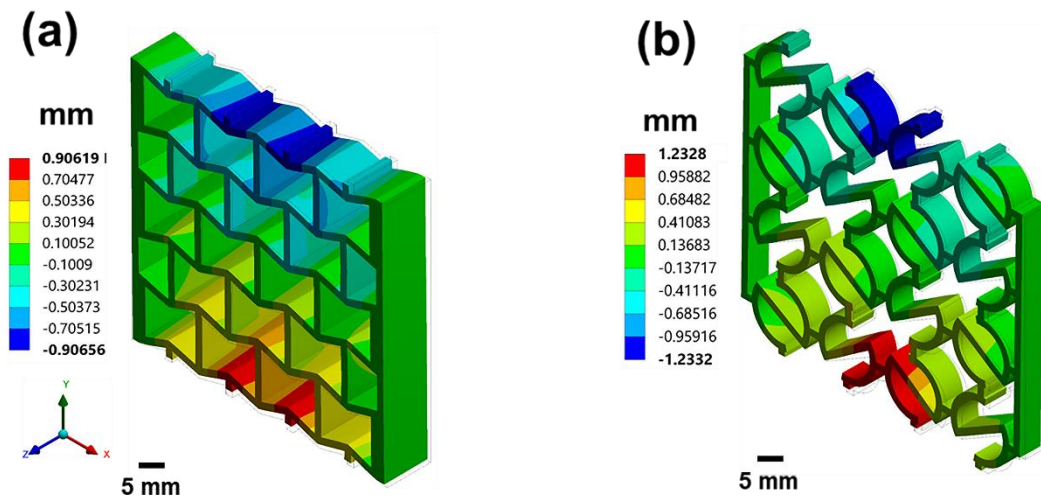


Fig. 5.10 Numerical simulation of obtained lateral defromation of the (a) Re-entrant and the (b) S-shaped structures for the same longitudinal load.

For a comparative evaluation of the experimental and numerical results obtained, the structural variations at different levels of deformation of the S structure captured from the experimental and the finite element simulation are juxtaposed in the images of Fig. 5.11. The top row is made up images of the structure taken during experimental deformation to varying levels of strain percentages, 0, 4.67, 9.31, 14 and 21.8. The bottom row images are extracted from the FE simulation of the structure at the corresponding strain levels. First, it may be noted that the overall deformation pattern obtained based on the FE simulation is very close to the experimentally observed patterns, with the S shaped structure collapsing within itself, as against the sideways deformation of the re-entrant structure (Fig 5.5 (a) – (e)). Poisson's ratios directly calculated based on the overall deformation of the central units in each case are inserted under each image for an easy and quick comparison. Though the actual values are not exactly matching with the experimental results, Negative Poisson's ratios are obtained from the FE simulation, with an average value of -1.2967, considering the central three levels of displacement loads. With the displacement strain reaching 21.8%, the experimental result indicates the flaps of most of the S unit cells touching and ready to collapse further. However, the FE simulation for this case indicates an early collapse of the structure, which is possibly due to the material property data not exactly matching with the laser melted experimental structure. Though the average material properties of the laser melted 316L parts are known, the complex geometry of the structure often leads to varying thermal cycles at different locations and possibly varying mechanical properties across the structure.

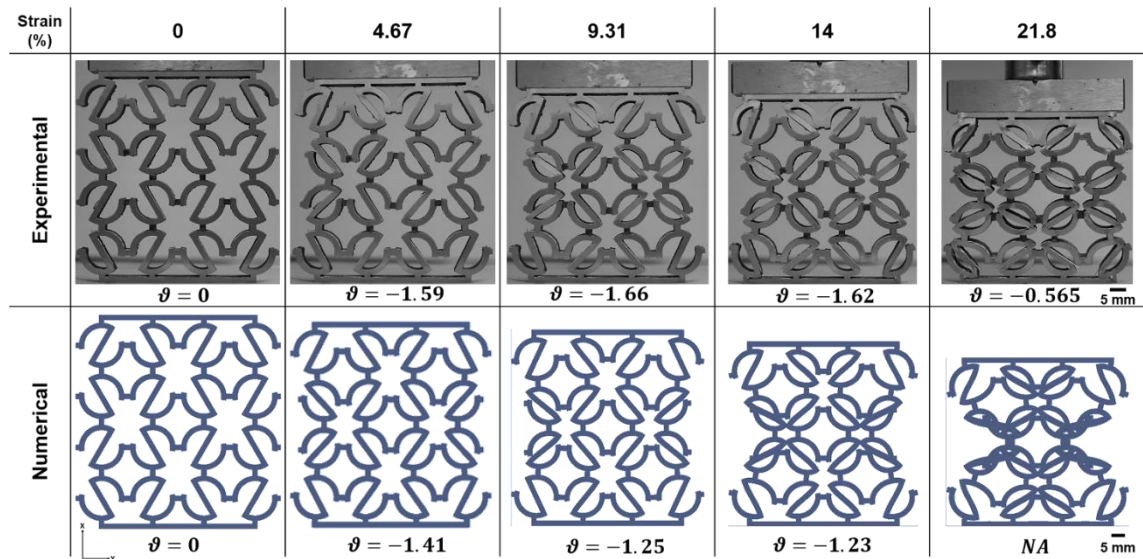


Fig. 5.11 Experimentally and numerically obtained deformation patterns of the S Structure at different levels of applied strains

A quantitative comparison of these results is attempted by considering the geometrical measurements based on the structural deformations obtained for the central three displacement cases corresponding to 4.67, 9.31, and 14% strains. Both θ_1 and θ_2 values are measured from the deformed structures based on experimental and numerical evaluations and then fed into the analytical models developed in order to calculate the Poisson's ratios. The average values of the Poisson's ratios obtained with the four central unit cells are presented in the bar graphs of Fig. 5.12, for a comparative assessment. Other than the first case (4.67% strain), where the Poisson's ratio calculated based on the numerical results is a trifle higher, both the experimental and numerical results are almost closely matching indicating the validity of the numerical evaluations undertaken.

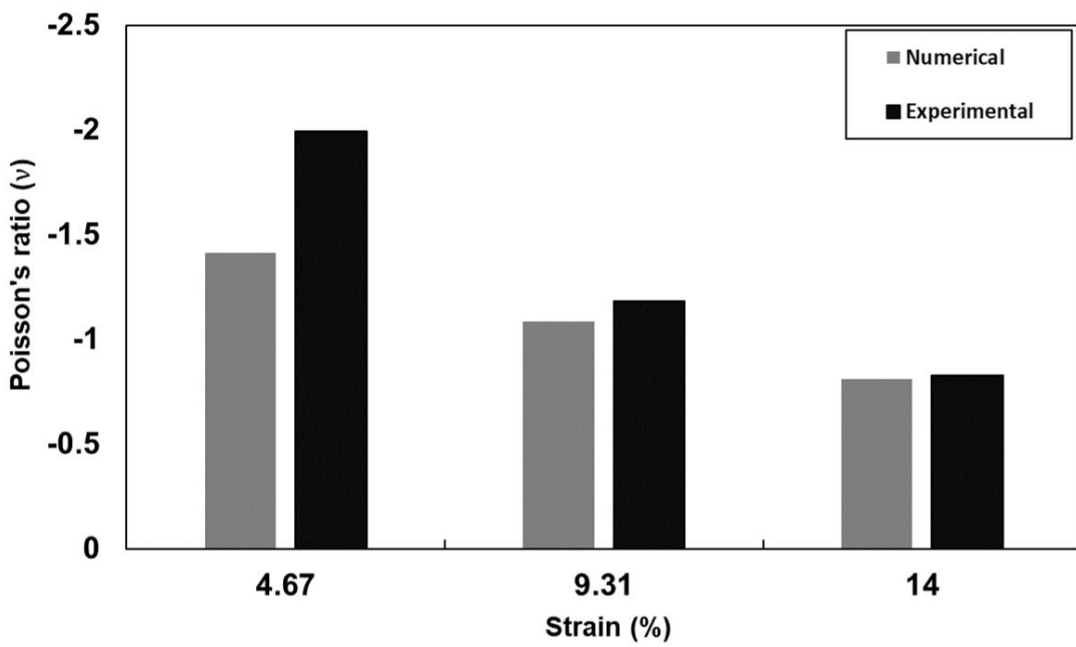


Fig. 5.12 Comparative sequence deformation modes of experimental and numerical analysis for the given applied strain

5.5 Summary of auxetic S-structure and stress concentration

A new auxetic structure based on a S-shaped unit cell was designed and analytically modelled. The auxetic responses were evaluated in comparison with a standard re-entrant structure by numerical, experimental and analytical means. Both the R- and S- structures were physically produced by selective laser melting of 316L stainless steel powder. Both the experimental and the numerical results proved the S-shaped structure to reduce the stress concentration effects, while also exhibiting better auxetic responses. The deformation responses of the S-shaped auxetic structure were far superior compared to those of the re-entrant structure, as there was no cracking and failure of the elements of the structure. The

re-entrant structures suffer from lateral displacement and row-wise collapsing, while the S-shaped unit cells share the deformation across the entire structure. The overall deformation modes and the higher auxetic nature over a large range of loading are the most promising features of the proposed new auxetic structure. However, the S-structure suffers from inferior mechanical properties (Young's modulus and compressive strength) compared to the re-entrant structure. Hybridisation is the possible means of enhancing the overall performance of the S-structures, while also exploiting the beneficial auxetic and stress concentration responses. This is the focus for the experimental and numerical work presented in the next chapter.

Chapter 6

Hybrid auxetic structures to enhance the in plane mechanical properties

6.1. Enhancement of the in plane mechanical properties

Comparative assessments based on experimental and numerical evaluations established the S-structures to be superior to the re-entrant ones, in terms of: (a) lesser stress concentration issues due to simpler geometrical features, (b) higher negative Poisson's ratios for larger ranges of applied strains, and (c) better deformation responses. However, the re-entrant structures outperformed the S-shaped structures with better mechanical properties, including higher compressive strength and Young's modulus values. In general, it may be pertinent to say that engineering applications require the overall performance of the structural solutions. Attempts have been made to enhance the in-plane mechanical properties of auxetic structures by inserting additional geometrical features.

Lu et al. (Lu et al. 2016) developed a novel 2D re-entrant model by inserting a narrow rib in the re-entrant structure. The numerical and analytical modelling of the re-entrant structure with the additional rib under tension was found to show the enhanced Young's modulus in both the directions (X and Y-directions). Ingrole et al. (Ingrole et al. 2017) modified an existing re-entrant auxetic structure by

introducing a split vertical strut instead of a simple vertical strut, and also developed two new hybrid auxetic structures by joining the conventional and re-entrant honeycombs together in a single structure. The finite element analysis and compression mechanical testing proved the modified re-entrant structure to possess higher compressive strengths and absorb higher total energy compared to the conventional honeycomb and re-entrant structures. However, the highest Young's modulus was obtained for the re-entrant auxetic structure. In the same lines, Fu et al. (Fu et al. 2017) embedded a rhombus shaped unit cell in the normal re-entrant hexagonal honeycomb structure to enhance the in-plane stiffness. Both the analytical and numerical analyses proved the resultant new honeycomb structure to be effective in overcoming the low stiffness limitation of the re-entrant cellular structure. To enhance the in - plane impact resistance, Wang et al. (Wang et al. 2019) introduced a new hybrid structure by combining the re-entrant and star shaped honeycombs in a single structure. The resultant geometric model was simulated numerically and validated by analytical models in impact testing with a range of velocities of striking. The simulation depicted the hybrid model to have higher impact energy absorption than the re-entrant and the star shaped honeycomb models for the same thickness and velocity.

The mechanical properties of any auxetic structure are as important as the ability to exhibit the auxetic behaviour. The foregoing discussion clearly elucidated that most of the previous work (Lu et al. 2016, Ingole et al. 2017, Fu et al. 2017 and Wang et al. 2019), was focused on enhancing the in-plane mechanical properties of the re-entrant structures alone. Comparatively, the S-shaped auxetic structure as introduced in Chapter 5, is more novel, and has the potential to outperform on

the basis of the stress concentration attributes as well as the auxeticity over a range of the applied strains. The main shortcomings are the low mechanical properties (Low Young's modulus and compressive strength) which are possible to be overcome by means of hybridising this structure. Structural modifications introducing a star shaped (Grima et al. 2005) re-entrant unit cell between two S-shaped unit cells, are proposed in this chapter, targeting to higher auxeticity as well as better mechanical properties. Both, the re-entrant hinging and flexure mechanisms of the star shaped re-entrant unit cells and the chiral (rotational folding and unfolding) deformation of the S-shaped unit cells will be crucial to dictating the overall deformation patterns and the mechanical properties of the hybrid structural models. Four hybrid models have been designed and analysed by numerical and experimental means and based on the results, an optimised hybrid model was identified with the best auxeticity and mechanical property responses.

6.2. Design, simulation and mechanical testing

6.2.1 CAD modelling

The unit cell model of the star shaped inclusion is presented in Fig. 6.1 along with the re-entrant and the S-shaped unit cells for easy understanding. The basic geometric formation of the re-entrant and the S-shaped unit cells in Fig. 6.1 (a) and (b) have already been discussed in Chapter 5. The shape of the star re-entrant unit cell is deduced from the simple re-entrant unit cell by protruding the vertical struts also inwards, the same way as the horizontal struts, at some angles. In the current design, the inclination angles of the horizontal and the vertical struts are kept the

same for the sake of symmetry. The geometrical dimensions of the S-shaped, re-entrant and star shaped re-entrant unit cells are as listed in Table 6.1.

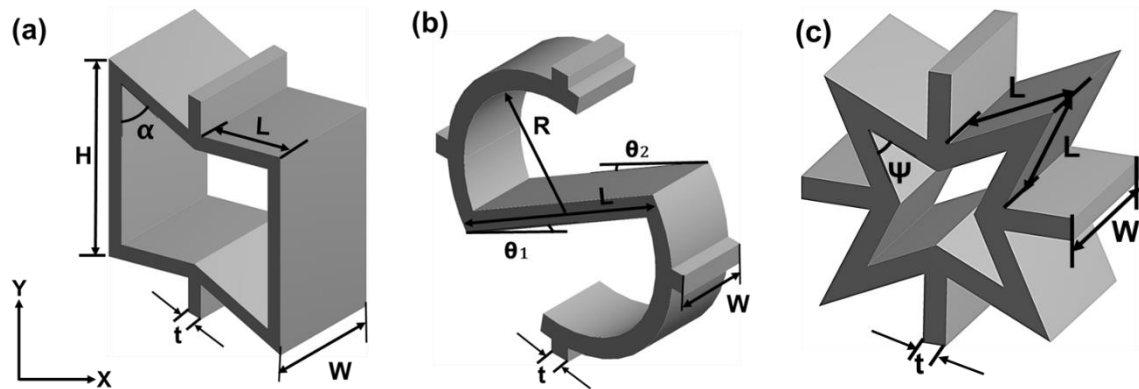


Fig. 6.1 The unit cell CAD models of (a) the re-entrant (b) the S-shaped and (c) the star shaped re-entrant designs

Table 6.1: Significant geometrical parameters of the unit cells

S-shaped				
L (mm)	R (mm)	θ_1 & θ_2 ($^{\circ}$)	t (mm)	W (mm)
10	5	30	1	7.5
Re-entrant				
H (mm)	L (mm)	α ($^{\circ}$)	t (mm)	W (mm)
10	5.17	75	1	7.5
Star- shaped				
L (mm)	Ψ ($^{\circ}$)	t (mm)	W (mm)	
4.97	40	1	7.5	

A total of 6 different models, including one re-entrant and one S-shaped structural designs were developed in SolidWorks 2016 and presented in Fig. 6.2. The 2D models of the re-entrant (Fig. 6.2 (a)) and the S-shaped (Fig. 6.2 (c)) structural models are designed in the same way as in Chapter 5 for the R- and S-shaped models. However, in this chapter, 5×5 unit cells are cross linked in the X- and Y-directions instead of the 4×4 cross linked structures as evaluated in Chapter 5. The other 4 hybrid structural models, were designed by introducing the star shaped re-entrant unit cells in between two consecutive S-shaped unit cells in different formats.

The first two hybrid models H1 (Fig. 6.2 (e)) and H1NC (Fig. 6.2 (g)) are designed by inserting one star shaped re-entrant unit cell in between two successive S-shaped unit cells in the Y-direction. In the case of the hybrid H1 model the star shaped re-entrant unit cell is all connected with the adjacent S-shaped and the other star shaped unit cells. In the other model, H1NC, the star shaped unit cell is connected with the adjacent S-shaped unit cells only, while the adjacent star shaped unit cells were left free. The other two hybrid models H2 and H2NC are depicted in Fig. 6.2 (i) and (k). In these models, the star shaped unit cells are sandwiched in between the S-shaped unit cells in the X- direction, as against the Y- direction employed in the H1 and H1NC models. Again, the star shaped re-entrant unit cells are connected with the adjacent S-shaped and also the other star shaped unit cells in the case of the H2 hybrid model, while they are only connected with adjacent S-shaped unit cells in the H2NC model.

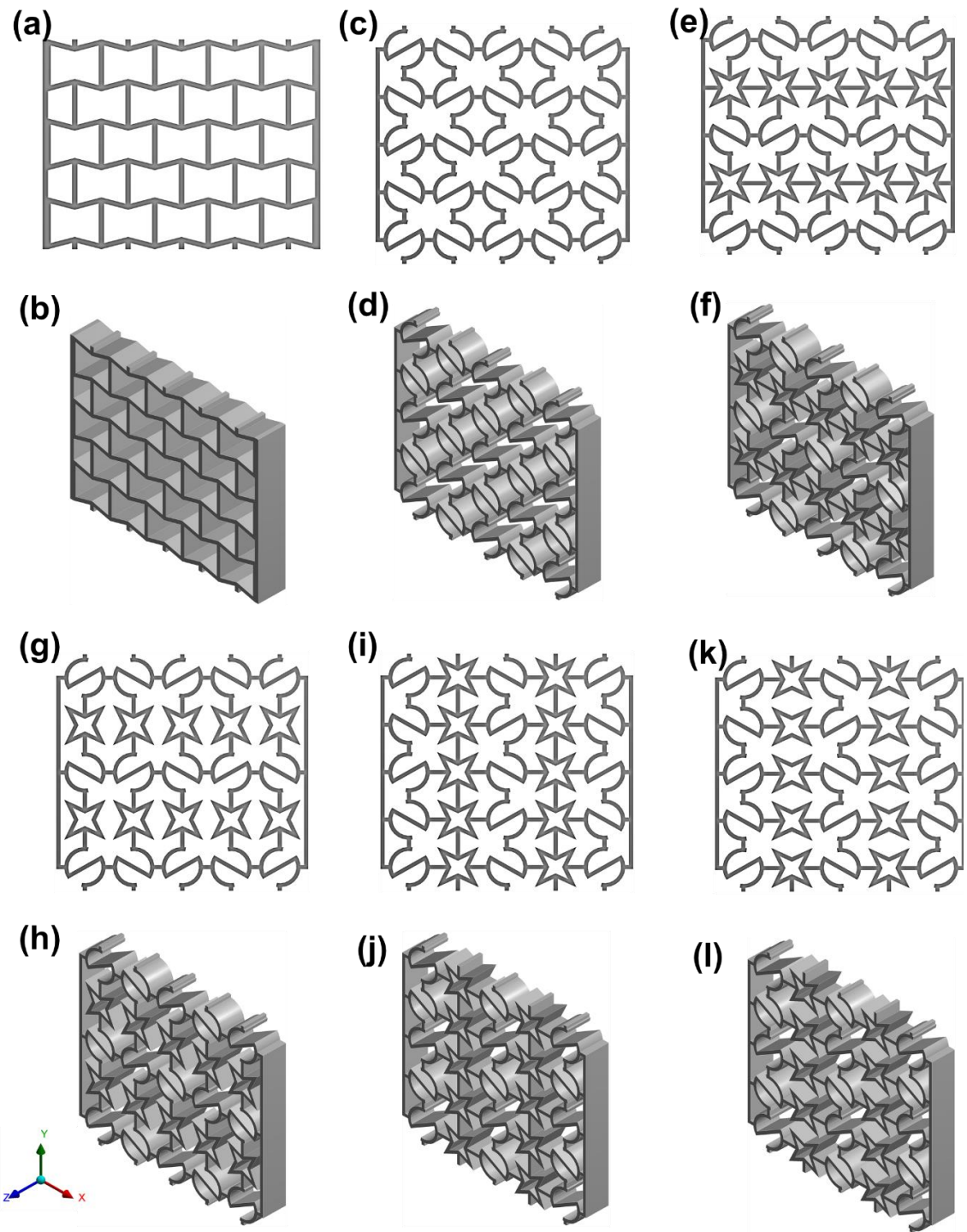


Fig. 6.2 The front elevation and the isometric rendering of the re-entrant (a & b), S-shaped (c & d), H1 (e & f), H1NC (g & h), H2 (i & j) and H2NC (k & l) structures.

The 2D forms as seen in the front elevation of each structure was first developed in SolidWorks sketching module and then the 3D forms were obtained by extruding through a depth of 7.5 mm along the Z-direction. A 1 mm thick plate of the same length and width as the actual models is attached at the top and the bottom of each of the structures, for better gripping during mechanical testing on the universal tensile testing machine. The isometric views of the CAD models of all the 6 structures are depicted in the Fig. 6. 2 (b), (d), (f), (h), (j) and (l). The overall dimensions of the re-entrant structure are 40.50 mm × 52 mm and for the other models including the S-shaped and all the hybrid models, the final dimensions are 58.75 mm × 60.75 mm.

6.2.2 Mechanical testing, measurements and numerical simulation

The fabrication by using selective laser melting, post-print processing, mechanical compression testing (displacement rate 2 mm/min) and the set-up of the camera to record the deformation under loading of all the samples were done in exactly the same manner as detailed in the Chapters 3. In the current analysis, the overall deformations of the samples i.e. overall lateral and longitudinal deformations under loading were taken into consideration instead of the internal deformations of specific marked unit cells, as was the case with the evaluation presented in Chapter 5. Some of the samples (H1, H1NC, H2 and H2NC) in this chapter are of hybrid in nature i.e. having more than one unit cell in the structure and those unit cells are connected in different ways to the adjacent unit cells. The two different unit cells dictating the deformation of the overall structure have differential individual

deformation patterns (re-entrant and chiral type of deformations) under loading. Due to these differential deformation responses of individual unit cells and the propagation of the same into the overall structure as influenced by the connection patterns, measurements on individual cells and calculation of Poisson's ratios based on localised deformations could be misleading. In order to maintain consistency and for comparative evaluation, the longitudinal and lateral displacements of the overall structure are measured. The average lateral displacement of the three middle columns of any model as depicted in Fig. 6.2, is considered as the lateral deformation to be used to calculate the Poisson's ratios of the models.

The numerical simulation of all the samples were carried out based on the ANSYS Workbench 16.2 software platform. The finite element discretisation of all the structural models and the overall applied boundary conditions are shown in Fig. 6.3. The inset diagrams present a closer look at the tetrahedral finite elements used for discretising the problem domains. A displacement based compressive load to a maximum extent of -5 mm was applied in the X direction to simulate the compressive loading conditions. The Peak Von-Mises stresses and the lateral displacement results for the specific loading conditions are the critical responses, as will be discussed later in this Chapter. The size of the tetrahedral element is uniformly kept at around 0.50 mm, based on the results of a mesh convergence analysis undertaken for all the structural models. The element uses a liner interpolation scheme to evaluate the displacements within the elements, based on the nodal displacement values.

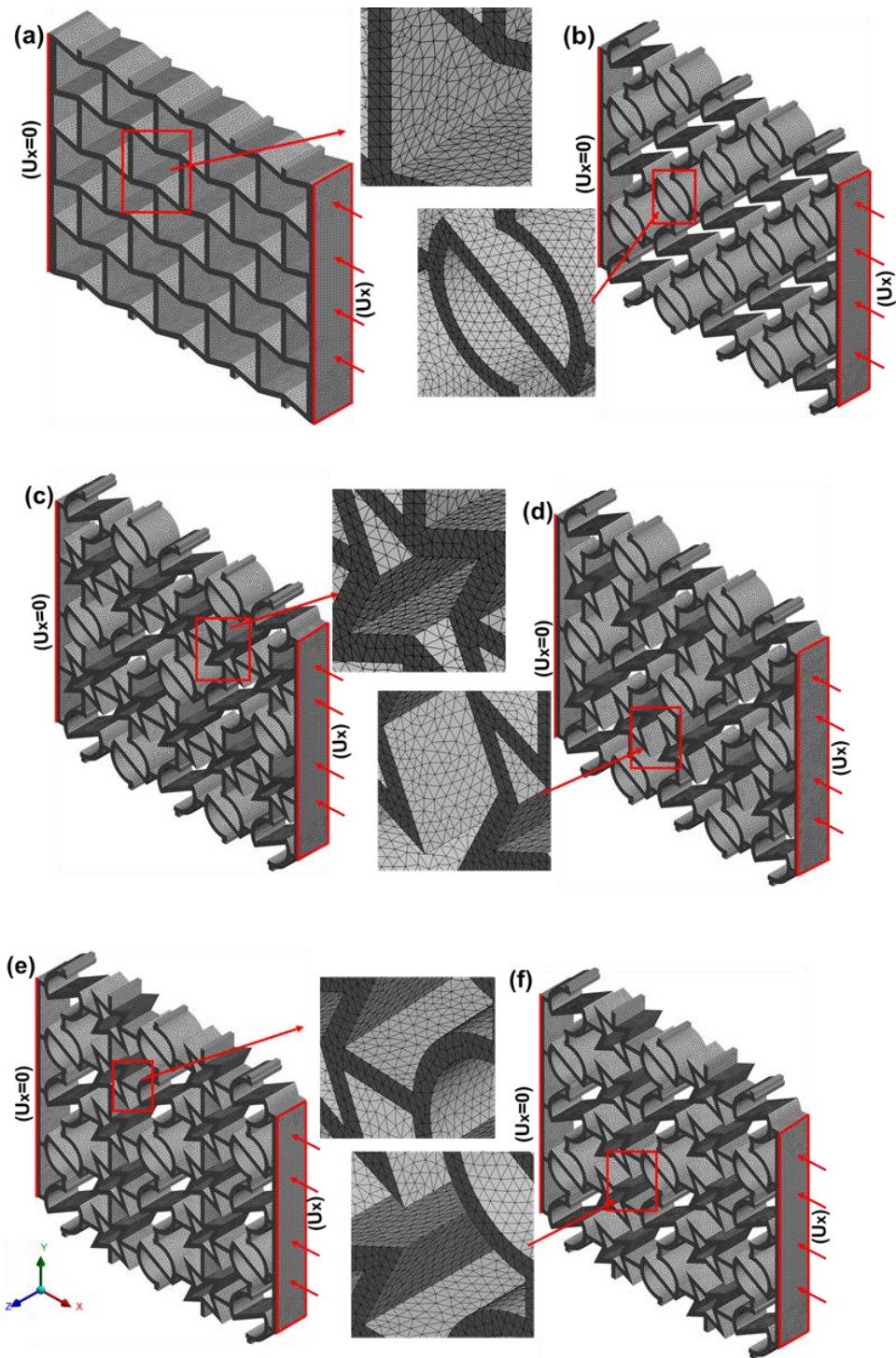


Fig. 6.3 Finite element mesh and boundary conditions applied on (a) Re-entrant and (b) S-shaped (c) Hybrid H1 (d) Hybrid H1 NC (e) Hybrid H2 (f) Hybrid H2 NC structures

6.3. Results and discussion

6.3.1 Deformation modes

The deformation patterns of the re-entrant, the S-shaped and the hybrid structures subjected to the displacement-controlled compression loading are presented in Fig. 6.4. These were based on images taken by the Nikon camera mounted in front of the loaded specimen at intervals of 5 mm of displacement. The re-entrant and the S-shaped models as shown in the first (re-entrant model) and second row (S-shaped) of Fig. 6.4 depicts the sideways and the within collapsing deformation patterns respectively. Similar deformation patterns were also noted in Chapter 5 for the re-entrant (R) and the S-shaped (S) models and the detailed deformation mechanisms of both the models were already discussed in Chapter 5. It may be pertinent to clarify here that the additional unit cell as employed here (5 instead of 4) compared to the structures evaluated in the Chapter 5 did not impart any significant changes to the ways both the structures deform under the compression loading.

The third and the fourth rows of Fig. 6.4, depict the deformation patterns of the H1 and H1NC hybrid models respectively. Both models almost followed the same within collapsing deformation patterns of the S-shaped model as evident from the second and third row. The connections between the star re-entrant unit cells with the adjacent S-shaped unit cells in both the structures are crucial in deciding the deformation modes in both the cases. The geometric configurations of the H1 and H1NC models are such that the lateral (+Y and -Y direction) outer boundaries of

are formed by the S-shaped unit cells, while the columns of the star re-entrant unit cells in both the cases (H1 and H1NC) are sandwiched between the columns of S-shaped unit cells and are also aligned with the loading direction (X- direction). Under loading, the star re-entrant unit cells in the H1 model, attempt to contract i.e. angle Ψ tends to decrease due to the lateral and longitudinal hinging and flexing emanating from the bending of the cell walls of the unit cells. However, the strong adjacent lateral pulling from the rotational inward deformation of the curved members of the linked S-shaped unit cells does not allow the star re-entrant unit cells to contract under the influence of the applied load. However, with the increased load the star re-entrant unit cells start touching each other in their respective columns and gradually get locked. On the other hand, the outer curved parts of the S-shaped unit cells at the lateral boundaries start moving inward and the structure assumes an overall concave shape. On further increasing the load, the columns of the star shaped re-entrant unit cells slowly start moving towards a side (Wang et al. 2019). However, the overall deformation of the structure is controlled by the deformation pattern adopted by the S-shaped unit cells at the boundaries and therefore, the H1 hybrid model largely follows the within collapsing deformation pattern, irrespective of the sideways deformation of the internal star shaped unit cells.

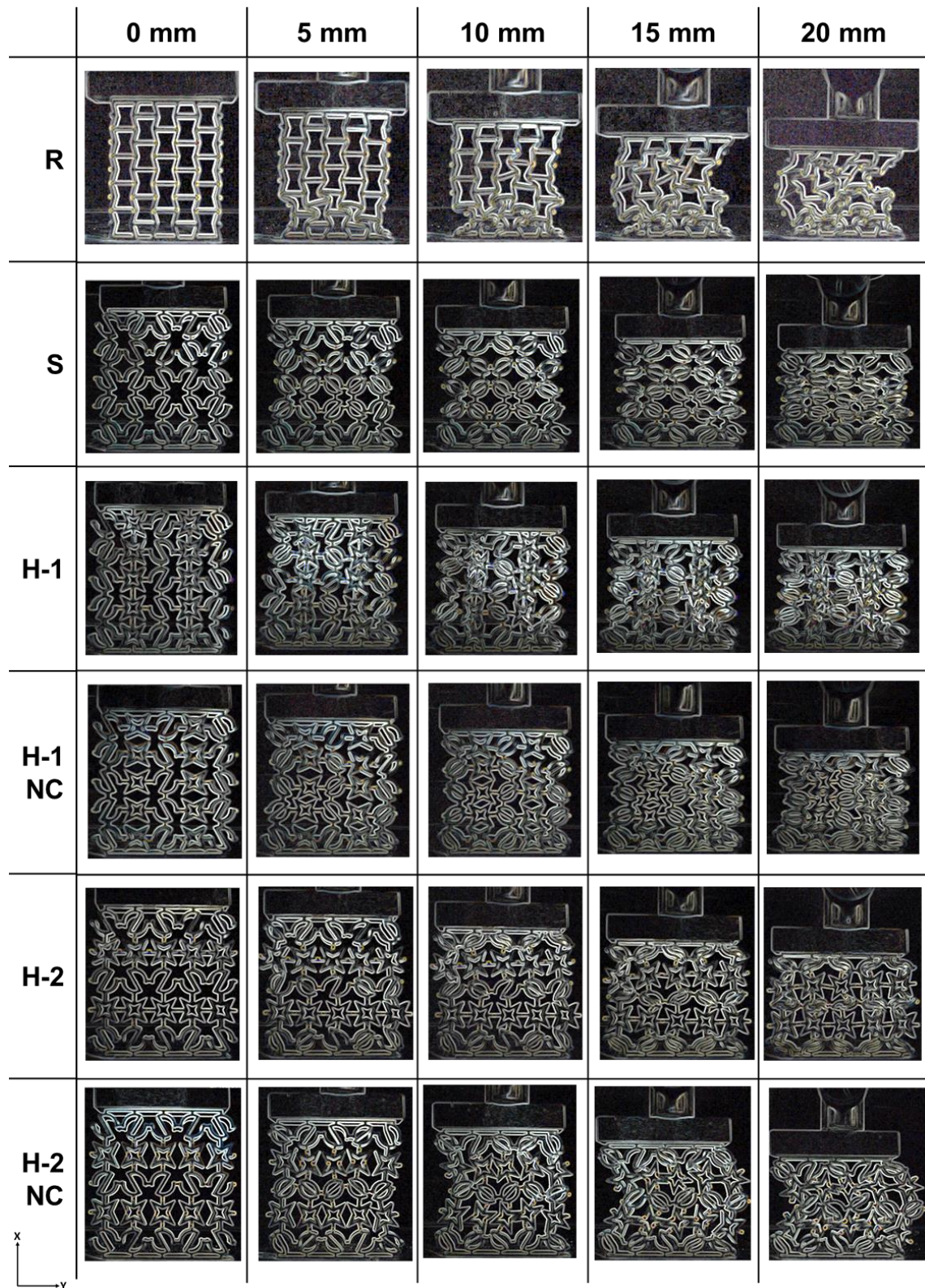


Fig.6.4 Deformation modes of the re-entrant, S-shaped and hybrid auxetic structures

The deformation pattern of the H1NC model is also the same as that of the H1 model. However, the absence of the connecting links between the successive star re-entrant unit cells in their respective columns offer substantial unconstrained free sideways movement of the star re-entrant unit cells as a result of the pulling from the adjacent S-shaped unit cells. A sideways movement of the star re-entrant unit cells can be observed in the fourth row of H1NC model in Fig 6.4. However, in this case also the overall outer deformation of the H1NC model is controlled by the S-shaped unit cells at the lateral boundaries, following the within collapsing deformation pattern of the structure.

The deformation patterns of the other two hybrid structures, H2 and H2NC are depicted in the fifth and the sixth rows of Fig. 6.4. In both the cases, the overall deformation patterns of the structures are also controlled by the unit cells at the lateral boundaries. Unlike the previous two hybrid models (H1 and H1NC), the outer boundaries of these two models (H2 and H2NC) are formed by both the star re-entrant and the S-shaped unit cells and hence the deformation patterns of the models are controlled by both these unit cells. In the case of the H2 model, as seen in the fifth row of Fig. 6.4, the S-shaped unit cells at the lateral boundaries of the model start moving inward by rotational deformation action under loading. On the other hand, the star re-entrant unit cells have deformed by the hinging and flexing actions and the simultaneous gradual shifting towards a side, instead of a lateral inward movement, due to the typical geometric features. However, the sideways movement of the star re-entrant unit cells is restricted by the strong pull created by the adjacent S-shaped unit cells due to their rotational deformation action. Consequently, the H2 model adopts the within collapsing deformation mode like

the S-shaped, H1 and H1NC models. In the case of the H2NC model as depicted in the sixth row of Fig. 6.4, there are no connecting links in between the star shaped unit cells as in the case of the H2 model. For the initial loading condition, the sideways movement of the star re-entrant unit cells at the outer boundaries is controlled by the pull created by the deformation of the connected S-shaped unit cells. As a result, the overall deformation is within the collapsing type. However, as the load increases, the unconstrained movement of the star re-entrant unit cells becomes quite significant and the unit cells adopt a sideways movement. At the end, the sideways movement of the star shaped unit cells becomes dominant to impart the overall sideways deformation pattern of the whole H2NC structural model.

6.3.2 Mechanical characterisation

Stress strain curves

The nominal stress-strain curves, depicting the elastic-plastic deformation of all the six models (R, S, H1, H1NC, H2, and H2NC) are presented in Fig. 6.5. The coding E1, E2 and E3 in each plot represent the 3 repetitions carried out for each structural model. The stress-strain patterns of the re-entrant (R) in Fig. 6.5 (a) and the S-shaped (S) in Fig. 6.5 (b) models may be noted to be the same as was the case in the results of Chapter 5. However, due to geometrical differences (number and sizes of unit cells) the extent of linear stress-strain regions of both the models (R and S) are different from the same (R and S) models evaluated in Chapter 5. The results based on the R structural model as in Fig. 6.5 (a), the linear stress-strain

region extended up to 35 MPa, which is the highest among all the other models. However, beyond the yield point, the stress values got reduced up to 22-23 MPa, and further stabilised almost from 15% to 35% of the applied strains (Ingrole et al. 2017).

The relatively higher values of the generated stresses in the linear stress-strain region of the re-entrant structures compared to the other samples depict the design complexity leading to more number of critical corners or joints and associated stress concentration issues (Wang et al. 2015). The stress-strain curves based on the S-shaped structure as seen in Fig. 6.5 (b), resulted in the stress values of around 6 to 7 MPa within the elastic region, which is almost one fifth that of the re-entrant (R) structures.

Beyond the yield point, there is a certain degree of waviness probably due to the interchanging of the deformation from one cell to the other within the overall structure based on the S-unit cells. However, the curves depict a steady rise in the stress values up to almost 22 MPa and then stabilising at that level. The peak stress generated in the re-entrant structure was almost at around 35-40 MPa, which is as already noted, five times more than the stress generated in the S-structure for the same applied loads. This is again, as explained in Chapter 5, mostly due to the reduced stress concentration effects of the relatively simpler S-shaped geometry.

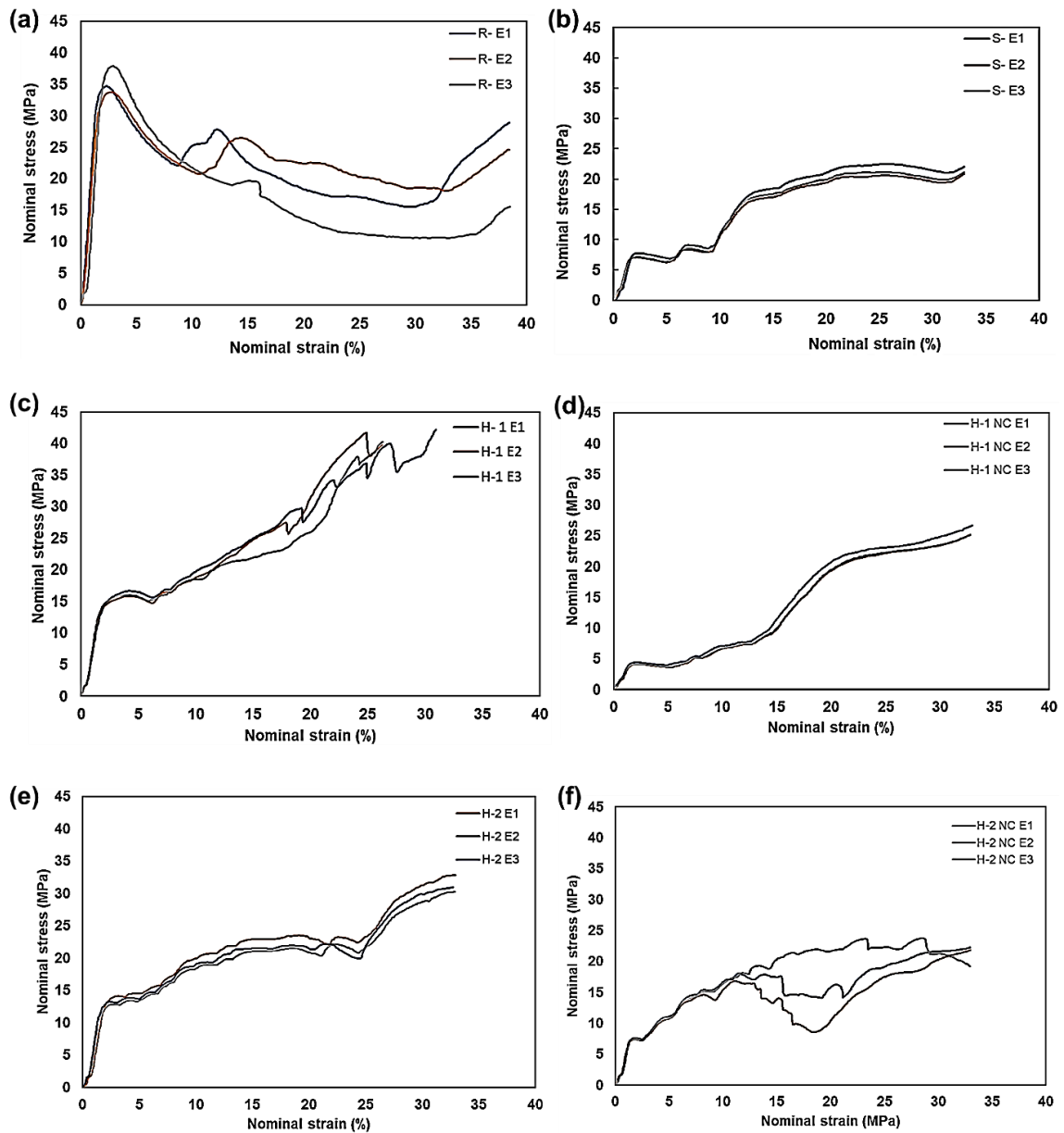


Fig. 6.5 The nominal stress-strain curves for (a) re-entrant (b) S-shaped (c) H1 (d) H1NC (e) H2 (f) H2NC structures

The stress-strain graphs of all the hybrid structural models including H1, H1NC, H2 and H2NC models in Fig's. 6.5 (c), (d), (e) and (f) followed the same pattern as of the S- shape structure in the linear stress-strain region. However, the yield point

stresses varied from one model to the other, depending on the specific geometrical features. In the case of the H1 hybrid model, the linear stress-strain region is extended up to 15 MPa. Beyond the yield point, the stress values of the H1 model gradually increased with strain levels increasing from 6% to up to 35%. The star re-entrant unit cells in the H1 model are aligned with the load direction (Fig. 6.4, third row) and with the increasing load, these cells are stressed more than the S-shaped unit cells due to the geometrical complexities. Consequently, the stress-strain curves are showing a tendency to rise continuously unlike the other structural models, in which, the stresses stabilise towards the higher limits of the applied strains. The S-shaped unit cells at the boundaries of the H1 hybrid model mostly contributed to maintain the within collapsing deformation pattern as depicted in the third row of Fig. 6.4.

The linear stress-strain region of the H1 NC model in Fig. 6.5 (d) is the shortest among the other models with a limiting yield stress of around 5 MPa. The overall stress-strain pattern of the H1NC model followed the same pattern as exhibited by the H1 and S-shaped models. In the case of H1 model, the star unit cells are connected by a link, while in H1NC, there is no such connectivity which results in a lack of transfer of the load from one star re-entrant unit cell to the other. Consequently, the stress values are lowered slightly beyond the yield point, but, as the star-re-entrant unit cells come together under the load, they offer resistance to the further movement due to interference and lead to increased stress levels in the cells. This has been the probable cause for the increasing stress levels beyond the 15% limit of the applied strain.

The linear stress-strain region of the H2 hybrid model is extended up to a yield limit of 12-13 MPa almost close to the values obtained with the H1 structure. Beyond the Yield point, the stress-strain curves showed a gradual rise, but, for the large part of the applied load i.e. from almost 13% to 23% of the applied strain, the stress values are constant which could be due to the gradual collapsing of the rows of the S-shaped unit cells arranged perpendicular to the load direction. However, as soon as the star re-entrant unit cells take over the load further to the collapsing of the S-shaped unit cells, and the stress-strain curves begin to rise again. It may be noted here that the hybrid structural model H1 and H2 having star re-entrant unit cells connected with both the adjacent unit cells contributed to enlarge the stress-strain region for both the hybrid models. However, the H1NC and H2NC models also having star unit cells and sandwiched between the S-shaped unit cells have not deformed actively under the externally applied strains. The S-shaped unit cells in both the cases are the only active unit cells and thus play significant roles in determining the shape of the stress-strain curves. Beyond the yield point, the H2NC model followed the same stress-strain pattern as that of the H2 model, with the stress values rising gradually with increasing strains. However, as soon as the star re-entrant unit cells become dominant in taking up the load, the whole structure adopts to the sideways movement due to the unrestricted free movement of the star re-entrant unit cells. This results in the lowering of the stress values as in the case of a re-entrant model, as the strain values applied are from 13% to 20%. Beyond the 20% strain limit, the stress values continuously increased with increasing strains, most probably due to the complete crumbling and densification of the S-shaped unit cells.

Young's modulus

The Young's modulus extracted from the linear region of stress-strain graphs obtained from all structural forms (R, S, H1, H1NC, H2 and H2NC) are presented as the bar charts in Fig 6.6. The highest Young's modulus is obtained with the re-entrant (R) structural model, followed by the H1 and H2 structures. The re-entrant model performs absolutely better in the linear stress-strain region, compared to other models. However, beyond the yield point, the structure starts adopting the sideways deformation pattern (Fig. 6.4, first row) which will eventually reduce the auxeticity of the re-entrant model as will be ascertained further in the next section. It may be noted here that the Young's modulus values of the H1, H2 and H2 NC models are better than the parent S-shaped model.

The inclusion of the star re-entrant unit cells in the H1, H2 and H2NC models appear to resist the deformation of the hybrid models and thus increasing the strength of the overall structure against the applied strain. This is similar to creating obstacles such as inclusions, defects, or dislocations that cause hindrances and help elevate the resistance of the material to deform under the action of external applied loads, though at a macro scale. However, the S-shaped unit cells in the S and other hybrid models deform with ease against the star re-entrant unit cells and play pivotal roles in deriving the auxeticity of the structures as would be discussed later in this chapter. The H1NC model attained the least Young's modulus value. The missing connecting link in the case of the H2NC model between adjacent star re-entrant unit cells allowed the free lateral movement which reduced stiffness

through the structure and resulted in the reduction of the Young's modulus of the overall structure.

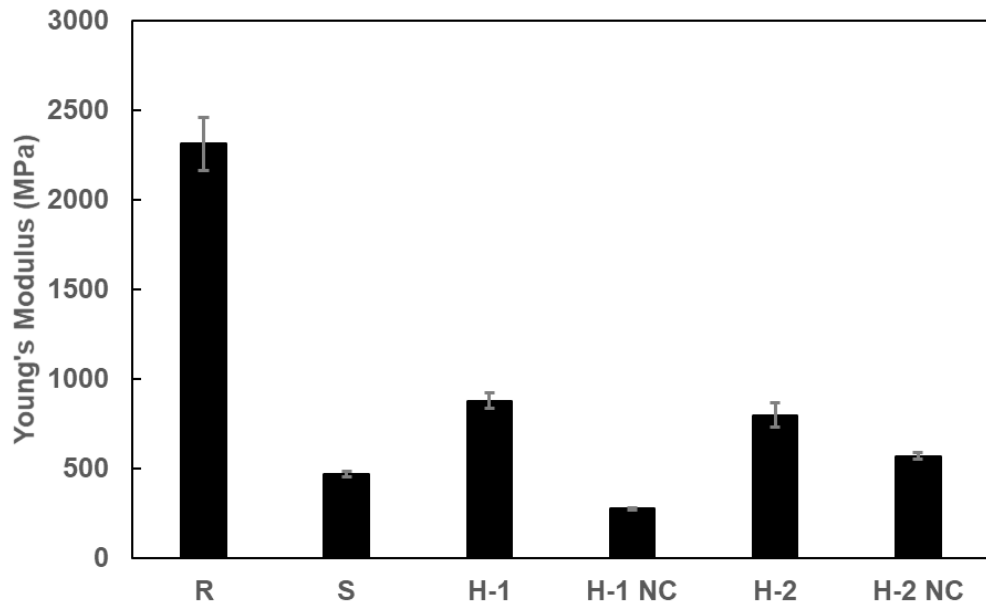


Fig. 6.6 Comparative levels of Young's modulus responses of the R, S and hybrid structural models (H1, H1NC, H2 and H2NC)

Compressive strength

The compressive strength values presented in Fig. 6.7 indicate that the re-entrant structure scored 1.5 times more compressive strength compared to the S-structure. Similar trend was also noticed from the compressive strength results based on the re-entrant structure with four unit cells as discussed in Chapter 5. Next, it may be noted that the compressive strength values increased when the S-shaped structures are hybridised in the H1 and H2 forms as evident clearly from Fig. 6.7. In fact, the compressive strength is the highest with the H1 hybrid model, clearly

showing better performance than the re-entrant structure. The compressive strength of the H2 hybrid model is also at comparable levels to the re-entrant structural model. Reiterating once again, the re-entrant structures are rigid, and the S-shaped structures are softer and flexible. Naturally, the compressive strength is higher with the re-entrant models compared to the S-models. With hybridisation, the presence of the re-entrant star unit cells in between changed the deformation mechanics of the S-shaped structures towards a more rigid framework. The modulus of elasticity in Fig. 6.6, though increased to a degree with the H1 and H2 models, compared to the S-shaped structure, the changes are not as dramatic as with the compressive strength responses. This is mainly due to the fact that within the elastic limit, the role of the star-unit cell inclusions is minimum as their presence becomes more apparent only within the plastic deformation zone, when the cells start physically aligning against each other.

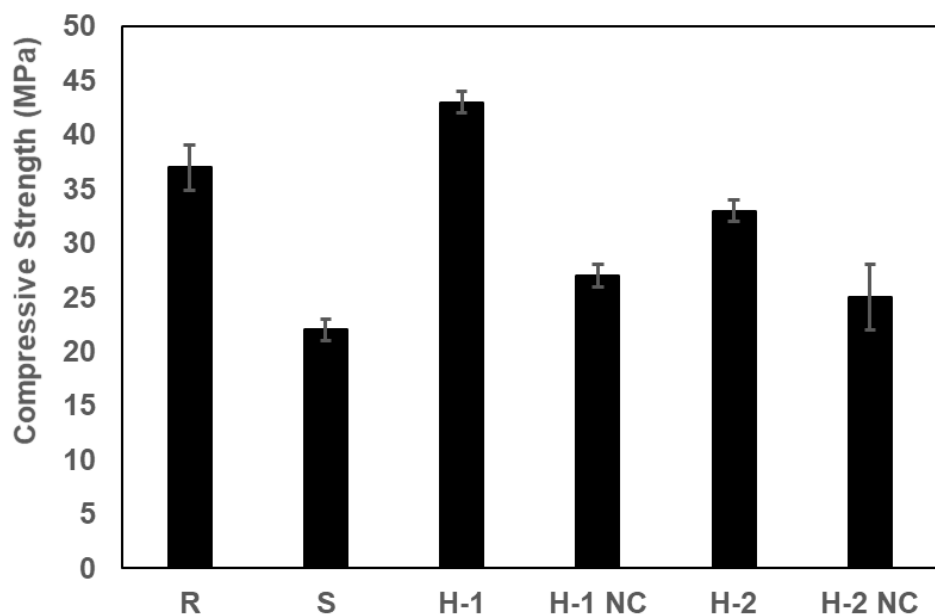


Fig. 6.7 Comparative compressive strength representation of R, S and hybrid structural models (H1, H1NC, H2 and H2NC)

Poisson's ratio

The Poisson's ratio values calculated with each structure are plotted against the nominal strain values and presented in the graphs of Fig 6.8. Incidentally, the differences between the Poisson's ratios exhibited by both the re-entrant (R) and the S-shaped (S) structural models at around -2 at the start of the loading are not too widely different, compared to the responses reported in Chapter 5. These variations are mainly emanating from the differences in the methods adopted for assessing the Poisson's ratio and also possibly due to the increased number of unit cells used to construct the structures evaluated here. The overall deformation values, i.e., the total lateral and longitudinal deformation responses of the samples are taken into consideration in the current case as against the deformation of internal unit cells. As the applied load increases, the negative Poisson's ratio instantly falls from -2 to almost about -0.9, which is attributed to the sideways deformation of the re-entrant structure with the increasing load as shown in Fig. 6.4, first row. On the other hand, the S-shaped structure (S) responded with a gradual decrease in the values of negative Poisson's ratio. The S-shaped structure maintained a great auxetic behaviour from the start to almost 20% of the applied strain, unlike the re-entrant structure (R), which drastically lost most of the auxetic nature by around 10% of the external applied strain. However, both the structures (R and S) reached to approximately zero Poisson's ratio at the maximum load conditions.

The Poisson's ratios obtained with the H1 and H1NC hybrid models were close to -1.3 which then gradually decreased with the increasing load conditions. Both the structures (H1 and H1NC) maintained good auxetic nature from the start to almost 15- 20% of the external applied strain. The auxeticity of both the structures is lesser though, compared to that of the parent S-structure. The replacement of the S-shaped unit cells by the star re-entrant units in the hybrid models though helped elevating the mechanical responses, these improvements came at the cost of losing some of the auxeticity. The crumbling of the unit cells and the ensuing densification across the structure cause the loss of auxeticity at higher loading conditions.

The H2 model resulted in a maximum auxeticity at Poisson's ratio -0.8, which then gradually decreased with increased external load, as evident from Fig 6.8 (C). This is the least auxetic of all the structures evaluated. The difference between the H1 and H2 structural models is the direction in which the star re-entrant cells are inserted; second and fourth columns in H1 as against the second and fourth rows in H2 (Fig. 6.4 third and fifth rows). As a result, the star unit cells became part of the lateral boundary in H2 and adversely affected the auxetic responses. Evidently, the S-shaped unit cells mainly contribute to the auxetic transformations, while the star-unit cells add to the mechanical responses. Further, the geometric placement of the two different unit cells within the overall will also play significant roles in controlling the overall performance of the structure depending on the direction of loading. The particular configuration in H2 led to the least auxetic response of the structure, while its mechanical performance was better than that of the S-structure and almost close to that of the R structure (Fig. 6.7).

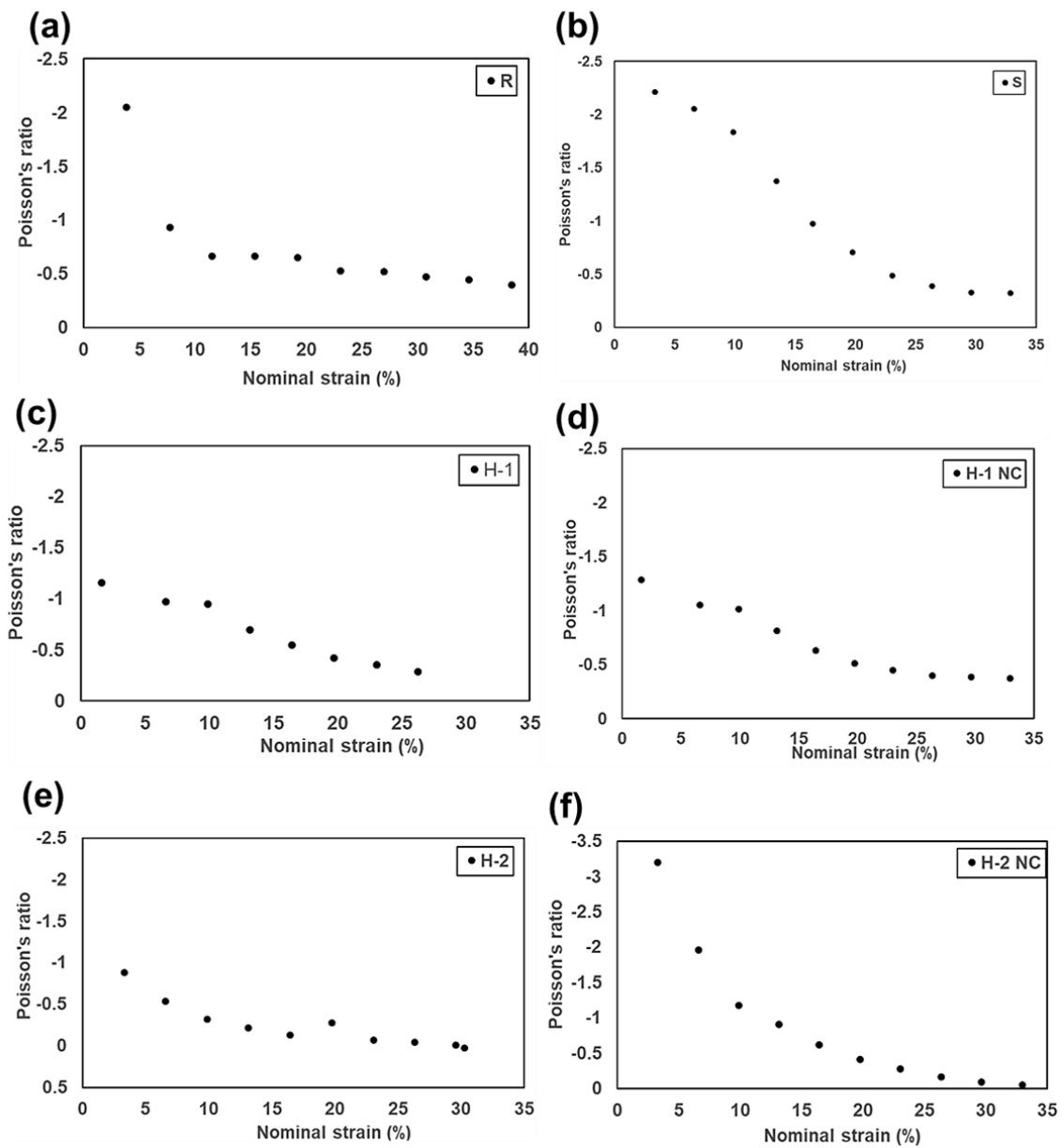


Fig. 6.8 Poisson's ratio vs nominal strain plots for (a) re-entrant (b) S-shaped (c) H1 (d) H1NC (e) H2 and (f) H2NC structures

A strikingly different response is evident from the Poisson's ratio distribution obtained with the H2NC structure as presented in Fig. 6.8 (f). Despite the fact that the star re-entrant cells are at the lateral boundaries, the structure resulted in a Poisson's ratio of -3.0, which then decreased gradually, with the increasing external strains. An almost hyperbolic variation is evident in Fig. 6.8 (f). The fact that the star units are not connected led to this differential response in the lateral displacement of the overall structure. In the absence of the cross-connecting members, the star cells are mainly pushed inwards, due to the deformation of the S-unit cells under the action of the applied load, up to a certain extent. As a result, the star cells moved inwards, at relatively lower external strains applied, and resulted in the higher auxetic performance of the structure. Gradually, the star cells get closer, and begin to restrict the inward deformation of the structure. Further, due to the differential orientations of the S structures at the lateral boundaries, the deformation pattern gradually attained a concave shape on the left most boundary, while it is a convex deformation on the right boundary as may be noted in Fig. 6.4, sixth row. This will eventually lead to a sliding of the structure in a particular preferred direction as dictated by the relative placement of the two unit cells and a loss of the auxeticity.

6.3.3 Numerical simulations

The Von-Mises stress distribution patterns obtained by the finite element evaluation of the re-entrant (R), S-shaped (S) and the hybrid structural models H1, H1NC, H2 and H2NC are depicted in Fig. 6.9. The blue colour indicates areas of

lower stresses, while the teal blue and yellowish areas are the more significantly stressed zones. It may be observed from Fig 6.9 that the stress patterns in all the models (R, S, H1, H1NC, H2, H2NC) are concentrated at the critical junctions (greenish yellow colour) of the different unit cells, though with varied peak values of the Von-Mises stress. The highest value of the Peak Von-Mises stress was obtained for the re-entrant model followed by the H2NC and H2 models. The star re-entrant unit cells used in the hybrid structures influenced the stress distributions to varying extents, depending on the overall structural formats.

Quantitatively, the re-entrant structural design model is stressed almost 1.25-1.75 times higher than the S-shaped and the other hybrid models, for the same loading conditions, reaching a maximum Von Mises' stress of around 835 MPa at the peak stress locations. The H1 hybrid model, despite the presence of the star re-entrant unit cells, is less stressed compared to the S-shaped structural model. It is pertinent to point out here that the inclusion of the star re-entrant unit cells in the H1 model has contributed to enhance the Young's modulus value, surpassing even the compressive strength of the re-entrant model, as discussed in section 6.3.2. The hybrid models H2 and H2NC in which the star re-entrant unit cells are sandwiched between the S-shaped unit cells perpendicular to the loading direction, attained higher levels of Von- Mises stresses, compared to the S- shaped and the other hybrid models (H1 and H1NC).

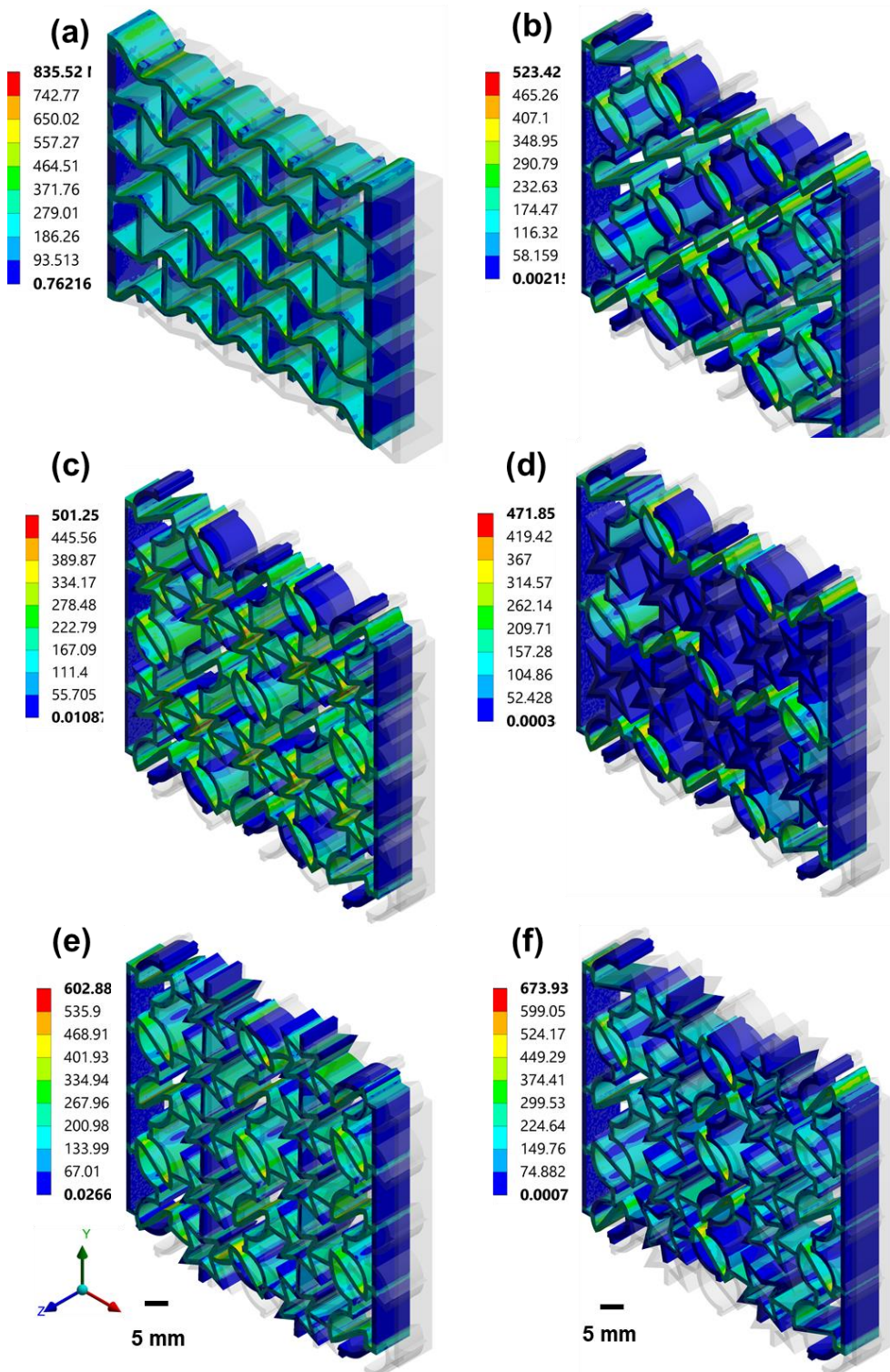


Fig. 6.9 Von Mises stress distribution patterns in the (a) R, (b) S, (c) H1 (d) H1NC (e) H2 (f) H2NC structures based on the non- linear material conditions

Both rows of the star re-entrant unit cells in H2 and H2NC models are oriented perpendicular to the direction of the load. Under loading, the 4 unit cells of each row take the load directly from the top S-shaped rows and as a result, all the star re-entrant unit cells are stressed to a greater extent. This has also led to a stress build up in the whole structure, as compared to the H1 and H1NC models. The star re-entrant unit cells in H1 and H1NC models are in line with the direction of loading and only the unit cells which are directly in contact with the loading plate are stressed to a significant extent. This has also led to the stressed zones being confined to these elements, as the pathways for the propagation of stress into the other areas of the overall structure are limited. The least Von-Mises stress at around 471 MPa, is obtained for the H1NC model as depicted in Fig. 6.9 (d), due to the absence of the cross-linking elements and the unconstrained lateral movement of the star re-entrant unit cells, apart from their alignment along the loading direction (X-direction). These numerical simulation results depicting the stress distribution patterns further confirmed the nature of the re-entrant structures getting stressed more severely than the S-shaped as well as all the other hybrid models analysed as a result of the geometrical complexities.

The deformation patterns of all the structural models (R, S, H1, H1NC, H2, H2NC) obtained from both the experimental and numerical simulations are presented next to each other in Fig. 6.10, for easy comparison. The results in Fig. 6.10 correspond to the deflection condition, equivalent to a -5 mm displacement or the strain at 8.25%. The top row is the set of images taken on the physical models from the experimental loading setup. The second row presents the images from the numerical simulation of the deformation of the corresponding structures, for the

same displacement boundary conditions. It may be clearly observed that the deformation responses of individual unit cells as well as the overall structures correlate closely between the experimental and numerical responses of corresponding structural cases.

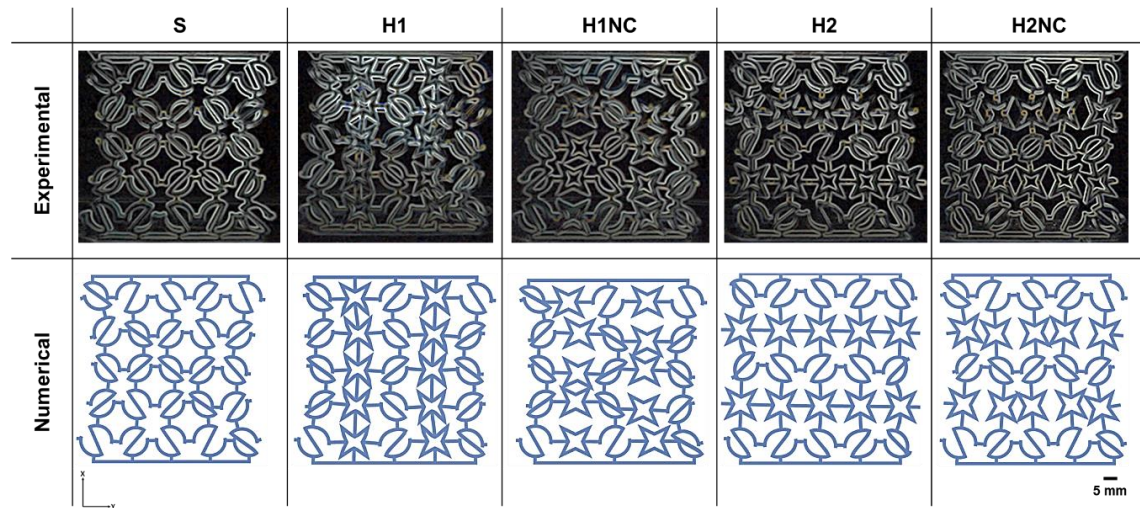


Fig. 6.10 Numerical and experimental deformation corresponding to -5 mm of displacement load for S and all hybrid structural models

The Poisson's ratios calculated based on the deflections of different structural models under the same loading equivalent to a -5 mm compression measured from both experimental and numerical results are juxtaposed for each case in the form of the bar charts presented in Fig. 6.11. The same procedure is applied to calculate the poisson's ratios from the numerical simulation results, as used in the case of the experimental results. The deformation images as shown in Fig. 6.10 obtained from the finite element analysis were extracted and fed into the ImageJ software where the lateral and longitudinal deformation were able to be measured based on

the image processing technique. The lateral and longitudinal displacements thus obtained are used to further calculate the Poisson's ratio in each case.

It may be observed that in most cases the Poisson's ratios calculated based on both experimental and numerical results correlated closely, barring the case of the re-entrant model, where there is a difference of almost around 25%. Considering the overall auxetic responses, the S- shaped model resulted in the highest negative Poisson's ratio at around -2.0, compared to the other structures, under the same external displacement load applied (-5 mm displacement or 8.25% strain). This was followed by H1NC and H2NC, at around -1.2 and -1.6 Poisson's ratios, as evident from the results of Fig. 6.11. The H2 hybrid and the re-entrant (R) structures scored the least in terms of the auxetic Poisson's ratio responses at around -0.35 and -0.9 respectively, on average.

It may be further elucidated here that the H2NC models began with the highest (around -3) negative Poisson's ratio responses, but almost hyperbolically lost the auxeticity with increasing load conditions (Fig. 6.8 (f)). As already stated, the sideways movement of the star re-entrant unit cells (Fig. 6.4 last row) leads the structure to lose the ability to retain the higher auxetic nature. However, it is pertinent to highlight here that by flipping the S-structural forms on either side of the central vertical symmetry line would lead to the lateral movement of the star re-entrant unit cells to be in the opposite directions from the two sides of the structure. This is most likely to create inward shifts from either ends of the structure in the lateral direction and lead to better auxeticity. However, the symmetry of arrangement of the unit cells as mirror images around the central vertical line will

only be possible with an even number of vertical rows. This will be an interesting aspect for further study in the future. On the other hand, the within collapsing nature of the S-unit cells allows the structure to retain the high negative Poisson's ratios and the auxetic nature, compared to the other models, as the deflection due to external loading increases.

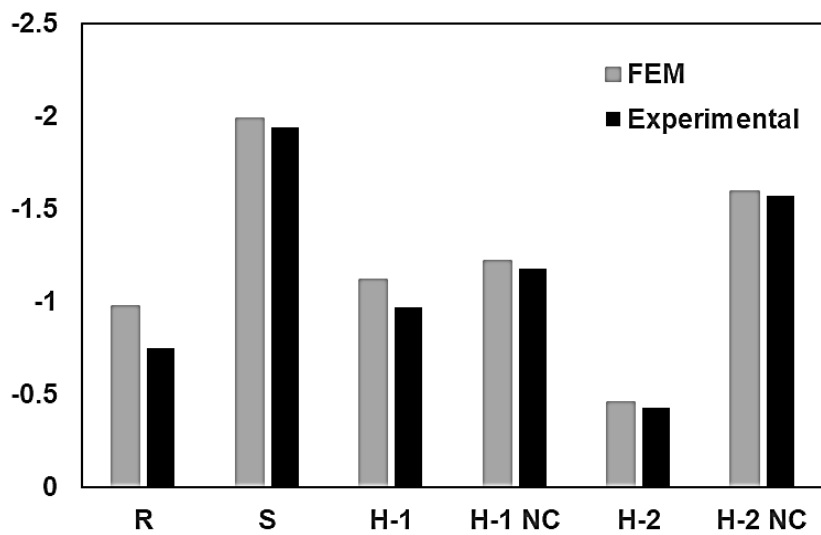


Fig. 6.11 Comparative chart of numerically and experimentally evaluated Poisson's ratios of all the structural models for the same external loading equivalent to a -5 mm compression.

6.4 Summary

Four novel hybrid models (H1, H1NC, H2, and H2NC) along with the re-entrant and the S-shaped structures were evaluated for their in-plane auxeticity and other critical mechanical properties under compressive loading, both experimentally and numerically. The hybrid models are based on the S-structure, modified by

introducing the star re-entrant unit cells in between the S-unit cells along (H1, H1NC) or at right angles (H2 and H2NC) to the load direction, in order to improve the in-plane deformation modes, auxetic responses, Young's modulus and the compressive strength results. Physical models of all the structures were fabricated by selective laser melting of stainless steel 316L based on the Renishaw system.

Considering the compressive strength, all the hybrid models performed better than the parent S-shaped model, while the H1 hybrid model even surpassed the compressive strength of the re-entrant model. The Young's modulus responses of all the hybrid (H1, H1NC and H2) structures, except the H2 model were improved and performed better than the S-shaped mode. However, Young's modulus was the highest, with the re-entrant structure. The highest negative Poisson's ratio was obtained with the H2NC hybrid model followed by the S-shaped model with the initial deflection loading conditions. As the external deflection loading increases, the H2NC structure loses auxeticity due to the sideways deflection of the relatively rigid star re-entrant units. The S-structure performs better auxetically, in all these conditions. The deformation responses of the hybrid models, and in particular the H1 and H1NC structures are more favourable for auxetic nature, due to the large influences of the S-unit cells and their within collapsing deformation modes at the lateral boundaries. However, the deformation modes of the H2NC and the re-entrant structures were influenced by the deformation responses of the star and the re-entrant unit cells respectively, which is predominantly side-ways movement. This may destroy the auxetic nature of the H2NC structures at higher deformation levels, depending on the number of columns of and the orientations of the unit cells on either side of the central vertical symmetry line.

Chapter 7

Conclusions

7.1. Objectives and achievements

The overarching objective of the research is to explore the substantial application potential of the selective laser melting technique to build metal auxetic structures. Once established, the structures produced are to be used to experimentally verify the true auxetic nature of at least one of the commonly researched auxetic structure. Considering the expensive nature of the additive manufacturing applications, a numerical scheme is also to be built for simulation of the experimental conditions. Correlating the experimental and numerical results, an overall scheme has to be developed, where the numerical method, approved to be closer to the reality based on the comparison with the experimental responses could be used to further optimise the structure for better auxetic nature.

Evaluation of the stress concentration effects in auxetic structures that were neglected for most part and establishment of structural variations that could eliminate these effects are also objectives of the current research. Further, the relative performance of a given structure responding to varying target responses is an aspect of interest too. Integration of different structural elements in hybrid structures of varying forms, targeting specific combinations of auxetic and

mechanical responses is the final step of the proposed research. All these objectives have been successfully achieved through the experimental, analytical and numerical research undertaken.

The re-entrant square grid structure was evaluated by experimental and numerical means in order to establish the research methodology as planned and also to ascertain the auxetic nature of this common structural form by experimental means. Selective laser melting based on the Renishaw AM400 system was the experimental basis for producing all the proposed auxetic structures. Further to ascertaining a good correlation between the experimental and numerical results, the finite element schemes were used to optimise the square grid structure in the form of a non-square grid structure, enhancing the negative Poisson's ratio from about -1 to almost -10. Experimental results proved this to be close to -7, which is a substantial improvement over the currently popular auxetic structures based on metallic materials. The sharply varying geometrical features proved to be detrimental to the spread of the stress concentration zones.

The S-unit cell was developed first analytically, to establish the preliminary auxetic nature of the unit cell form. Once this was proved, the integrated experimental and numerical scheme established for the re-entrant structure was extended to the complete analysis of the S-structure, from the unit cell to the full structural form. The results clearly elucidated the rounded S-structure to be far better than the re-entrant model in terms of stress concentration responses. The auxetic nature was also improved compared to the square-grid form. The mechanical responses were

inferior though, considering the relatively flexible nature of the critical structural elements. The hybrid structures developed by inserting the re-entrant star unit cells into the S- structures in different configurations proved to be the best compromise in terms of achieving an overall auxetic and mechanical performance of the newly designed structures. The most significant conclusions drawn both generally and quantitatively based on the results of the current work are more closely stated in the following sections.

7.2. General conclusions

The square grid structure

- The square grid structure (H/L ratio 1) fabricated by the selective laser melting technique was proved auxetic by both experimental and numerical means, with specific variations in the results.
- The numerical simulation trials carried out to evaluate the effects of the geometrical parameters predicted the roles of the flap inclination angle and the strut thickness to be negligible in terms of improving the auxeticity of the square grid structure.
- Non-square grid structures developed by extending the Height to length H/L ratios beyond 1 were found to enhance the auxeticity quite significantly.
- The instability and buckling problems of the non-square grid structures i.e. for the H/L ratio greater than 1 was proved to be eliminated based on the

numerical simulation results by extending the 2D structure in the 3D without affecting the auxeticity of the structures.

- Numerical results were not indicative of any reduction in the peak Von Mises' stresses due to the filleting of the re-entrant structure, the stress concentration points moved away from the critical junctions and towards the central regions of the stressed members.
- The square grid structure modified by filleting had a minor improvement in the auxetic nature as evident from the numerical simulation results.

The S-shaped auxetic structure

- The deformation responses of the S-shaped auxetic structure were far superior to those of the re-entrant structure, as there was no cracking and failure of the elements of the structure.
- The re-entrant structures suffer from the lateral displacements and the row-wise collapsing, while the S-shaped unit cells share the deformation across the entire structure and adopt the within collapsing deformation mode.
- The S-structures begin with relatively high negative Poisson's ratios and continue to maintain the same for a wide range of the applied strains, as compared to the re-entrant structure.
- The number, size, and distribution of the stress concentration points are far higher in the re-entrant structures as compared to the S-shaped structure,

with consequent generation of higher stresses levels in the re-entrant structure.

- The average Poisson's ratio values obtained by numerical simulation are slightly lower than those from the experimental trials.

Hybrid auxetic structures

- All the hybrid models based on the parent S-shaped structure except the H2NC model, exhibited the within collapsing deformation patterns, unlike the sideways deformation of the re-entrant structure based on both experimental and numerical results.
- The re-entrant model outperformed the S-shaped and the other hybrid structures, showing the highest Young's modulus, followed by the H1 and H2 models.
- The highest compressive strength was obtained for the H1 hybrid model followed by the re-entrant and H2 models.
- The H2NC hybrid model exhibited the highest negative Poisson's ratio, among all the six structural models. However, it loses the auxeticity rapidly as the load increases. The re-entrant model also depicted the rapid fall in the negative Poisson's ratio with the increasing load.
- The S-shaped structure was the only model resulting in a high negative Poisson's ratio over a wide range of the applied strains.

- The numerical results depicted the highest Von-Mises stress for the re-entrant models as compared to the S-shaped and other hybrid models.
- The Poisson's ratios predicted by the numerical and experimental schemes correlated closely for the S- and all the other hybrid structures, though a slight variation is obtained in the case of the re-entrant structure.

7.3. Quantitative conclusions

The square-grid structure

- The numerical simulations for the geometrical parameters with H/L ratio less than 1 predicted a diminishing auxetic nature of the square grid structure.
- Contrarily, with a H/L ratio more than 1, the auxetic nature of the structure greatly enhanced.
- The square grid structure (H/L=1) resulted in Poisson's ratio values of -1.45 and -1.2 based on the numerical and experimental results respectively.
- A constant Poisson's ratio -1.45 was obtained based on the numerical analyses carried out on the square-grid structure with varying strut inclination angles from 0-30° and the strut thicknesses from 1.5-3 mm.
- The reduced Poisson's ratio from -1.45 to -0.6 was obtained when the value of H/L ratio had been reduced from 1 to 0.6.
- Numerical results predicted the non-square grid structure with H/L ratio equal to 3 to exhibit a Poisson's ratio of around - 10.0.

- Experimental validation of the above prediction based on the non-square grid structure with H/L ratio 3.0 resulted in a Poisson's ratio of - 7.0 as against the -10 based on the numerical simulation.
- The finite element predictions based on the Nonsquare grid auxetic structures indicated Poisson's ratios as high as - 20, with the H/L ratio increased to 4.

Stress concentration in square grid structures

- With the introduction of a fillet of radius 1mm, the peak Von-Mises stress values increased from 370 MPa to 424 MPa and from 333 MPa to 355 MPa with linear and non-linear material conditions respectively in the case of the square-grid auxetic structures.
- A 1.5 mm fillet radius at the critical corners led to a reduction in the stress intensity and enhancements in stress distribution patterns based on both linear and non-linear material conditions.
- A minor rise in the Poisson's ratio from -1.5 to -1.65 was obtained after filleting to a radius of around 2.0 mm within the linear material loading condition.
- For the non-linear material condition the optimum radius level was at around 1.5 mm. Conclusively, the optimum fillet radius value lies in between 1.5-2 mm for enhanced auxeticity considering both linear and non-linear material conditions.

The S-shaped auxetic structure

- The re-entrant cells underwent strut detachment with the displacement load between 15-20 mm, while the S-structures showed no evidence of the formation of any cracks for the same loading.
- The re-entrant structure began sideways movement, when the applied displacement load crosses 10 mm, while the S-shaped structure maintained within collapsing deformation modes up to 20mm of load (end of loading).
- The S-shaped structure exhibited higher negative Poisson's ratios, at around -2.5 in the elastic region and also remained auxetic up to almost 15% of the externally applied strain.
- The re-entrant form only attained a maximum of around -1.2 for the Poisson's ratio, and with the auxetic responses almost lost within 5% of external strains.
- The re-entrant strucutre has 8 critical points as against the 2 points in the case of the S-shaped strucutre. The numerical results indicated the stresses generated in the re-entrant structures to be 2.5 times higher with the linear and 1.9 times higher with the non-linear material options, compared to the S-structure.

Hybrid structures

- Both the S-shaped and the hybrid models maintained the within collapsing deformation mode up to the full range of the displacement load considered,

0-20 mm, while the re-entrant and the H2NC models could only maintain auxeticity up to 5 mm of the applied displacement loads.

- The re-entrant structure exhibited a Young's modulus value of around 2350 MPa which is almost 2.5 times higher than the Young's modulus of the H1 and the H2 models.
- The highest compressive strength of around 45 MPa is obtained for the H1 model followed by 36 MPa and 34 MPa attained by the re-entrant and the H2 structural models respectively.
- The H2NC began with a -3 Poisson's ratio at the start of the displacement loading and rapidly reduced to less than -2 as the displacement boundary condition reaches 5mm.
- Similarly, the Poisson's ratio varied from -2 to -1 as the displacement load condition varied from 0 to 5 mm, in the case of the re-entrant model.
- The S-shaped model exhibited a reasonably higher negative Poisson's ratio, at around -1 from the start and up to 15 mm of the applied displacement load, while the re-entrant and the hybrid models reached almost -0.5 Poisson's ratio as the displacement condition reaches 15 mm.
- In the range of 10-25 mm of applied displacement load the re-entrant model attains a constant Poisson's ratio of about -0.5. However, a lower Poisson's ratio below -0.5 was attained by the H-2 model.
- For the same load range (10-25 mm) the Poisson's ratio varied from -1.8 – 0.8, -1 to -0.3, -1 to -0.5 and -1 to -0.2 for the S-shaped, H-1, H-1 NC and H-2 NC structural models respectively.

7.4. Future Scope

The experimental and numerical schemes developed and the overall schemes of evaluating auxetic structures by integrating them together as evident from the current research allows to significantly enhance the performance attributes of different auxetic structural forms. The non-square grid structure proving to be auxetic at -7.0 Poisson's ratio by experimental means is evidence of the limit to which many auxetic structures may be stretched. In fact, the numerical predictions indicate a possible extension of this almost up to -20, though buckling issues restricted the practical implementation of this structure. However, the buckling problems can be avoided, by expanding the structure in the third dimension, and building a truly 3D auxetic structure. It will be interesting to evaluate how such a 3D non-square grid structure with H/L ratios over 3.0 will perform in reality. One significant bottleneck is the need to use support structures while building such complex 3D forms using selective laser melting. Appropriate schemes optimising the placement and removal of the support structures and possible design of the structure for additive manufacturing by selective laser melting need to be developed, which is the future scope of this work.

Further, the hybrid structures proposed by integrating the re-entrant star unit cells within the S-structural format resulted in higher auxeticity at lower levels of external displacement loading. With increasing load, the auxeticity was quickly lost in some structural arrangements such as the H1NC, due to the sideways displacement of the star units bodily. However, there is a possibility to induce such displacement of the star units in preferred directions to happen from either ways, by developing a

mirror image of the S-structures on either side of the central symmetry line. This requires a careful consideration of structures with typically odd number of vertical columns and appropriate orientation of the S-units on either side of the central symmetry. It is predicted that such an arrangement will push the star-units inwards from either directions, leading to high auxeticity under compression, apart from all the other benefits of these hybrid structures such as low stress concentration and better mechanical responses. This is also work for the future.

References

- Abdeen, D. H., & Palmer, B. R. (2016). Effect of processing parameters of electron beam melting machine on properties of Ti-6Al-4V parts. *Rapid Prototyping Journal*, 22(3), 609-620.
- Abdelaal, O. A., & Darwish, S. M. (2012). Analysis, fabrication and a biomedical application of auxetic cellular structures. *Int J Eng Innov Technol*, 2(3), 218-23.
- Alderson, K. L., & Evans, K. E. (1992). The fabrication of microporous polyethylene having a negative Poisson's ratio. *Polymer*, 33(20), 4435-4438.
- Alderson, A. (1999). A triumph of lateral thought. *Chemistry & Industry*, 17, 384-391.
- Alderson, A., Rasburn, J., Ameer-Beg, S., Mullarkey, P. G., Perrie, W., & Evans, K. E. (2000). An auxetic filter: A tuneable filter displaying enhanced size selectivity or defouling properties. *Industrial & engineering chemistry research*, 39(3), 654-665.
- Alderson, A., Rasburn, J., Evans, K. E., & Grima, J. N. (2001). Auxetic polymeric filters display enhanced de-fouling and pressure compensation properties. *Membrane Technology*, 2001(137), 6-8
- Alderson, K. L., Alderson, A., Smart, G., Simkins, V. R., & Davies, P. J. (2002). Auxetic polypropylene fibres: Part 1-Manufacture and characterisation. *Plastics, Rubber and Composites*, 31(8), 344-349.
- Alderson, A., & Alderson, K. (2005). Expanding materials and applications: exploiting auxetic textiles. *Technical textiles international*, 14(6), 29-34.

Alderson, A., & Alderson, K. L. (2007). Auxetic materials. *Proceedings of the Institution of Mechanical Engineers, Part G: Journal of Aerospace Engineering*, 221(4), 565-575.

Alderson, A., Rasburn, J., & Evans, K. E. (2007). Mass transport properties of auxetic (negative Poisson's ratio) foams. *physica status solidi (b)*, 244(3), 817-827

Alderson, A., Alderson, K. L., Chirima, G., Ravirala, N., & Zied, K. M. (2010). The in-plane linear elastic constants and out-of-plane bending of 3-coordinated ligament and cylinder-ligament honeycombs. *Composites Science and Technology*, 70(7), 1034-1041.

Ali, M. N., & Rehman, I. U. (2015). Auxetic polyurethane stents and stent-grafts for the palliative treatment of squamous cell carcinomas of the proximal and mid oesophagus: a novel fabrication route. *Journal of Manufacturing Systems*, 37, 375-395.

Arcam, E. B. M. at Sirris Belgium. Uploaded Jun. 17, 2010. 2 pages.<http://www.arcam.com/wp-content/uploads/justaddbrochure-web.pdf>

Aslam, M. U., & Darwish, S. M. (2015). Development and Analysis of Different Density Auxetic Cellular Structures. *International Journal on Recent and Innovation Trends in Computing and Communication*, 3(1), 27-32.

Attaran, M. (2017). The rise of 3-D printing: The advantages of additive manufacturing over traditional manufacturing. *Business Horizons*, 60(5), 677-688.

Baughman, R. H., Shacklette, J. M., Zakhidov, A. A., & Stafström, S. (1998). Negative Poisson's ratios as a common feature of cubic metals. *Nature*, 392(6674), 362.

- Bettini, P., Airoldi, A., Sala, G., Di Landro, L., Ruzzene, M., & Spadoni, A. (2010). Composite chiral structures for morphing airfoils: Numerical analyses and development of a manufacturing process. *Composites Part B: Engineering*, 41(2), 133-147.
- Bhullar, S. K., Mawanane, H. A. T., Alderson, A., Alderson, K., & Martin, B. G. J. (2013). Influence of negative Poisson's ratio on stent applications. *Adv. Mater*, 2(3), 42-47.
- Bhullar, S. K., Rana, D., Lekesiz, H., Bedeloglu, A. C., Ko, J., Cho, Y., ... & Ramalingam, M. (2017). Design and fabrication of auxetic PCL nanofiber membranes for biomedical applications. *Materials Science and Engineering: C*, 81, 334-340.
- Bourell, D., Kruth, J. P., Leu, M., Levy, G., Rosen, D., Beese, A. M., & Clare, A. (2017). Materials for additive manufacturing. *CIRP Annals*, 66(2), 659-681.
- Burke, M. (1997). A stretch of the imagination. *New Scientist*, 154(2085), 36-9.
- Burriesci, G., & Bergamasco, G. (2011). U.S. Patent No. 8,034,103. Washington, DC: U.S. Patent and Trademark Office.
- Carneiro, V. H., Puga, H., & Meireles, J. (2016). Analysis of the geometrical dependence of auxetic behavior in reentrant structures by finite elements. *Acta Mechanica Sinica*, 32(2), 295-300.
- Chan, N., & Evans, K. E. (1997). Fabrication methods for auxetic foams. *Journal of Materials Science*, 32(22), 5945-5953.

Chang, Y., Ma, P., & Jiang, G. (2017). Energy absorption property of warp-knitted spacer fabrics with negative Poisson's ratio under low velocity impact. *Composite Structures*, 182, 471-477.

Chen, H., Chan, C. T., & Sheng, P. (2010). Transformation optics and metamaterials. *Nature materials*, 9(5), 387.

Choi, J. B., & Lakes, R. S. (1991). Design of a fastener based on negative Poisson's ratio foam. *Cellular Polymers*, 10(3), 205-212.

Choi, J. B., & Lakes, R. S. (1996). Fracture toughness of re-entrant foam materials with a negative Poisson's ratio: experiment and analysis. *International Journal of fracture*, 80(1), 73-83.

Choi, H. J., Lee, J. J., Lee, J. B., Sung, H. J., Shin, J. W., Shin, J. W., ... & Kim, J. K. (2016). MG-63 cells proliferation following various types of mechanical stimulation on cells by auxetic hybrid scaffolds. *Biomaterials research*, 20(1), 32.

Dolla, W. J., Fricke, B. A., & Becker, B. R. (2007). Structural and drug diffusion models of conventional and auxetic drug-eluting stents. *Journal of Medical Devices*, 1(1), 47-55.

Dong, H. W., Zhao, S. D., Wang, Y. S., & Zhang, C. (2017). Topology optimization of anisotropic broadband double-negative elastic metamaterials. *Journal of the Mechanics and Physics of Solids*, 105, 54-80.

Douglas, G. R., Phani, A. S., & Gagnon, J. (2014). Analyses and design of expansion mechanisms of balloon expandable vascular stents. *Journal of biomechanics*, 47(6), 1438-1446.

Elipe, J. C. Á., & Lantada, A. D. (2012). Comparative study of auxetic geometries by means of computer-aided design and engineering. *Smart Materials and Structures*, 21(10), 105004.

EPMA European Powder Metallurgy Association. Introduction to additive manufacturing technology-A guide for Designers and Engineers.

Evans, K. E., Nkansah, M. A., & Hutchinson, I. J. (1991). Molecular network design.

Evans, K. E., & Alderson, A. (2000a). Auxetic materials: functional materials and structures from lateral thinking!. *Advanced materials*, 12(9), 617-628.

Evans, K. E., & Alderson, K. L. (2000b). Auxetic materials: the positive side of being negative. *Engineering Science and Education Journal*, 9(4), 148-154.

Faroughi, S., & Shaat, M. (2018). Poisson's ratio effects on the mechanics of auxetic nanobeams. *European Journal of Mechanics-A/Solids*, 70, 8-14.

Flodberg, G., Pettersson, H., & Yang, L. (2018). Pore analysis and mechanical performance of selective laser sintered objects. *Additive Manufacturing*, 24, 307-315.

Friis, E. A., Lakes, R. S., & Park, J. B. (1988). Negative Poisson's ratio polymeric and metallic foams. *Journal of Materials Science*, 23(12), 4406-4414.

Fu, M. H., Chen, Y., & Hu, L. L. (2017). Bilinear elastic characteristic of enhanced auxetic honeycombs. *Composite Structures*, 175, 101-110.

Fu, M., Chen, Y., Zhang, W., & Zheng, B. (2016). Experimental and numerical analysis of a novel three-dimensional auxetic metamaterial. *physica status solidi (b)*, 253(8), 1565-1575.

- Gaspar, N., Ren, X. J., Smith, C. W., Grima, J. N., & Evans, K. E. (2005). Novel honeycombs with auxetic behaviour. *Acta Materialia*, 53(8), 2439-2445.
- Ghaedizadeh, A., Shen, J., Ren, X., & Xie, Y. (2016). Tuning the performance of metallic auxetic metamaterials by using buckling and plasticity. *Materials*, 9(1), 54.
- Gibson, L. J., Ashby, M. F., Schajer, G. S., & Robertson, C. I. (1982). The mechanics of two-dimensional cellular materials. *Proceedings of the Royal Society of London. A. Mathematical and Physical Sciences*, 382(1782), 25-42.
- Gibson, L. J., & Ashby, M. F. (1999). *Cellular solids: structure and properties*. Cambridge university press.
- Gibson, I., Rosen, D. W., & Stucker, B. (2010). Design for additive manufacturing. In *Additive Manufacturing Technologies* (pp. 299-332). Springer, Boston, MA.
- Gibson, I., Rosen, D. W., & Stucker, B. (2014). *Additive manufacturing technologies* (Vol. 17). New York: Springer.
- Grima, J. N., Jackson, R., Alderson, A., & Evans, K. E. (2000). Do zeolites have negative Poisson's ratios?. *Advanced Materials*, 12(24), 1912-1918.
- Grima, J. N., & Evans, K. E. (2000a, August). Networked polymers with negative Poisson's ratios. In *ABSTRACTS OF PAPERS OF THE AMERICAN CHEMICAL SOCIETY* (Vol. 220, pp. U348-U348). 1155 16TH ST, NW, WASHINGTON, DC 20036 USA: AMER CHEMICAL SOC.
- Grima, J. N., & Evans, K. E. (2000b). Auxetic behavior from rotating squares. *Journal of Materials Science Letters*, 19(17), 1563-1565.
- Grima, J. N., Alderson, A., & Evans, K. E. (2004). Negative Poisson's ratios from rotating rectangles. *Comput. Methods Sci. Technol*, 10(2), 137-145.

- Grima, J. N., Alderson, A., & Evans, K. E. (2005). Auxetic behaviour from rotating rigid units. *Physica status solidi (b)*, 242(3), 561-575.
- Grima, J. N., Alderson, A., & Evans, K. E. (2005a). An alternative explanation for the negative Poisson's ratios in auxetic foams. *Journal of the Physical Society of Japan*, 74(4), 1341-1342.
- Grima, J. N., Gatt, R., Alderson, A., & Evans, K. E. (2005). On the potential of connected stars as auxetic systems. *Molecular Simulation*, 31(13), 925-935.
- Grima, J. N., Gatt, R., Alderson, A., & Evans, K. E. (2005b). On the origin of auxetic behaviour in the silicate α -cristobalite. *Journal of Materials Chemistry*, 15(37), 4003-4005.
- Grima, J. N., & Evans, K. E. (2006). Auxetic behavior from rotating triangles. *Journal of materials science*, 41(10), 3193-3196.
- Grima, J. N., Attard, D., Gatt, R., & Cassar, R. N. (2009). A Novel Process for the Manufacture of Auxetic Foams and for Their re-Conversion to Conventional Form. *Advanced Engineering Materials*, 11(7), 533-535.
- Grima, J. N., Zammit, V., Gatt, R., Alderson, A., & Evans, K. E. (2007). Auxetic behaviour from rotating semi-rigid units. *physica status solidi (b)*, 244(3), 866-882.
- Grima, J.N., Gatt, R., Farrugia, P.S.. (2008). On the properties of auxetic meta-tetrachiral structures. *Phys. Status Solidi B* 245, 511–520.
- Grima, J. N., & Caruana-Gauci, R. (2012). Mechanical metamaterials: materials that push back. *Nature materials*, 11(7), 565-566.
- Han, S. C., Kang, D. S., & Kang, K. (2018). Two nature-mimicking auxetic materials with potential for high energy absorption. *Materials Today*.

Ho, D. T., Park, S. D., Kwon, S. Y., Park, K., & Kim, S. Y. (2014). Negative Poisson's ratios in metal nanoplates. *Nature communications*, 5, 3255.

Howell, B., Prendergast, P., & Hansen, L. (1991). *Acoustic behavior of negative Poisson's ratio materials* (No. DTRC/SME-91/01). DAVID TAYLOR RESEARCH CENTER BETHESDA MD SHIP MATERIALS ENGINEERING DEPT.

Howell, B., Prendergast, P., & Hansen, L. (1994). Examination of acoustic behavior of negative Poisson's ratio materials. *Applied Acoustics*, 43(2), 141-148.

<https://www.americanwireedm.com/edm-services/edm-machining>

https://www3.panasonic.biz/ac/ae/service/tech_support/fasys/tech_guide/measurement/laser/index.jsp

Hu, L. L., Zhou, M. Z., & Deng, H. (2019). Dynamic indentation of auxetic and non-auxetic honeycombs under large deformation. *Composite Structures*, 207, 323-330.

Huang, C., & Chen, L. (2016). Negative Poisson's ratio in modern functional materials. *Advanced Materials*, 28(37), 8079-8096.

Imbalzano, G., Tran, P., Ngo, T. D., & Lee, P. V. (2016). A numerical study of auxetic composite panels under blast loadings. *Composite Structures*, 135, 339-352.

Imbalzano, G., Tran, P., Ngo, T. D., & Lee, P. V. (2017). Three-dimensional modelling of auxetic sandwich panels for localised impact resistance. *Journal of Sandwich Structures & Materials*, 19(3), 291-316.

Imbalzano, G., Linforth, S., Ngo, T. D., Lee, P. V. S., & Tran, P. (2018). Blast resistance of auxetic and honeycomb sandwich panels: comparisons and parametric designs. *Composite Structures*, 183, 242-261.

Ingole, A., Hao, A., & Liang, R. (2017). Design and modeling of auxetic and hybrid honeycomb structures for in-plane property enhancement. *Materials & Design*, 117, 72-83.

J. Schwerdtfeger, F. Schury, M. Stingl, F. Wein, R.F. Singer, C. Körner, Mechanical characterisation of a periodic auxetic structure produced by SEBM, *Phys. Status Solidi B* 249 (2012) 1347–1352.

Jayanty, S., Crowe, J., & Berhan, L. (2011). Auxetic fibre networks and their composites. *physica status solidi (b)*, 248(1), 73-81.

Jiang, Y.Y. & Li, Y.N. Comparison of auxetic effects induced by re-entrant angle and chirality. *Proceedings of the 24th International Congress of Theoretical and Applied Mechanics*, (2016).

Jiang, Y., & Li, Y. (2017). 3D printed chiral cellular solids with amplified auxetic effects due to elevated internal rotation. *Advanced Engineering Materials*, 19(2), 1600609.

Jiang, Y., & Li, Y. (2018). 3D Printed Auxetic Mechanical Metamaterial with Chiral Cells and Re-entrant Cores. *Scientific reports*, 8(1), 2397.

Jiao, L., Chua, Z., Moon, S., Song, J., Bi, G., & Zheng, H. (2018). Femtosecond Laser Produced Hydrophobic Hierarchical Structures on Additive Manufacturing Parts. *Nanomaterials*, 8(8), 601.

- Jin, S., Korkolis, Y. P., & Li, Y. (2019). Shear resistance of an auxetic chiral mechanical metamaterial. *International Journal of Solids and Structures*.
- Karnati, S., Axelsen, I., Liou, F. F., & Newkirk, J. W. (2016). Investigation of tensile properties of bulk and SLM fabricated 304L stainless steel using various gage length specimens. In *Proceedings of the 27th Annual International Solid Freeform Fabrication Symposium—An Additive Manufacturing Conference* (pp. 592-604).
- Kolken, H. M., & Zadpoor, A. A. (2017). Auxetic mechanical metamaterials. *RSC Advances*, 7(9), 5111-5129.
- Lakes, R. (1987). Foam structures with a negative Poisson's ratio. *Science*, 235, 1038-1041.
- Lakes, R. (1993). Advances in negative Poisson's ratio materials. *Advanced Materials*, 5(4), 293-296.
- Lakes, R. S., & Elms, K. (1993). Indentability of conventional and negative Poisson's ratio foams. *Journal of Composite Materials*, 27(12), 1193-1202.
- Lakes, R., & Wojciechowski, K. W. (2008). Negative compressibility, negative Poisson's ratio, and stability. *physica status solidi (b)*, 245(3), 545-551.
- Lan, X., Feng, S., Huang, Q., & Zhou, T. (2019). A comparative study of blast resistance of cylindrical sandwich panels with aluminum foam and auxetic honeycomb cores. *Aerospace Science and Technology*, 87, 37-47.
- Larsen, U. D., Signund, O., & Bouwsta, S. (1997). Design and fabrication of compliant micromechanisms and structures with negative Poisson's ratio. *Journal of microelectromechanical systems*, 6(2), 99-106.

Lees C, Vincent JFV, Hillerton JE (1991). Poisson's ratio in skin. *Biomed. Mater. Eng.*, 1: 19-23.

Li, S., Hassanin, H., Attallah, M. M., Adkins, N. J., & Essa, K. (2016). The development of TiNi-based negative Poisson's ratio structure using selective laser melting. *Acta Materialia*, 105, 75-83.

Li, Y., & Zeng, C. (2016). Room-Temperature, Near-Instantaneous Fabrication of Auxetic Materials with Constant Poisson's Ratio over Large Deformation. *Advanced Materials*.

Liu, Y., & Hu, H. (2010). A review on auxetic structures and polymeric materials. *Scientific Research and Essays*, 5(10), 1052-1063.

Lorato, A., Innocenti, P., Scarpa, F., Alderson, A., Alderson, K. L., Zied, K. M., ... & Evans, K. E. (2010). The transverse elastic properties of chiral honeycombs. *Composites Science and Technology*, 70(7), 1057-1063.

Love, A.E.H. (1944). *A Treatise on the Mathematical Theory of Elasticity*, 4th ed., Dover, New York.

Lu, Z. X., Li, X., Yang, Z. Y., & Xie, F. (2016). Novel structure with negative Poisson's ratio and enhanced Young's modulus. *Composite Structures*, 138, 243-252.

Masters, I. G., & Evans, K. E. (1996). Models for the elastic deformation of honeycombs. *Composite structures*, 35(4), 403-422.

Milton, G. W. (1992). Composite materials with Poisson's ratios close to—
1. *Journal of the Mechanics and Physics of Solids*, 40(5), 1105-1137.

- Mohsenizadeh, S., Alipour, R., Rad, M. S., Nejad, A. F., & Ahmad, Z. (2015). Crashworthiness assessment of auxetic foam-filled tube under quasi-static axial loading. *Materials & Design*, 88, 258-268.
- Moyers, R. E. (1992). U.S. Patent No. 5,108,413. Washington, DC: U.S. Patent and Trademark Office.
- NEGATIVNIM, S. S. M. Z., RAZMERJEM, P., NEPOSREDNIM, P. Z., & TISKANJEM, T. (2016). Compressive properties of auxetic structures produced with direct 3D printing. *Materiali in tehnologije*, 50(3), 311-317.
- Novak, N., Vesenjak, M., & Ren, Z. (2016). Auxetic Cellular Materials-a Review. *Strojniški vestnik-Journal of Mechanical Engineering*, 62(9), 485-493.
- Prall, D., & Lakes, R. S. (1997). Properties of a chiral honeycomb with a Poisson's ratio of—1. *International Journal of Mechanical Sciences*, 39(3), 305-314.
- R. E. Moyers, US Patent No. 5 108 413, 1992.
- Rad, M. S., Prawoto, Y., & Ahmad, Z. (2014). Analytical solution and finite element approach to the 3D re-entrant structures of auxetic materials. *Mechanics of Materials*, 74, 76-87.
- Rasburn, J., Mullarkey, P. G., Evans, K. E., & Alderson, A. (2001). Auxetic structures for variable permeability systems. *American Institute of Chemical Engineers. AIChE Journal*, 47(11), 2623.
- Ravirala, N., Alderson, K. L., Davies, P. J., Simkins, V. R., & Alderson, A. (2006). Negative Poisson's ratio polyester fibers. *Textile research journal*, 76(7), 540-546.
- Rehme, O., & Emmelmann, C. (2009). Selective laser melting of honeycombs with negative Poisson's ratio. *J. Laser Micro/Nanoeng*, 4, 128-134.

Ren, X., Shen, J., Tran, P., Ngo, T. D., & Xie, Y. M. (2018). Auxetic nail: Design and experimental study. *Composite Structures*, 184, 288-298.

Renishaw. Data sheet: CoCr-0404 powder for additive manufacturing.

[http://www.renishaw.com/en/data-sheetsadditive-manufacturing-17862\(2016\)](http://www.renishaw.com/en/data-sheetsadditive-manufacturing-17862(2016)).

Accessed July 2018

Renishaw. Data sheet: SS 316L-0407 powder for additive manufacturing.

[http://www.renishaw.com/en/data-sheetsadditive-manufacturing-17862\(2018\)](http://www.renishaw.com/en/data-sheetsadditive-manufacturing-17862(2018))

Robert, F. (1985). An isotropic three-dimensional structure with Poisson's ratio=-1. *Journal of Elasticity*, 15, 427-430.

Sabatino, A. (2016). U.S. Patent No. 9,241,808. Washington, DC: U.S. Patent and Trademark Office.

Sanami, M., Raviralaa, N., Kim, A., Alderson, A. (2014). AuxeticMaterials for Sport Applications. Procedia Engineering, 72, 453 – 458. (crash helmets and body armours).

Scarpa, F. (2008). Auxetic materials for bioprostheses [In the Spotlight]. *IEEE Signal Processing Magazine*, 25(5), 128-126.

Scarpa, F., Ciffo, L. G., & Yates, J. R. (2003). Dynamic properties of high structural integrity auxetic open cell foam. *Smart Materials and Structures*, 13(1), 49.

Scarpa, F., Giacomin, J., Zhang, Y., & Pastorino, P. (2005). Mechanical performance of auxetic polyurethane foam for antivibration glove applications. *Cellular Polymers*, 24(5), 253-268.

Schwerdtfeger, J., Heinl, P., Singer, R. F., & Körner, C. (2010). Auxetic cellular structures through selective electron-beam melting. *physica status solidi (b)*, 247(2), 269-272.

Schwerdtfeger, J., Schury, F., Stingl, M., Wein, F., Singer, R. F., & Körner, C. (2012). Mechanical characterisation of a periodic auxetic structure produced by SEBM. *physica status solidi (b)*, 249(7), 1347-1352.

Shalaev, V. M., Cai, W., Chettiar, U. K., Yuan, H. K., Sarychev, A. K., Drachev, V. P., & Kildishev, A. V. (2005). Negative index of refraction in optical metamaterials. *Optics letters*, 30(24), 3356-3358.

Shen, J., Zhou, S., Huang, X., & Xie, Y. M. (2014). Simple cubic three-dimensional auxetic metamaterials. *physica status solidi (b)*, 251(8), 1515-1522.

Smith, C. W., Grima, J. N., & Evans, K. (2000). A novel mechanism for generating auxetic behaviour in reticulated foams: missing rib foam model. *Acta materialia*, 48(17), 4349-4356.

Smith, W. A. (1994). *U.S. Patent No. 5,334,903*. Washington, DC: U.S. Patent and Trademark Office.

Soman, P., Lee, J. W., Phadke, A., Varghese, S., & Chen, S. (2012). Spatial tuning of negative and positive Poisson's ratio in a multi-layer scaffold. *Acta Biomaterialia*, 8(7), 2587-2594.

Soukoulis, C. M., & Wegener, M. (2010). Optical metamaterials—more bulky and less lossy. *Science*, 330(6011), 1633-1634.

Spagnoli, A., Brighenti, R., Lanfranchi, M., & Soncini, F. (2015). On the auxetic behaviour of metamaterials with re-entrant cell structures. *Procedia Engineering*, 109, 410-417.

Tanaka, H., Suga, K., Iwata, N., & Shibutani, Y. (2017). Orthotropic laminated open-cell frameworks retaining strong auxeticity under large uniaxial loading. *Scientific reports*, 7, 39816.

Valentine, J., Zhang, S., Zentgraf, T., Ulin-Avila, E., Genov, D. A., Bartal, G., & Zhang, X. (2008). Three-dimensional optical metamaterial with a negative refractive index. *nature*, 455(7211), 376.

Veronda DR, Westmann RA (1970). Mechanical characterization of skin finite deformations. *J. Biomech.*, 3: 111-124.

Wan, H., Ohtaki, H., Kotosaka, S., & Hu, G. (2004). A study of negative Poisson's ratios in auxetic honeycombs based on a large deflection model. *European Journal of Mechanics-A/Solids*, 23(1), 95-106.

Wang, F., Sigmund, O. & Jensen, J. S. Design of materials with prescribed nonlinear properties. *J. Mech. Phys. Solids* **69**, 156–174, <https://doi.org/10.1016/j.jmps.2014.05.003> (2014).

Wang, H., Lu, Z., Yang, Z., & Li, X. (2019). A novel re-entrant auxetic honeycomb with enhanced in-plane impact resistance. *Composite Structures*, 208, 758-770.

Wang, K., Chang, Y. H., Chen, Y., Zhang, C., & Wang, B. (2015). Designable dual-material auxetic metamaterials using three-dimensional printing. *Materials & Design*, 67, 159-164.

- Wang, X. T., Li, X. W., & Ma, L. (2016). Interlocking assembled 3D auxetic cellular structures. *Materials & Design*, 99, 467-476.
- Warmuth, F., Osmanlic, F., Adler, L., Lodes, M. A., & Körner, C. (2016). Fabrication and characterisation of a fully auxetic 3D lattice structure via selective electron beam melting. *Smart Materials and Structures*, 26(2), 025013.
- Warner, J. J., Gillies, A. R., Hwang, H. H., Zhang, H., Lieber, R. L., & Chen, S. (2017). 3D-printed biomaterials with regional auxetic properties. *Journal of the mechanical behavior of biomedical materials*, 76, 145-152.
- White, L. (2009). Auxetic foam set for use in smart filters and wound dressings. *Urethanes Technology International*, 26(4), 34-36.
- Williams, J.L., Lewis, J.L. (1982). Properties and an anisotropic model of cancellous bone from the proximal tibial epiphysis. *J. Biomech. Eng.*, 104: 50-56.
- Wojciechowski, K. W. (1989). Two-dimensional isotropic system with a negative Poisson ratio. *Physics Letters A*, 137(1-2), 60-64.
- Wu, W., Song, X., Liang, J., Xia, R., Qian, G., & Fang, D. (2018). Mechanical properties of anti-tetrachiral auxetic stents. *Composite Structures*, 185, 381-392.
- Xiong, J., Gu, D., Chen, H., Dai, D., & Shi, Q. (2017). Structural optimization of re-entrant negative Poisson's ratio structure fabricated by selective laser melting. *Materials & Design*, 120, 307-316.
- Xue, Y., Wang, X., Wang, W., Zhong, X., & Han, F. (2018). Compressive property of Al-based auxetic lattice structures fabricated by 3-D printing combined with investment casting. *Materials Science and Engineering: A*, 722, 255-262.

Yadroitsev, I., & Yadroitsava, I. (2015). Evaluation of residual stress in stainless steel 316L and Ti6Al4V samples produced by selective laser melting. *Virtual and Physical Prototyping*, 10(2), 67-76.

Yan, Y., Li, Y., Song, L., & Zeng, C. (2017). Pluripotent stem cell expansion and neural differentiation in 3-D scaffolds of tunable Poisson's ratio. *Acta biomaterialia*, 49, 192-203.

Yang, C., Vora, H. D., & Chang, Y. B. (2016, November). Evaluation of auxetic polymeric structures for use in protective pads. In *ASME 2016 International Mechanical Engineering Congress and Exposition* (pp. V009T12A066-V009T12A066). American Society of Mechanical Engineers.

Yang, L. (2011). Structural Design, Optimization and Application of 3D Re-entrant Auxetic Structures.

Yang, L., Cormier, D., West, H., Harrysson, O., & Knowlson, K. (2012). Non-stochastic Ti–6Al–4V foam structures with negative Poisson's ratio. *Materials Science and Engineering: A*, 558, 579-585.

Yang, L., Harrysson, O., West, H., & Cormier, D. (2012a). Compressive properties of Ti–6Al–4V auxetic mesh structures made by electron beam melting. *Acta Materialia*, 60(8), 3370-3379.

Yang, L., Harrysson, O., West, H., & Cormier, D. (2013). A comparison of bending properties for cellular core sandwich panels. *Materials Sciences and Applications*, 4(08), 471.

Yang, S., Chalivendra, V. B., & Kim, Y. K. (2017). Fracture and impact characterization of novel auxetic Kevlar®/Epoxy laminated composites. *Composite Structures*, 168, 120-129.

Yeganeh-Haeri, A., Weidner, D. J., & Parise, J. B. (1992). Elasticity of α -cristobalite: a silicon dioxide with a negative Poisson's ratio. *Science*, 257(5070), 650-652.

Yuan, S., Shen, F., Bai, J., Chua, C. K., Wei, J., & Zhou, K. (2017). 3D soft auxetic lattice structures fabricated by selective laser sintering: TPU powder evaluation and process optimization. *Materials & Design*, 120, 317-327.

Zadpoor, A. A. (2016). Mechanical meta-materials. *Materials Horizons*, 3(5), 371-381.

Zhang, J., Lu, G., Wang, Z., Ruan, D., Alomarah, A., & Durandet, Y. (2018). Large deformation of an auxetic structure in tension: Experiments and finite element analysis. *Composite Structures*, 184, 92-101.

Zhao, Y., Belkin, M. A., & Alù, A. (2012). Twisted optical metamaterials for planarized ultrathin broadband circular polarizers. *Nature communications*, 3, 870.

Appendix

Critical values of θ , k and γ and their interdependence in the S-shaped structure

		C= 10.6																				
		Experimental																				
0 mm	Sample 1	Sample 2			Sample 3			$\Phi_{avg.}$	$\gamma_{avg.}$	θ												
		Φ	γ	Φ	γ	Φ	γ				θ	θ	θ	θ	θ	θ	θ	θ	θ	θ	θ	
58.24	28.58	59.10	29.62	59.20	29.14	58.85	29.11	29.74														
58.21	28.70	59.22	29.37	58.71	28.56	58.71	28.88	29.84														
59.38	27.80	58.46	28.54	58.56	28.01	58.80	28.12	30.68														
58.80	28.57	59.28	30.46	58.98	29.46	59.02	29.49	29.53														
58.44	28.37	59.92	29.09	58.88	28.47	59.08	28.64	30.43														
58.67	28.63	59.64	29.79	58.20	28.73	58.84	29.05	29.79														
58.74	28.98	59.69	30.57	58.98	28.57	59.14	29.37	29.77														
59.92	28.82	58.86	29.95	58.87	28.23	59.21	29.00	30.21														
1mm	Sample 1	Sample 2			Sample 3			$\Phi_{radia n}$	$\gamma_{avg.}$	θ	$\theta_{radia n}$	$\Delta\Phi$	$\Delta\theta$	k	$\cot\theta$	$2CK_{cos\Phi}$	$L_{cos\theta}$	$2C_{sin\Phi}$	$L_{sin\theta}$	$2CK_{cos\Phi-L_{cos\theta}}$	$2C_{sin\Phi-L_{sin\theta}}$	PR
		Φ	γ	Φ	γ	Φ	γ															
58.63	28.32	58.98	27.11	59.31	28.77	58.97	1.03	28.07	30.91	0.54	-0.13	-1.17	0.11	1.67	1.18	10.17	18.17	6.09	-8.99	12.08	-1.24	
59.52	27.33	58.75	27.61	58.03	27.54	58.76	1.03	27.49	31.27	0.55	-0.05	-1.43	0.04	1.65	0.40	10.13	18.13	6.15	-9.73	11.98	-1.34	
58.81	27.13	58.75	28.28	58.50	26.90	58.68	1.02	27.44	31.25	0.55	0.11	-0.56	-0.20	1.65	-2.25	10.13	18.11	6.15	-12.39	11.96	-1.71	
58.75	27.21	57.45	27.13	58.03	27.93	58.08	1.01	27.42	30.65	0.54	0.95	-1.13	-0.84	1.69	-9.41	10.19	17.99	6.04	-19.61	11.95	-2.77	
59.21	28.25	58.57	26.24	58.83	26.74	58.87	1.03	27.08	31.79	0.55	0.21	-1.36	-0.15	1.61	-1.67	10.07	18.15	6.24	-11.75	11.90	-1.59	
57.68	25.68	59.09	27.47	58.33	26.40	58.37	1.02	26.52	31.85	0.56	0.47	-2.06	-0.23	1.61	-2.53	10.07	18.05	6.25	-12.60	11.80	-1.72	
57.66	26.52	58.74	28.02	58.00	27.74	58.13	1.01	27.43	30.70	0.54	1.01	-0.94	-1.07	1.68	-12.01	10.19	18.00	6.05	-22.20	11.95	-3.13	
59.15	28.90	58.28	27.03	58.16	27.42	58.53	1.02	27.78	30.75	0.54	0.68	-0.54	-1.27	1.68	-14.03	10.18	18.08	6.06	-24.21	12.02	-3.38	
																						-2.11
2mm	Sample 1	Sample 2			Sample 3			$\Phi_{radia n}$	$\gamma_{avg.}$	θ	$\theta_{radia n}$	$\Delta\Phi$	$\Delta\theta$	k	$\cot\theta$	$2CK_{cos\Phi}$	$L_{cos\theta}$	$2C_{sin\Phi}$	$L_{sin\theta}$	$2CK_{cos\Phi-L_{cos\theta}}$	$2C_{sin\Phi-L_{sin\theta}}$	PR
		Φ	γ	Φ	γ	Φ	γ															
57.86	24.66	57.05	22.89	59.37	25.93	58.09	1.01	24.49	33.60	0.59	0.76	-3.86	-0.20	1.51	-2.19	9.87	18.00	6.56	-12.06	11.44	-1.59	
58.41	25.79	58.63	24.94	58.93	24.97	58.66	1.02	25.23	33.42	0.58	0.05	-3.59	-0.01	1.52	-0.16	9.89	18.11	6.53	-10.05	11.58	-1.32	
57.82	24.51	57.65	24.07	57.64	23.23	57.71	1.01	23.94	33.77	0.59	1.09	-3.08	-0.35	1.50	-4.01	9.85	17.92	6.59	-13.86	11.33	-1.83	
58.24	25.17	58.52	24.83	59.04	24.53	58.60	1.02	24.84	33.76	0.59	0.42	-4.23	-0.10	1.50	-1.10	9.85	18.10	6.58	-10.95	11.51	-1.42	
58.31	25.84	58.24	25.67	57.86	25.03	58.14	1.01	25.51	32.63	0.57	0.94	-2.19	-0.43	1.56	-4.80	9.98	18.01	6.39	-14.78	11.62	-1.99	
58.00	24.59	56.96	25.36	57.25	24.23	57.40	1.00	24.73	32.68	0.57	1.44	-2.89	-0.58	1.56	-5.69	9.97	17.86	6.40	-15.66	11.46	-2.13	
60.13	24.69	59.09	24.59	58.23	24.70	59.15	1.03	24.66	34.49	0.60	-0.01	-4.73	0.00	1.46	0.03	9.77	18.20	6.71	-9.73	11.49	-1.23	
57.50	22.60	57.05	22.94	57.19	23.11	57.25	1.00	22.89	34.36	0.60	1.97	-4.15	-0.47	1.46	-5.44	9.78	17.83	6.69	-15.23	11.14	-2.00	
																						-1.69

3mm	Sample 1		Sample 2		Sample 3		$\Phi_{avg.}$	$\theta_{radia n}$	$\Delta\Phi$	$\Delta\theta$	k	$\cot\theta$	2CK cosΦ	L cos θ	2C sin Φ	L sin θ	2CK cosΦ- L cos θ	2C sin Φ- L sin θ	PR		
	Φ	γ	Φ	γ	Φ	γ															
54.91	17.07	55.44	17.12	56.31	19.44	55.55	0.97	17.88	37.68	0.66	3.29	-7.94	-0.41	1.29	-4.97	9.38	17.48	7.24	-14.35	10.24	-1.81
60.54	23.79	61.70	23.70	61.01	24.14	61.08	1.07	23.87	37.21	0.65	-2.37	-7.37	0.32	1.32	3.29	9.44	18.56	7.17	-6.14	11.39	-0.71
55.77	21.70	54.28	20.38	54.91	20.75	54.99	0.96	20.94	34.04	0.59	3.81	-3.36	-1.13	1.48	-13.79	9.82	17.36	6.63	-23.61	10.73	-3.26
58.52	24.48	58.92	25.40	58.77	24.09	58.74	1.03	24.66	34.08	0.59	0.28	-4.55	-0.08	1.48	-0.69	9.82	18.12	6.64	-10.50	11.48	-1.35
57.50	26.31	57.40	25.12	57.30	24.53	57.40	1.00	25.32	32.08	0.56	1.68	-1.65	-1.02	1.60	-11.59	10.04	17.86	6.29	-21.63	11.57	-2.98
54.69	22.93	56.31	23.04	54.61	22.29	55.20	0.96	22.75	32.45	0.57	3.64	-2.66	-1.37	1.57	-16.53	10.00	17.41	6.36	-26.53	11.05	-3.78
62.26	21.36	62.29	20.98	61.68	21.44	62.07	1.08	21.26	40.81	0.71	-2.94	-11.05	0.27	1.16	2.64	8.97	18.73	7.75	-6.33	10.99	-0.67
57.67	17.44	56.56	16.41	56.39	16.17	56.87	0.99	16.67	40.20	0.70	2.34	-9.98	-0.23	1.18	-2.72	9.05	17.75	7.65	-11.77	10.11	-1.38
																					-1.99
4mm	Sample 1		Sample 2		Sample 3		$\Phi_{avg.}$	$\theta_{radia n}$	$\Delta\Phi$	$\Delta\theta$	k	$\cot\theta$	2CK cosΦ	L cos θ	2C sin Φ	L sin θ	2CK cosΦ- L cos θ	2C sin Φ- L sin θ	PR		
	Φ	γ	Φ	γ	Φ	γ															
53.5	9.5	54.0	10.3	54.4	12.2	54.0	0.9	10.7	43.3	0.8	4.9	-13.6	-0.4	1.1	-4.5	8.6	17.1	8.1	-13.1	9.0	-1.5
63.7	19.8	64.7	20.8	63.4	20.4	64.0	1.1	20.3	43.6	0.8	-5.2	-13.8	0.4	1.0	3.5	8.6	19.0	8.2	-5.0	10.9	-0.5
52.5	18.1	51.9	16.8	52.2	17.9	52.2	0.9	17.6	34.6	0.6	6.6	-3.9	-1.7	1.4	-21.7	9.8	16.8	6.7	-31.5	10.0	-4.5
58.7	25.0	58.3	23.6	58.6	23.9	58.5	1.0	24.2	34.3	0.6	0.5	-4.8	-0.1	1.5	-1.2	9.8	18.1	6.7	-11.0	11.4	-1.4
58.0	25.5	57.8	25.4	57.6	26.0	57.8	1.0	25.6	32.1	0.6	1.3	-1.7	-0.8	1.6	-8.7	10.0	17.9	6.3	-18.8	11.6	-2.6
51.1	18.5	52.5	19.5	50.9	19.5	51.5	0.9	19.2	32.4	0.6	7.3	-2.6	-2.9	1.6	-37.6	10.0	16.6	6.3	-47.6	10.3	-7.3
64.4	19.4	64.7	19.0	63.2	18.2	64.1	1.1	18.8	45.3	0.8	-5.0	-15.5	0.3	1.0	3.0	8.3	19.1	8.4	-5.4	10.7	-0.5
54.6	9.4	54.8	9.8	54.1	9.0	54.5	1.0	9.4	45.1	0.8	4.7	-14.9	-0.3	1.0	-3.9	8.4	17.3	8.4	-12.3	8.9	-1.4
																					-2.47
5mm	Sample 1		Sample 2		Sample 3		$\Phi_{avg.}$	$\theta_{radia n}$	$\Delta\Phi$	$\Delta\theta$	k	$\cot\theta$	2CK cosΦ	L cos θ	2C sin Φ	L sin θ	2CK cosΦ- L cos θ	2C sin Φ- L sin θ	PR		
	Φ	γ	Φ	γ	Φ	γ															
52.47	11.50	53.65	12.02	53.67	12.56	53.26	0.93	12.03	41.24	0.72	5.58	-11.50	-0.49	1.14	-6.16	8.91	16.99	7.81	-15.07	9.18	-1.87
61.57	21.64	62.46	19.95	61.82	20.74	61.95	1.08	20.78	41.17	0.72	-3.24	-11.34	0.29	1.14	2.85	8.92	18.71	7.80	-6.07	10.91	-0.64
54.40	12.85	54.27	13.02	54.59	14.91	54.42	0.95	13.59	40.83	0.71	4.38	-10.14	-0.43	1.16	-5.33	8.97	17.24	7.75	-14.30	9.49	-1.74
57.60	17.17	57.86	18.06	57.77	18.69	57.74	1.01	17.97	39.77	0.69	1.28	-10.24	-0.12	1.20	-1.41	9.11	17.93	7.58	-10.52	10.35	-1.22
55.96	19.21	56.06	18.09	55.27	17.16	55.76	0.97	18.16	37.61	0.66	3.31	-7.18	-0.46	1.30	-5.51	9.39	17.53	7.23	-14.89	10.29	-1.88
53.19	15.72	54.50	16.36	54.70	16.41	54.13	0.94	16.16	37.97	0.66	4.71	-8.18	-0.58	1.28	-7.15	9.34	17.18	7.29	-16.49	9.89	-2.14
63.86	16.95	61.84	16.84	61.59	14.02	62.43	1.09	15.94	46.49	0.81	-3.29	-16.73	0.20	0.95	1.93	8.16	18.79	8.59	-6.23	10.20	-0.58
54.85	8.91	54.35	9.21	54.64	7.40	54.61	0.95	8.51	46.11	0.80	4.60	-15.89	-0.29	0.96	-3.55	8.22	17.28	8.54	-11.77	8.74	-1.29
																					-1.42
6mm	Sample 1		Sample 2		Sample 3		$\Phi_{avg.}$	$\theta_{radia n}$	$\Delta\Phi$	$\Delta\theta$	k	$\cot\theta$	2CK cosΦ	L cos θ	2C sin Φ	L sin θ	2CK cosΦ- L cos θ	2C sin Φ- L sin θ	PR		
	Φ	γ	Φ	γ	Φ	γ															
54.10	12.75	52.75	11.78	54.43	11.68	53.76	0.94	12.07	41.69	0.73	5.09	-11.95	-0.43	1.12	-5.33	8.85	17.10	7.88	-14.18	9.22	-1.73
59.79	18.16	58.24	16.82	59.13	16.20	59.05	1.03	17.06	42.00	0.73	-0.34	-12.16	0.03	1.11	0.31	8.81	18.18	7.93	-8.50	10.25	-0.92
57.77	10.86	56.17	9.92	56.44	10.16	56.79	0.99	10.32	46.48	0.81	2.01	-15.79	-0.13	0.95	-1.48	8.16	17.74	8.59	-9.64	9.15	-1.00
55.09	9.95	56.08	11.23	56.17	10.45	55.78	0.97	10.54	45.24	0.79	3.24	-15.71	-0.21	0.99	-2.46	8.34	17.53	8.41	-10.80	9.12	-1.18
54.04	13.67	54.62	11.54	54.46	11.92	54.37	0.95	12.38	42.00	0.73	4.70	-11.56	-0.41	1.11	-5.02	8.81	17.23	7.93	-13.83	9.30	-1.65
56.73	15.91	57.93	15.41	57.70	14.17	57.45	1.00	15.16	42.29	0.74	1.38	-12.50	-0.11	1.10	-1.26	8.77	17.87	7.97	-10.03	9.90	-1.11
60.02	11.60	58.75	12.27	58.58	9.24	59.12	1.03	11.04	48.08	0.84	0.02	-18.31	0.00	0.90	-0.01	7.92	18.19	8.82	-7.93	9.38	-0.76
55.25	6.94	55.64	7.57	54.97	6.88	55.29	0.96	7.13	48.16	0.84	3.93	-17.94	-0.22	0.90	-2.64	7.90	17.43	8.83	-10.55	8.60	-1.10
																					-1.18
7mm	Sample 1		Sample 2		Sample 3		$\Phi_{avg.}$	$\theta_{radia n}$	$\Delta\Phi$	$\Delta\theta$	k	$\cot\theta$	2CK cosΦ	L cos θ	2C sin Φ	L sin θ	2CK cosΦ- L cos θ	2C sin Φ- L sin θ	PR		
	Φ	γ	Φ	γ	Φ	γ															
53.02	12.67	52.57	12.76	53.81	11.88	53.13	0.93	12.44	40.70	0.71	5.71	-10.96	-0.52	1.16	-6.63	8.98	16.96	7.73	-15.61	9.23	-1.97
58.82	17.90	58.06	16.97	59.33	18.29	58.74	1.03	17.72	41.02	0.72	-0.03	-11.18	0.00	1.15	0.02	8.94	18.12	7.78	-8.92	10.34	-0.99
57.53	7.60	57.72	7.44	57.51	6.73	57.59	1.01	7.26	50.33	0.88	1.21	-19.65	-0.06	0.83	-0.70	7.56	17.90	9.12	-8.26	8.78	-0.78
57.36	6.94	57.28	6.01	58.15	7.57	57.60	1.01	6.84	50.76	0.89	1.42	-21.23	-0.07	0.82	-0.76	7.50	17.90	9.18	-8.26	8.72	-0.77
52.85	12.92	53.79	12.81	51.81	12.42	52.82	0.92	12.72	40.10	0.70	6.26	-9									

9mm	Sample 1		Sample 2			Sample 3			$\Phi_{avg.}$	$\theta_{avg.}$	θ	$\theta_{radia n}$	$\Delta\Phi$	$\Delta\theta$	k	cot θ	ZCK cos Φ	L cos θ	ZC sin Φ	L sin θ	2CK cos Φ -L cos θ	2C sin Φ -L sin θ	PR
	Φ	γ	Φ	γ	Φ	γ	$\Phi_{avg.}$	$\theta_{avg.}$															
55.83	8.25	55.80	7.61	56.61	7.10	56.08	0.98	7.65	48.43	0.85	2.77	-18.69	-0.15	0.89	-1.75	7.86	17.59	8.87	-9.61	8.73	-0.98		
58.00	10.94	57.45	9.44	58.46	9.61	57.97	1.01	10.00	47.97	0.84	0.74	-18.14	-0.04	0.90	-0.46	7.93	17.97	8.80	-8.39	9.17	-0.83		
56.91	5.90	58.00	6.39	57.46	5.79	57.45	1.00	6.03	51.43	0.90	1.34	-20.74	-0.06	0.80	-0.74	7.39	17.87	9.26	-8.13	8.61	-0.75		
57.88	6.04	58.24	5.53	58.85	7.05	58.32	1.02	6.21	52.12	0.91	0.70	-22.59	-0.03	0.78	-0.34	7.28	18.04	9.35	-7.62	8.69	-0.68		
56.00	7.19	56.24	9.42	55.70	8.16	55.98	0.98	8.25	47.73	0.83	3.10	-17.29	-0.18	0.91	-2.12	7.97	17.57	8.77	-10.10	8.80	-1.04		
58.37	11.14	58.32	11.15	57.62	9.51	58.10	1.01	10.60	47.50	0.83	0.74	-17.71	-0.04	0.92	-0.47	8.01	18.00	8.74	-8.47	9.26	-0.84		
59.16	7.23	57.62	5.44	58.00	6.35	58.26	1.02	6.34	51.92	0.91	0.88	-22.15	-0.04	0.78	-0.44	7.31	18.03	9.33	-7.75	8.70	-0.70		
57.53	5.86	57.18	6.31	57.10	5.75	57.27	1.00	5.97	51.29	0.90	1.95	-21.08	-0.09	0.80	-1.06	7.41	17.83	9.25	-8.47	8.59	-0.79		
10mm	Sample 1		Sample 2			Sample 3			$\Phi_{avg.}$	$\theta_{avg.}$	θ	$\theta_{radia n}$	$\Delta\Phi$	$\Delta\theta$	k	cot θ	ZCK cos Φ	L cos θ	ZC sin Φ	L sin θ	2CK cos Φ -L cos θ	2C sin Φ -L sin θ	PR
Φ	γ	Φ	γ	Φ	γ	$\Phi_{avg.}$	$\theta_{avg.}$																
57.969	6.629	58.067	6.907	57.74	6.027	57.926	1.011	6.521	51.405	0.8972	0.921	-21.67	-0.043	0.798	-0.478	7.3922	17.9641	9.262	-7.870644	8.702432	-0.72		
58.378	7.88	58.696	7.096	58.48	7.21	58.517	1.0213	7.3953	51.122	0.8922	0.195	-21.29	-0.009	0.806	-0.101	7.4378	18.0793	9.225	-7.53907	8.854284	-0.69		
58.449	7.059	57.817	6.394	57.97	6.246	58.08	1.0137	6.5663	51.514	0.8991	0.719	-20.83	-0.035	0.795	-0.387	7.3746	17.9943	9.276	-7.76132	8.718622	-0.71		
57.653	6.942	57.811	6.615	57.29	6.086	57.584	1.005	6.5477	51.036	0.8908	1.436	-21.51	-0.067	0.809	-0.759	7.4516	17.8962	9.214	-8.21052	8.682672	-0.76		
57.611	6.282	58.663	7.07	58.23	6.502	58.169	1.0152	6.618	51.551	0.8997	0.908	-21.12	-0.043	0.794	-0.481	7.3685	18.0117	9.28	-7.8495	8.731209	-0.71		
59.115	7.245	58.442	6.467	56.22	4.727	57.917	1.0108	6.1463	51.771	0.9036	0.921	-21.98	-0.042	0.788	-0.472	7.3329	17.9623	9.309	-7.804704	8.653675	-0.71		
59.522	7.976	57.947	5.974	58.18	8.049	58.549	1.0219	7.333	51.216	0.8939	0.587	-21.45	-0.027	0.804	-0.303	7.4226	18.0855	9.237	-7.725486	8.848231	-0.7		
58.213	6.96	56.912	6.194	56.87	5.962	57.333	1.0006	6.372	50.961	0.8894	1.881	-20.75	-0.091	0.811	-1.038	7.4637	17.8466	9.204	-8.501379	8.642521	-0.8		
11mm	Sample 1		Sample 2			Sample 3			$\Phi_{avg.}$	$\theta_{avg.}$	θ	$\theta_{radia n}$	$\Delta\Phi$	$\Delta\theta$	k	cot θ	ZCK cos Φ	L cos θ	ZC sin Φ	L sin θ	2CK cos Φ -L cos θ	2C sin Φ -L sin θ	PR
Φ	γ	Φ	γ	Φ	γ	$\Phi_{avg.}$	$\theta_{avg.}$																
59.071	5.487	59.073	5.692	58.72	6.199	58.956	1.029	5.7927	53.163	0.9279	-0.109	-23.43	0.0047	0.749	0.0509	7.1045	18.1636	9.484	-7.053634	8.679434	-0.61		
59.759	6.617	59.112	5.685	59.11	6.383	59.325	1.0354	6.2283	53.097	0.9267	-0.613	-23.26	0.0264	0.751	0.2852	7.1155	18.2337	9.476	-6.830308	8.757761	-0.59		
58.786	5.586	58.627	4.43	58.89	6.155	58.767	1.0257	5.4077	53.36	0.931	-0.228	-0.001	0.744	-0.015	0.7072	18.1275	9.508	-7.087149	8.619047	-0.61			
59.3	6.296	60.038	6.208	58.78	5.219	59.372	1.0362	5.9077	53.464	0.9331	-0.351	-23.94	0.0147	0.741	0.1585	7.0546	18.2424	9.521	-6.896103	8.721119	-0.59		
59.143	4.959	59.175	6.045	59.25	6.149	59.19	1.0331	5.7177	53.472	0.9333	-0.113	-23.04	0.0049	0.741	0.0531	7.0532	18.2081	9.522	-7.000146	8.685756	-0.6		
59.973	6.185	60.096	6.85	57.75	4.842	59.272	1.0345	5.959	53.313	0.9305	-0.434	-23.52	0.0184	0.745	0.1999	7.0797	18.2236	9.503	-6.879849	8.720929	-0.59		
59.729	5.716	59.513	5.767	58.16	5.761	59.134	1.0321	5.748	53.386	0.9318	0.002	-23.62	-1E-04	0.743	-0.001	7.0675	18.1975	9.512	-7.068608	8.685795	-0.6		
58.806	5.182	57.792	4.923	57.97	6.07	58.191	1.0156	5.3917	52.799	0.9215	1.024	-22.58	-0.045	0.759	-0.506	7.1647	18.0159	9.439	-7.67116	8.577151	-0.68		
12mm	Sample 1		Sample 2			Sample 3			$\Phi_{avg.}$	$\theta_{avg.}$	θ	$\theta_{radia n}$	$\Delta\Phi$	$\Delta\theta$	k	cot θ	ZCK cos Φ	L cos θ	ZC sin Φ	L sin θ	2CK cos Φ -L cos θ	2C sin Φ -L sin θ	PR
Φ	γ	Φ	γ	Φ	γ	$\Phi_{avg.}$	$\theta_{avg.}$																
60.881	6.554	59.534	5.162	60.57	6.495	60.329	1.0259	6.0703	54.259	0.947	-1.482	-24.52	0.0604	0.772	0.6343	6.9218	18.4204	9.618	-6.287503	8.802124	-0.51		
61.618	6.866	60.781	6.244	59.69	6.242	60.1953	1.0593	6.4507	54.244	0.9467	-1.983	-24.41	0.0812	0.772	0.843	6.9243	18.487	9.616	-6.081316	8.870496	-0.49		
60.622	5.773	60.046	4.427	59.9	4.509	60.188	1.0055	4.903	55.285	0.9649	-1.39	-24.6	0.0565	0.693	0.5953	6.7485	18.3945	9.741	-6.153109	8.653802	-0.49		
60.111	4.449	60.745	5.356	60.2	4.772	60.351	1.0533	4.859	55.492	0.9685	-1.331	-25.96	0.0512	0.687	0.5375	6.7133	18.4243	9.765	-6.175804	8.659372	-0.49		
61.042	5.513	60.792	5.647	60.22	4.261	60.683	1.0591	5.1403	55.493	0.9694	-1.006	-25.11	0.0639	0.688	0.6638	6.7046	18.4848	9.771	-6.040818	8.713899	-0.48		
61.796	6.135	61.535	6.133	60.28	4.464	61.202	1.0682	5.5773	55.625	0.9708	-2.364	-23.84	0.0915	0.684	0.9346	6.6906	18.5781	9.781	-5.756009	8.797602	-0.45		
61.828	6.115	60.383	6.926	59.78	4.737	60.665	1.0588	5.926	54.739	0.9554	-1.528	-24.97	0.0612	0.707	0.6355	6.8411	18.4815	9.676	-6.205596	8.805618	-0.5		
60.396	5.563	58.615	4.793	59.32	4.548	59.445	1.0375	4.968	54.477	0.9508	-0.23	-24.26	0.0095	0.714	0.1023	6.8853	18.2561	9.644	-6.782942	8.611673	-0.64		
13mm	Sample 1		Sample 2			Sample 3			$\Phi_{avg.}$	$\theta_{avg.}$	θ	$\theta_{radia n}$	$\Delta\Phi$	$\Delta\theta$	k	cot θ	ZCK cos Φ	L cos θ	ZC sin Φ	L sin θ	2CK cos Φ -L cos θ	2C sin Φ -L sin θ	